Fabrication and Characterization of Surface Grating DFB Lasers Using AlGaAs/GaAs Quantum Well Material

A Thesis submitted for the degree of Doctor of Philosophy
in the Faculty of Engineering, University of Glasgow

by

Manuel Vitor A. Moreira

January, 1997

ProQuest LLC.
789 East Eisenhower Parkway
P.O. Box 1346
Ann Arbor, MI 48106 – 1346

Sweet is the melody, so hard to come by
It is so hard to make every note bend just right
You lay down the hours and leave not one trace
But a tune for the dancing is there in its place

(Iris DeMent)

This thesis is dedicated to my family

Acknowlegments

I would like to thank my supervisor Professor Richard De La Rue for his advice and useful suggestions during the project, and also for accepting me as a research student in the Optoelectronics Group, Department of Electronics and Electrical Engineering.

I would also like to express my thanks to former Research Assistant Dr. Stephen Ayling for his supervision on many aspects of the experimental and theoretical work, and his very helpful suggestions.

I would like to thank Dr. José Ribera Salcedo and Dr. António Pereira Leite from the Physics Department of Porto University for their support during the project. I am particularly indebted to Dr. Leite for his encouragement, friendship, constant enthusiasm and help concerning this research project.

The help and assistance of members of the Mechanical and Electronic Workshops at Glasgow university is gratefully appreciated. Special thanks also go to Joan Carson, Margaret Henderson, Linda Pollock and Lois Hobbs in the clean room; Jim Gray for his help with the laser systems and bonding; Dr. S. Thoms and D. McIntyre for their assistance in the electron-beam writing; Dr. Bill Parkes in the dry-etching section.

The Physics Department of Porto University is to be thanked for providing office, library and word processing facilities.

During the project I made many friends and I thank them all for their encouragement, in particular João, Pedro, Vojta, Viorel, and Lina for their friendship, advice and help during my stay at Glasgow.

The Junta Nacional de Investigação Científica e Tecnológica (JNICT) is acknowledged for providing financial support for the project, under a CIENCIA and PRAXIS XXI studentship.

Finally, and most of all, I would like to thank my family for their constant support throughout my period of study. I am particularly indebted to my sister Gustava, my uncle Victor and my father for their help in particularly difficult moments.

Abstract

The aim of the research project was to fabricate and characterize surface grating DFB lasers, using AlGaAs/GaAs quantum well material, and also demonstrate its potential for integration. The operation of this surface grating DFB laser combines both lateral optical confinement and distributed feedback provided by gratings etched along the side of the laser stripe in the top cladding layer. The material structure was optimized for this type of device, consisting of two 80A GaAs quantum wells surrounded by a 0.7μm thick 40% AlGaAs top cladding layer and a 0.5μm thick 80% AlGaAs lower cladding layer. The typical lasing wavelength was about 860nm.

Research concentrated on establishing a reliable fabrication process for surface 3^{rd}-order, 2^{nd}-order and 1^{st}-order gratings DFB lasers using a combination of electron-beam lithography technology and reactive ion etching (RIE). The fabrication process of 3^{rd}-order and 2^{nd}-order grating structures was optimised and consisted of transferring an e-beam generated pattern to a 150 nm thick SiO_2 layer. This patterned SiO_2 layer was then used as a dry-etching mask of the AlGaAs/GaAs material.

Measurement of the coupling coefficient of surface 3^{rd}-order grating DFB waveguides was performed using a transmission technique. Maximum coupling coefficient values of $10cm^{-1}$ and $15\ cm^{-1}$ were measured in 1 μm deep surface grating waveguides, respectively for fundamental and second transverse modes. Dependence of the coupling coefficient on the stripe width and grating etch depth were studied, which allowed optimization of the waveguide. The light-current characteristics and spectral behaviour of surface 3^{rd}-order, 2^{nd}-order, and 1^{st}-order grating DFB lasers were assessed in pulsed and CW operation. Typical values for threshold current, threshold current density, and slope efficiency were respectively, 25mA, 1400A cm^{-2}, and 0.25mW/mA per facet in CW operation for 500 μm long devices. The stopband width was measured near threshold in surface 3^{rd}-order grating DFB lasers; using this value, the coupling coefficient was estimated to be $\kappa=9cm^{-1}$. The dependence of the FP and DFB modes on the temperature of operation was measured, in uncoated devices, to be 0.36nm/°C and 0.066nm/°C, respectively.

A flared amplifier was integrated with a surface grating DFB laser using electron-beam lithography, photolithography, and reactive ion etching (RIE). For $I_{DFB}=90mA$, the device external quantum efficiency was measured to be 0.125mW/mA and an output power as high as 45mW CW was achieved.

Table of Contents

List of Tables

List of Illustrations

Chapter 1: Introduction

1.1 Introduction

Distributed feedback (DFB) lasers have unique performance characteristics that give them distinct advantages over conventional Fabry-Perot lasers. These advantages are fundamentally related to: (i) Wavelength selectivity; (ii) Optical emission linewidth; (iii) Stability of the emitted wavelength with injection current and temperature of operation; and (iv) Potential for integration. This makes the DFB laser an useful source for a variety of important applications, such as coherent optical communications, interferometric optical measurements, and high-resolution laser spectroscopy.

The lasing wavelength in DFB lasers can be easily selected by changing the spatial period of the grating. It is therefore simple, for instance, to fabricate DFB laser sources emitting on different wavelengths, from the same epitaxial material [1.1]. The modulation bandwidth is ultimately limited by the linewidth of the laser source. In long-cavity AlGaAs/GaAs multi-quantum well DFB lasers emitting at 0.86μm, a minimum linewidth of 1.5MHz has been reported [1.2]. Better results have been achieved in three-section corrugation-pitch-modulated DFB (CPM-DFB) lasers emitting at 1.55μm with a spectral linewidth of less than 98kHz [1.3]. The lasing wavelength of the DFB lasers follows only the temperature dependence of the refractive index. The DFB laser presents a typical temperature drift of 0.06-0.08nm/°C, whereas the conventional Fabry-Perot laser presents a value of 0.3-0.4nm/°C. The shift in the lasing wavelength is a problem when the laser is used both in CW and pulsed operation. In CW operation, the wavelength can become mismatched from the lowest dispersion wavelength of an optical fibre. In pulsed operation, the temperature changes in the junction during the pulses result in chirp. This aspect is particularly important for applications such as optical processing involving wavelength filtering or wavelength division multiplexing (WDM). Because DFB lasers use a planar surface geometry and do not require cleaved facets, they are also useful as optical sources in integrated optics based on miniature optical waveguide components, such as optical amplifiers, modulators and passive waveguides using disordering of quantum well structures[1.4,1.5].

Until recently, most DFB lasers have been fabricated by forming a feedback grating parallel to the growth plane, either below or above the active region, during a growth interruption. This approach is complicated by the need for epitaxial regrowth, particularly for short wavelength devices with high Al content and long wavelength GaSb based devices. A new method for incorporating distributed feedback in a laser structure by means of lateral

gratings and a single growth step has been demonstrated by Miller et al.[1.6,1.7]. The necessary distributed feedback was provided by etched gratings in the top cladding laser structure, on either side of the contact stripe. The advantages of this approach are that the laser structures can be fabricated in any material system with any standard growth process, the relatively simple fabrication, and the possibility of full characterization of the wafer before processing into DFB lasers.

Fig.1.1 summarises distributed feedback structures using surface gratings proposed so far.

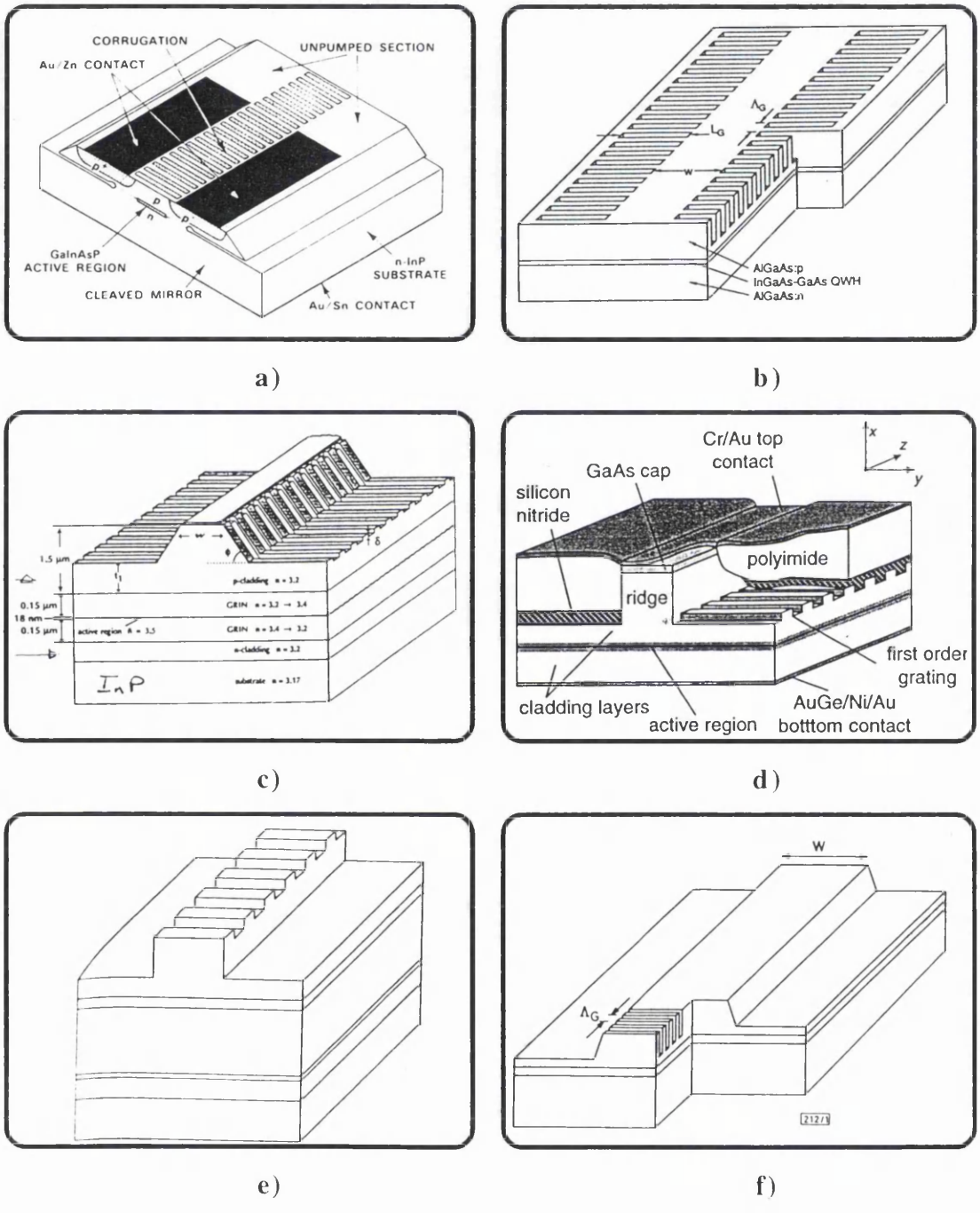

Fig.1.1: Schematic drawings of distributed feedback lasers using surface grating structures

One way to eliminate the regrowth problem is to rely on evanescent coupling of the electromagnetic field to a surface grating. This approach has been demonstrated by etching the grating directly over the waveguide and injecting current from the side (Fig.1.1 **a)** Liau et al. [1.8]), or by etching the grating through the cap and upper cladding layer to provide the lateral index guiding for the *ridge* and selective feedback (Fig.1.1 **b)** Miller at al.[1.6-1.7]). Using the later technique, a laser array consisting of fourteen elements with a cavity length of 430μm [1.9], and a parallel configuration of four uncoupled emitters with 9A variation between adjacent laser periods [1.10] have been demonstrated.

Alternative approaches are to etch the ridge first and then define the grating on the sidewalls (Fig.1.1 **c)** Wong et al. [1.11]) or on either side of the ridge (Fig.1.1 **d)** Martin et al. [1.12-1.14]). In the sidewall-grating structure, computer simulations have shown a coupling coefficient κ of 54.8 cm^{-1} for a grating etch depth of 200 nm. It was found that 33.5% of the coupling is due to the sidewall gratings, and the remaining 66.5% to the gratings on the flat surfaces. In the laser structure proposed by Martin et al, a theoretical coupling coefficient of 8.6 cm^{-1} was determined by applying coupled-mode theory to a rectangular grating with 70 nm etch depth and 16.6% duty cycle.

Fig.1.1 **e)** and **f)** show other proposed laser structures where surface gratings are used. Korn et al. [1.15] demonstrated a laser structure (Fig.1.1 **e)**), in which the grating is patterned on top of the ridge by e-beam lithography followed by reactive ion etching (RIE). The amplitude of the grating must be in the range 50-80nm to provide sufficient feedback (coupling coefficient $\kappa > 100\ cm^{-1}$). A ridge waveguide distributed Bragg reflector (RW-DBR) laser was proposed by Smith et al. [1.16]. The resonant cavity is formed by a cleaved facet and a single DBR (Fig.1.1 **f)**) which is dry etched to a depth sufficiently near the active region to provide coupling for wavelength selective feedback.

In the research work presented in this thesis, deep surface grating structures as proposed by Miller et al. were chosen. The main aim of the author is to demonstrate that these structures are particularly suitable to fabricate DFB laser sources for integration with other optoelectronic components.

1.2 Synopsis

The objective of the research work described in this thesis was to fabricate and characterize surface grating DFB lasers fabricated using different Bragg-orders and demonstrate integration of flared optical amplifiers with surface grating DFB lasers

Chapter 2 reviews several techniques proposed to reduce the hole burning effects on both the light-current (L-I) characteristics and spectral behaviour of $\lambda/4$-shifted DFB lasers. The final section of the chapter discusses the monolithic integration of a master oscillator with a power amplifier (MOPA).

In Chapter 3, the theory of periodic structures and DFB lasers as well as calculation of the coupling coefficient and radiation power losses in surface grating structures are presented. The coupled-mode theory is derived for analysing passive periodic waveguides and also distributed feedback lasers. The perturbation solution of the Floquet-Bloch expansion is used to calculate radiation losses introduced by higher-order gratings.

Analysis and improvements in the epitaxial wafer structure for use in surface grating DFB laser is described in Chapter 4. In particular, an asymmetric material structure is designed so that the internal quantum efficiency, optical losses, QW gain parameter,g_o, transparency current J_t and the interaction between the guided electric field and gratings are optimized.

Chapter 5 deals with the fabrication of surface 3^{rd}-order, 2^{nd}-order, and 1^{st}-order grating DFB lasers, giving details of the electron-beam lithographic, photolithographic and reactive ion etching (RIE) processes. The Chapter also concentrates on the origin and characteristics of stitching errors.

Methods for measurement of the laser characteristics, experimental results obtained and its interpretation are discussed in Chapter 6. The measurement of the coupling coefficient, κ, in surface grating DFB waveguides is performed using a transmission technique. The L-I curve and spectral behaviour with injection current and temperature of operation for surface 3^{rd}-order, 2^{nd}-order, and 1^{st}-order grating DFB lasers in pulsed and CW operation are thoroughly described. In the last section, the lasing characteristics of an integrated flared amplifier with surface grating DFB laser are also presented.

Finally, Chapter 7 contains the conclusions of the research work and discusses the areas of future work, which can be carried out in order to achieve further characterization of the devices and also improvements in terms of performance.

References:

[1.1] M. Nakao, K. Sato, T. Nishida, T. Tamamura, A. Ozawa, Y. Saito, I. Okada, H. Yoshihara, "1.55μm DFB laser array with λ/4-shifted first-order gratings fabricated by x-ray lithography", Electronics Lett., Vol.25, pp. 148-149, (1989)

[1.2] K. Kojima, K. Hara, K. Kameya and K. Kyuma, "Narrow-linewidth AlGaAs/GaAs multiple quantum well distributed feedback lasers", Electronics Lett., Vol.25, pp. 240-241, (1989)

[1.3] M. Okai and T. Tsuchiya, "Tuneable DFB lasers with ultra-narrow spectral linewidth", Electronics Lett., Vol.29, pp. 349-351, (1993)

[1.4] J.H. Marsh, S.I. Hansen, A.C. Bryce and R.M. De LaRue, "Applications of neutral impurity disordering in fabricating low-loss optical waveguides and integrated waveguide devices", Optical and Quantum Electronics, Vol.23, pp.S941-s957, (1991)

[1.5] I. Gontijo, T. Krauss, R.M. De La Rue, J. S. Roberts and J. H. Marsh, "Very low loss extended cavity GaAs/AlGaAs lasers made by impurity-free vacancy diffusion", Electronic Lett., Vol.30, pp.145-146, (1994)

[1.6] L.M. Miller, J.T. Verdeyen, J.J. Coleman, R.P. Bryan, J.J. Alwan, K.J. Beernink, J.S. Hughes, and T.M. Cockerill, "A distributed feedback ridge waveguide quantum well heterostructure laser", IEEE Photonics Techn. Lett., Vol.3, pp.6-8, 1991

[1.7] L.M. Miller, K.J. Beernink, J.T. Verdeyen, J.J. Coleman, J.S. Hughes, G.M. Smith, R.P. Bryan, J.Honing, and T.M. Cockerill, "Characterization of an InGaAs-GaAs-AlGaAs strained-layer distributed-feedback ridge-waveguide quantum-well heterostructure laser", IEEE Photonics Techn. Lett., Vol.4, pp.296-299, 1992

[1.8] Z.L. Liau, D.C. Flanders, J.N.Walpole, and N.L.Demeo, "A novel GaInAsP/InP distributed feedback laser", Appl. Phys. Lett., Vol.46, pp.221-223, (1985)

[1.9] L.M. Miller, K.J. Beernink, J.T. Verdeyen, J.J. Coleman, J.S. Hughes, G.M. Smith, J. Honig, and T.M. Cockerill, "InGaAs/GaAs/AlGaAs strained-layer distributed feedback ridge waveguide quantum-well heterostructure laser array", Electronic Lett., Vol.27, pp.1943-1945, (1991)

[1.10] L.M. Miller, K.J. Beernink, J.S. Hughes, S.G. Bishop, J.J. Coleman, "Four wavelength distributed feedback ridge waveguide quantum-well heterostructure laser array", Appl. Phys. Lett., Vol.61, pp.2964-2966, (1992)

[1.11] V.V. Wong, W.Y. Choi, J.M. Carter, C.G. Fonstad, H.I. Smith, Y. Chung, and N.Dagli, "Ridge-waveguide sidewalls-grating distributed feedback structures fabricated by x-ray lithography" J. Vac. Sci. Techn. B11, pp.2621-2624, (1993)

[1.12] R.D. Martin, S. Forouhar, S. Keo, R.J. Lang, R.G. Hunsperger, R.Tiberio, and P.F. Chapman, "InGaAs/GaAs/AlGaAs Laterally-coupled distributed feedback (LC-DFB) ridge laser diode", Electronic Lett., Vol.30, pp.1058-1060, (1994)

[1.13] R.D. Martin, S. Forouhar, R.J. Lang, R.Tiberio, and P.F. Chapman, "Laterally coupled distributed feedback laser fabricated with electron-beam lithography and chemically assisted ion-beam etching" J. Vac. Sci. Techn. B12, pp.3476-3749, (1994)

[1.14] R.D. Martin, S. Forouhar, S. Keo, R.J. Lang, R.G. Hunsperger, R.Tiberio, and P.F. Chapman, "CW performance of an InGaAs-GaAs-AlGaAs laterally-coupled distributed feedback (LC-DFB) ridge laser diode", IEEE Photonics Techn. Lett., Vol.7, pp.244-246, 1995

[1.15] M. Korn, T. Korfer, A. Forchel, and P. Roentgen, "First order distributed feedback gratings (92.5-105nm period) for GaInP/AlGaInP lasers emitting in the visible range" J. Vac. Sci. Techn. B8, pp.1404-1407, (1990)

[1.16] G.M. Smith, J.S. Hughes, M.L. Osowski, D.V. Forbes, and J.J. Coleman, "Ridge waveguide distributed Bragg reflector InGaAs/GaAs quantum well lasers", Electronic Lett., Vol.30, pp.651-653, (1994)

Chapter 2: Survey of the Hole Burning Effect and the MOPA Laser Configuration.

2.1 Introduction

The purpose of this review is to discuss techniques for achieving single longitudinal mode (SLM) operation, as well as for reducing hole burning effects both on the light/current and on the spectral characteristics of DFB lasers. Several techniques to provide SLM operation and overcome the problems of the hole-burning effects will be discussed, namely: (i) optimization of the κL product to obtain a constant intensity distribution along the DFB laser cavity; (ii) introduction of a $\lambda/4$ phase shift, located in the centre of the cavity or distributed over a certain section; (iii) use of a DFB laser configuration with multiple phase shift regions; (iv) use of a dual-pitch DFB laser; (v) use of a DFB laser configuration with an amplitude modulated coupling coefficient; (vi) use of a non-uniform injection current scheme; (vii) use of a gain coupling mechanism for DFB action.

The monolithic integration of a master oscillator with a power amplifier (MOPA) is also reviewed. More specifically, early MOPA configurations consisting of either an array of collinear amplifiers and output couplers or a broad-area amplifier are discussed. Approaches for obtaining high power from single mode laser as a master oscillator are presented. In particular, the integration of a flared power amplifier with a single mode diode laser is thoroughly described.

2.2 Spectral Stabilization of DFB lasers

The phenomenon of wave propagation in periodic structures occurs in many branches of physics and technology. For instance, consider the phenomena of X-ray and electron diffraction in crystals, the diffraction of light from the periodic strain variation caused by a sound wave, and the band structures and energy gaps of the phonon spectrum and the energy of electrons in a crystal. There are also many practical devices making use of this phenomenon, among which are the travelling wave tube, the linear particle accelerator, diffraction gratings, holograms, grating-filters, distributed feedback (DFB) lasers, and distributed Bragg reflector (DBR) laser structures which are widely used to make frequency tunable lasers and also vertical-cavity surface-emitting lasers.

The distributed feedback laser was proposed and realized by Kogelnik and Shank [2.1], [2.2], in which Bragg scattering of a spatially periodic variation of index, gain coefficient, or

guide thickness can be used. DFB structures have the advantage of providing better frequency stability of the oscillation mode than cavities formed by partially reflecting mirrors at the ends. However, the mode spectrum of the DFB laser with index coupling as analysed by Kogelnik and Shank [2.1] exhibits a gap at the characteristic Bragg wavelength. In addition, modes of equal threshold occur symmetrically on the two sides of this gap. This threshold degeneracy is a drawback in practical applications in which single-mode operation at a predictable frequency is desired.

To overcome the multilongitudinal mode operation, a quarter-wavelength shifted DFB laser was proposed by Haus and Shank, [2.3]. The main characteristic of the quarter wavelength DFB laser is its single longitudinal mode (SLM) operation, with the lowest threshold gain at the Bragg wavelength, providing a larger threshold gain difference between modes than that of the asymmetric mirror structure DFB laser. There are essentially two kinds of structures that have been used to attain optical phase matching in DFB lasers: (i) a structure with a directly phase shifted corrugation (Sekartedjo et al., [2.4]); (ii) a structure with a nonuniform waveguide structure (Tada et al., [2.5]).

Although $\lambda/4$ shifted DFB lasers operate in a single longitudinal mode operation just above threshold, it has been observed that multilongitudinal mode operation tends to occur as the optical output power is increased. Soda et al [2.9] suggested the spatial hole burning effect as the mechanism responsible for such multilongitudinal mode behaviour at high output power levels*.

So far, several techniques have been proposed to achieve SLM operation and reduce hole burning effects in DFB lasers. We report here on some of them: (i) optimization of the normalized coupling coefficient, κL, so that the intensity distribution in the DFB laser is constant along the longitudinal axis [2.9]; (ii) use of a structure in which the $\lambda/4$ shift is distributed over a section of the laser located in the central region, instead of being located pointedly at the centre of the laser cavity [2.5,2.11,2.16]; (iii) use of a DFB laser configuration with multiple phase-shift regions [2.22]; (iv) use of a dual-pitch DFB laser [2.27]; (v) use of a DFB laser configuration with an amplitude modulated coupling coefficient [2.28]; (vi) use of a non-uniform injection current scheme[2.32]; and (vii) gain coupling effects[2.34].

Technique 1: Optimization of the normalized coupling coefficient.

Soda et al, [2.9] assumed that the mechanism responsible for multilongitudinal mode operation in $\lambda/4$ shifted DFB lasers is the spatial refractive index distribution induced by spatial hole burning, which is caused by the concentration of optical power in the centre of

the DFB laser. The causes of the spatial hole burning mechanism can be outlined as follows. As the injection current is increased, the light intensity in the laser also increases. In the $\lambda/4$ shifted DFB laser, the distribution of the light intensity along the laser axis is not uniform. In the strongly coupled case, the light concentrates near the centre. Thus, the carrier density in the active region near the centre is reduced remarkably by the stimulated recombination. Such a deformed carrier density profile causes a change in the spatial refractive index. In a DFB laser, a small change in the spatial refractive index drastically affects the lasing modes because the oscillating wavelength, λ_B, depends strongly on the equivalent refractive index ($\lambda_B=2n_{eff}\Lambda$, where Λ is the grating period). In the strongly coupled case, the refractive index near the output facets is reduced, compared to the average value over the laser length. This happens because the derivative dn/dN, where N is the carrier concentration, is negative, which means that as the carrier concentration increases in the active region the refractive index decreases. Therefore, as the carrier concentration is diminished near the centre due to the hole burning effect, the refractive index in the central region becomes higher than near the output facets; this gives shortening of the effective Bragg wavelength near the output facets. As a result, the $+1^{st}$ side mode, which is at the short wavelength side, matches the resultant effectively modified corrugation well, and therefore the associated threshold gain decreases.

A complete study of the L-I characteristics, as well as of the lasing spectral characteristics of $\lambda/4$ shifted DFB lasers with different κL values, was performed by several authors [2.9,2.10]. The main conclusion of these studies is that the optimum value of the normalized coupling coefficient is $\kappa L=1.25$. With this value, an optimum flatness of the intensity distribution inside the cavity is obtained, reducing as a consequence the hole burning effects.

However, experimental results of $\lambda/4$-shifted distributed feedback lasers with high coupling coefficient were reported, in which and contrary to the previous studies, low threshold current, single-mode operation up to high output power and side-mode suppression ratio as high as 50dB were measured [2.40]. However, the authors do not show the L-I characteristics of the laser or even mention the value of the maximum output power achieved. Their main interest was the studies of the influence of the high coupling coefficient value on the spectral characteristics at high bit rates. High coupling was found to have several important advantages, such as lower feedback sensitivity, lower threshold gain for the Bragg mode, lower relative intensity noise, and lower influence on the facet reflectivity and on the end-facet phase.

Technique 2: DFB laser with a gradual phase shift region.

A DFB laser structure in which the $\lambda/4$ phase shift is distributed over a section of the laser located in the central region has been proposed to reduce hole burning effects. There are essentially three approaches to introduce a distributed $\lambda/4$ phase shift in a laser structure: (i) use of a DFB laser with a modulated stripe width structure [2.5,2.7]; (ii) use of a DFB laser with a corrugation pitch-modulated structure [2.11,2.14]; (iii) use of a DFB laser with a chirped grating section structure [2.16,2.21].

With the primary purpose of removing the threshold degeneracy in conventional DFB lasers, Tada et al, [2.5] proposed a new DFB laser structure in which the stripe width is varied symmetrically along the laser axis. This simple method will cause a symmetric distribution of the effective index along the cavity and thus removal of the threshold degeneracy. Stable single-mode operation of DFB lasers were demonstrated by Soda et al, [2.6] using a step-like nonuniform stripe width structure for phase adjustment.

A theoretical study of the effects of spatial hole burning on the spectral characteristics of DFB lasers, with distributed phase-shift structures as proposed by Tada et al, caused by nonuniform strip width, was performed by Chen, et al, [2.8]. The main conclusions of this study are as follows: (1) In a DFB laser with a distributed phase shift, the intensity nonuniformity is reduced significantly by increasing the length of the shifted region. It was found that when the length of the shifted region is half of the total laser length, the peak photon intensity is reduced to only 1.6 times the value at the facet output (this value can be compared to 3 times the ratio peak photon intensity/ facet output photon intensity, obtained in a conventional $\lambda/4$ shifted DFB laser); (2) when $\Delta\beta_z l_2$ ($\Delta\beta_z$ is the propagation constant difference between unshifted and shifted regions, and l_2 is the length of the shifted region) increases, the two lowest gain modes separate out (they have the same threshold at $\Delta\beta_z.l_2=0$, i.e., for a conventional DFB laser) and the different modes have different threshold gains. When $\Delta\beta_z l_2$ is around $\pi/2$, the gain margin is more than $45cm^{-1}$ between the two lowest gain oscillation modes, and single-mode operation can be achieved. For $\Delta\beta_z l_2$ between $\pi/2$ and π, the gain margin is relatively insensitive to changes of $\Delta\beta_z l_2$. This fact allows a large tolerance in fabricating DFB lasers with a distributed phase shift structure and also makes this type of laser insensitive to spatial hole burning, since the extra phase shift caused by spatial hole burning does not result in a large gain margin reduction.

A new corrugation structure, which is illustrated in Fig.2.1, was proposed by Okai et al, [2.11] to reduce the spatial-hole burning effect. It can be shown theoretically that such a pitch-modulated structure presents a more uniform intensity distribution along the longitudinal axis, even at high output power. In fact, a laser with a stable single mode and

reduced linewidth up to high output powers has been achieved using this structure [2.11,2.13].

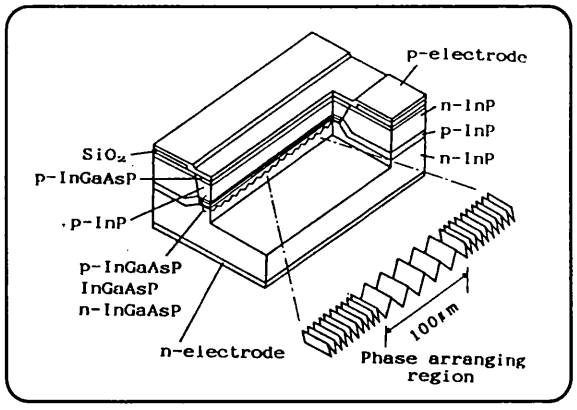

Fig.2.1: Structure of corrugation-pitch-modulated λ/4 shifted DFB laser [2.11]

The point about structure shown in Fig.2.1 is that, as for a conventional λ/4 shifted laser, the light intensity concentrates at the centre of the laser cavity, where the λ/4 phase shift is located. This concentration of light causes an increase in the effective phase shift. As a result, both the single longitudinal mode operation and linewidth deteriorate drastically . On the other hand, in the case of the corrugation pitch-modulated (CPM) DFB laser, the light concentration is greatly reduced by introducing a gradual phase shift.

It has been demonstrated that the CPM-DFB laser is very effective in maintaining SLM operation at high output by suppressing the spatial hole burning effect [2.14]. A further improvement in the modulated pitch structure was proposed by Okai et al, [2.13] in order to narrow the linewidth. This is achieved by: (i) using MQW structures, thus reducing both the linewidth enhancement factor and the internal loss α_0; (ii) using a long cavity; (iii) sputter-depositing SiN_x onto both output facets, so as to reduce the reflectivity to below 1.0%.

The use of chirped gratings for improving the performance of DFB lasers was first proposed by Suzuki and Tada, [2.15,2.16]. In their early work, it was pointed out that small and gradual variations in the grating period Λ or the effective index of refraction n_{eff} along the laser axis could have remarkable effects on the lasing properties. They predicted that the mode degeneracy would be removed in a DFB laser with a symmetric, such as cosine or quadratic, distribution of Λ or n_{eff} along the laser axis, and also that the lowest threshold gain of such a laser could be much lower than that in the conventional DFB laser with uniform distribution of Λ or n_{eff}. These predictions were confirmed in optically pumped GaAs DFB lasers with a quadratic distribution of Λ [2.16].

Chirped grating distributed feedback lasers for suppression of spatial hole burning and for keeping the threshold gain difference large was theoretically proposed for the first time by Zhou and Lee, [2.17,2.18]. The recent demonstration of simple fabrication methods for implementation of such chirped gratings [2.19] motivate the use of this approach so as to optimize the design of DFB cavities for dynamic single-mode operation up to high output power [2.20]. Lasing devices with continuously distributed phase shifts were fabricated, showing single-mode operation with powers exceeding 20mW and side-mode suppression ratios of 40dB even at high output power [2.21].

Technique 3: Distributed feedback lasers with multiple phase-shift regions.

An approach to reduce the hole burning effect consists of making the axial distribution of the mode intensity more uniform over the laser cavity. Agrawal et al, [2.22] proposed the use of two or three phase-shift regions with optimum phase shift (generally less than $\pi/2$) for providing a more uniform axial intensity distribution than the conventional $\lambda/4$ shifted DFB lasers.

The main conclusions of Agrawal's theoretical work are: (1) The introduction of multiple phase shifts in a DFB laser cavity can provide significant gain margin, in the range of 20-30 cm^{-1}, for optimum values of phase shifts (ϕ_{sh}). The gain margin is roughly reduced by a factor of 2 compared with that obtained for a conventional phase shifted DFB with $\phi_{sh}=\pi/2$. However, it is still sufficient to suppress the side modes by 30dB or more as long as $\Delta\alpha$>8-10cm^{-1} ($\Delta\alpha$ is the threshold gain difference) [2.23,2.24]; (2) The use of multiple phase shifts considerably reduces the range over which the intensity distribution varies inside the laser cavity. As a result, spatial hole burning is less effective, and the performance of such a phase shifted DFB laser is expected to be less dependent on the operating output power level.

A joint theoretical and experimental study of the performance of a 2x $\lambda/8$ DFB laser has been carried out by Whiteaway, et al., [2.25]. The main conclusion of this study is that there are useful advantages in using a moderate κL 2 x $\lambda/8$ DFB laser design compared with a low κL $\lambda/4$ DFB structure if insensitivity to spatial hole burning is desired. More specifically, it was shown that reducing the κL product of $\lambda/4$ phase-shifted DFB to about 1.20 removed side mode problems at high power, light-current characteristic curvature, wavelength chirp, and amplitude patterning effects. Similar improvements in terms of performance in a 2 x $\lambda/8$ DFB laser design have also been demonstrated, which is more practical as far as fabrication is concerned because grating design can tolerate a higher κL product.

Technique 4: Dual-pitch DFB laser.

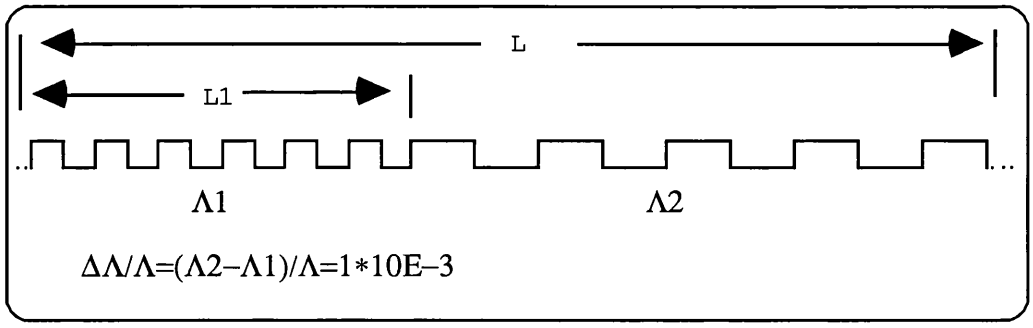

Fig. 2.2: Schematic illustration of the dual-pitch structure

A conventional single-pitch DFB laser with nonreflecting facets (R_1=R_2=0) has two modes with the same threshold gain located at the edge of the stop-band, Kogelnik et al, [2.1]. In a dual-pitch DFB laser, the structure consists of two sections of slightly different grating periods, Fig.2.2. A dual-pitch DFB laser can be viewed as two coupled conventional DFB lasers whose stopbands are shifted with respect to each other by $\Delta\lambda_B=2n_{eff}\Delta\Lambda$. Note that a relatively small change $\Delta\Lambda/\Lambda=1\times10^{-3}$, corresponds to $\Delta\lambda_B$=1.5nm (for λ_B=1.55μm) which is a typical value for the stopband width.

If the shift $\Delta\lambda_B$ is suitably chosen such that the left-hand edge of one stopband coincides with the right-hand side edge of the other stopband, this particular mode will be favoured in both sections and will have the lowest threshold gain (Fig.2.3). The other modes will be negatively discriminated, since they are not supported simultaneously by both sections. In this respect, a dual-pitch DFB laser selects a single longitudinal mode in a manner similar to that of a coupled-cavity laser [2.26].

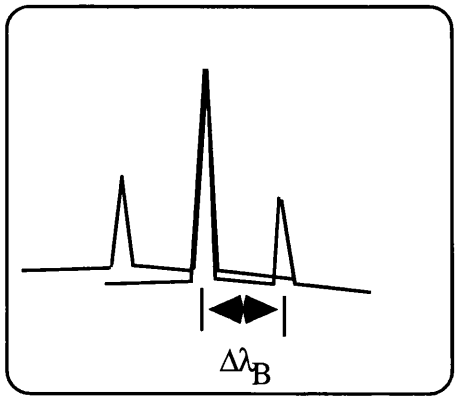

Fig.2.3: Illustration of the emission spectrum of a Dual-Pitch DFB laser

The main conclusions of the theoretical work performed by Agrawal et al, [2.27] are as follows: (1) Numerical results show that for a relative section length of L_1/L=0.25-0.35, the dual-pitch DFB laser can have a gain margin comparable to that of a quarter wavelength-shifted DFB laser. The amount of gain margin $\Delta\alpha$ increases with the value of $\Delta\Lambda/\Lambda$;

$\Delta\alpha$=30cm^{-1} can be obtained for $\Delta\Lambda/\Lambda$=0.1%. However, for values of $\Delta\Lambda/\Lambda$ larger than 1.5 x 10^{-3} the gain margin versus L_1/L curve presents kinks, which correspond to mode jumps. These mode jumps are caused by the fact that, for such large values of $\Delta\Lambda$, the stopbands of the two sections are separated by more than the widths of the individual stopbands. As a result, the laser oscillates in the vicinity of one stopband or the other, depending on the section length (L_1/L value); (2) In the symmetric case, when the laser cavity consists of two sections of equal length but with different pitches, the dual-pitch DFB laser acts as a dual-wavelength laser, i.e., the output from the facets is dominated by two different modes oscillating at wavelengths whose difference is governed by the difference in the grating periods. In other words, light is predominantly emitted at one wavelength from one facet and at a different wavelength from the other facet. The reasons for such behaviour can be understood by considering that for L_1=L/2, the device has two sections of equal length with zero gain margin, i.e., the main and side mode present the same threshold. However, since the two sections have different Bragg wavelengths, the main mode of one section becomes the side mode of the other section. The side-mode suppression ratio was calculated [2.27] to be 6:1, in terms of power ratio at the two wavelength from each facet. This value of the mode-suppression ratio is not large enough for single-mode applications. However, such dual-wavelength lasers may be useful for many other applications, in which the wavelength difference $\Delta\lambda_B$ is required ($\Delta\lambda_B$ can be controlled by adjusting the difference $\Delta\Lambda$ in the grating period of the two sections).

Technique 5: $\lambda/4$ shifted-DFB lasers with amplitude modulated coupling coefficient

It was suggested by Morthier et al, [2.28] that complete elimination of the spatial hole burning in AR-coated DFB-lasers can theoretically be achieved by introduction of a grating, in which the amplitude of the coupling coefficient varies in the longitudinal direction. Alternative fabrication approaches for such a structure are as follows: (i) production of a grating with variable amplitude; (ii) use of a grating withvariable duty cycle; (iii)production of a multi-order grating, i.e., a grating with several sections having different pitches which are integer multiples of the first-order grating.

The first technique is difficult to apply. The second approach, however, can be performed by a double exposure of a photoresist with two holographic interference patterns of slightly different periods (Λ-dΛ/2) and (Λ+dΛ/2) [2.29]. This double exposure defines in the resist, a shape of continuously variable duty cycle including a $\Lambda/2$ shift between each half period $\Lambda_{beat}/2$, with respect to a Λ single exposure. The κ distribution is given by:

$$\kappa = \kappa_0 \mathrm{Cos}\left(\frac{2\pi z}{\Lambda_{beat}}\right) \qquad \Lambda_{beat}=\Lambda^2/d\Lambda$$

The cavity length is chosen equal to $L=\Lambda_{beat}/2$, so that $\kappa=0$ in the centre of the cavity and $\kappa=\kappa_0$ on the facets, i.e., the coupling coefficient κ is distributed along the laser cavity, in order to be stronger in the regions of low field intensity, and weaker in the regions of high field intensity. Phase shifted DFB lasers using this fabrication approach were demonstrated by Talneau et al., [2.30]. In their work, it was shown that, due to the high uniformity of the field along the cavity, the gain margin does not decrease at high output power and allows single-mode operation at powers as high as 78mW.

The dynamic characteristics, such as the turn-on transient, the chirp, and the time dependent spatial hole burning for this type of laser has been also investigated by Zhang, et al., [2.31].

The third technique is straightforward to realize using electron beam lithography. The third approach consists of designing a multi-section grating, in which the first section corresponds to a first-order/second-order grating, the second section to a second-order/third-order grating (Fig.2.4). The point behind this approach is that, although all the sections of the laser structure present approximately the same etch depth, they have different coupling coefficients. This results from the fact that κ is proportional to the amplitude of the harmonic that has a period $\Lambda_B=\lambda_B/2n_{eff}$, which decreases as the order of the grating increases. Similarly to the previous approach, a nonuniform distribution of κ is obtained along the laser cavity, in which κ is stronger near the facets where the field intensity is low and weaker in the central region where the field intensity tends to be higher. It is clearly important to optimize the grating profile of the 2^{nd}-order grating so as to increase the feedback into the laser cavity rather than the radiation perpendicular to the grating [2.32].

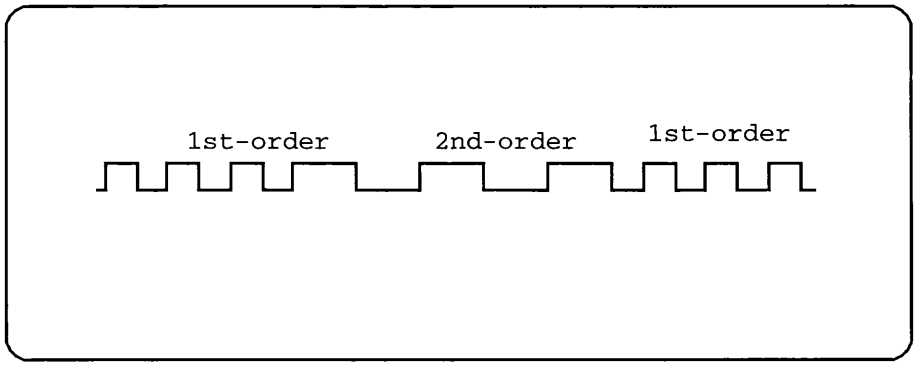

Fig. 2.4: Illustration of the multi-order-section grating

Technique 6: λ/4 shifted-DFB laser with nonuniform current distribution.

In order to minimize the longitudinal spatial hole-burning effect, Usami et al, [2.33] proposed the use of an appropriate distribution of the injection current along the cavity. The motivation behind this approach is as follows. As discussed previously, the hole-burning effect is a result of the nonuniform intensity distribution along the cavity. An optimum coupling coefficient (κL=1.25, Soda et al,[2.9]) was determined to solve this problem in the case of the symmetric λ/4-shifted DFB laser. However, it is not easy, in practice, to control the coupling coefficient precisely. In addition, the hole-burning effect cannot be suppressed satisfactorily by controlling only the coupling coefficient in the asymmetric λ/4 shifted DFB laser (Usami, [2.33]), which is a very effective scheme to increase the output power from one facet (Usami, [2.34]). Fig.2.5 shows the structure proposed by Usami to solve the hole burning effect in the asymmetric λ/4 shifted DFB laser.

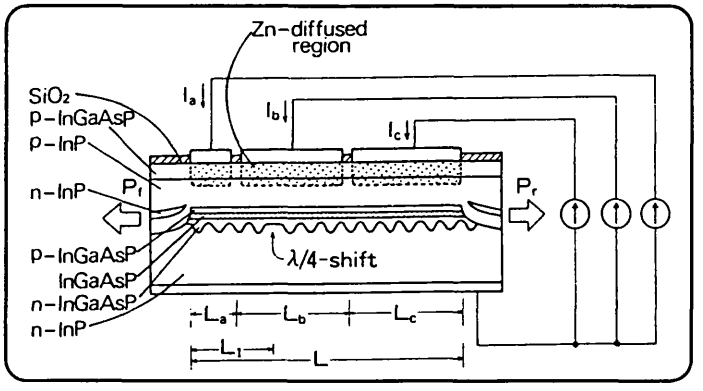

Fig.2.5: Schematic structure of the nonuniform current distribution on the asymmetric λ/4-shifted DFB laser [2.32]

The main conclusion of this work is that current injection with a fixed F (this parameter measures the similarity between the current density profile and the light intensity distribution along the cavity) cannot compensate for the hole-burning effect perfectly, because the hole-burning effect occurs only above the threshold current while the refractive index change due to the nonuniform current injection occurs even below the threshold. On the other hand, the hole-burning effect can be perfectly compensated, for any current range, if the current is biased uniformly at the threshold level and then a component of the current with the same distribution as the intensity is superimposed over the threshold current.

Technique 7: DFB laser with a gain-coupling mechanism

As discussed previously, the oscillation wavelength uncertainty or degeneracy in the vicinity of the Bragg wavelength is a major problem in semiconductor distributed feedback (DFB) lasers. Several schemes, such as a quarter-wave phase shift or a modulated stripe width, were shown to fix the oscillation on the Bragg wavelength, and thus solving the degeneracy problem on the condition that cleaved facet reflectivities are sufficiently reduced, typically

below 1%. Another interesting scheme for removing wavelength degeneracy in DFB lasers is the introduction of a gain-coupling mechanism, which was initially proposed by Kogelnik and Shank, [2.1]. In these lasers, the feedback necessary for laser operation is provided by reflections at periodic loss [2.35] or gain [2.37] variations along the laser cavity. It has been shown that AR-coated DFB lasers with gain-coupling mechanism and without phase shifts can provide low losses, minor longitudinal spatial hole burning, and a large threshold gain difference [2.36]. In addition, effects of cleaved facet reflection on the characteristics of a gain-coupled DFB laser have been both threoretically and experimentally demonstrated to be lower compared to other DFB lasers [2.35,2.37,2.38].

High performance gain-coupled DFB lasers have been fabricated [2.39], presenting very high single-mode yields and a minimum linewidth of 1.6MHz at about 10mW CW output power. All these results make the gain-coupled DFB laser a very promising device for applications such as in coherent optical communication systems.

2.3 Monolithic Integration of a Master Oscillator with Power Amplifier (MOPA)

Although excellent performance is provided by the erbium-doped fibre amplifiers, interest in semiconductor laser amplifiers is increasing due to their unique feature of easy integration with other photonic devices, as well as to their capability of performing sophisticated multifunctions such as switching, signal tapping, pulse-shape regeneration, etc [2.41]. Until recently, high-power, diffraction-limited diode lasers have only been found in the research laboratories. However, there has been a significant breakthrough when the first commercial single-mode diode laser with a continuous output power greater than 1 watt was achived [2.42].

Although high power can be achieved by combining an array of diode lasers on a chip, the output is not diffraction-limited [2.43], [2.44]. Diffraction-limited laser sources produce beams with the minimum possible divergence and are critical for applications that require beams to be focused to a spot as small as possible. Diffraction-limited sources produce radiation with a Gaussian-shape intensity profile and a constant phase front. Gaussian beams have the lowest possible divergence and can therefore be focused to the smallest spot size. Such beams also limit diffraction losses, which can be important in applications such as satellite communications.

One development, in particular, the monolithic integration of a master oscillator diode laser and a power amplifier, known as a MOPA, has precipitated a second revolution in diode laser technology [2.45], [2.46]. Applications that would previously have used solid-state and gas lasers, e.g. satellite communications, frequency-doubling and thermal printing, are now looking towards diode lasers, which are more compact, efficient and reliable [2.42]. Diode lasers have been shown to operate over almost the entire spectrum from 480nm to 2μm. Examples of the different material systems used to access different wavelengths are AlGaInP between 630nm and 680nm, AlGaInAs between 780nm and 1060nm, and InGaAsP between 1.1μm and 2.0μm. All these materials can be processed to make MOPA-like structures. High power, diffraction-limited operation will eventually be possible throughout the visible and the near-infrared.

The MOPA architecture is essential for diffraction-limited output. However, to monolithically integrate the components, high-power amplifiers that could produce diffraction-limited beams from diode laser oscillators are needed. Single-stripe devices are generally limited to a few hundred mW of output power, at which point reliability problems associated with the high optical intensity at the output facet begin to limit device performance. The simplest solution to the problem of facet power density has been to

increase the lateral dimension of the laser from 3-4 μm to a hundred μm. However, this approach has simply traded one problem (facet degradation) for another, control of the spatial mode.

Broad-area lasers, the simplest configuration with a wide output facet, typically operate in an unpredictable combination of lateral spatial modes. Over the years, numerous geometries have been proposed and demonstrated in an attempt to reach high optical powers while maintaining a well-behaved mode [2.47], i.e., one that can be focused to a diffraction-limited spot with relatively simple optics. The contenders for high-power lasers have included both monolithic and multichip solutions.

Initially, monolithic integration of amplifier and laser was achieved with a 5μm single mode waveguide [2.48]; this development of a single stripe MOPA demonstrated that high power spectrally coherent operation was possible. These early MOPA's comprised a serial array of collinear amplifiers and output couplers, either cleaved facets or grating output couplers [2.45]. The beams from each output were then combined to create a coherent radiation pattern. However, the phase front of the output beam was significantly distorted by the discrete nature of the individual amplifier output couplers.

In the early stages, a separate master oscillator, either a Ti-Sapphire laser [2.47] or a diode laser [2.49], was used to inject a broad-area amplifier, typically a rectangular gain region mounted on a heatsink. The facets were covered with anti-reflection coatings to achieve a reflectivity of 0.1% and eliminate self-oscillation of the amplifier. The signal from the master oscillator only passes through the gain region once. Power amplifiers with this configuration have demonstrated as much as a 22W pulsed output beam, significantly higher than the 100mW or so commercially available at the time. A disadvantage of broad-area laser amplifiers is the relatively high injection power needed to saturate the gain of the amplifier and obtain efficient energy extraction, typically 1mW/μm of output facet width.

To operate in a single transverse mode, the amplifier gain must be 'saturated' to limit the effects of variation in the carrier density in the active (gain) region. Injected carriers alter the local refractive index, which in turn changes the phase of the light across the beam. Saturation reduces this index variation, allowing the beam to propagate through the amplifier without any significant phase distortions. But broad-area amplifiers typically have input apertures of several hundred microns and need several hundred milliwatts of input power to saturate the gain [2.47]. Such powers cannot readily be achieved by diode lasers, and this constrained the monolithic integration of the master oscillator with power amplifiers. Amplifiers that could be saturated by lower injection powers were needed.

The breakthrough came in 1992 with the demonstration, by Walpole et al., of the 'Flared' power amplifier [2.50]. These amplifiers are similar to broad-area amplifiers in that the gain region is defined by the region into which the current is injected. However, they differ in that the width of the gain region increases along the length of the amplifier, allowing the input beam to diffract freely. The expanding mode size minimises the opportunities for the light to converge on itself or 'filament' and the amplifier thus preserves the diffraction-limited nature of the injected signal.

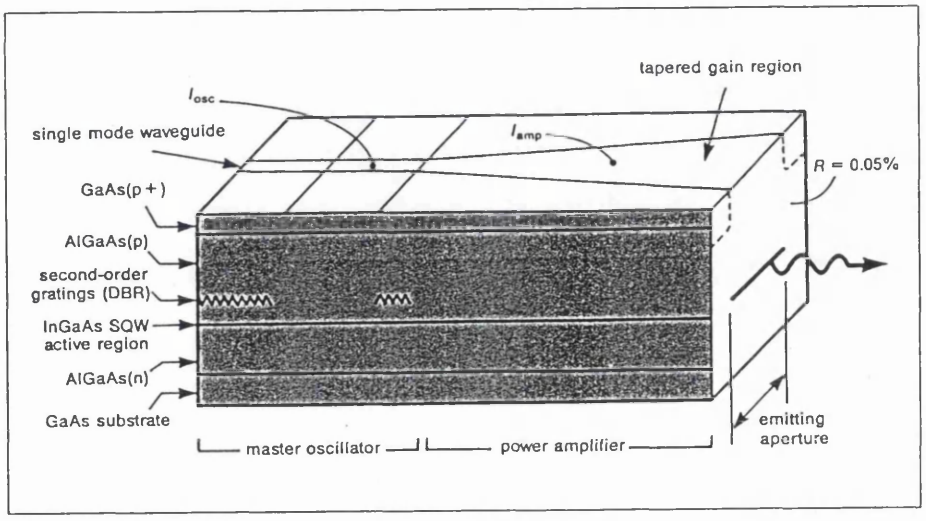

Fig. 2.6: Schematic of the monolithically integrated master oscillator and power amplifier (MOPA) on a single semiconductor chip

Because flared amplifiers have narrow input apertures, they can be saturated with much lower injected power levels. The input power then diverges within the gain region and, to first order, the output power of the amplifier is proportional to the aperture size. Assuming approximately 1mW saturation power per 1μm of the aperture width, the input aperture of a flared amplifier of 2μm width can be saturated with only 2-3mW of power. This makes flared amplifiers ideal for monolithic integration with typical diode laser oscillators [2.51], [2.52].

It was only when the research on discrete flared amplifiers was combined with work on the monolithic oscillator-amplifier configurations that the first demonstration of multiwatt, diffraction-limited output from a semiconductor laser diode was achieved. The use of flared amplifiers substantially eliminates problematic phase distortions. The best performance to date has been from a monolithic integrated flared amplifier-MOPA, which performed at power levels greater than 2W continuous wave (CW) in a single diffraction-limited beam [2.52]. The realization of a coherent, diffraction limited source operating at powers in excess of 1W will have a significant impact on blue/green sources, printing, satellite communications, and ranging. The optical quality of the beam is important for the above-mentioned applications and has been investigated in detail in several papers [2.53], [2.54].

References

[2.1] H. Kogelnik, and C.V. Shank, "Coupled-Wave Theory of Distributed Feedback Lasers", Journal of Applied Physics, Vol.43; pp.2327-2335,(1972)

[2.2] H. Kogelnik, and C.V. Shank, "Stimulated emission in a periodic structure", Appl. Phys. Lett., Vol.18; pp.152-154, 1971

[2.3] H.A.Haus, C.V. Shank, "Antisymmetric taper of distributed feedback lasers" IEEE Journal of Quantum Electronics, Vol. 12; pp.532-539;(1976)

[2.4] K.Sekartedjo, N.Eda, K. Furuya, Y.Suemastu, F.Koyama, T.Tanbun-Ek, "1.5μm Phase–Shifted DFB Lasers for Single–mode Operation", Electronic Letters, Vol. 20; pp.80-81;(1984)

[2.5] K.Tada, Y.Nakano, and A.Ushirokawa, "Proposal of a Distributed Feedback Laser with Nonuniform Stripe Width for Complete Single-mode Oscillator", Electronics Letters, Vol.20,pp.82-84,1984

[2.6] H.Soda, K.Wakao, H.Sudo, T.Tanahashi, and I.Imai, "GaInAsP/InP phase-adjusted distributed feedback lasers with a step-like nonuniform stripe width structure", Electronics Letters, Vol.20,pp.1016-1018,1984

[2.7] Y.Nakano, and K. Tada, "Analysis, Design, and fabrication of GaAlAs/GaAs DFB lasers with modulated stripe width structure for complete single longitudinal mode oscillation", IEEE Journal of Quantum Electronics, Vol. 24; pp.2017-2033;(1988)

[2.8] G.Chen, S.R.Seshadri, and F.Cerrina, "Distributed feedback lasers with distributed phase-shift structure", Applied Physics Letters, Vol. 60; pp.2586-2588;(1992)

[2.9] H.Soda, Y.Kotaki,H.Sudo, H.Ishikawa, S. Yamakoshi, and H. Imai, "Stability in Single Longitudinal Mode Operation in GaInAsP/InP Phase–Adjusted DFB Lasers", IEEE Journal of Quantum Electronics, Vol. 23; pp.804-814;(1987)

[2.10] J.E.A. Whiteaway, G.H.B. Thompson, A.J. Collar, and C.J.Armistead, "The design and assessment of λ/4 phase shifted DFB laser structures", IEEE Journal of Quantum Electronics, Vol. 25; pp.1261-1279;(1989)

[2.11] M.Okai, N. Chinone, H.Taira,T. Harada, "Corrugation–Pitch–Modulation Phase–Shifted DFB Laser" IEEE Photonics Technology Letters, Vol. 1; pp.200–201;(1989)

[2.12] M.Okai, S. Tsuji, and N. Chinone, "Stability of the longitudinal mode in λ/4-shifted InGaAs/InP DFB lasers", IEEE Journal of Quantum Electronics, Vol. 25; pp.1314-1319;(1989)

[2.13] M.Okai, T. Tsuchiya, K. Uomi, N. Chinone, and T.Harada "Corrugation–Pitch–Modulated MQW–DFB Laser with Narrow Spectral Linewidth (170KHz)." IEEE Photonics Technology Letters, Vol. 2; pp.529–530;(1990)

[2.14] M. Okai, "Spectral characteristics of distributed feedback semiconductor lasers and their improvement by corrugation pitch modulated structures", Journal of Applied Physics, Vol.75; pp.1-29,(1994)

[2.15] A.Suzuki, and K.Tada, "Fabrication of chirped gratings on GaAs optical waveguides", Thin Solid Films, Vol. 72; pp.419-426;(1980)

[2.16] A.Suzuki, and K.Tada, "Theory and experiment on distributed feedback lasers with chirped gratings", Proc. SPIE, Vol. 239; pp.10-18;(1981)

[2.17] P.Zhou, and G.S.Lee, "Mode selection and spatial hole burning suppression of a chirped grating distributed feedback laser", Applied Physics Letters, Vol. 56; pp.1400-1402;(1990)

[2.18] P.Zhou, and G.S.Lee, "Chirped grating λ/4 shifted DFB laser with uniform longitudinal field distribution", Electron. Lett., Vol. 26; pp.1660-1661;(1990)

[2.19] H.Hillmer, K.Magari, and Y.Suzuki, "Chirped gratings for DFB laser diodes using bent waveguides", IEEE Photonics Technology Letters, Vol. 5; pp.10-12;(1993)

[2.20] H.Olesen, J.Salzman, B.Jousson, B.Tromborg, "Single-mode stability of DFB lasers with longitudinal Bragg detuning", IEEE Photonics Technology Letters, Vol. 7; pp.461-463;(1995)

[2.21] H.Hillmer, A.Grabmaier, S.Hansmann, and H.Burkhard, "Continuosly distributed phase shifts in chirped DFB lasers using bent waveguides", Electron. Lett., Vol. 30; pp.1483-1484;(1994)

[2.22] G.P. Agrawal, J.E. Geusic, and P.J. Anthony, "Distributed Feedback Lasers with Multiple Phase–Shift Regions", Applied Physics Letters, Vol. 53; pp.178-179;(1988)

[2.23] G.Motosugi, Y. Yoshikuni, T. Ikegami, "Single–Longitudinal–mode Condition for DFB Lasers" Electronics Letters, Vol. 21; pp.351-53;(1985)

[2.24] T.Matsuok, Y.Yoshikuni, and G.Motosugi, "Dependence of single-longitudinal-mode probability on DFB laser facet structure" Electronics Letters, Vol. 21; pp.1151-1152;(1985)

[2.25] J.E.A. Whiteaway, B. Garret, G.H.B. Thompson, A.J. Collar, C.J.Armistead, and M.J. Fice, "The static and dynamic characteristics of single and multiple-phase-shifted DFB laser structures", IEEE Journal of Quantum Electronics, Vol. 28; pp.1277-1293;(1992)

[2.26] M.J. Adams, A.G. Steventon, W.J. Devlin, and I.D. Henning, *Semiconductor lasers for long-wavelength optical-fibre communications systems*, Peter Peregrinus Ltd, 1987, section 4.4.

[2.27] G.P.Agrawal, and A.H.Bobeck, "Modeling of Distributed Feedback Semiconductor Lasers with Axially-Varying Parameters", IEEE Journal of Quantum Electronics, Vol. 24; pp.2407-2414;(1988)

[2.28] G.Morthier, K.David, P.VankWikelberge, and R.Baets, "A new DFB-laser diode with reduced spatial hole burning", IEEE Photonics Technology Letters, Vol. 2; pp.388-390;(1990)

[2.29] G.Heise, R.Matz, and U.Wolff, "Phase-shifted holographic gratings for distributed feedback lasers", SPIE, 1986, 651

[2.30] A.Talneau, J.Charil, A.Ougazzadeu, and J.C.Bouley, "High power operation of phase-shifted DFB lasers with amplitude modulated coupling coefficient", Electronic Letters, Vol.28, pp.1395-1396, (1992)

[2.31] L.M. Zhang, and J.E.Carrol, "Dynamics of index-coupled DFB laser with minimal spatial hole burning", IEEE Photonics Technology Letters, Vol. 6; pp.486-488;(1994)

[2.32] G.H.B. Thompson, *Physics of semiconductor laser devices,* New York: Wiley, 1980, Chap.8

[2.33] M.Usami, and S. Akiba, "Suppression of longitudinal spatial hole-burning effect in $\lambda/4$ shifted lasers by nonuniform current distribution", IEEE Journal of Quantum Electronics, Vol. 25; pp.1245-1253;(1989)

[2.34] M.Usami, and S.Akiba, "Asymmetric $\lambda/4$ shifted InGaAsP/InP DFB lasers", IEEE Journal of Quantum Electronics, Vol. 23; pp.815-821;(1987)

[2.35] Y. Nakano, Y. Luo, and K. Tada, "Facet reflection independent single longitudinal mode oscillation of GaAlAs/GaAs DFB laser equipped with a gain-coupling mechanism", Appl. Phys. Lett., Vol.55; pp.1606-1608, 1989

[2.36] G.Morthier, P.Vankwikelberge, K.David, and R.Baets, "Improved performance of AR-coated DFB lasers by the introduction of gain coupling", IEEE Photonics Technology Letters, Vol. 2; pp.170-172;(1990)

[2.37] Y.Luo, Y.Nakano, and K.Tada, "Purely gain-coupled distributed feedback semiconductor lasers", Appl. Phys. Lett., Vol.56; pp.1620-1622, 1990

[2.38] K.David, G.Morthier, P.Vankwikelberge, R.G.Baets, T.Wolf, and B.Borchert, "Gain-coupled DFB lasers versus index-coupled and phase-shifted DFB lasers: A comparasion based on spatial hole burning corrected yield", IEEE Journal of Quantum Electronics, Vol. 27; pp.1714-1723;(1991)

[2.39] B. Borchert, K. David, B. Stegmuller, R. Gessner, M. Beschorner, D. Sacher, and G. Franz, "1.55μm gain-coupled quantum-well distributed feedback lasers with high single-mode yield and narrow linewidth", IEEE Photonics Tech. Lett., Vol.3, pp. 955-957, 1991

[2.40] H.Hillmer, S.Hansmann, and H.Burkhard, "First-order λ/4-shifted distributed feedback lasers with high coupling coefficients", IEEE Journal of Quantum Electronics, Vol. 27; pp.1753-1758;(1991)

[2.41] G. Bendelli, K. Komori, and S.Arai, "Gain Saturation and Propagation Characteristics of Index-Guided Tapered-Waveguide Traveling-Wave Semiconductor Laser Amplifiers (TTW-SLA's), Journal of Quantum Electronics, Vol.28, pp.447-458, (1992)

[2.42] D. Welch, "New Dawn Beckons for semiconductor Lasers", Physics World, Feb.94, pp.35-38, (1994)

[2.43] D. R. Scifres, R. D. Burnham, and W. Streifer, "Phase-locked semiconductor laser array", Appl. Phys. Lett., Vol.33, pp. 1015-1017,(1978)

[2.44] G. R. Hadley, J. P. Hohimer, and A. Owyoung, "Comprehensive modeling of diode arrays and broad-area devices with applications to lateral index tailoring", IEEE Journal of Quantum Electronics, Vol.24,pp. 2138-2152, (1988)

[2.45] D.F. Welch,, D. Mehuys, R. Parke, R. Waarts, D. Scifres, and W. Streifer "Coherent operation of monolithically integrated master oscillator amplifiers", Electronics Letters, Vol.26, pp. 1327-1329,(1990)

[2.46] D. Mehuys, D. Welch, R.G. Waarts, R. Parke, A. Hardy, and W. Streifer, "Analysis of monolithic integrated master oscillator power amplifiers", IEEE Journal of Quantum Electronics, Vol.27, pp. 1900-1909, (1991)

[2.47] L. Goldberg, and D. mehuys, "21W broad area near-diffraction limited semiconductor amplifier", Appl. Phys. Lett., Vol.61, pp. 633-635,(1992)

[2.48] U. Koren, R. M. Jopson, B. I. Miller, M. Chien, M. G. Young, C. A. Burrus, C. R. Giles, H. M. Presby, G. Raybon, J. D. Evankow, B. Tell, and K. Brown-Goebeler, "High power laser-amplifier photonic integrated circuit for 1.48μm wavelength operation", Appl. Phys. Lett., Vol.59, pp. 2351-2353,(1991)

[2.49] D. Mehuys, L. Goldberg, and D. Welch, "Quasi-CW 3 watt diffraction-limited diode-to-diode optical amplifier", Tech. Dig. of conf. on lasers and electro-optics, paper CWA5, 1992, pp. 224-225

[2.50] J.N. Walpole, E.S. Kintzer, S.R. Chinn, C. A. Wang, and L. J. Missaggia, "High-power strained-layer InGaAs/AlGaAs tapered traveling wave amplifier", Appl. Phys. Lett., Vol.61, pp. 740-742,(1992)

[2.51] D.F. Welch, R. Parke, D. Mehuys, A.Hardy, R.Lang, S.O'Brien and S.Scifres, "1.1W CW, Diffration-Limited Operation of a Monolithically Integrated Flared-Amplifier Master oscillator Power Amplifier", Electronics Letters, Vol.28, pp2011-2013,(1992)

[2.52] R. Parke, D. Welch, A. Hardy, R. Lang, D. Mehuys, S. O´Brien, K. Dzurko, and D. Scifres, "2W CW, diffraction-limited operation of a monolithically integrated master oscillator power amplifier", IEEE Photonics Technol. Lett., Vol.5, pp. 297-300, (1993)

[2.53] R. J. Lang, A Hardy, R. Parke, D. Mehuys, S. O´Brien, J. Major, and D. Welch, "Numerical analysis of flared semiconductor laser amplifiers", IEEE Journal of Quantum Electronics, Vol.29,pp. 447-458, (1993)

[2.54] S. O'Brien, D.F. Welch, R.A.Parke, D. Mehuys, K.Dzurko, R.J.Lang, R.Waartsn and D. Scifres, "Operating Characteristics of a High-Power Monolithically Integrated Flared Amplifier Master Oscillator Power Amplifier", IEEE Journal of Quantum Electronics, Vol.29,pp. 2052-2057, (1993)

Chapter 3: Theory of Periodic Structures and DFB Lasers

3.1 Introduction

There are two important theoretical methods used to analyse distributed-feedback (DFB) structures. One is the matrix method [3.1-3.3], and the other is the coupled-wave method [3.4-3.6]. The use of the matrix metrod in the study of the propagation of plane electromagnetic waves through a stratified medium is well known in Optics. However, it is difficult to obtain a simple analytic expression for the reflectance spectrum of stratified periodic structures when a matrix method is used. The coupled-wave method has long been used to analyse the characteristics of a periodic layered medium because it gives simple analytic expressions for the reflectivity spectrum of Bragg reflectors and DFB structures. However, when using the coupled-wave method in its simplest form, it is often assumed that the beam is incident upon the distributed-feedback structure from a medium with the average refractive index of the distributed feedback structure. This condition means that, for the coupled-wave method, the effects of end reflections occurring at the boundaries of the distributed feedback structure are usually ignored [3.1].

3.2 The Coupled-mode equations

In this section, the coupled-mode equations, which describe the behaviour of the electromagnetic waves in a waveguide with a periodic perturbation, are derived. The treatment which follows, including the notation, is based closely on *Waves and Fields in Optoelectronics* by Haus [3.7]. Basically, the central problem concerning DFB lasers is the phenomenon of coupling between two waves of opposite propagation directions. To produce appreciable coupling, the two propagation constants must not differ significantly, i.e., synchronism is required. However, waves with opposite propagation directions may have greatly different propagation constants. Let us show how the wave with a positive group velocity is made synchronous with the wave with negative velocity [3.7].

Consider a structure of the type shown in Fig.3.1. The wave with positive group velocity, the 'forward' wave in the guiding structure, is denoted by $\underline{b}$; the wave with negative group velocity, also called 'backward' wave, is denoted by $\underline{a}$. When there is no coupling, the differential equations obeyed by $\underline{a}$ and $\underline{b}$ are, respectively,

$$\frac{da}{dz} = j\beta a \tag{3.2.1}$$

$$\frac{db}{dz} = -j\beta b \qquad (3.2.2)$$

where a and b are of the form $Exp[j(\omega t+\beta z)]$ and $Exp[j(\omega t-\beta z)]$, respectively. β is the propagation constant in the unperturbed waveguide.

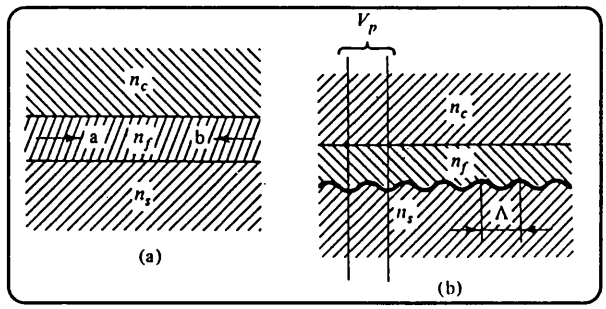

Fig.3.1: a) Guiding structure with no periodic coupling; b) Guiding structure with periodic coupling [3.2]

Suppose, now, that a finite periodic perturbation in the guiding structure is introduced (see Fig.3.1b). The spatial component associated with the electromagnetic field of the wave travelling along the periodic structure acquires modulation components because the fields interact with the perturbation with spatial dependence of the form $Cos[(\frac{2\pi}{\Lambda})z]$. The resulting sidebands are called space harmonics. The space harmonics are part of the field structure of the wave in the periodic guiding structure and are responsible for coupling to other waves with propagation constants close to the propagation constant of the space harmonic. In the present case of a sinusoidal perturbation and a spatial dependence of b of the form exp(-jβz), the sidebands follow from

$$Exp(-j\beta z)Cos(\frac{2\pi}{\Lambda})z = \frac{1}{2}\left\{Exp\left[-j\left(\beta-\frac{2\pi}{\Lambda}\right)z\right]+Exp\left[-j\left(\beta+\frac{2\pi}{\Lambda}\right)z\right]\right\} \qquad (3.2.3)$$

If $(\beta - \frac{2\pi}{\Lambda})$ is close to -β, this component of the field radiates in the backward direction and the radiation superimposes coherently over extended distances. The exponential with the argument $(\beta+\frac{2\pi}{\Lambda})z$ does not produce backward radiation because its spatial dependence differs greatly from that of exp(+jβz). The effect of coupling of b to a can be introduced in (3.1.1) through a coupling term produced by the backward radiating contribution of b:

$$\frac{da}{dz} = j\beta a + \kappa_{ba} b e^{j\left(\frac{2\pi}{\Lambda}\right)z} \qquad (3.2.4)$$

where κ_{ba} is the coupling coefficient from backward radiating contribution of b to backward wave a. A similar effect is produced by the interaction of the backward wave with the periodic perturbation (symmetry gives $\kappa_{ba}=\kappa_{ab}$).

$$\frac{db}{dz} = j\beta b + \kappa_{ba} a e^{-j\left(\frac{2\pi}{\Lambda}\right)z} \tag{3.2.5}$$

The equations above can be reduced to coupled mode equations with space-independent coefficients by the introduction of new variables.

$$a = A(z)e^{j\left(\frac{\pi}{\Lambda}\right)z} \qquad b = B(z)e^{-j\left(\frac{\pi}{\Lambda}\right)z}$$

resulting in

$$\frac{dA}{dz} = j(\beta - \frac{\pi}{\Lambda})A + \kappa_{ba} B \tag{3.2.6}$$

$$\frac{dB}{dz} = -j(\beta - \frac{\pi}{\Lambda})B + \kappa_{ba} A \tag{3.2.7}$$

The previous equations can be simplified in appearance by the introduction of the detuning parameter

$$\Delta\beta = \beta - \frac{\pi}{\Lambda} \tag{3.2.8}$$

which measures the deviation of the propagation constant from π/Λ. In the neighbourhood of the frequency ω_0 for which $\beta(\omega_0)=\pi/\Lambda$, we have

$$\beta = \beta(\omega_0) + \frac{d\beta}{d\omega}(\omega - \omega_0) \tag{3.2.9}$$

and thus

$$\Delta\beta = \frac{\omega - \omega_0}{v_g} \tag{3.2.10}$$

where v_g is the group velocity $\frac{d\omega}{d\beta}$. Using the detuning parameter $\Delta\beta$, equations (3.2.6) and (3.2.7) assume the simple form:

$$\frac{dA}{dz} = j\Delta\beta A + \kappa_{ba} B \tag{3.2.11}$$

$$\frac{dB}{dz} = -j\Delta\beta B + \kappa_{ba} A \tag{3.2.12}$$

The dispersion diagram corresponding to (3.2.11) and (3.2.12) is given in Fig.3.2 for the case of $\kappa_{ba}^2=|\kappa|^2>0$. The propagation constant s of the coupled systems is

$$s = \pm\sqrt{\Delta\beta^2 - |\kappa|^2} \tag{3.2.13}$$

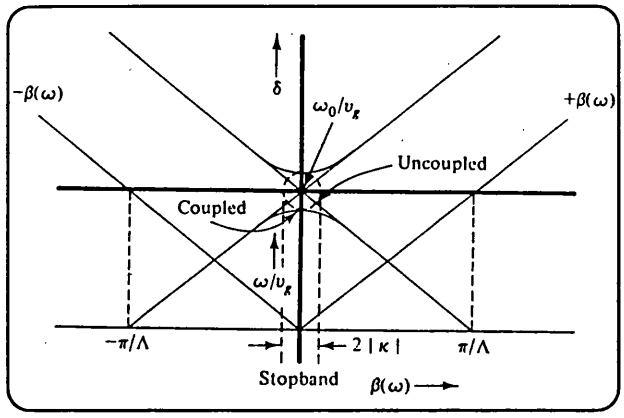

Fig.3.2: Dispersion curve from (3.2.9) and (3.2.10) with the unperturbed propagation constant $\beta(\omega)$ proportional to ω[3.2].

Note that the unperturbed dispersion curves for $\beta(\omega)$ are taken as straight lines. An important point regarding the coupled case is the appearance of the stopband, represented in Fig.3.2. The consequences of the stopband on the behaviour of the waveguide are analysed in the next section.

3.3 The coupled-mode solutions: The passive periodic waveguide.

Let us now analyse the solutions of the coupled mode equations derived in the previous section. The following analysis is based on *Quantum Electronics* by Yariv [3.8] and [3.6]. The equations considered in this section are more general, since they describe the behaviour of the electromagnetic waves in a waveguide with an arbitrary periodic perturbation and the spatial dependence is now taken into account. The coupled equations may be written as:

$$\frac{dA}{dz} = \kappa_{ba} B e^{-j2(\Delta\beta)z} \tag{3.3.1}$$

$$\frac{dB}{dz} = \kappa_{ba} A e^{j2(\Delta\beta)z} \tag{3.3.2}$$

where

$$\Delta\beta = \beta - \beta_0 \qquad \text{and} \qquad \beta_0 = \frac{m\pi}{\Lambda} \qquad \text{with} \quad m=1,2,3...$$

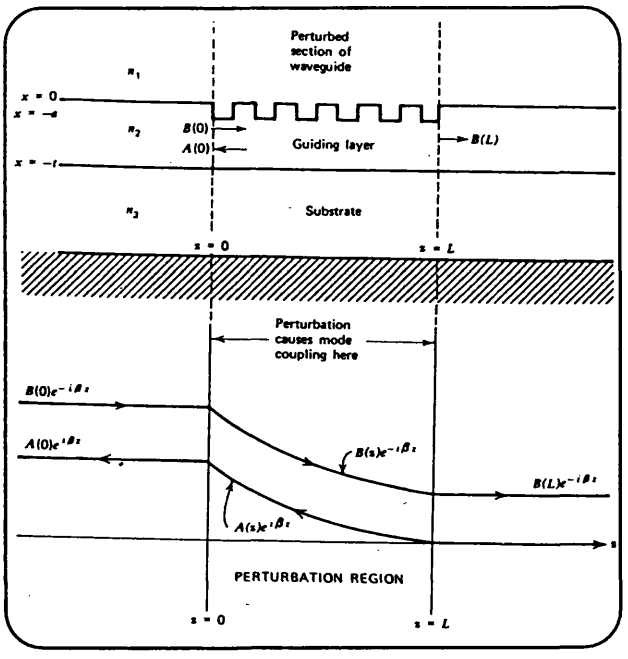

Fig.3.3: a)Dielectric waveguide with a periodic perturbation; b)The incident and reflected fields[3.8]

Consider a corrugated section of length L as in Fig.3.3. A wave with amplitude B(0) is incident from the left on the perturbed section of the waveguide. The solution of (3.3.1) and (3.3.2) for this case, in which the boundary condition A(L)=0 is assumed, is the following

$$A(z)e^{j\beta z} = B(0)\frac{j\kappa e^{j\beta_0 z}\mathrm{Sinh}[s(z-L)]}{-\Delta\beta\mathrm{Sinh}(sL)+js\mathrm{Cosh}(sL)} \tag{3.3.3}$$

$$B(z)e^{-j\beta z} = B(0)\frac{e^{-j\beta_0 z}}{-\Delta\beta\mathrm{Sinh}(sL)+js\mathrm{Cosh}(sL)}\{\Delta\beta\mathrm{Sinh}[s(z-L)]+js\mathrm{Cosh}[s(z-L)]\} \tag{3.3.4}$$

where

$$s=\sqrt{\kappa^2-(\Delta\beta)^2} \qquad \kappa=|\kappa_{ba}| \tag{3.3.5}$$

The total field, which is given by A(z)Exp(jβz)+B(z)Exp(-jβz), and its derivative, are continuous at z=0 and z=L (the field at z>L and z<0 is assumed as in Fig.3.3).

$$A(z)=B(0)\left(\frac{\kappa_{ba}}{\kappa}\right)\frac{\mathrm{Sinh}[\kappa(z-L)]}{\mathrm{Cosh}(\kappa L)} \tag{3.3.6}$$

$$A(z)=B(0)\frac{\mathrm{Cosh}[\kappa(z-L)]}{\mathrm{Cosh}(\kappa L)} \tag{3.3.7}$$

A plot of the modal powers $|A(z)|^2$ and $|B(z)|^2$ is shown in Fig.3.3b).

There are two important points about this result. Firstly, it can be shown that for sufficiently large arguments of the Cosh and Sinh functions in (3.3.6) and (3.3.7), the incident power drops off exponentially along the perturbation region. Secondly, this behaviour is due not to absorption in the perturbation region, but to reflection of power into the backward travelling mode A.

The width of the forbidden frequency zone is

$$(\Delta\omega)_{gap} = \frac{2\kappa c}{n_{eff}} \tag{3.3.8}$$

where κ is the coupling coefficient associated to m=1, the first harmonic component of the periodic perturbation. Equation (3.3.8) allows the coupling coefficient to be calculated if the effective refractive index and stopband, which can be measured experimentally from the output spectrum of the distributed feedback laser, are known.

The previous results show that a finite length section of a periodic waveguide can act as a high-reflectivity mirror for frequencies near the Bragg value ω_0. The transmission (T_{eff}) and reflection (R_{eff}) coefficient of such a filter can be calculated from equations (3.3.3) and (3.3.4) as follows

$$T_{eff} = \left|\frac{B(L)}{B(0)}\right|^2 \tag{3.3.9}$$

$$R_{eff} = \left|\frac{A(0)}{B(0)}\right|^2 \tag{3.3.10}$$

The transmission coefficient $T_{eff} = \left|\frac{B(L)}{B(0)}\right|^2$ is plotted in Fig.3.4. The transmissivity T of the filter is calculated from the relation T=1-R, assuming a lossless DFB waveguide,i.e.,that there are no other guided or radiation modes, to which coupling is possible. Defining a new variable x, T is given by

$$T = \frac{1 - Tanh^2\left(\kappa\left(1-x^2\right)^{\frac{1}{2}}L\right)}{1+\left(\frac{x^2}{1-x^2}\right)Tanh^2\left(\kappa\left(1-x^2\right)^{\frac{1}{2}}L\right)} \tag{3.3.11}$$

where $x = \frac{2\pi n_{eff}}{\kappa}\left(\frac{1}{\lambda} - \frac{1}{\lambda_B}\right)$, n_{eff} is the refractive index of the waveguide and λ_B is the Bragg wavelength.

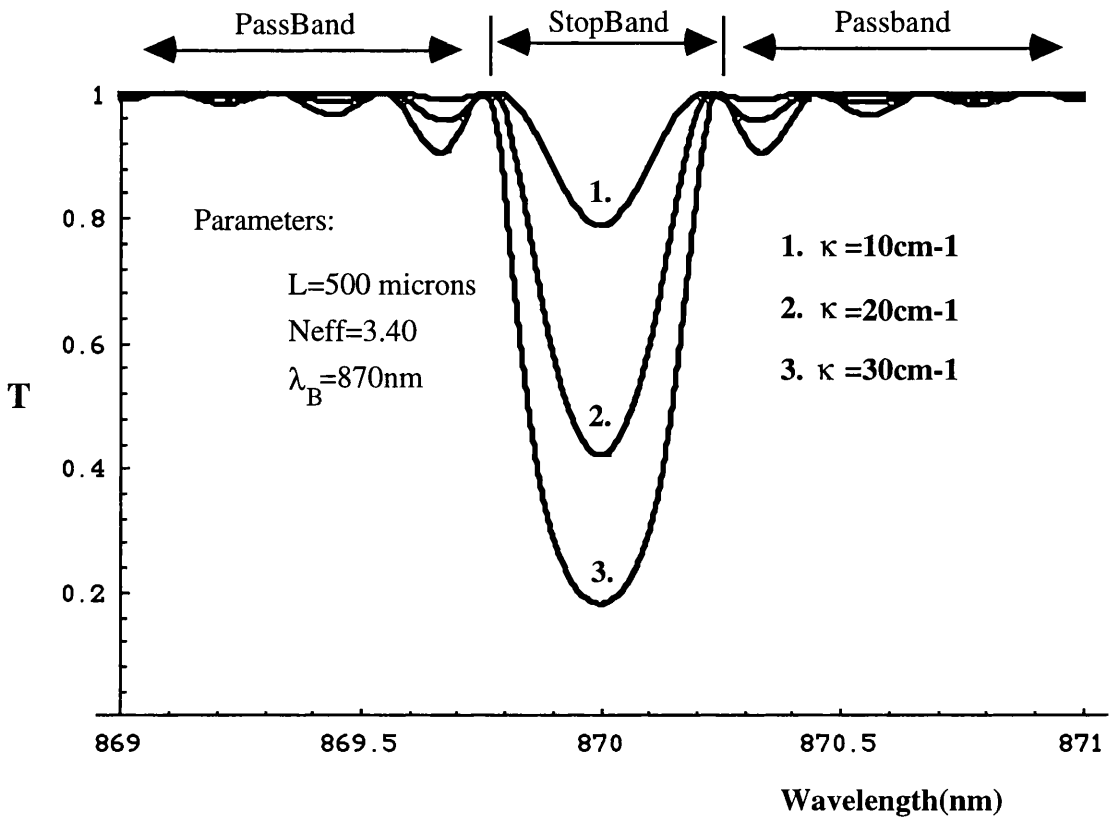

Fig.3.4: Transmission characteristic of a DFB waveguide as a function of the wavelength in the weak-coupling range: κL=0.5-1.5

Fig.3.4 shows the transmission characteristics of a DFB waveguide as a function of the wavelength for different values of the coupling coefficient. The dip in the transmission at the Bragg wavelength is caused by coherent back reflections and increases with the grating coupling coefficient. The transmissivity is unity at a discrete set of wavelengths within the passband. According to the coupled-wave equations, at these wavelengths the backward wave has a sinusoidal distribution within the structure and vanishes at the two end planes of the structure. These wavelengths correspond to the resonant modes of the periodic structure.

Note also that the transmissivity is extremely sensitive to the coupling coefficient. This fact will be used in chapter 6 to measure the coupling coefficient of DFB waveguides by measuring the transmissivity of different DFB waveguides, which presents values of κ in the

range 10-20cm^{-1}. In deriving Eq.(3.3.11), both waveguide losses and coupling to radiation modes were ignored. A different expression, e.g. Eq. (88) reference [3.6], can be used in which a loss constant parameter α is taken into account. The reflection and transmission coefficient formulae, including loss effects, are now presented:

$$R = \left| \frac{\kappa Sinh(sL)}{(\alpha + j\Delta\beta)Sinh(sL) + sCosh(sL)} \right|^2 \qquad (3.3.12)$$

$$T = \left| \frac{-se^{-j\beta_0 L}}{(\alpha + j\Delta\beta)Sinh(sL) + sCosh(sL)} \right|^2 \qquad (3.3.13)$$

where:

$s^2=\kappa^2+(\alpha+j\Delta\beta)^2$

α - Loss constant of the corrugated section

κ - Coupling Coefficient

$\Delta\beta$ - Bragg detuning

L- Length of the corrugated section

Follows plots of (R,T) for different loss values.

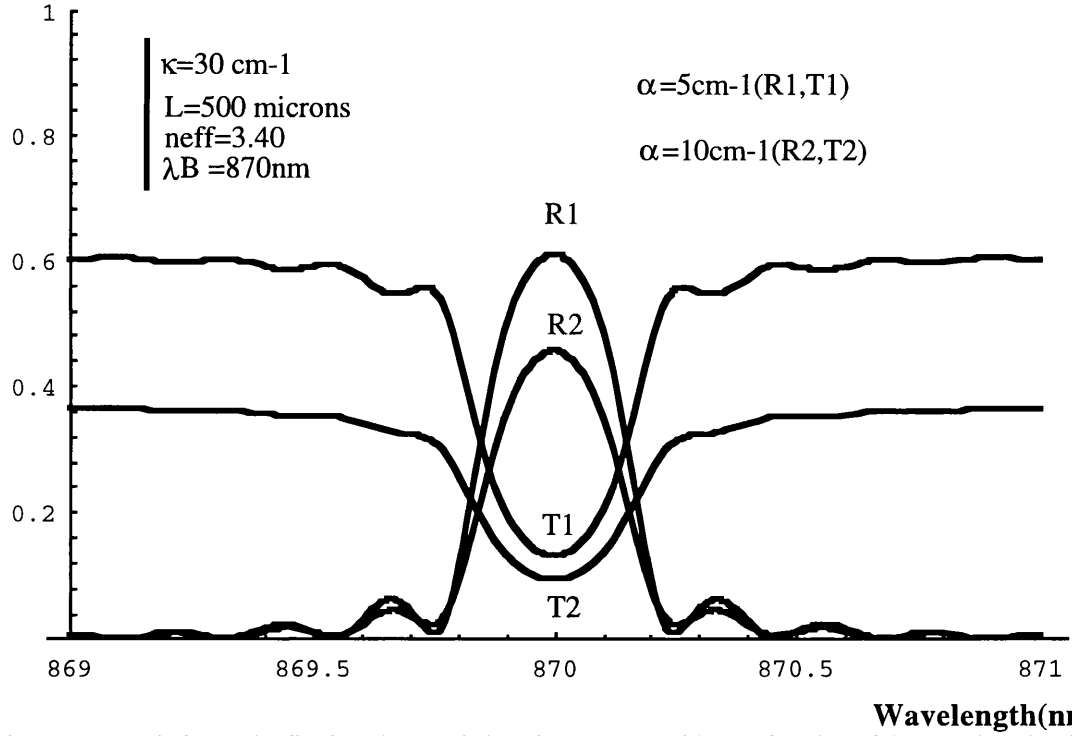

Fig.3.5: Transmission and reflection characteristics of DFB waveguide as a function of the wavelength. The waveguide loss is used as a parameter.

Fig.3.5 shows the reflection and transmission characteristics of a DFB waveguide as a funtion of the wavelength for different values of the waveguide loss (α). Contrary to the lossless situation, where the transmissivity is unity at a discrete set of wavelengths within the passband, the loss situation presents a transmissivity less than unity. The transmissivity value away from the Bragg wavelength can be calculated using following eqs:

$$\frac{dP}{dz} = -\alpha P \Rightarrow \frac{Pout}{Pin} = Exp(-\alpha L);$$

$$T = \frac{Pout}{Pin} = Exp(-10 \times 0.05) = 0.6$$

This value agrees with curve T_1 shown above.

From the curves shown in Fig.3.5, the maximum reflection (or corresponding max. transmission) decreases with the waveguide losses. In calculating the maximum reflection value (R_{max}) from the transmission spectrum its value is lower than the one calculated directly from the reflection spectrum. This result is important since experimentally the maximum reflection value (R_{max}) is calculated from the transmission spectra and then used to calculate the coupling coefficient. The following table illustrated the errors introduced when different losses are considered and the coupling coefficient is calculated from the reflection spectrum (κ_{ref}) or from the transmission spectrum (κ_{trans}).

Amplitude Loss (cm^{-1})	Power Loss (cm^{-1})	$\kappa_{ref.}(cm^{-1})$	Error (%)	$\kappa_{trans}(cm^{-1})$	Error (%)
0	0	30	0%	30	0%
5	10	20.9	30%	16.7	44%
10	20	16.4	45%	11.5	62%

Table 3.1: Coupling coefficient values calculated from reflection (κ_{ref}) and transmission (κ_{trans}) spectrum. Waveguide loss is used as a parameter.

Table 3.1 shows that the error introduced in the coupling coefficient (DFB waveguide is assumed to have $30cm^{-1}$) when losses in the waveguide are considered. Two different methods to calculate coupling coefficient (κ) are used, namely measurement of maximum reflection (R_{max}) from reflection spectrum (κ_{ref}) and from transmission spectrum (κ_{trans}). The results show that the errors introduced are significantly higher when R_{max} is calculated from the transmission spectrum rather than from reflection spectrum.

3.4 The Distributed feedback laser

The case of a passive waveguide with periodic perturbation is described by equations (3.3.1) and (3.3.2) in the previous section. For a guiding medium with gain, these equations simply need to be modified by adding gain terms, so that, when $\kappa=0$, the two independent solutions, A(z) and B(z), correspond to exponentially growing waves along the -z and z directions, respectively. Adding gain terms to (3.3.1) and (3.3.2), we have

$$\frac{dA}{dz} = \kappa_{ba} B e^{-j2(\Delta\beta)z} - \gamma A \tag{3.4.1}$$

$$\frac{dB}{dz} = \kappa_{ba} A e^{j2(\Delta\beta)z} + \gamma B \tag{3.4.2}$$

where κ_{ba} is the coupling coefficient and γ is the exponential gain constant of the medium. These equations can be simplified if we define new variables such as

$$A(z)=A'(z)e^{-\gamma z}, \qquad B(z)=B'(z)e^{\gamma z}$$

Equations (3.4.1) and (3.4.2) become

$$\frac{dA'}{dz} = \kappa_{ba} B' e^{-j2(\Delta\beta+j\gamma)z} \tag{3.4.3}$$

$$\frac{dB'}{dz} = \kappa^{*}_{ab} A' e^{j2(\Delta\beta+j\gamma)z} \tag{3.4.4}$$

These are the equations for a waveguide with distributed feedback and optical gain. Note, however, that equations (3.4.3) and (3.4.4) become identical to equations (3.3.1) and (3.3.2), provided that $\Delta\beta$ is replaced by $\Delta\beta+j\gamma$. With this substitution, equations (3.4.3) and (3.4.4) can be used to obtain directly the solution for the total complex field $E(z)=B'(z)\exp[(-j\beta+\gamma)z]+A'(z)\exp[(j\beta-\gamma)z]$ within the periodic section of length L of the waveguide. Assuming an input incident field of B(0) at z=0, the 'forward' wave $B'(z)\exp[(-j\beta+\gamma)z]$ and the 'backward' wave $A'(z)\exp[(j\beta-\gamma)z]$ are:

$$B'(z)e^{[(-j\beta+\gamma)z]} = B(0)\frac{e^{-j\beta_0 z}\left\{(\gamma - j\Delta\beta)Sinh[s(L-z)] - sCosh[s(L-z)]\right\}}{(\gamma - j\Delta\beta)Sinh(sL) - sCosh(sL)} \tag{3.4.5}$$

$$A'(z)e^{[(j\beta+\gamma)z]} = B(0)\frac{k_{ab}e^{j\beta_0 z}Sinh[s(L-z)]}{(\gamma - j\Delta\beta)Sinh(sL) - sCosh(sL)} \tag{3.4.6}$$

where

$$s^2 = \kappa^2 + (\gamma - j\Delta\beta)^2$$

The behaviour of the incident and reflected fields for a high gain case is sketched in Fig.3.5.

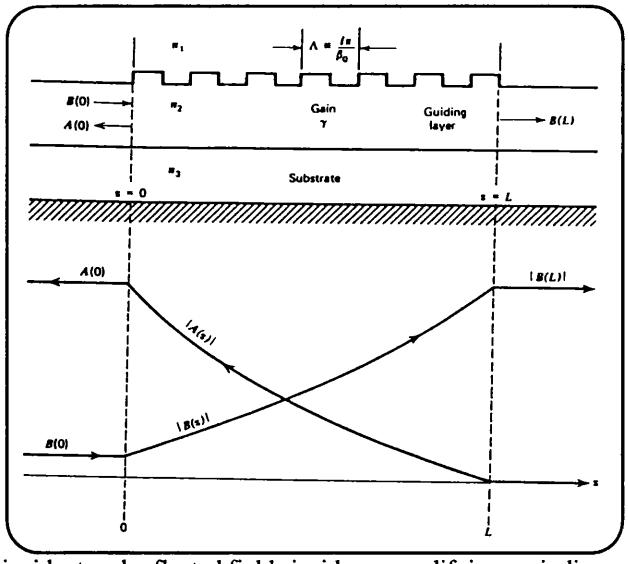

Fig.3.5: Illustration of incident and reflected fields inside an amplifying periodic waveguide near the Bragg condition $\beta \approx m\pi/\Lambda$ [3.8]

3.5 The Oscillation Condition

Notice that $\underline{s}$ is now complex (It is also complex for the passive case when $\Delta\beta > \kappa$). This fact introduces a qualitative difference between the behaviour of the passive periodic waveguide, given by (3.3.3) and (3.3.4), and the periodic waveguide with gain given by expressions (3.4.5) and (3.4.6). To demonstrate this difference, consider the case when the condition

$$(\gamma - j\Delta\beta)Sinh(sL) = sCosh(sL) \qquad (3.5.1)$$

is satisfied. From (3.4.5) and (3.4.6), it follows that both reflectance and transmittance, given by $(E_r(0)/E_i(0))$ and $(E_i(L)/E_i(0))$ respectively, become infinite (See peaks in fig.3.6).This means that, for a device of given length L and given coupling coefficient κ, solutions are possible only for a discrete set of gain constants γ and associated frequencies $\Delta\beta$. These frequencies are the resonant frequencies of the DFB structure and the associated gains are the values needed at threshold. Relation (3.5.1) is, therefore, the oscillation condition for a distributed feedback laser. Note, however, that for the case of $\gamma=0$, the coefficients obey $|E_i(L)/E_i(0)|<1$ and $|E_r(0)/E_i(0)|<1$, as is appropriate for a passive device with no internal gain.

The periodic waveguide with gain acts as a high gain amplifier under the following conditions: (i) For frequencies very near the Bragg frequency $\omega_0(\Delta\beta=0)$; (ii) For sufficiently high gain so that the oscillation condition (3.4.1) is nearly satisfied.

The amplitude gain is available either in reflection or in transmission. The reflection and transmission coefficients are given, respectively, by

$$\frac{E_r(0)}{E_i(0)} = \frac{\kappa_{ba}\,\mathrm{Sinh}(sL)}{(\gamma - j\Delta\beta)\mathrm{Sinh}(sL) - s\mathrm{Cosh}(sL)} \tag{3.5.2}$$

$$\frac{E_i(L)}{E_i(0)} = \frac{-se^{-j\beta_0 L}}{(\gamma - j\Delta\beta)\mathrm{Sinh}(sL) - s\mathrm{Cosh}(sL)} \tag{3.5.3}$$

The behaviour of the transmitance $|E_i(L)/E_i(0)|^2$ is sketched in Fig.3.6.

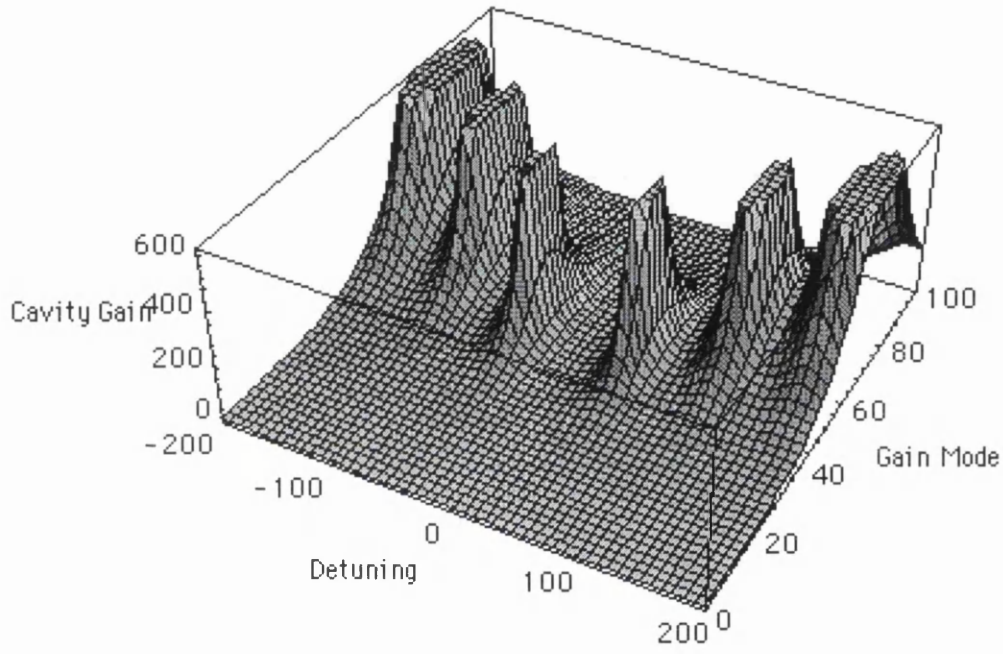

Fig.3.6: Calculated transmission gain $|E_i(L)/E_i(0)|^2$ for values of the coupling coefficient of $10cm^{-1}$ and cavity length 500μm. Detuning and modal gain are in cm^{-1}

The most important aspect represented in Fig. 3.6 is the fact that DFB lasers exhibit longitudinal mode selectivity, which is in contrast to conventional Fabry-Perot cavities where all allowed modes have the same threshold gain. This effect is further illustrated in the following contour map of Fig.3.6.

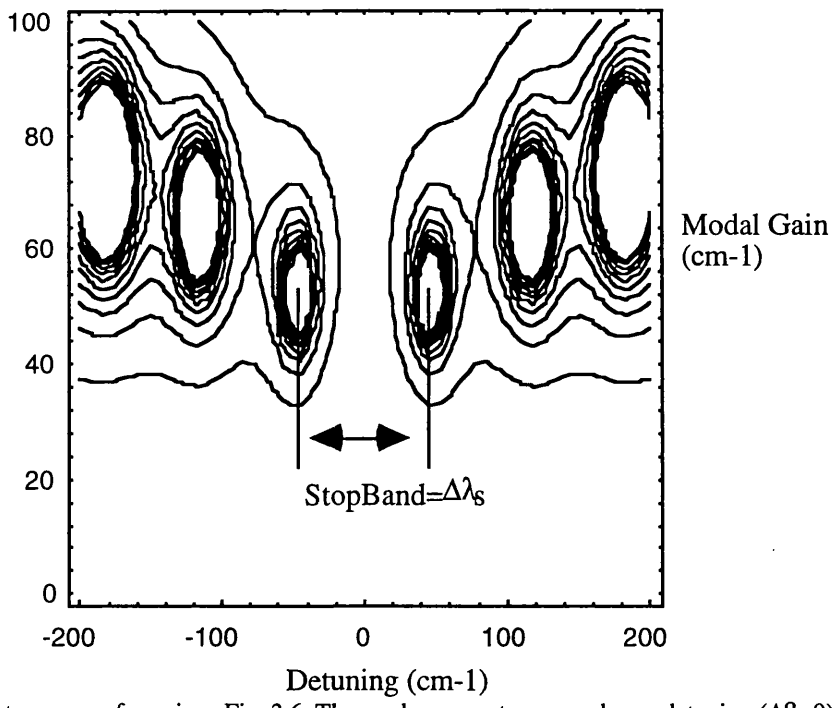

Fig.3.7: Contour map of previous Fig. 3.6. The mode symmetry around zero detuning ($\Delta\beta=0$) is clear . Six longitudinal modes are illustrated

As illustrated in Fig.3.7, the conventional DFB laser has two spectral modes or wavelengths of operation with exactly the same required threshold gains. In this example, the main modes (lowest threshold gain modes) have a 52.2cm^{-1} intensity gain and 46.3cm^{-1} detuning from the Bragg wavelength. The stopband width can be calculated using the following expression, which relates the normalized detuning with the stopband width:

$$\Delta\lambda_s = -\frac{\lambda^2}{2\pi n_{eff} L}(\Delta\beta L) \qquad (3.5.4)$$

The stopband width is calculated to be 3.1A, where typical values of L=500μm, λ=860nm and n_{eff}=3.5 were assumed in the calculation. The difference in the threshold gain between the main and side modes is 13.2 cm^{-1}, which is sufficient for only the two main modes with lowest threshold gain to oscillate [3.9].

The longitudinal modes are equidistant from the Bragg wavelength, i.e., on either side of the stopband. However, this only happens for completely symmetric homogeneous, infinite structures. Normally this symmetry of period is interrupted and the degeneracy removed when the output facet is cleaved. The asymmetry in the required threshold gain caused by reflection at one or both facets has been studied by Streifer et al[3.10].

The phase of the grating where it is interrupted by the cleaved output mirror, the facet phase, is an important parameter. The importance of this facet phase in determining the lasing

threshold and oscillation wavelength has been experimentally demonstrated by Matsuoka et al. [3.12]. Several methods of removing the spectral degeneracy have been thoroughly discussed in Chapter 2.

3.6 Calculation of lasing modes and modal threshold gain in DFB laser structures

For a DFB laser cavity, characterized by a given length L and coupling κ, only a discrete pair of values for the threshold gain and detuning are possible. In Fig.3.8, the gain required at threshold as a function of detuning from the Bragg wavelength is represented, in which two different regimes are observed: (1) For small values of the coupling coefficient, the threshold gain is very large and the resonances are close to $\nu=mc/2n_{eff}L$ (m is integer, n_{eff} - effective refractive index), which are equal to the longitudinal mode spacing of a FP laser; (2) When the coupling coefficient is large, the threshold gain is small and the first resonance is pushed away from the Bragg wavelength by as much as three times the value for the low-coupling case.

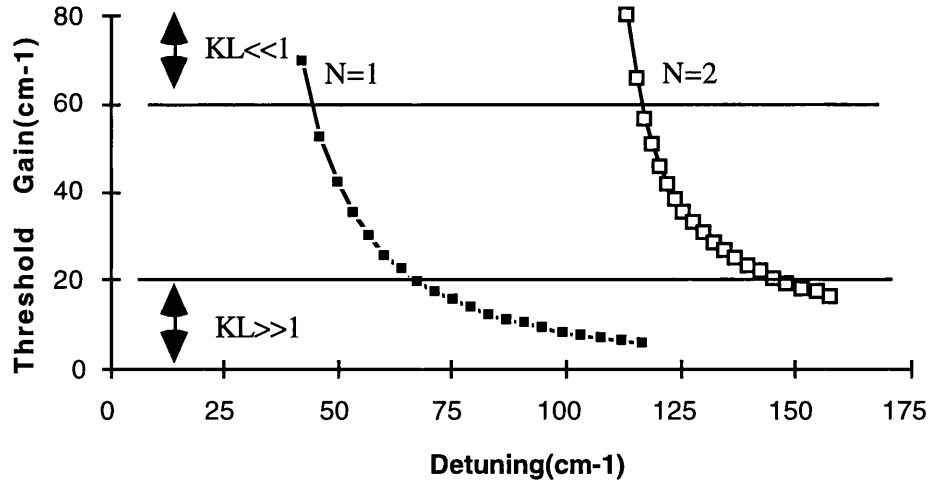

Fig.3.8: Threshold gain versus detuning from the Bragg condition for an index periodicity. Because of symmetry with respect to Bragg frequency ($\Delta\beta=0$), only half of the spectrum is shown.

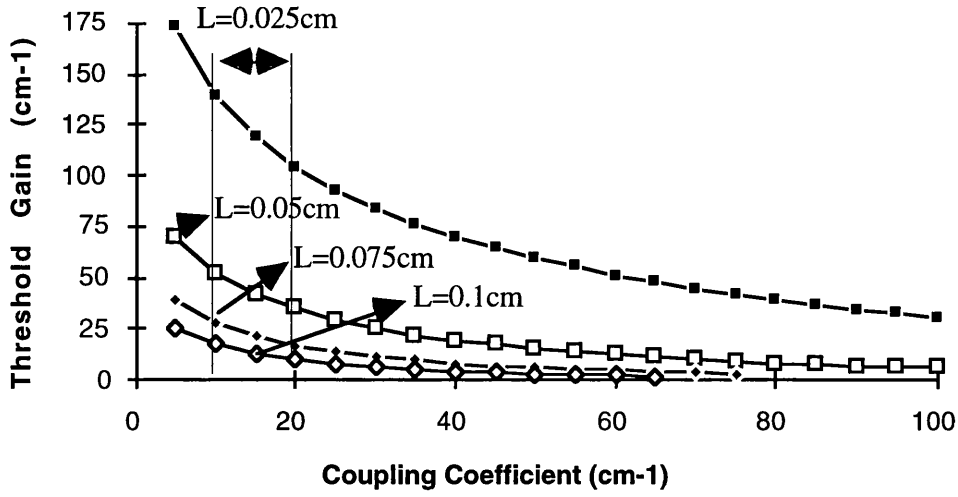

Fig.3.9: Threshold gain versus coupling coefficient with length as a parameter

The threshold gain and laser frequencies of DFB devices depend greatly on the strength of the coupling coefficient (between forward- and backward travelling waves). The case of a pure DFB (no external reflectors) was treated by Kogelnik and Shank [3.4] and their results are presented in a slightly different form in Fig.3.9. Threshold gain is plotted versus the coupling coefficient, with the device length as parameter. Using this figure, one can determine the minimum necessary device length L, given κ and gain available, or alternatively, given the gain and L the plot specifies the minimum value of κ required. In the coupling coefficient range 10-20cm^{-1} (the case of surface grating structures), the gain required for threshold decreases drastically as the device length increases, specifically from L=250μm to L=500μm. It is therefore important to use gratings longer than 500μm to obtain laser action at moderate threshold current.

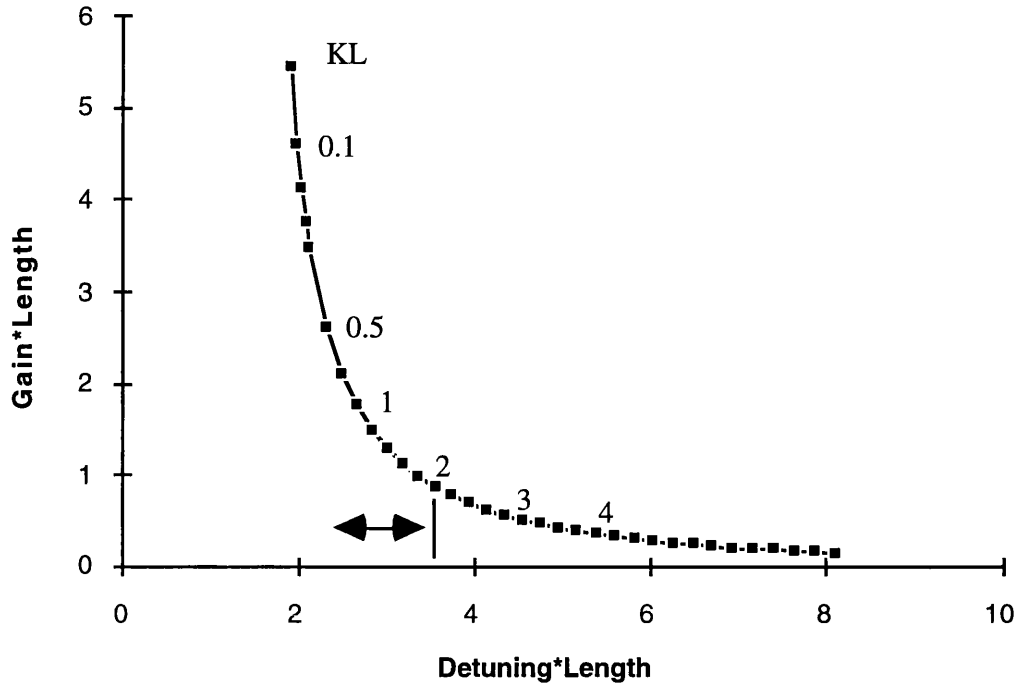

Fig.3.10: Normalized threshold gain versus normalized detuning

In Fig.3.10, the normalized gain versus normalized detuning is plotted. Usually, this plot is used to determine the κL product by experimentally measuring the stopband width, which is related to the normalized detuning (Δβ$_s$L) by the following relation:

$$(\Delta\beta_s L) = -\frac{2\pi n_{eff} L}{\lambda^2}\Delta\lambda_s \qquad (3.6.1)$$

Note that for a κL product less than 2, the stopband width is less sensitive to variations in κL(Fig.3.10). For instance, when the κL product varies from 1 to 1.5 (50% increase) the stopband width increases only by 10%, so large inaccuracies in calculating the coupling coefficient can be introduced when the stopband width measuring method is used in this particular κL range (κL<2). To avoid this problem, an alternative technique for measuring the coupling coefficient in deep surface grating structures (where κL=0.5 - 1) will be discussed in chapter 6, in which a transmission approach rather than the stopband width measurement is applied.

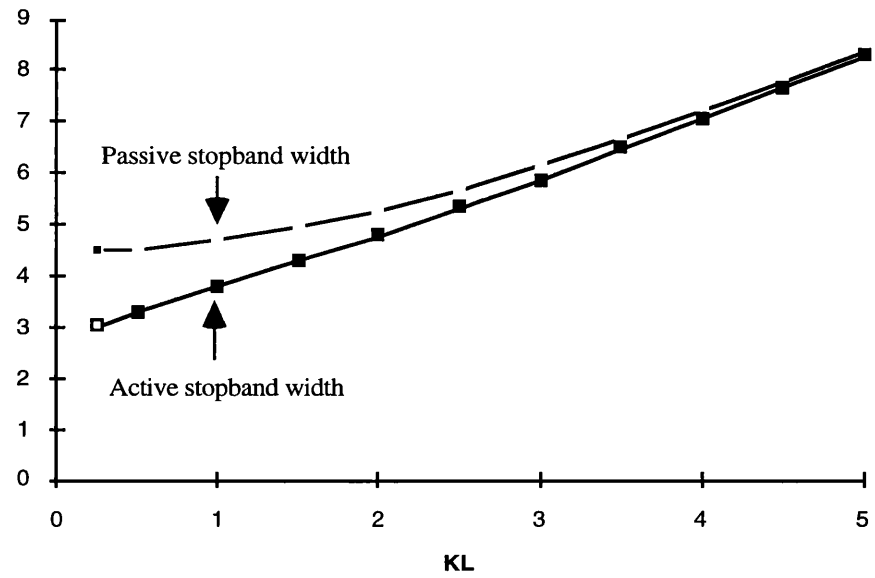

Fig.3.11: Stopband width for active and passive devices as a funtion of the κL product

Fig.3.11 shows the stopband width as a function of the κL product for active and passive devices. The stopband width for passive devices is calculated using equation (3.3.11), which relates the transmission of a DFB waveguide with the wavelength. The stopband width for active devices was calculated using relation (3.4.1), which relates the threshold gain with the detuning for a given κL product.

3.7 Calculation of κ as a function of the grating depth using different theoretical models.

3.7.1 Introduction

Index-coupled DFB lasers differ from conventional lasers in that feedback is provided by a distributed periodic spatial variation in refractive index and/or geometry, rather than by discrete reflectors. The analysis of these devices has been carried out as a function of the coupling coefficient κ [3.4]. Genererally, κ has been expressed in terms of refractive index variations, but in many situations the feedback is introduced instead by periodic corrugations. In order to employ the results for thresholds and frequencies derived for a pure DFB laser [3.4] or similar results for DFB lasers with external reflectors [3.10],[3.11], the coupling coefficient of such corrugation structures must be first calculated. This calculation has been formally performed by several authors [3.13],[3.14] using a perturbation technique in which modes of the unperturbed waveguide are analysed in their interaction with the corrugation.

Analytic and numerical results for TE-mode coupling coefficients for various tooth shapes, namely rectangular, sinusoidal, triangular, and sawtooth, as well as Bragg scattering orders m have been reported in the literature [3.15],[3.16]. In the following analysis only rectangularly shaped gratings are considered since one is interested in deep surface grating structures, which are characterized by that shape. It should be pointed out that this is a classical shallow grating analysis, and therefore it is not wholly applicable to deep surface grating structures. However, many features presented by shallow grating results are common to deep surface grating structures, as will be discussed in the next sections.

In this section, different models for calculating the coupling coefficient of a certain corrugation structure are considered. Basically, the main difference between the normal-mode analysis by Streifer et al.[3.15],[3.16] and the improved coupled-mode analysis by Yamamoto [3.17] is the geometry selected for computing the unperturbed guided mode E(x), i.e., the waveguide geometry without grating. In reference [3.30], a specific waveguide structure is considered, where four different waveguide geometries are selected for calculating the coupling coefficient.

3.7.2 Normal coupled-mode analysis by Streifer et al. [3.15], [3.16].

In the three-layer laser structure, illustrated in Fig.3.12, there exists forward and backward TE and TM modes coupled by the corrugation. A perturbation analysis is used to obtain an expression for the coupling coefficient produced by the corrugation. The result of the perturbation analysis, as given in [3.14] for TE modes, is

$$\kappa = \frac{k_0}{2\beta N^2} \int_{corrugation} \Delta[n^2(x,z)]E^2(x)dx \qquad (3.7.1)$$

where κ is the coupling coefficient, $k_0=2\pi/\lambda_0$ is the free space wavenumber, β is the TE-mode propagation constant, E(x) is the y component of the unperturbed E-field, and N^2 is a normalization constant given by

$$N^2 = \int_{-\infty}^{+\infty} E^2(x)dx \qquad (3.7.2)$$

A. The theoretical model

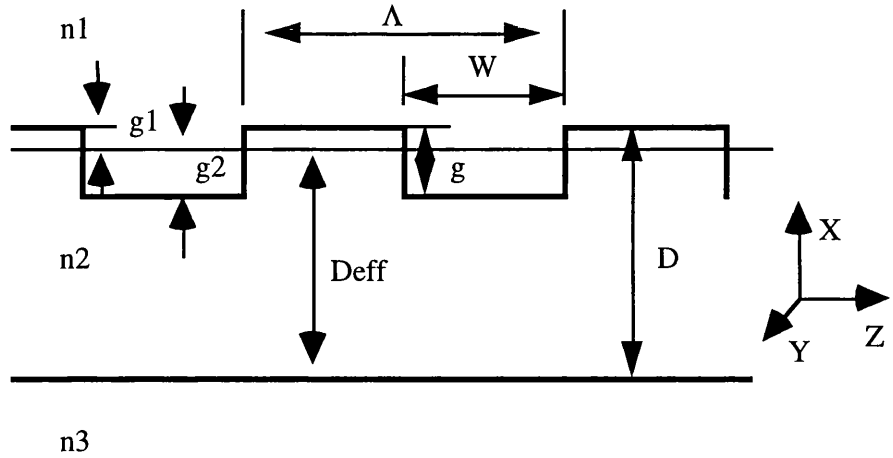

Fig.3.12: Three-layer DFB laser structure

Waveguide parameters:

n_1- Refractive Index of the upper cladding layer

n_2-Refractive Index of Waveguide

n_3- Refractive Index of the lower cladding layer

D- Waveguide thickness

Grating parameters:

Λ- Grating period

g- Grating depth

W- Tooth width

m- Bragg order

$$g_1 = \left(\frac{w}{\Lambda}\right)g$$

$$g_2 = \left(1 - \frac{w}{\Lambda}\right)g$$

As shown in Fig.3.12, g_1 and g_2 are the maximum tooth heights in media 1 and 2, respectively; g_1 and g_2 are used as the integration limits of eq. (3.7.1).

B. *Summary of the Theory*

The coupling coefficient for a rectangularly shaped grating is given by the following expression, which results from the integration of (3.7.1) and (3.7.2).

$$\kappa = \kappa_1\{g_2 + \kappa_2 + \kappa_3 + \kappa_4 + \kappa_5\} \tag{3.7.3}$$

Where:

$$\kappa_1 = \frac{k_0^2\left(n_1^2 - n_2^2\right)}{4\pi\beta_0 mN^2} Sin\left(\frac{\pi mW}{\Lambda}\right) \tag{3.7.4}$$

$$\kappa_2 = \frac{Sin(2g_2u_2)}{2u_2} \tag{3.7.5}$$

$$\kappa_3 = \frac{u_1}{u_2^2}\left[1 - Cos(2g_2u_2)\right] \tag{3.7.6}$$

$$\kappa_4 = \frac{u_1^2}{u_2^2}\left[g_2 - \frac{Sin(2g_2u_2)}{2u_2}\right] \tag{3.7.7}$$

$$\kappa_5 = \frac{1}{u_1}\left[1 - Exp(-2g_1u_1)\right] \tag{3.7.8}$$

$$N^2 = \frac{\left(u_2^2 - u_1^2\right)\left(D_{eff} + u_1^{-1} + u_3^{-1}\right)}{2u_2^2} \tag{3.7.9}$$

and, (u1,u2,u3) are the tranverse propagation relations given by

$$u_1 = \sqrt{\beta_0^2 - n_1^2 k_0^2} \tag{3.7.10}$$

$$u_2 = \sqrt{n_2^2 k_0^2 - \beta_0^2} \tag{3.7.11}$$

$$u_3 = \sqrt{\beta_0^2 - n_3^2 k_0^2} \tag{3.7.12}$$

$$k_0 = \frac{2\pi}{\lambda_0}$$

$$D_{eff} = D - \left(\frac{w}{\Lambda}\right) g \tag{3.7.13}$$

D_{eff} is the effective unperturbed guide thickness, as shown in Fig.3.12. It is chosen such that the volume of n_1 material extending into region 2 just equals the volume of n_2 material extending into region 1.

β_0- Propagation constant of the fundamental mode, found by solving:

$$Tan(u_2 D_{eff}) = \frac{u_2(u_1 + u_3)}{u_2^2 - u_1 u_3} \tag{3.7.14}$$

Firstly, it should be stressed that the coupling coefficient, Eq.(3.7.3) is valid only for small values of $|\kappa|$ which result when $|n_1^2 - n_2^2|$ and/or the ratio g/D_{eff} are small.

Dependence on the Bragg-scattering order m is completely described by the multiplicative term:

$$\frac{\mathrm{Sin}[\pi m W / \Lambda]}{m}$$

and for integral values of mW/Λ, κ is zero, e.g., $W/\Lambda=0.5$, and m=2,4,6,... Although the variation of $|\kappa|$ with the tooth height g is completely contained in the bracketed expression in Eq.(3.7.3) that dependence is rather complex and best exhibited graphically as shown in reference [3.15].

The procedure to calculate the coupling coefficient κ is the following:

1. For a given grating depth g, evaluate D_{eff}.

2. Using D_{eff} and the eigenequation (3.7.14) for the guided modes, all the other parameters can be calculated: u_1, u_2, u_3, β, N

3. Replacing the above calculated values in the κ_i expressions, compute κ.

3.7.3 Improved coupled mode analysis by Yamamoto et al. [3.17]

The coefficient $\kappa_{ab}^{(m)}$ is the coupling coefficient for the m^{th}-order grating diffraction and is given by

$$\kappa_{ab}^{m} = \frac{w\varepsilon_0}{4}\int A_m(x)E_{ya}^{*}E_{yb}dx \qquad (3.7.15)$$

where ε_0 is a vacuum permittivity and $A_m(x)$ is the m^{th}-order Fourier coefficient of the refractive-index perturbation: $\Delta n^2(x,z)=n^2(x,z)-n_0^2(x)$.

A.The theoretical model

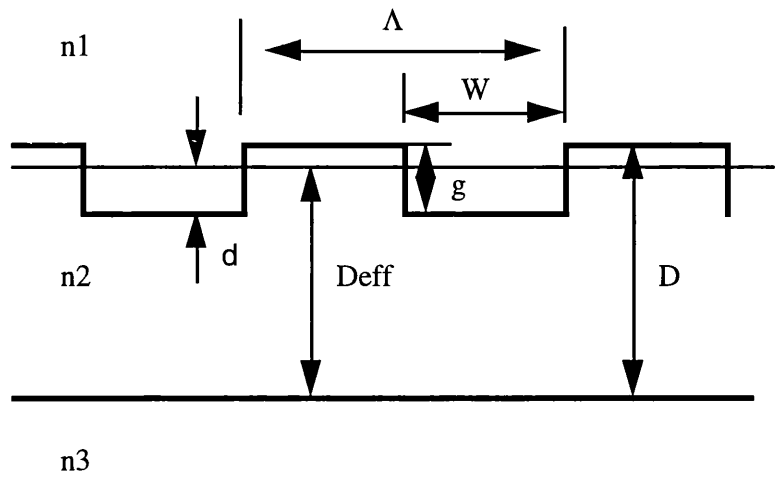

Fig.3.13: Three layer DFB Laser Structure

Where:

(n_1,n_2,n_3,D) - Waveguide parameters as described above

(Λ,w,g,m) - Grating parameters as described previously

B. Summary of the Theory

The Coupling Coefficient for a rectangularly shaped grating is given by following expression, which results from integration of (3.7.15):

$$\kappa = \kappa_1\{d + \kappa_2 + \kappa_3 + \kappa_4\} \qquad (3.7.16)$$

where:

$$\kappa_1 = \frac{k_0^2\left(n_2^2 - n_1^2\right)}{2\pi\beta m\left(\frac{1}{u_1} + \frac{1}{u_3} + D_{eff}\right)} Sin\left(\frac{\pi m W}{\Lambda}\right) \tag{3.7.17}$$

$$\kappa_2 = \frac{u_1}{k^2\left(n_2^2 - n_1^2\right)}\left[1 - Cos(2u_2 d)\right] \tag{3.7.18}$$

$$\kappa_3 = \frac{\left(u_2^2 - u_1^2\right)}{2u_2 k^2\left(n_2^2 - n_1^2\right)} Sin(2u_2 d) \tag{3.7.19}$$

$$\kappa_4 = \frac{1 - Exp\left[-2u_1(g-d)\right]}{u_1} Sin^2(\phi_0) \tag{3.7.20}$$

with $u_1, u_2, u_3, \phi_0, \beta$ being implicit functions of $\underline{d}$, which depends on both waveguide and grating parameters; (u_1, u_2, u_3) are defined as in section 3.7.2, and ϕ_0 as follows:

$$\phi_0 = Tan^{-1}\left(\frac{u_2}{u_1}\right) \tag{3.7.21}$$

As illustrated in Fig.3.13, $\underline{d}$ is the distance between the unperturbed waveguide boundary and the bottom of the grating. It is determined so as to nullify the self-coupling coefficient of the guided mode, which represents a change of the propagation constant of the guided mode due to the corrugation [3.14]. The condition is:

$$\int A_0(x) E_{ym}(x)^2 = 0 \tag{3.7.22}$$

where $A_0(x)$ is the zeroth order Fourier coefficient of the refractive-index perturbation $\Delta n(x,z)^2$. $\underline{d}$ is given for a rectangular shaped grating by:

$$\frac{W}{\Lambda} Sin^2(\phi_0)\frac{1 - Exp\left[-2u_1(g-d)\right]}{u_1} - \left(1 - \frac{W}{\Lambda}\right)\left[d - \frac{Cos(u_2 d + 2\phi_0) Sin(u_2 d)}{u_2}\right] = 0 \tag{3.7.23}$$

Once the value of $\underline{d}$ is known, all the implicit functions of $\underline{d}$ can be evaluated using D_{eff} defined as follows:

$$D_{eff} = D - g + d$$

D_{eff} is the effective unperturbed guide thickness, as shown in Fig.3.13.

The procedure to calculate κ is, then:

1. Estimate d using the approximate expression

$$d = \left(\frac{w}{\Lambda}\right)g$$

2. Use the estimated value of d to evaluate $u_1, u_2, u_3, \phi_0, \beta$.

3. Use the previous values of $u_1, u_2, u_3, \phi_0, \beta$ and the grating parameter Λ,w,g to compute d using equation (3.7.23).

4. Repeat (iterative process) steps 2. and 3. until convergence of d.

5. Use the final value of d to calculate the 'exact' solution of $u_1, u_2, u_3, \phi_0, \beta$.

6. Replace the above values in the κ_i expressions, and then compute the κ value .

3.7.4 Simple Effective Refractive Index Theory [3.18]

The coupling coefficient κ is derived assuming that the two sections of the grating act as multilayer dielectric mirrors [3.7], the reflectivity of one pair of sections being given by:

$$\Gamma = \kappa.\Lambda_g = \frac{\left(n_{eff\,1}^2 - n_{eff\,2}^2\right)}{\left(n_{eff\,1}^2 + n_{eff\,2}^2\right)} \mathrm{Sin}\left[\frac{m\pi W}{\Lambda_g}\right] \qquad (3.7.24)$$

where n_{eff1} is the refractive index of the unetched slab waveguide, Fig.3.14. The refractive index for a ridge waveguide, n_{eff2} was calculated (using a finite difference method), which had the same width as the grating waveguide. The ridge height was taken as the depth of the etched grating, g. The final term is derived from the phase difference of the waves reflected at each section interface, where W is the width of the etched section, Λ_g the spatial period of the grating, and m the Bragg-scattering order.

A. The theoretical model

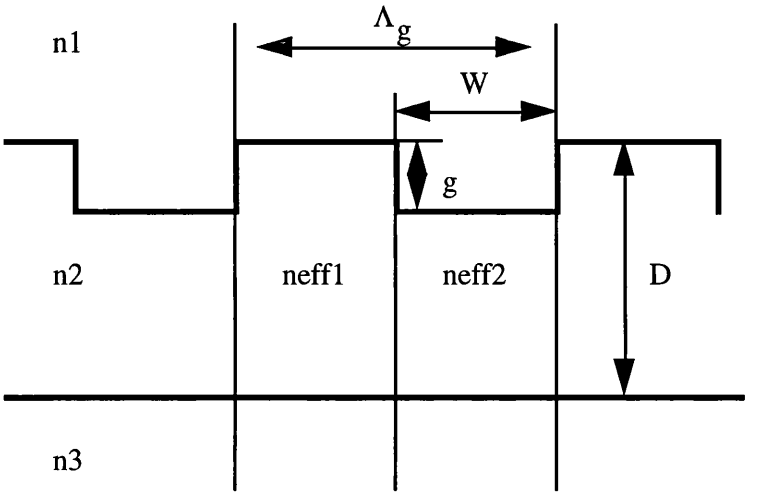

Fig.3.14: Cross-section of three layer grating waveguide structure

(n_1,n_2,n_3,D) - Waveguide parameters as described above

(Λ_g,w,g) - Grating parameters as described previously

B. Summary of the Theory

After some manipulation of Eq.(3.7.24), the coupling coefficient is simply given by

$$\kappa = \frac{\left(n_{eff\,1} - n_{eff\,2}\right)}{n_{aveg}} \frac{1}{\Lambda_g} Sin\left(\frac{m\pi W}{\Lambda_g}\right) \tag{3.7.25}$$

It was assumed that $n_{eff1} \sim n_{eff2}$ and then $(n_{eff1}-n_{eff2}) << n_{eff1}$. n_{aveg} is the average refractive index of the grating waveguide, given by $(n_{eff1}+n_{eff2})/2$ as the grating was assumed to have a 1:1 mark-space ratio.

Procedure to calculate κ:

1. n_{eff1},n_{eff2} are calculated using a finite difference method for each g.

2. Use the computed values of n_{eff1} and n_{eff2} as well as the grating parameters (Λ_g,W,m) to calculate κ.

3.7.5 Four-layer model by Wang [3.13]

The basic structure proposed by Wang consists of a thin film (the laser medium) sandwiched betweeen a substrate and a top dielectric layer. In such structure, the waveguiding property can be changed by varying either the thickness d or the refractive index n_d of the top layer, Fig.3.15.

If d or n_d is varied periodically, the transverse wavenumber k_x in the film changes accordingly. Since k_x and k_z (the longitudinal wavenumber) are related, a periodic change in k_x produces a corresponding periodic change in k_z. The resultant spatial variation of k_z will periodically produce a reflected wave, and this periodic reflection can provide the necessary feedback for the laser action.

A. The theoretical model

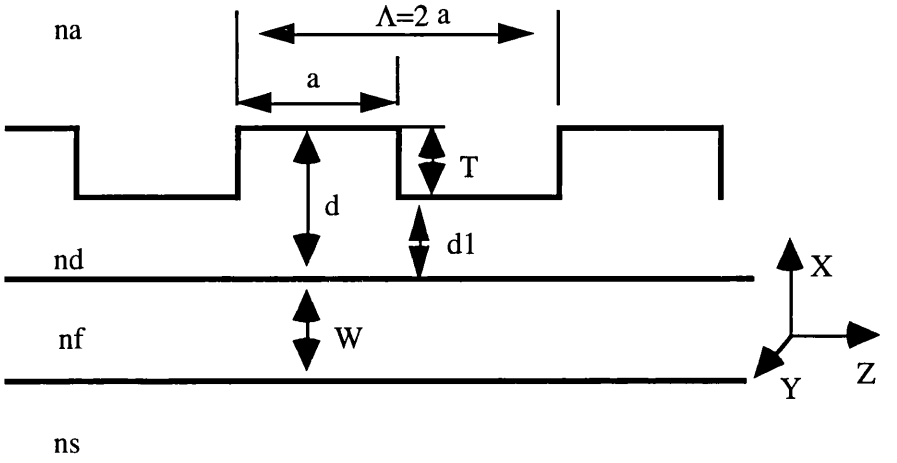

Fig.3.15: Four-layer DFB laser structure

Parameters:

n_f - refractive index of film
n_d - refractive index of top dielectric layer
n_a - refractive index of air
n_s - refractive index of substrate
W - film thickness
d - top dielectric thickness
a - grating tooth width
λ_o - free-space wavelength

***B.** Summary of the theory*

The coupling coefficient is given by the following expression:

$$\kappa = \frac{2}{a}\left(\frac{k_x}{k_z}\right)^2 \frac{l_{fd}^2}{l_d(l_d + l_s + W)}\left(\frac{l_d - l_a}{l_d + l_a}\right)\mathrm{Exp}\left(-\frac{2d_1}{l_d}\right) \tag{3.7.26}$$

This equation is valid under the condition: $p_d(d-d_1)>1$

where:

k_X is calculated using a wave propagation method. A new variavel $\underline{x}$ is defined as $x=k_X.W$.

$$k_0 = \frac{2\pi}{\lambda_0} \tag{3.7.27}$$

$$p_d = \left[\left(n_f^2 - n_d^2\right)k_0^2 - \frac{x^2}{W^2}\right]^{\frac{1}{2}} \tag{3.7.28}$$

$$p_a = \left[\left(n_f^2 - n_a^2\right)k_0^2 - \frac{x^2}{W^2}\right]^{\frac{1}{2}} \tag{3.7.29}$$

$$p_s = \left[\left(n_f^2 - n_s^2\right)k_0^2 - \frac{x^2}{W^2}\right]^{\frac{1}{2}} \tag{3.7.30}$$

$$\phi_{ed} = \mathrm{Tan}^{-1}\left(\frac{p_d.W}{x}.\frac{p_a + p_d\mathrm{Tanh}(p_d.d)}{p_d + p_a\mathrm{Tanh}(p_d.d)}\right) \tag{3.7.31}$$

$$\phi_{es} = \mathrm{Tan}^{-1}\left(\frac{p_s.W}{x}\right) \tag{3.7.32}$$

$$k_X.W - \phi_{ef} - \phi_{es} = q\pi \tag{3.7.33}$$

Solving eq.(3.7.33), which is a function of x, the value of k_X is found. Then all the parameters in eq.(3.7.26) can be calculated using the following relations:

k_X ,p_a, p_d,p_s

$l_a=p_a^{-1}$, $l_d=p_d^{-1}$, $l_s=p_s^{-1}$

$$k_z = \left(nf^2k_0^2 - k_x^2\right)^{\frac{1}{2}} \tag{3.7.34}$$

$$l_{fd} = \frac{\lambda_0}{2\pi\left(n_f^2 - n_d^2\right)^{\frac{1}{2}}} \tag{3.7.35}$$

The procedure to calculate κ is as follows:

1. Calculate k_x using the wave propagation method and parameters of unperturbed waveguide.

2. Use previous value of k_x to calculate p_a, p_d, p_s and k_z, l_{fd} through eqs (3.7.34) and (3.7.35), respectively.

3. Replace previous values of (k_x, p_a, p_d, p_s, k_z, l_{fd}) to compute κ using Eq.(3.7.26).

3.7.6 Numerical Calculations

The following example was studied using the different models discussed above. Fig.3.16 shows the coupling coefficient versus the grating depth. The parameters used in the calculation were as follows:

n_1=3.4, n_2=3.6, n_3=3.5
D=1μm, g=0-0.2μm (Step 50A), w/Λ=0.5 (Λ=380nm, W=190nm), m=3
λ=870nm

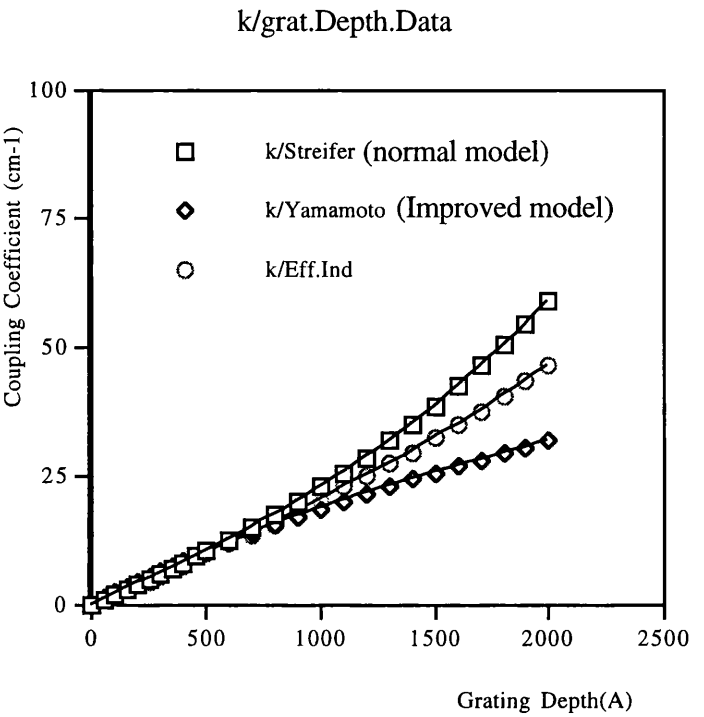

Fig. 3.16: Coupling Coefficient as a function of Grating Depth for the first three models discussed

For small grating depths, <500A, all models are in good agreement concerning the calculated value of the coupling coefficient. However, as the grating depth increases beyond 1000A, a large discrepancy between the coupling coefficients calculated by the three different models is observed. This difference can be mainly explained by the technique used in computing d and g_1.

As discussed in ref.[3.30], depending on the geometry used for calculating the unperturbed guided mode, there are significant differences in the coupling coefficient values obtained. For grating etch depth larger than 1000A, the effective refractive index method presents better results than the normal-coupled method since the geometry effects in the former are 'averaged' by the calculation, whereas using the coupled-mode approach the coupling coefficient is overestimated as shown in [3.30].

The accuracy of the evaluated coupling coefficient depends mainly upon the choice of the unperturbed waveguide structure, parameter D_{eff}, which is related to g_1(normal coupled mode analysis) or d (improved coupled mode analysis). In the normal coupled mode analysis, g_1 is calculated taking into account simply the mark space ratio, i.e., $g_1=(W/\Lambda)g$. In the improved coupled mode analysis, however, d is calculated using a more sophisticated approach, which consists of nullifying the self-coupling coefficient of the guided mode, Eq.(3.7.22).

In Fig.3.17 the coupling coefficient dependence on the toothwidth/pitch ratio is shown. The parameters used in the calculation were as follows:

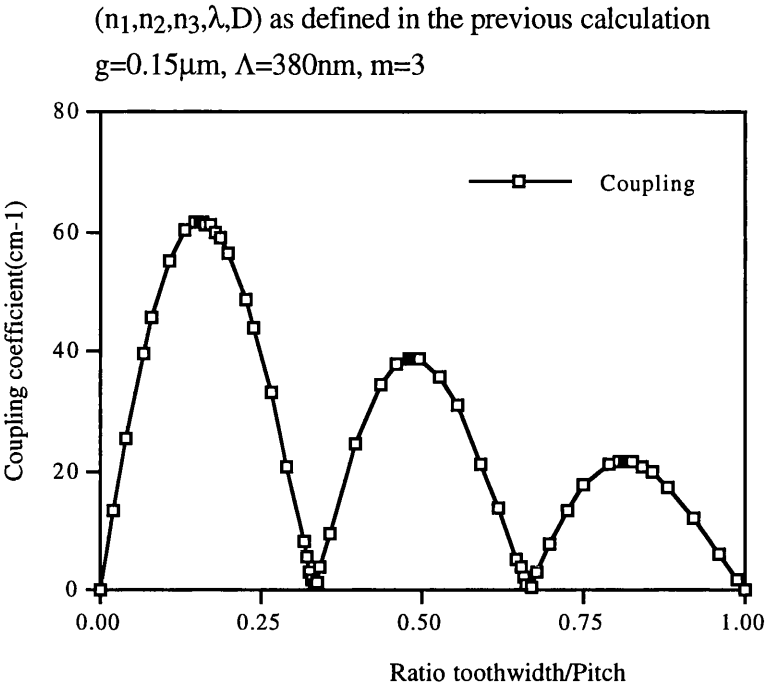

Fig.3.17: Coupling coefficient as a function of the ratio toothwidth/pitch calculated by normal coupled mode analysis

The features presented by this plot depend on several factors. Firstly, as W/Λ increases, the evanescent part of the mode and the teeth interact more strongly in region 1 rather than the more intense oscillatory part of the mode. In other words, as W/Λ increases the effective waveguide thickness D_{eff} decreases, and thus the mode is more confined. This effect is responsible for the general decrease in the coupling coefficient with (W/Λ). Secondly, as W/Λ changes, there exist different degrees of interference from various parts of the tooth along the z direction, this phenomenon accounting for the zeros in κ.

Similar results to Fig.3.17 have been published in the literature, for instance Fig.14 of [3.15].

In Fig.3.18, the calculated coupling coefficient versus thickness (T in Fig.3.15) of the top cladding layer is shown. The coupling coefficient is calculated by Wang's theory for two different material structures. For a symmetric material structure with 40% AlGaAs in both cladding layers, k(40%,40%Al), the parameters are:

n_f=3.49, n_d=n_s=3.36

W=0.23μm, d=0.7μm

λ=860nm

For an asymmetric material structure consisting of 40% AlGaAs in upper cladding layer and 80% AlGaAs in lower cladding layer, k(40%,80%Al), the parameters are:

n_f=3.49, n_d=3.36, n_s=3.12

W=0.23μm, d=0.7μm

λ=860nm

The refractive indices of the different epitaxial layers in the material structures were calculated using Adachi's data [3.19].

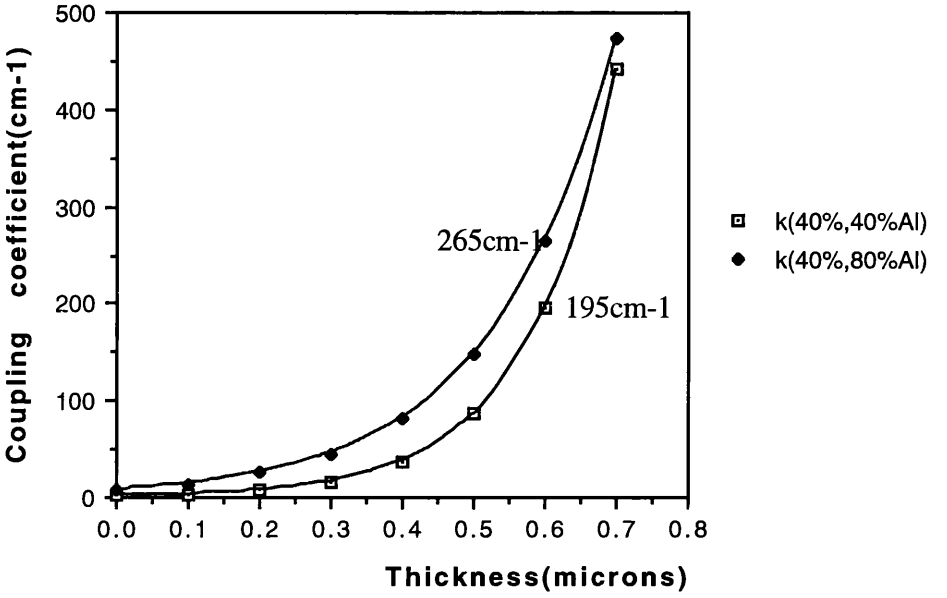

Fig.3.18: Coupling coefficient as a function of thickness for two different material structures

As expected, the coupling coefficient is larger for the material structure 40%,80%Al by as much as 70cm^{-1} (T>0.5μm). For values of T>0.4 μm, the coupling coefficient increases exponentially with T for both material structures, whereas for values of T<0.4μm, the coupling coefficient increases more slowly.

3.8 Calculation of κ in Deep Surface Grating Guide Structures

The laser structure illustrated in Fig.3.19 was chosen for experimental work because of its fabrication simplicity. In addition, DFB lasers fabricated with such structure have presented high performance[3.20],[3.21]. The fabrication requires only a single MOCVD growth step and provides both lateral optical confinement and distributed feedback without additional processing steps beyond the fabrication of the lateral gratings. The design of the device is also suitable for integration in general, and for coupling of individual devices into phase locked laser arrays[3.22].

As already pointed out, the theoretical results for the coupling coefficient discussed in the previous section 3.7 are not directly applied to this surface grating structure. In particular, the gratings are not located in the top of the guiding layer, as assumed in the models by Streifer and Yamamoto. In the present DFB structure, the etched gratings are located along the ridge in the top confining layer of the laser, on either side of the contact stripe. A different approach has been, therefore, used to estimate the coupling coefficient in these structures.

In order to theoretically estimate the coupling coefficient in surface grating waveguides, a simple model, based on the effective refractive index method, has been used. The model allows one to study the dependence of the coupling coefficient on the grating parameters, such as grating etch depth, stripe width and grating period, as well as on the material structure, namely refractive indices and thicknesses of the different layers. In this model, the grating period is decomposed into two waveguide sections: a slab waveguide corresponding to the region where the material is not removed, and a ridge waveguide, corresponding to the other section where the material is removed (see Fig.3.19). The effective refractive index variation between these two waveguide sections is then calculated using the effective refractive index method described in detail elsewhere [3.23]. In the results presented here, a four layer model was used to calculate the effective refractive index of each section. The material structure is symmetric, with $n_1=n_3=3.36$ ($Al_{0.4}Ga_{0.6}As$) and $n_2=3.49$, corresponding to the refractive index average in the active region and $n_4=1$(air) .

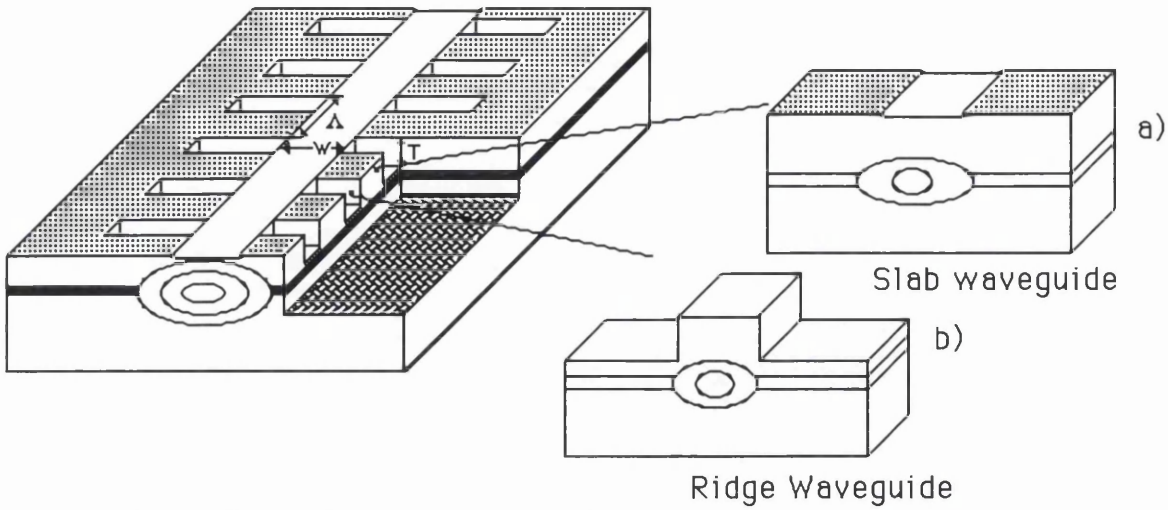

Fig. 3.19: Schematic diagram of a DFB waveguide with deep surface gratings: Λ-grating period, W- stripe width and T-grating etch depth

As mentioned a simple model which relates the periodic variations of the effective refractive index to the coupling coefficient has been used. The coupling of the forward-propagating wave into the counter-propagating wave is usually described by the coupling coefficient, κ. The coupling coefficient of the grating with a spatial period Λ can be obtained from the multiple dielectric layers problem analized by Haus[3.7] and is given by:

$$\kappa = \frac{\Delta n_{eff}}{n_{eff}\Lambda} \qquad (3.8.1)$$

The periodic length of the grating Λ, which has to obey the Bragg condition so that reflections from individual layers interfere constructively, is given by $\Lambda = m\frac{\lambda_0}{2n_{eff}}$ (Λ is a multiple m of one-half of the emission wavelength in the material). The quantity Δn_{eff} is the longitudinal effective refractive index step between the two waveguide sections of the grating period. Using the Bragg condition in equation (8), the coupling coefficient is given by:

$$\kappa = \frac{2}{m}\frac{\Delta n_{eff}}{\lambda_0} \qquad (3.8.2)$$

Procedure to calculate κ:

1. The Fwave program is used to calculate directly n_z(slab) and n_z(ridge).

2. Use n_z(slab)-n_z(ridge) to calculate Δn_{eff}.

3. Eq.(8) can then be used to compute κ, for a given grating order m.

The thickness of the active region used in the calculation was 0.23μm.

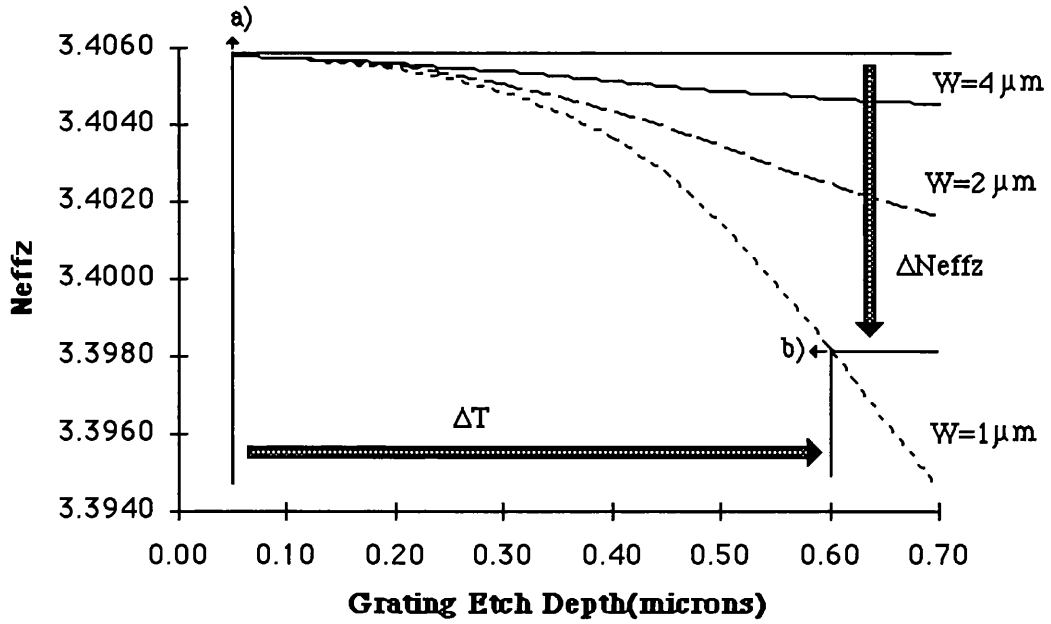

Fig. 3.20: Dependence of the effective refractive index n_{effz} of the fundamental TE_0 mode with the grating etch depth. The stripe width is the parameter

Fig.3.20 shows the calculated effective refractive index of the fundamental TE_0 mode n_{effz} as a function of the grating etch depth. The upper limit of n_{effz} corresponds to the effective refractive index of a slab waveguide [a) in Figs.3.19 and 3.20], whereas n_{effz} at point b) in Fig.3.20 corresponds to the effective index of a ridge waveguide characterised by 0.6 μm ridge depth and 1 μm stripe width. From Fig.3.20, it is apparent that any periodic variation of the etch depth ΔT along the propagation direction can be related to a periodic change of the effective refractive index Δn_{effz} and this variation increases for small stripe widths.

In our calculation, third-order gratings are considered, since these structures are significantly easier to fabricate than first-order gratings. Fig.3.21 shows the coupling coefficient for a third-order grating as a function of the grating etch depth, m=3 and λ_B=870nm. For small grating etch depths, the coupling coefficient increases very slowly with the grating depth, which is explained by the fact that the light is well confined near the active region. However, as the grating etch depth approaches the active region, the coupling coefficient increases significantly, especially for devices with small waveguide stripe widths.

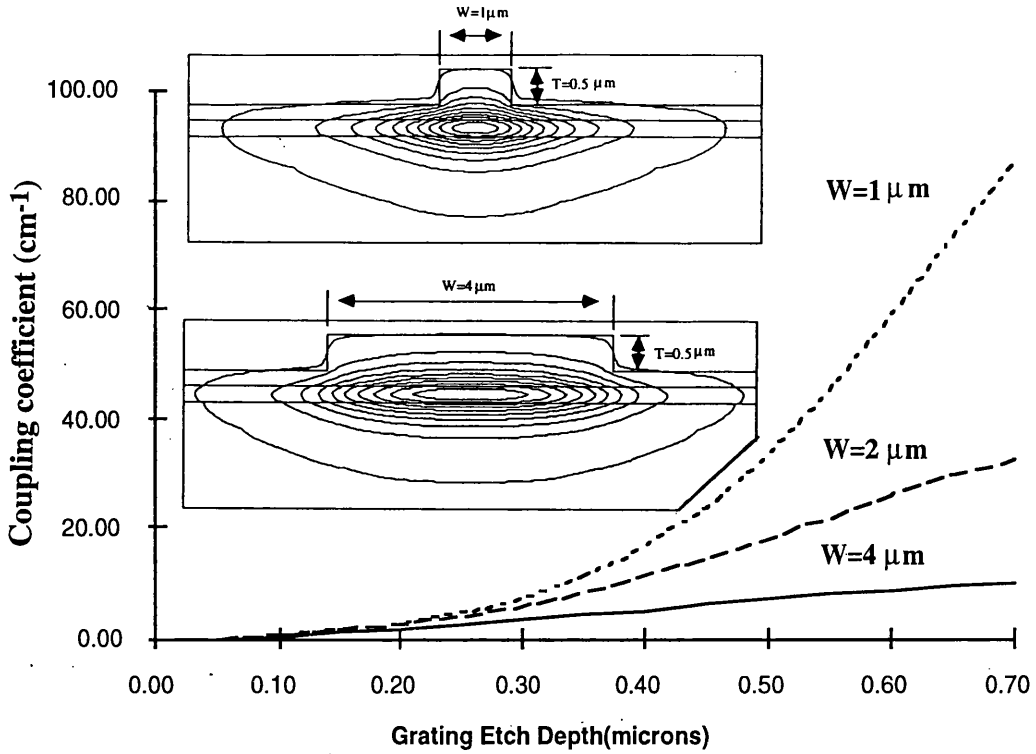

Fig.3.21: Coupling coefficient of 3rd-order grating in a GaAs/AlGaAs symmetric structure as a function of the grating etch depth. Insets show field distributions of TE_0 mode for waveguides with W=1μm and W=4μm stripe widths and constant etch depth of 0.5μm.

3.9 Radiation Losses in DFB laser structures

3.9.1 Reflection from higher-order gratings

The reflections from higher-order gratings, as shown in fig.3.22, have been analysed by Scifres et al.[3.15], [3.24]. Consider a wave travelling to the right in the corrugated waveguide. In order for the rays scattered from successive teeth to all be in phase, the path lengths must all be integral multiples of the wavelength. Hence a condition is imposed which requires that

$$b + \Lambda = \frac{m\lambda_0}{n_g}, \qquad \text{m=0,1,2...} \tag{3.9.1}$$

where b is the distance shown in fig. 3.22.

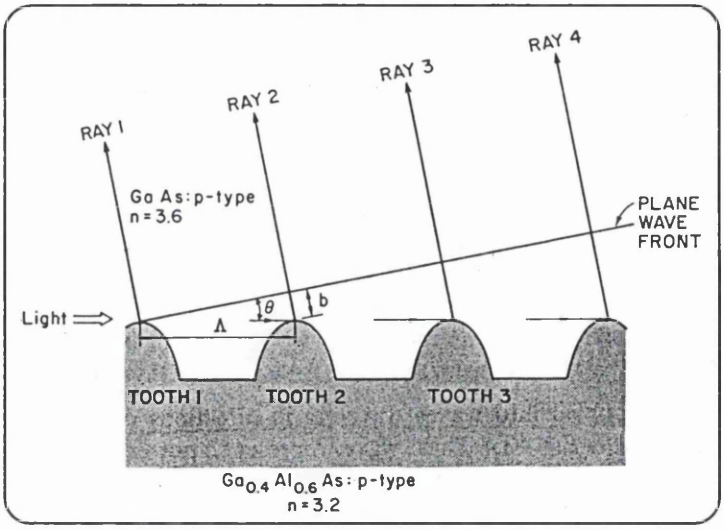

Fig.3.22: Rays scattered from a waveguide with a higher-order Bragg grating[3.20]

From geometrical considerations, it can be seen that

$$b=\Lambda\sin\theta, \tag{3.9.2}$$

where θ is the angle that the scattered wavefront makes with the plane of the waveguide. Thus, from (3.9.1) and (3.9.2), θ is given by

$$\sin\theta = \frac{m\lambda_0}{n_g\Lambda} - 1, \qquad m=0,1,2.. \tag{3.9.3}$$

For θ to be real, the magnitude of the right-hand side cannot exceed unity. For example, if $\lambda_0/n_g=\Lambda$, which is the condition for second-order Bragg scattering, then

$$\sin\theta=m-1 \tag{3.9.4}$$

and solutions exist for m=0,1,2. The m=0 solution describes light scattered in the forward direction. DFB is produced by the m=2 solution and corresponds to light scattered backwards. For m=1, θ=0, and the wave front is parallel to the junction, and the rays are orthogonal to the junction. Similar solutions can be obtained for higher-order Bragg reflection gratings as shown in Fig.3.23.

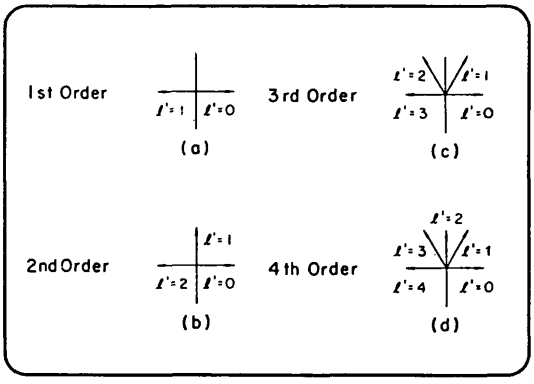

Fig.3.23: Reflected wave directions for higher-order Bragg diffraction gratings [3.25]

3.9.2 Calculation of radiation losses from higher-order gratings

Periodic structures in waveguides are utilized in couplers and lasers. When used in couplers, the structure contains a wave propagating in one direction. Through its interaction with a periodic grating the propagating wave excites one or more radiating waves which provide the output coupling. When used in lasers, the grating period is approximatly an integral multiple of half the propagating wavelength in the guide (the Bragg condition), and then a strong coupling also exists between the propagating wave and an identical contradirectional wave. This is the situation which exists in a distributed feedback (DFB) and Bragg reflection (DBR) laser. In other words, when the grating provides the feedback, two contradirectional propagating waves always exist and both simultaneously contribute to the radiation field. It is therefore essential to distinguish these two situations, designated respectively for the first case by nonresonant and resonant for the second.

Radiation from corrugated waveguides in the nonresonant case is well understood[3.27],[3.28], but the resonant situation introduces complications. For the nonresonant case, which is discussed in detail in this section, gratings in AlGaAs/GaAs structures which are used either as waveguides or as lasers are analysed. For the latter case, the oscillation wavelength is not in the vicinity of the Bragg wavelength. In the resonant case, the two contradirectional wave are coherent and therefore their relative phases along the length of the laser must be taken into account in computing radiated power. In addition, the radiation reacts on the resonant waves to change the thresholds and resonant wavelengths, and the overall process is dependent on the longitudinal mode structure.

The analysis of radiation losses from DFB waveguides has been carried out by several authors. The theoretical approach developed by Tamir et al. [3.26] is based on the Floquet-Bloch expansion method and offers the most accurate value of the radiation loss coefficient for a nonresonant situation. A perturbation solution of the coupled mode equations for

guided modes and the radiation continuum of an unperturbed waveguide has also been proposed by Yamamoto et al [3.17].

The theoretical analysis presented here is based on the perturbation solution of the Floquet-Bloch expansion theory by Streifer et al [3.23]-[3.26]. This theoretical model is used to study analytically the radiation properties of gratings in AlGaAs/GaAs structures which are used either as waveguides or as lasers, where in the latter case the oscillation wavelength is not in the immediate vicinity of that determined by the Bragg condition. This section comprises three sub sections: **A**, **B**, and **C**. In subsection **A**, the theoretical model is illustrated and the parameters used in the model are defined; the general analysis of rectangular gratings is presented in **B.1**. Then, the specific case of first-order perturbation solution for $\varepsilon_m(x)$ is described in **B.2**. The procedure for calculating radiation losses in a DFB waveguide is given in **B.3**. Finally, in subsection **C**, the analytic results of radiation losses in grating waveguides are plotted and commented.

A. The theoretical model

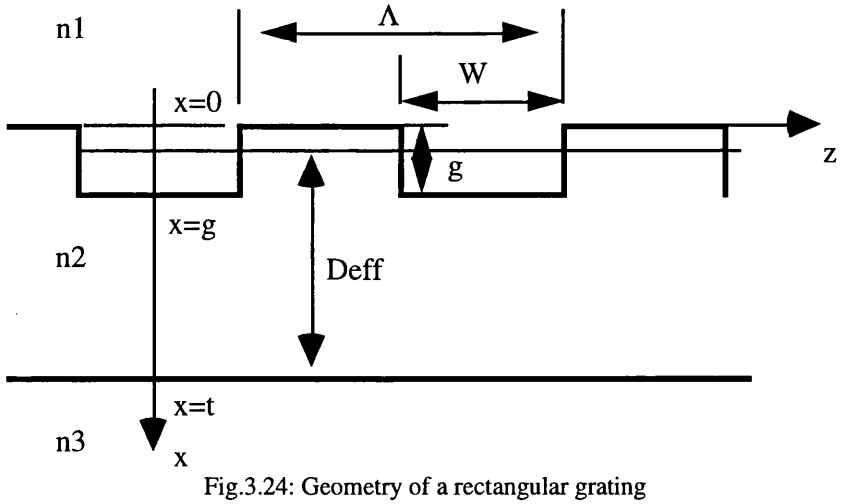

Fig.3.24: Geometry of a rectangular grating

Where:

Waveguide parameters:

n_1- Refractive Index of the upper cladding layer

n_2-Refractive Index of the waveguide

n_3- Refractive Index of the lower cladding layer

t - Waveguide thickness

Grating parameters:

Λ- Grating period

g- Grating depth

W- Tooth width

$D_{eff}=t-(w/\Lambda)g$

B. Summary of the Theory

B.1 General analysis for rectangular gratings

Consider TE modes of the structure shown in Fig.3.24. The E-field is in the y direction and can be expressed as an infinite summation of partial waves in a form dictated by Floquet`s theorem,

$$E_y(x,z) = \sum_{m=-\infty}^{+\infty} \varepsilon_m(x)\, Exp(i\beta_m z) \tag{3.9.5}$$

with

$$\beta_m = \beta_0 + \frac{2\pi m}{\Lambda} \tag{3.9.6}$$

where Λ is the grating period as defined above. If no grating were present, then all $\varepsilon_m(x)$ with $m\neq 0$ would be zero, whereas $\varepsilon_0(x)$ and β_0 would be the mode pattern and the propagation constant of that unperturbed waveguide structure.

For a rectangular grating, the partial waves $\varepsilon_m(x)$ satisfy the wave equation,

$$\frac{d\varepsilon_m(x)}{dx^2} + k_m^2 \varepsilon_m(x) = \zeta_m(x) \qquad \forall_m \tag{3.9.7}$$

The system of (3.9.7), satisfied by all $\varepsilon_m(x)$, determines a single mode of the corrugated waveguide when summed according to (3.9.5), where:

$$\zeta_m(x) = \begin{cases} -k_0^2 \sum_{q=-\infty}^{\infty} A_{m-q}(x)\varepsilon_q(x) & q \neq m \quad 0 < x < g \\ 0 & x < 0, \quad x > g \end{cases} \tag{3.9.8}$$

The term $A_q(x)$ is the Fourier coefficient of the refractive index perturbation along z, which, for rectangular gratings, is given by

$$A_q(x) = \begin{cases} -\dfrac{(n_2^2 - n_1^2)}{\pi q} Sin\left(\dfrac{\pi q w}{\Lambda}\right) & 0 < x < g \\ 0 & x < 0, \quad x > g \end{cases} \tag{3.9.9}$$

$$k_m^2 = k_0^2 n_0^2(x) - \beta_m^2 = k_{mj}^2 \qquad j = 1,2,3, and\ 4 \tag{3.9.10}$$

where j=1,2,3 refers to regions 1,2,3, whereas j=4 refers to the grating region.

$$n_0^2(x) \begin{cases} n_1^2 & x < 0 \\ n_4^2 = [w n_1^2 + (\Lambda - w) n_2^2]/\Lambda & 0 < x < g \\ n_2^2 & g < x < t \\ n_3^2 & x > t \end{cases} \tag{3.9.11}$$

Clearly, $n_0^2(x)$ describes a four-layer waveguide structure; outside the grating region, for $x<0$ and $x>g$, this waveguide is identical to the original, for $0<x<g$, $n_0^2(x)$ is a constant equal to the average of n^2 in the grating.

Each equation in (3.8.7) is formally solved using variation of parameters. Then, imposing continuity conditions on ε_m and $d\varepsilon_m/dx$ at x=0 and t, one obtains

$$\varepsilon_m(x)=\begin{cases} c_{m1}Exp(-ik_{m1}x) & x<0 \\ c_{m1}\left\{Cos(k_{m4}x)-(\frac{ik_{m1}}{k_{m4}})Sin(k_{m4}x)\right\}+T_m(x) & 0<x<g \\ c_{m3}\left\{Cos(k_{m2}(t-x)-\left(\frac{ik_{m3}}{k_{m2}}\right)Sin[k_{m2}(t-x)]\right\} & g<x<t \\ c_{m3}Exp[ik_{m3}(x-t)] & x>t \end{cases} \tag{3.9.12}$$

where:

$$T_m(x)=\frac{1}{k_{m4}}\int_0^x \zeta(e)\,Sin[k_{m4}(x-e)]de \tag{3.9.13}$$

B.2 First-order perturbation solution for ε_m

Consider only the left side of (3.9.7) for m=0,

$$\frac{d^2\varepsilon_0(x)}{dx^2}+k_0^2\varepsilon_0(x)=\frac{d^2\varepsilon_0(x)}{dx^2}+(k_0^2n_0^2-\beta_0^2)\varepsilon_0(x)=0 \tag{3.9.14}$$

If (3.9.14) is solved for $\underline{\varepsilon_0}$ and $\underline{\beta_0}$, and then only ε_0 is used to drive other $\varepsilon_m(m\neq 0)$ in the right side of (3.9.7), i.e.

$$\frac{d^2\varepsilon_m(x)}{dx^2}+k_m^2\varepsilon_m(x)=-k_0A_m(x)\varepsilon_0(x) \tag{3.9.15}$$

a first-order perturbation solution for $\varepsilon_m(x)$ is obtained.

The value of β_0 calculated by (3.8.14) alone is real and therefore does not reflect power lost through radiation. Instead, the time-averaged power lost by the partial wave ε_m, per unit length, is found using the Poynting vector, to be

$$P_m=\frac{1}{2\omega\mu_0}\left\{Re\left[\sqrt{k_0^2n_1^2-\beta_m^2}\right]|\varepsilon_m(0)|^2+Re\left[\sqrt{k_0^2n_3^2-\beta_m^2}\right]|\varepsilon_m(t)|^2\right\} \tag{3.9.16}$$

The first and second bracketed terms are the parts radiated into regions 1 and 3, respectively. If β_m^2 exceeds $k_0^2 n_1^2$ and/or $k_0^2 n_3^2$, imaginary terms occur in (3.9.16) which do not contribute to P_m. Thus $P_m=0$ for all terms with $m \geq 0$ and with sufficiently large negative m, which could be m=-1 for a small grating period Λ.

It is convenient to use the normalized measure of radiated power, defined as α, which is the exponential rate at which power is lost by the ε_0 wave, given by

$$\alpha = \frac{\sum P_m}{\left(\frac{\beta_0}{2\omega\mu_0}\right)\int_{-\infty}^{+\infty}|\varepsilon_0(x)|dx} = \frac{Re\left\{\sqrt{k_0^2 n_1^2 - \beta_m^2}\right\}|\varepsilon_m(0)|^2 + Re\left\{\sqrt{k_0^2 n_3^2 - \beta_m^2}\right\}|\varepsilon_m(t)|^2}{\beta_0 \int_{-\infty}^{+\infty}|\varepsilon_0(x)|dx} \qquad (3.9.17)$$

B.3 Procedure to calculate losses in DFB waveguide

1st step: Calculation of β_0 and $\varepsilon_0(x)$

β_0 is calculated using Streifer's theory described previously in this chapter (section 3.7.1). When β_0 is known, the propagation constants k_{01}, k_{04}, k_{02}, k_{03}, can be calculated through following equations:

$$\begin{cases} k_{01} = \sqrt{k_0^2 n_1^2 - \beta_0^2} \\ k_{04} = \sqrt{k_0^2 n_4^2 - \beta_0^2} \\ k_{02} = \sqrt{k_0^2 n_2^2 - \beta_0^2} \\ k_{03} = \sqrt{k_0^2 n_3^2 - \beta_0^2} \end{cases}$$

$\varepsilon_0(x)$ can now be calculated by replacing m=0 in eq. (3.8.12),

$$\varepsilon_0(x) = \begin{cases} c_{01} Exp(-ik_{01}x) & x < 0 \\ c_{01}\left\{Cos(k_{04}x) - \left(\frac{ik_{01}}{k_{04}}\right)Sin(k_{04}x)\right\} & 0 < x < g \\ c_{03}\left\{Cos[k_{02}(t-x)] - \left(\frac{ik_{03}}{k_{02}}\right)Sin[k_{02}(t-x)]\right\} & g < x < t \\ c_{03} Exp[ik_{03}(x-t)] & x > t \end{cases}$$

The coefficients c_{01}, c_{03} are evaluated by setting $c_{01}=1$, solving for c_{03} by requiring continuity of $\varepsilon_0(x)$ at x=g, i.e.,

$$c_{01}=1 \text{ and } c_{03}=\frac{Cos(k_{04}g)-\left(\frac{ik_{01}}{k_{04}}\right)Sin(k_{04}g)}{Cos[k_{02}(t-g)]-\left(\frac{ik_{03}}{k_{02}}\right)Sin[k_{02}(t-g)]}$$

2nd step: Calculation of $\varepsilon_m(x)$ and k_{mj}

Let us now calculate $\varepsilon_m(x)$ and k_{mj} for m=-1. In most practical situations only terms m=-1 and m=-2 are of interest, since β_{-1} and β_{-2} are lower than terms $k_0^2n_1^2$ and/or $k_0^2n_3^2$ and thus partial waves with β_{-1} and β_{-2} radiate according to eq. (3.9.16).

<u>m=-1</u>

$$\beta_{-1}=\beta_0-\frac{2\pi}{\Lambda}$$

$$\begin{cases} k_{-11}=\sqrt{k_0^2n_1^2-\beta_{-1}^2} \\ k_{-14}=\sqrt{k_0^2n_4^2-\beta_{-1}^2} \\ k_{-12}=\sqrt{k_0^2n_2^2-\beta_{-1}^2} \\ k_{-13}=\sqrt{k_0^2n_3^2-\beta_{-1}^2} \end{cases}$$

Partial wave $\varepsilon_{-1}(x)$ is given by,

$$\varepsilon_{-1}(x)=\begin{cases} c_{-11}Exp(-ik_{-11}x) & x<0 \\ c_{-11}\left\{Cos(k_{-14}x)-\left(\frac{ik_{-11}}{k_{-14}}\right)Sin(k_{-14}x)\right\}+T_{-1}(x) & 0<x<g \\ c_{-13}\left\{Cos[k_{-12}(t-x)]-\left(\frac{ik_{-13}}{k_{-12}}\right)Sin[k_{-12}(t-x)]\right\} & g<x<t \\ c_{-13}Exp[ik_{-13}(x-t)] & x>t \end{cases}$$

$$T_{-1}(x)=\frac{(n_2^2-n_1^2)k_0^2}{\pi k_{-14}}Sin\left(\frac{\pi w}{\Lambda}\right)\int_0^x \varepsilon_0(x)Sin[k_{-14}(x-e)]de \qquad 0<x<g$$

Now, the coefficients c_{-11}, c_{-13} can be determined by requiring the continuity of $\varepsilon_{-1}(x)$ and $d\varepsilon_{-1}/dx$ at x=g, i.e.

$$\begin{cases} \varepsilon_{-1}(g^-)=\varepsilon_{-1}(g^+) \\ \left.\frac{d\varepsilon_{-1}(x)}{dx}\right|_{g^-}=\left.\frac{d\varepsilon_{-1}(x)}{dx}\right|_{g^+} \end{cases}$$

Solving this system, the coefficients c_{-11} and c_{-13} are evaluated.

3rd step: calculation of α

Finally, the coefficient α, which expresses the total radiated power per unit length, is calculated to be

$$\alpha = \frac{Re\left\{\sqrt{k_0^2 n_1^2 - \beta_{-1}^2}\right\}|c_{-11}|^2 + Re\left\{\sqrt{k_0^2 n_3^2 - \beta_{-1}^2}\right\}|c_{-13}|^2}{\beta_0 \int_{-\infty}^{+\infty} |\varepsilon_0(x)| dx}$$

C. Numerical Results

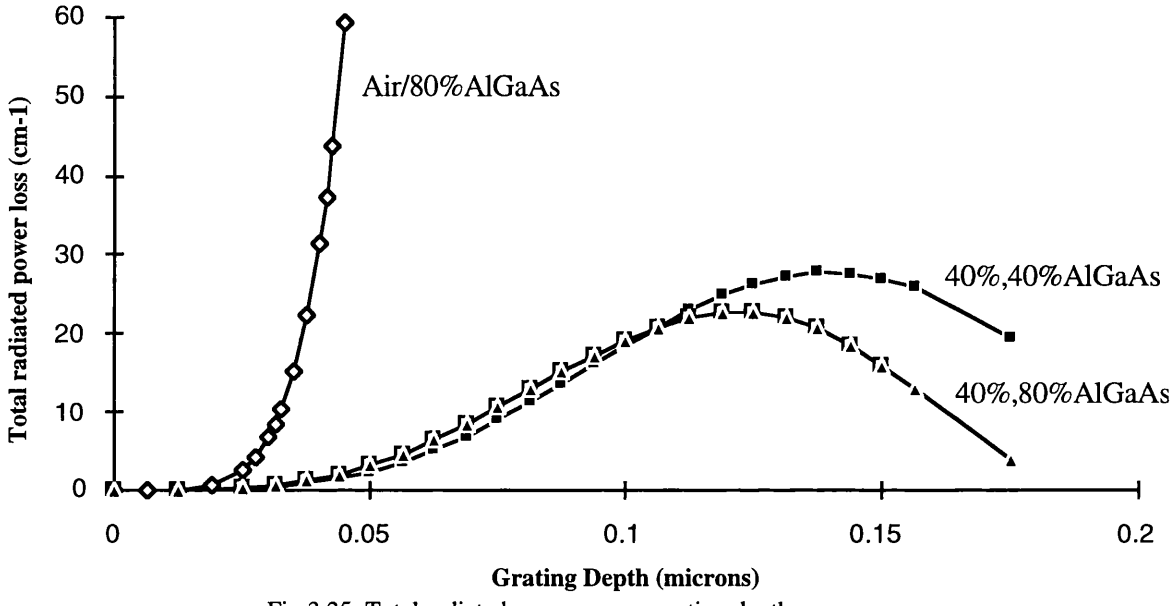

Fig.3.25: Total radiated power versus grating depth

Fig.3.25 shows total radiated power loss versus grating etch depth, the material structures were used as a parameter. The parameters used in the theoretical model were:

Symmetric structure 40%,40% AlGaAs:	n_1=3.36	t=0.23μm	λ=870nm
	n_2=3.49	Λ=380nm	
	n_3=3.36	W=190nm	
Asymmetric structure 40%,80%AlGaAs:	n_1=3.36	t=0.23μm	λ=870nm
	n_2=3.49	Λ=380nm	
	n_3=3.12	W=190nm	
Asymmetric structure Air,80%AlGaAs:	n_1=1	t=0.23μm	λ=870nm
	n_2=3.49	Λ=380nm	

n_3=3.12 W=190nm

For this specific case, only partial wave m=-1 is radiating. Partial wave m=-2 is equal to zero because the grating mark-space ratio is 1:1. From the Fig.3.25, the asymmetric structure Air/80%AlGaAs, which describes the case of air gratings, presents a very large radiation loss. For grating etch depth of just 0.045μm the radiation loss is about 60cm^{-1}. Material structures 40%,40%AlGaAs and 40%,80%AlGaAs present a maximum radiated losses of 28cm-^{1} and 23cm^{-1}, respectively for grating etch depth of 0.1375μm and 0.125μm.

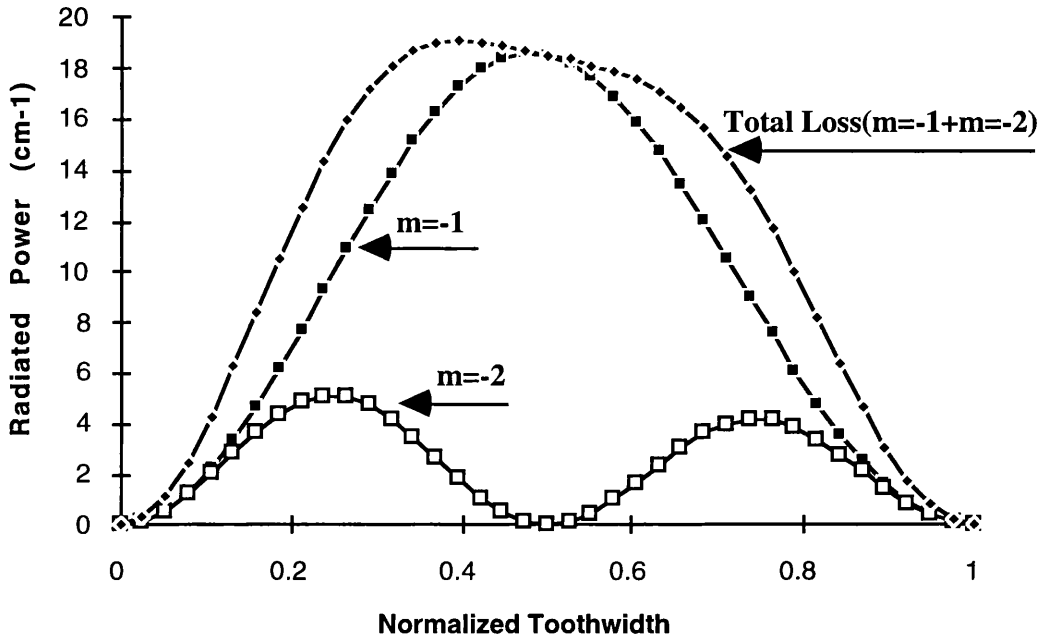

Fig.3.26: Radiated power as a funtion of the normalized toothwidth

Fig.3.26 shows partial (m=-1 and m=-2) and total (m=-1+m=-2) radiated power loss versus normalized toothwidth, for a symmetric material structure 40%,40%AlGaAs (parameters as defined before) and constant grating etch depth of 0.1μm. The maximum total radiated power loss of 19cm^{-1} is calculated for a normalized toothwidth of 0.4. For the case of 3rd-order grating with 380nm spatial period, the corresponding toothwidth would be 150nm.

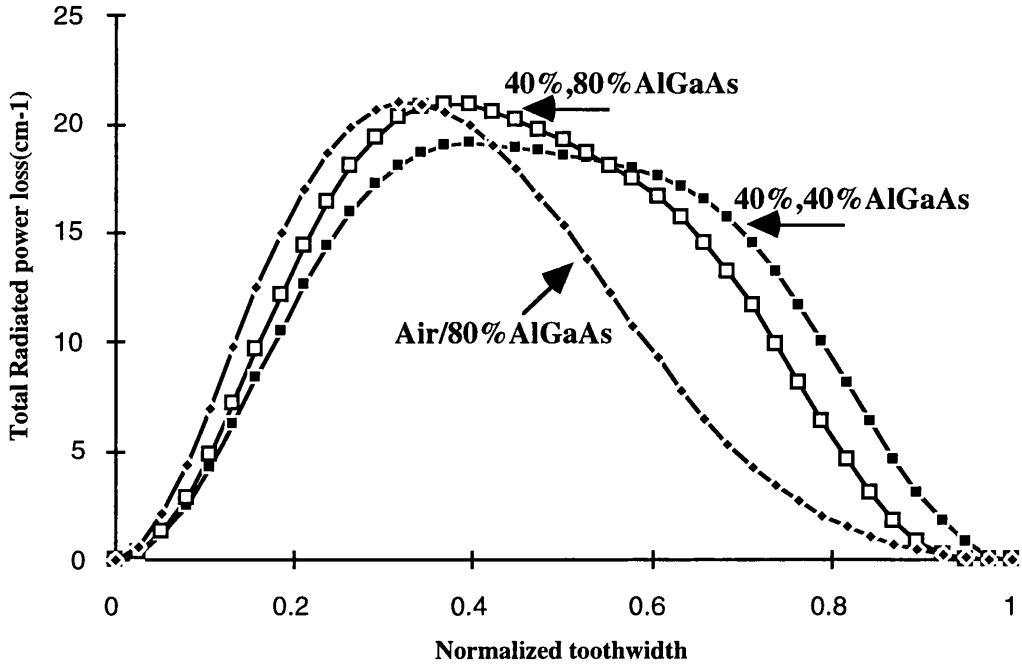

Fig.3.27: Total Radiated power loss versus normalized toothwidth for different material structures

Fig.3.27 shows total radiated power loss versus normalized toothwidth, for three different material structures: 40%,40%AlGaAs, 40%,80%AlGaAs, and Air,80%AlGaAs. The grating etch depth was 0.1μm for material structure 40%,40%AlGaAs, 40%,80%AlGaAs, whereas the grating etch depth in material structure Air,80%AlGaAs was just 0.035μm. Maximum total radiated power loss of $19cm^{-1}$, $21cm^{-1}$, and $21cm^{-1}$ were calculated in 40%,40%AlGaAs, 40%,80%AlGaAs, and Air,80%AlGaAs, for toothwidth of 150nm, 140nm, and 120nm, respectively.

References

[3.1] B. G. Kim, and E. Garmire, "Comparison Between the Matrix method and the Coupled-Wave method in the analysis of Bragg Reflector Structures", J. Opt. Soc. America, Vol.9,pp.132-136,(1992)

[3.2] M. Yamada, and K. Sakuda, "Analysis of almost-period distributed feedback slab waveguides via a fundamental matrix approach", Applied Optics, Vol.26, pp. 3474-3478, (1987)

[3.3] J.P. Weber, and S. Wang, "A new method for the calculation of the emission spectrum of DFB and DBR lasers", IEEE Journal of Quantum Electronics, Vol. 27,pp. 2256-2266, (1991)

[3.4] H. Kolgenik, and C.V.Shank, "Coupled-wave theory of distributed feedback lasers", J. Appl. Physics, Vol.43, pp.2327-2335, (1972)

[3.5] W. Streifer, D. R. Scifres, and R.D. Burnham, "Coupled wave analysis of DFB and DBR lasers", IEEE Journal of Quantum Electronics, Vol. 13, pp. 134-141, (1977)

[3.6] A. Yariv, and M. Nakamura, "Periodic structures for integrated optics", IEEE Journal of Quantum Electronics, Vol. 13, pp. 233-253, (1977)

[3.7] Hermann A. Haus, *Waves and fields in optoelectronics*, in Solid State Physical Electronics, Prentice-Hall, New Jersey, 1984.

[3.8] A. Yariv, *Quantum Electronics*, 3rd Edition, John Wiley & Sons, 1989.

[3.9] G.Motosugi, Y. Yoshikuni, T. Ikegami, "Single-longitudinal-mode condition for DFB Lasers", Electronics Letters, Vol.21, pp. 352-353, (1985)

[3.10] W. Streifer, D. R. Scifres, and R.D. Burnham, "Longitudinal modes in distributed feedback lasers with external reflectors", J. Appl. Phys., Vol. 46, pp. 247-249, (1975)

[3.11] W. Streifer, R.D. Burnham, and D. R. Scifres, "Effect of external reflectors on longitudinal modes of distributed feedback lasers", IEEE Journal of Quantum Electronics, Vol. 11, pp. 154-161, (1975)

[3.12] T. Matsuoka, H. Nagai, Y. Noguchi, Y. Suzuki, and Y. Kawaguchi, " ", Japan J. Appl. Phys., 23, L138-L140, (1984)

[3.13] S. Wang, "Proposal of periodic layered waveguide structures for distributed lasers", J. Appl. Physics, Vol.44, pp.767-780, (1973)

[3.14] A. Yariv, "Coupled-mode Theory for guided-wave Optics", IEEE Journal of Quantum Electronics, Vol. 9,pp. 919, (1973)

[3.15] R. D. Burnham, D.R.Scifres and W. Streifer, "Single-heterostructure distributed-feedback GaAs-diode lasers", IEEE Journal of Quantum Electronics, Vol. 11, pp. 439-449, (1975)

[3.16] W. Streifer, D. R. Scifres, and R.D. Burnham, "Coupling Coefficient for Distributed Feedback Single- and Double-Heterostructure Diode Lasers", IEEE Journal of Quantum Electronics, Vol. 11, pp. 867-873, (1975)

[3.17] Y. Yamamoto, T. Kamiya, and H. Yanai, "Improved Coupled Mode Analysis of Corrugated Waveguides and Lasers", IEEE Journal of Quantum Electronics, Vol. 14,pp. 245-257, (1978)

[3.18] H. Abe, S.G. Ayling, J.H. Marsh, R.M. De La Rue, and J.S. Roberts, "Single-mode operation of a surface grating distributed feedback GaAs-AlGaAs laser with variable-width waveguide" IEEE Photonics Tech. Lett. ,Vol.7, pp452-454, (1995)

[3.19] S. Adachi, "GaAs, AlAs and $Al_xGa_{1-x}As$: Material parameters for use in research and devices applications" J. Appl. Phys. , Vol.58, pp. R1-R29, (1985)

[3.20] L.M.Miller, J.T. Verdeyen, J.J. Coleman, R.P. Bryan, J.J. Alwan, K.J. Beernink, J.S.Hughes, and T.M. Cockerill, "A distributed feedback ridge waveguide quantum well heterostructure laser" IEEE Photonics Tech. Lett. ,Vol.3, pp. 6-8, (1991)

[3.21] L.M.Miller, K.J. Beernink, J.T. Verdeyen, J.J. Coleman, J.S.Hughes, G.M. Smith, J.Honig, and T.M. Cockerill, "Characterization of an InGaAs-GaAs-AlGaAs strained-layer distributed-feedback ridge-waveguide quantum well heterostructure laser" IEEE Photonics Tech. Lett. ,Vol.4, pp. 296-299, (1992)

[3.22] L.M.Miller, K.J. Beernink, J.T. Verdeyen, J.J. Coleman, J.S.Hughes, G.M. Smith, J.Honig, and T.M. Cockerill, "InGaAs-GaAs-AlGaAs strained-layer distributed feedback ridge waveguide quantum well heterostructure laser array" Electron. Lett. ,Vol.27, pp. 1943-1945, (1991)

[3.23] R. Schimpe, "Design considerations of the metal-clad ridge-waveguide laser with distributed feedback", IEE Proceedings,Vol.132,pp.133-135, (1985)

[3.24] D.R. Scifres, R.D.Burnham, and W.Streifer, " Highly Collimated laser beams from electrically pumped SH GaAs/GaAlAs distributed-feedback lasers" Appl. Physics Lett.,Vol.26, pp48-50, (1975)

[3.25] R.G. Hunsperger, *Integrated Optics: Theory and Technology*, 3rd edition, Spring-Verlag, (1991)

[3.26] a) S.T.Peng, H.L. Bertoni, and T. Tamir, "Analysis of periodic thin film structures with rectangular profile", Opt. Commun., Vol.10, pp.91, (1974)

b) S.T.Peng, T.Tamir, and H.L. Bertoni, "Theory of periodic dielectric waveguides", IEEE Trans. Microwave Theory Tech., , Vol.MTT-23, pp.123-133, (1975)

[3.27] W. Streifer, D. R. Scifres, and R.D. Burnham, "Analysis of grating-coupled radiation in GaAs:AlGaAs lasers and waveguides", IEEE Journal of Quantum Electronics, Vol. 12, pp. 422-428, (1976)

[3.28] W. Streifer, R.D. Burnham, and D. R. Scifres, "Analysis of grating-coupled radiation in GaAs:AlGaAs lasers and waveguides-II: Blazing effects", IEEE Journal of Quantum Electronics, Vol. 12, pp. 494-499, (1976)

[3.29] W. Streifer, R.D. Burnham, and D. R. Scifres, "Radiation losses in distributed feedback lasers and longitudinal mode selection", IEEE Journal of Quantum Electronics, Vol. 12, pp. 737-739, (1976)

[3.30] W. Streifer, D. R. Scifres, R.D. Burnham, and R.I. MacDonald, "On grating-coupled radiation from waveguides", IEEE Journal of Quantum Electronics, Vol. 13, pp. 67-68, (1977)

[3.31] H.Stoll, and A.Yariv, "Coupled-mode analysis of periodic dielectric waveguides", Opt.Commun., Vol. 8, pp. 5-8, (1973)

Chapter 4: Analysis and Improvement of Epitaxial Wafer Structure

4.1 Introduction

In this chapter, the analysis of the epitaxial wafer structure will be discussed as well as its improvement using broad area oxide stripe lasers. To improve the epitaxial wafer structures in terms of internal quantum efficiency, optical losses, QW gain parameter, g_0, and transparency current, J_t, several parameters of the wafer structure were optimized. The parameters were changed, also, in order to increase the interaction between the guided mode and the gratings, which are fabricated in the upper cladding layer. The parameters changed were, namely, the Al concentration in the cladding layers, the position of the quantum wells and the number of quantum wells.

4.2 Epitaxial Wafer Structure

Several epitaxial wafer structures were used in the process of optimization. The epitaxial wafer structures #QT270 and #A606 consisted of two 100A quantum wells and 100A $Al_{0.2}Ga_{0.8}As$ barriers within a standard symmetric structure, as shown in Fig.4.1. The wafer #QT270 was grown by MOCVD (Metal Organic Chemical Vapour Deposition) in the University of Sheffield, whereas the wafer #A606 was grown by MBE (Molecular Beam Epitaxy) at Glasgow University.

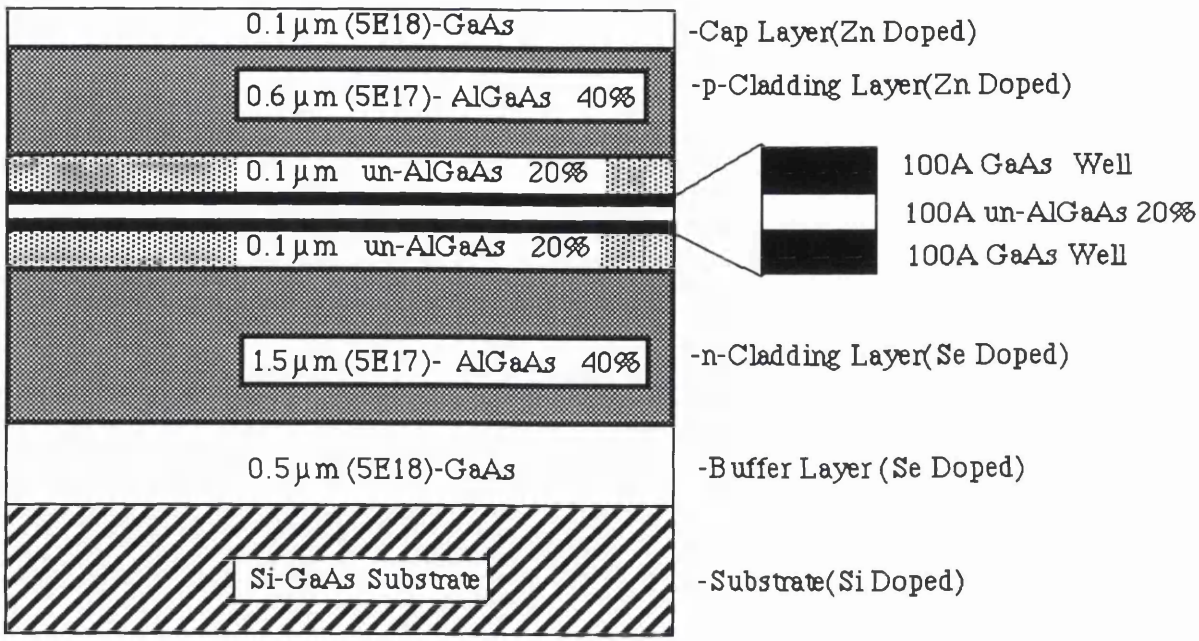

Fig.4.1: Schematic diagram of the epitaxial wafer structures: #QT270 and #A606

The epitaxial wafer structures #QT433, #QT433R and #A742 were asymmetric structures with four 100A quantum wells. The dimensions of the different layers were the same as for structures #QT270 and #A606, but different compositions were used for the upper and lower cladding regions. Further details of these structures are given immediately below:

#QT433

-Grown by MOCVD

- Cap doping level 8 x10^{18} Zn GaAs
- p Cladding layer <1 x10^{16} Zn 30% AlGaAs

-MQW exciton 861nm/core composition 20% AlGaAs

- n-Cladding layer 2.1x 10^{17} Se 61% AlGaAs

-#QT433R

-Grown by MOCVD

- Cap doping 8x 10^{18} Zn GaAs
- p-Cladding layer 2x 10^{17} Zn 26% AlGaAs
- MQW exciton 865nm/Core composition 19% AlGaAs
- n-Cladding layer 2.6x 10^{17} Se 51% AlGaAs

-#A742

- Grown by MBE
- Cap doping 1x 10^{19} Be GaAs

- p Cladding Layer 2x 10^{17} 30% AlGaAs
- MQW exciton 858nm/ Core composition 20% AlGaAs
- n Cladding Layer 2x 10^{17} Si 60% AlGaAs

The epitaxial wafer structure #QT474d, illustrated in Fig.4.2, was an improved asymmetric structure with two quantum wells. The p-type layers were doped with carbon instead of Zn in order to avoid diffusion of Zn into the active layers. Note also that the upper cladding layer had a composition of 40% AlGaAs. This choice was made to provide good electrical and optical confinement. The position of the quantum wells was optimized to be at the maximum peak of the modal electric field, which was displaced from a central position due to the asymmetry of the cladding layers.

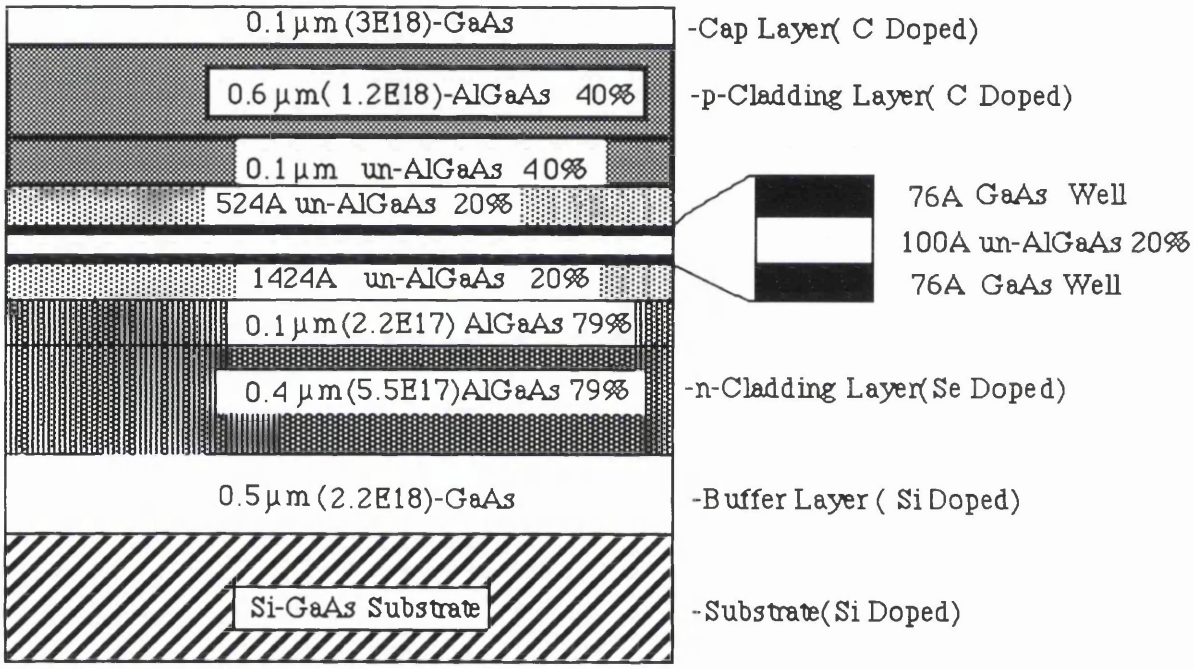

Fig.4.2: Schematic diagram of asymmetric epitaxial wafer structure: #QT474d

4.3 Theory of epitaxial wafer analysis

The theory relevant to epitaxial wafer analysis for semiconductor lasers is given in references [4.1] to [4.6]. In oxide stripe lasers, the following relation applies at threshold

$$\Gamma g_{th} = \alpha + \frac{1}{2L}\ln\left(\frac{1}{R_1 R_2}\right) \tag{4.1}$$

This is the relation for the nominal threshold gain g_{th}, which is constant over the whole length of the laser, in terms of R_1,R_2 and L. α is the optical loss per unit length from processes not directly associated with the gain mechanism, such as diffraction, scattering, and free-carrier absorption. R_1 and R_2 are the power reflection coefficients at the two ends of the resonator and L is its length. This equation shows that the gain per unit length must be sufficient to cancel out the optical losses due to absorption etc, and also the mirror loss $\frac{1}{L}\ln\left(\frac{1}{R}\right)$ (if R_1=R_2) due to light emission through the facets.

Above threshold, the gain is assumed to be clamped and the extra electrical power appears as light emission. The efficiency of conversion of electrons to photons is given by

$$\eta_e = \eta_i\left(1-\frac{\alpha}{g_{th}}\right) \tag{4.2}$$

where η_i is the fraction of the total injected carrier rate which is converted to stimulated photons above threshold. It is introduced to take into account any incomplete clamping of the injected carrier concentration and any other factor that may empirically affect the behaviour. η_e is the external differential quantum efficiency, as measured by the slope of the light-current curve above threshold.

It has been found that the gain for a quantum well laser, taking into account the effect of light guided outside the quantum wells, and up to threshold, can be related to the total current density in the laser, J, by the following relationship [4.4],

$$g(J) = n\Gamma g_0 Ln\left(\frac{J}{nJ_t}\right) \tag{4.3}$$

where n is the number of quantum wells, Γ is the optical confinement per well, g_0, is the gain coefficient for one well and J_t is the transparency current which is needed in a well to overcome the resonant absorption. The optical confinement per well, Γ, is the fraction of the power within the well divided by the whole power carried by the laser mode, which is defined by

$$\Gamma = \frac{\int_{Well} E(x)^2 dx}{\int_{Waveguide} E(x)^2 dx} \tag{4.4}$$

In broad area oxide stripe lasers, the approximate value of the optical confinement per well, Γ, can be calculated using a 2-dimensional waveguide model.

Fig. 4.3 shows an illustration of Eq. (4.3), which is the relationship between the gain produced by the quantum wells and the current density for material with different numbers of wells.

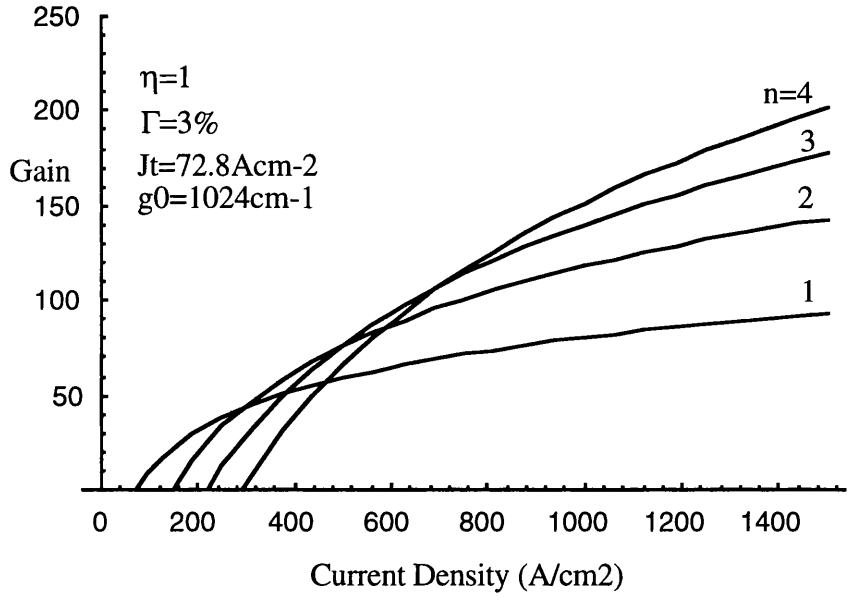

Fig.4.3: Calculated relation between the gain (taking into account he effect of light guided outside of the quantum wells) and the current density, for material with different numbers of wells, using eq.(4.3). The internal quantum efficiency is assumed to be $\eta_i=1$, the transparency current $J_t=72.8Acm^{-2}$, the gain coefficient per well $g_0=1024cm^{-1}$ and the optical confinement $\Gamma=3\%$.

Combining (4.1) and (4.2), the following equation is obtained

$$\frac{1}{\eta_e} = \frac{1}{\eta_i} - L\left(\frac{\alpha}{\eta_i \ln R}\right) \tag{4.5}$$

From the plot of the inverse external quantum efficiency, $1/\eta_e$ against the cavity length L, the internal quantum efficiency η_i can be calculated from the intercept, and the internal optical loss α can be estimated after assuming a reasonable value for the reflectivity R.

Combining (4.3) and (4.5) gives

$$\ln(J_{th}) = \left\{\frac{\alpha}{n\Gamma g_0} + \ln\left(\frac{nJ_t}{\eta_i}\right)\right\} - \frac{1}{L}\left(\frac{\ln R}{n\Gamma g_0}\right) \tag{4.6}$$

A plot of the natural logarithm of the threshold current density against the inverse of the cavity length 1/L gives the gain factor $n\Gamma g_0$ from the slope, and from the intercept it gives the transparency current J_t using the internal loss α calculated before. From these two last equations, (4.5) and (4.6), the quantum well epitaxial wafer can be analysed.

4.4 Improvement of the Epitaxial Wafer Structure

From the distribution of the electric field across the structure, as illustrated in Fig.4.3 (Y direction), it is possible to calculate the fraction of the optical modal power which is guided in the upper cladding layer. This result is important because it is the light in the upper cladding layer that interacts most strongly with the gratings. For the epitaxial wafer structure 30%Al/60%Al ($Al_{0.3}Ga_{0.7}As$ in the upper cladding layer and $Al_{0.6}Ga_{0.4}As$ in the lower cladding layer) 51% of the light is guided in the upper cladding layer. The percentage of guided modal power in the upper cladding layer is reduced to 42% in the material structure 40%Al/80%Al, and to 31% in the symmetric structure 40%Al/40%Al.

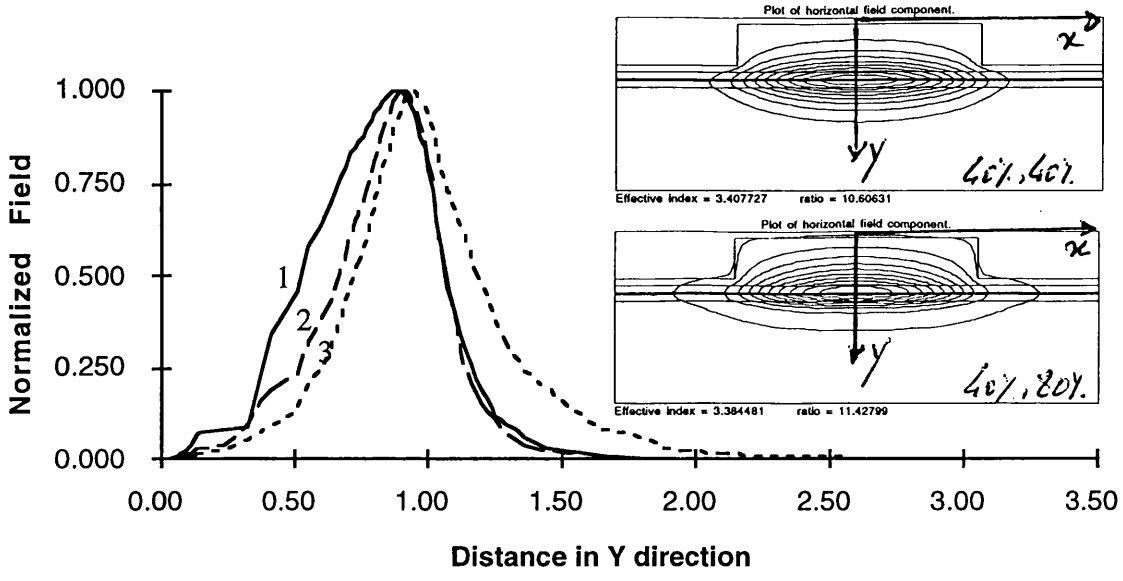

Fig. 4.4: Distribution of the electric field across the Y direction for three different material structures. Curve 1,: 30%Al/60%Al, and optical confinement factor Γ=51%; Curve 2: 40%Al/80%Al, Γ=42%; Curve 3: 40%Al/40%Al, Γ=31%

Fig.4.4 shows the coupling coefficient, estimated according to the theory developed in the previous chapter 3 (section 3.8), as a function of the grating etch depth, for three different material structures. The epitaxial wafer structures have the same amount of Al in the lower cladding, which is 40% for all material structures. This plot shows clearly that the reduction of the Al content in the upper cladding layer increases the coupling coefficient even for small etch depths, such as in the case of 30%Al/40%Al. The reason for such increase in the coupling coefficient is that a larger fraction of the modal power is guided in the upper cladding layer, consequently increasing the interaction between guided field and gratings.

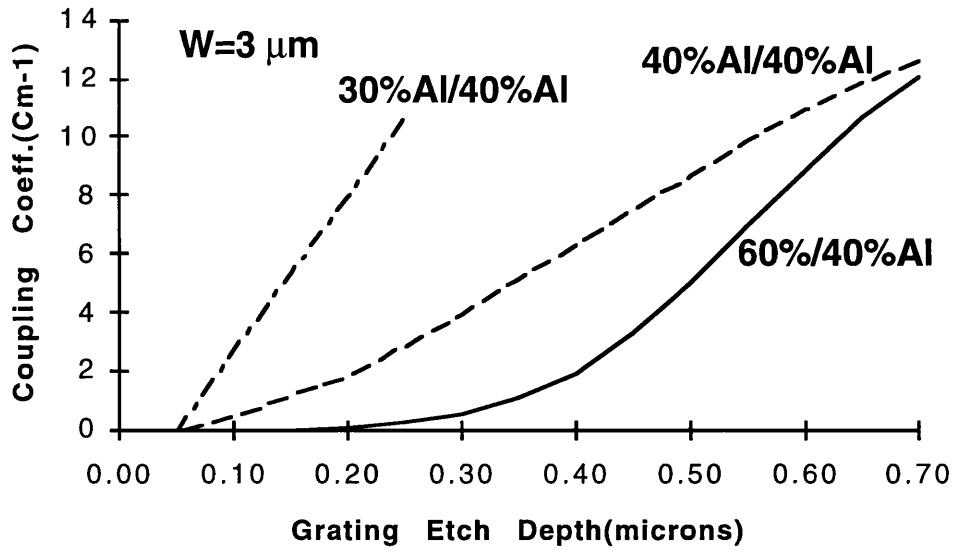

Fig.4.5: Coupling coefficient versus grating etch depth for three different material structures. W is the stripe width of laser waveguide.

4.5- Experimental Results

4.5.1- Broad area oxide stripe lasers for analysis of Epitaxial material

It is important to characterize the epitaxial wafer structure before fabrication of the deep surface grating DFB lasers. This implies measurement of the emission wavelength, internal loss α and the internal quantum efficiency, η_i.

To analyse the epitaxial wafer parameters, broad area oxide stripe lasers were fabricated, because the effect of current spreading outside the lasing region should be minimal in such lasers. 75μm width oxide stripe lasers were therefore fabricated, then cleaved into lengths from 200μm to 1200μm, and the threshold currents measured for devices that gave the lowest threshold current. The external quantum efficiency, η_e, was then estimated. The structure of the broad area oxide stripe laser is shown schematically in Fig.4.6.

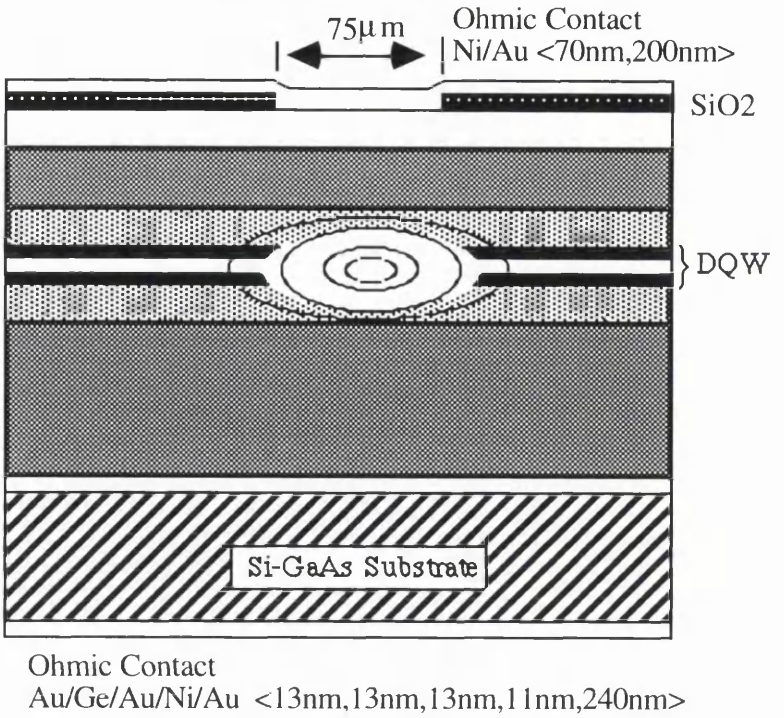

Fig.4.6: Schematic diagram of the broad area stripe laser.

4.5.2- Measurements and experimental results

The lasers were operated in the pulsed current mode in order to prevent excessive heating. The current pulse width was 400ns and the repetition rate was 1 kHz (duty cycle 1:2500). Fig.4.7 shows the measured L-I curves of the 200μm, 600μm, 800μm, and 1200μm cavity length broad area oxide stripe lasers fabricated from wafer #QT270, at room temperature. The lasers selected had the lowest threshold current among the five lasers within each category. Table 4.1 shows the slope efficiency for a single output facet, the threshold current and the threshold current density obtained from the L-I curves.

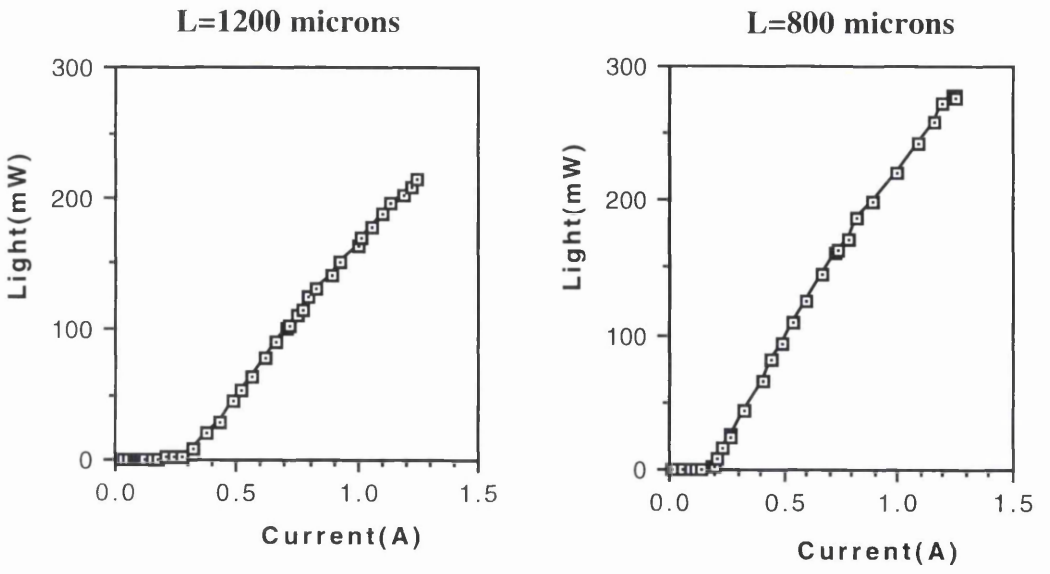

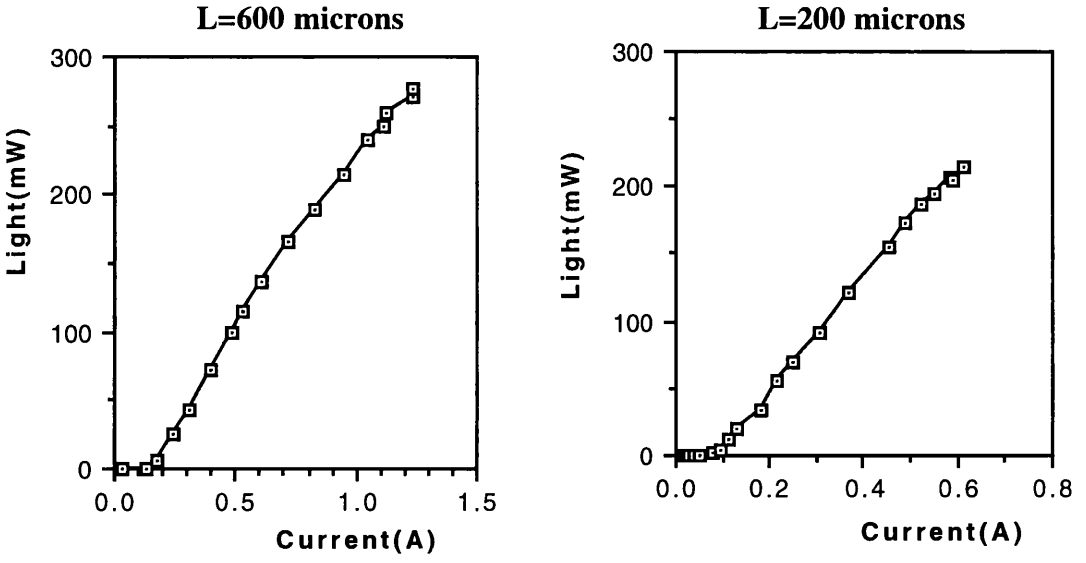

Fig.4.7: Measured Output power per facet as a function of the drive current in broad area oxide stripe lasers.

Cavity length (μm)	Slope efficiency per facet (W/A)	Threshold current (mA)	Threshold current density (A/cm2)
200	0.42	107	713
600	0.36	168	373
800	0.31	200	333
1000	0.28	230	307
1200	0.25	305	339

Table 4.1: Measured experimental results from the L-I characteristic, using broad area oxide stripe lasers

Fig.4.8 shows the relationship between the inverse of the external quantum efficiency, obtained from the slope of the L-I curves, and the cavity length for wafer #QT270. The linear dependence fit was good and, using Eq.(4.5), an internal quantum efficiency of 95% and an optical loss of 8.13 cm^{-1} were calculated. From Eq.(4.4), optical confinement factors were calculated to be 21.2% in the upper cladding layer, 57.5% in the confining and active layers, 21.2% in the lower cladding layer and 2.87% per well (Γ=2.87%) for wafer #QT270, using a 2-dimensional model.

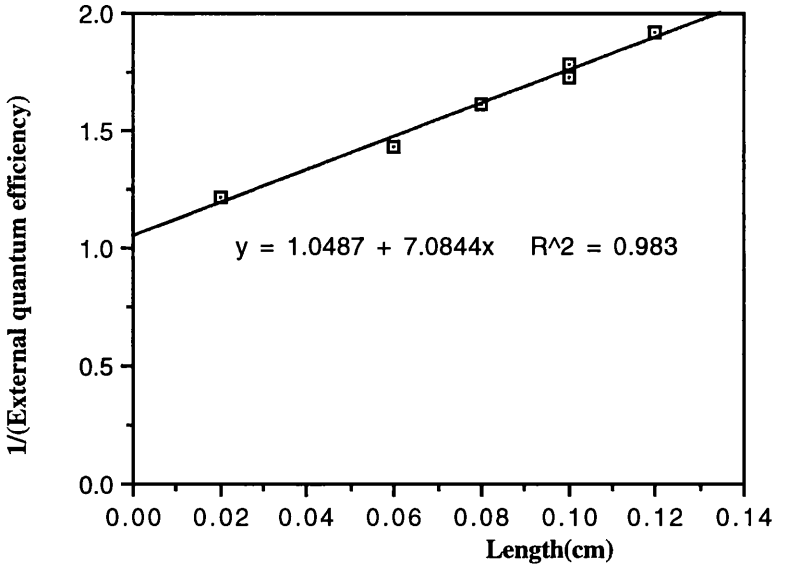

Fig.4.8: Inverse of the external quantum efficiency obtained from the slope of the L-I curves as a funtion of the cavity length

Fig.4.9 shows the relationship between the natural logarithm of the threshold current density and the inverse of the cavity length obtained from the L-I curves. The linear fit was good and, using Eq.(4.6), it gave $n\Gamma g_0=58.78cm^{-1}$ and $\ln\left(\frac{nJ_t}{\eta_i}\right)=5.39$. From this data, the transparency current density, J_t, and the gain coefficient per well, g_0, were calculated to be $J_t=72.8\ Acm^{-2}$ and $g_0=1024\ cm^{-1}$, respectively. The epitaxial wafer parameters obtained from the analysis are shown in table 4.2 for all the structures.

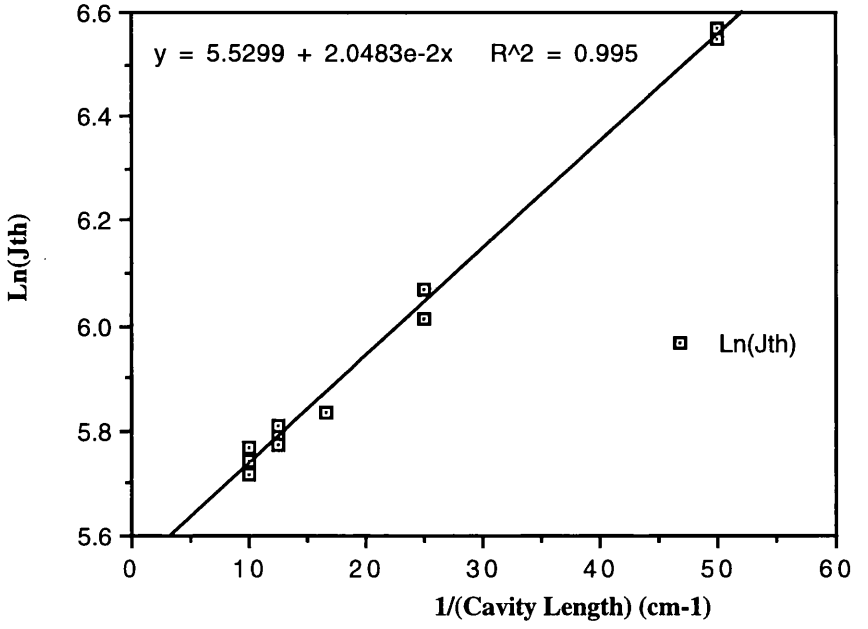

Fig. 4.9: Natural logarithm of the threshold current density against the inverse of the cavity length obtained from the L-I curves.

Materials	Wavelength	η_i(%)	α (cm^{-1})	g_0 (cm^{-1})	Jt(A/cm^2)	$J_{th,600}$
#QT270	862nm	95.0	8.13	1024.0	72.8	367 Acm^{-2}
#QT433	855nm	18.3	9.76	1234.6	27.6	1000 Acm^{-2}
#QT433R	865nm	63.2	20.75	1502.8	89.5	930 Acm^{-2}
#A606	865nm	89.0	10.40	2091.2	140.8	781 Acm^{-2}
#A742	857nm	55.0	28.00	885.8	154.6	1652 Acm^{-2}
#QT474d	861nm	60.7	11.20	1094.0	55.3	

Table 4.2: The epitaxial wafer parameters obtained from the analysis for all material structures

Wafers #QT270 and #A606 have identical structures. However, the estimated gain coefficient per well, g_0, and transparency current, J_t, are at least twice as high in the #A606 case. This difference is caused by traps (oxygen) in the AlGaAs barriers in the MBE material, where the carriers can suffer non-radiative recombination [4.7]. The epitaxial material #QT433 has very poor properties because the doping concentration in the upper cladding layer is very low ($<1x\ 10^{16}cm^{-3}$). Wafers #QT433R and #A742 have high optical propagation losses, which is due to the low concentration of Al in the upper cladding layer. Wafer #QT433R has an optical confinement factor of 64 % in the upper cladding layer; this leads to high absorption of light in this layer due to free-carrier absorption. These results lead to the conclusion that the Al concentration in the upper cladding layer should be about 40%Al in order to provide good electrical and optical confinement. Wafer #QT474d is an improved asymmetric structure consisting of 40% Al in the upper cladding layer and 79%Al in the lower cladding layer. Note also that 0.1μm of the upper cladding layer is 40%Al undoped AlGaAs in order to reduce optical losses.

References

[4.1] G.H.B.Thompson, "*Physics of semiconductor laser devices*", John Wiley and Sons, pp. 92-105, 1980

[4.2] S.M.Sze, "*Semiconductor Devices Physics and Technology*", John Wiley and Sons, pp.267-274, (1985)

[4.3] A. Yariv, "*Quantum Electronics*", John Wiley and Sons, pp.271-276, (1987)

[4.4] P.W.A.Mc Ilroy, A.Kurobe and Y.Uematsu, " Analysis and application of Theoretical gain curves to the design of multi-quantum-well lasers", IEEE Journal of quantum Electronics, Vol.21,pp1958-1963, (1985)

[4.5] J.Whiteaway, G.H.B. Thompson, P.D. Greene, R.W.Glew, "Logarithmic Gain/Current-Density Characteristic of InGaAs/InGaAlAs/InP multi-Quantum-Well Separate-Confinement-Heterostructure Lasers", Electronics Letters, Vol.27, pp.340-342, (1991)

[4.6] M.E.Givens,L.M.Miller, and J.J. Coleman, "Effect of design on the threshold Current Density of $Al_xGa_{1-x}As$ Separate confinement heterostructure Single Quantum Well Lasers", J. Appl. Physics, Vol.71, pp.4583-4588, (1992)

[4.7] Memo by S. Ayling 28/7/93, and also Memo by B. Voegele, February 1994.

Chapter 5: Device Structure and Fabrication.

5.1 Introduction

In this chapter, the deep surface grating DFB laser structure and its fabrication procedure are discussed. The surface grating DFB laser, as illustrated in Fig. 5.1, is fabricated entirely by planar processing, and involves a single, postgrowth reactive ion etch (RIE) using a patterned mask, previouly generated by electon-beam lithography. All the basic aspects of electron-beam lithography and procedures for fabrication of third-order, second-order, and first-order gratings as well as λ/4 phase shift and dual pitch gratings, are thoroughly discussed. The fabrication of a flared amplifier integrated with a surface grating DFB laser, measurement and characterization of stitching errors, and final processing steps of surface grating DFB laser fabrication, such as electrical contact metallization, anti-reflection coatings deposition, mounting and wire bonding, are described in the last sections of this chapter.

5.2 Device structure

In Fig.5.1 a schematic diagram is shown of the deep surface grating DFB stripe laser. The cavity length is in general 600 μm. The grating was etched to typically within 0.1 μm (T=0.6 μm in Fig.5.1) of the active layer and the width of the laser stripe was 3 μm. The grating period was about 0.38 μm, corresponding to a third-order grating.

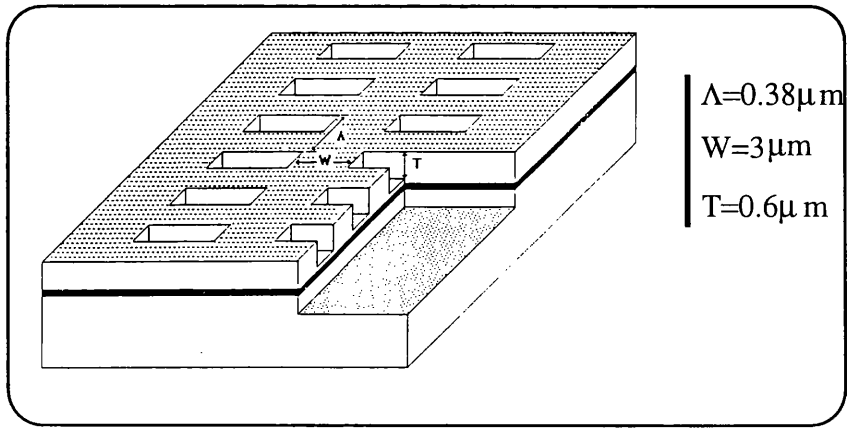

Fig.5.1: Schematic diagram of the deep surface grating DFB stripe laser.

5.3 Fabrication

The fabrication of the DFB laser required several steps, which are briefly described as follows:

1. Sample preparation:

The wafer was cleaved into a square with a suitable size, typically 8x8 mm^2, and cleaned using various solvents.

2. Fabrication of gratings alongside the ridge:

Third-order gratings (Λ=380nm) were fabricated using electron beam (e-beam) lithography and reactive ion etching.

3. Fabrication of contact window and contacts:

A contact window was opened by wet etching of the SiO_2 layer, which was deposited by Plasma Enhanced Chemical Vapour Deposition (PECVD). After suitable surface preparation, the final step was deposition and annealing of the contact metallisation.

4. Cleaving and deposition of anti-reflection coatings:

After cleaving the wafer section into several bars of lasers, anti-reflection coatings, consisting of a single Al_2O_3 layer, were deposited by sputtering on both facets.

5.Mounting and wire-bonding:

The laser chip was mounted on a laser header and wire-bonded.

5.3.1 Sample preparation

Samples were cleaved into 8×8mm^2 pieces using a scriber, this size being suitable for easy handling and corresponding also to the approximate size for 4 rows of lasers in the e-beam lithography. The wafer section was prepared for lithography by cleaning for 5 minutes in successive ultrasonic baths of trichloroethylene, methanol and acetone, with a final rinse in reverse osmosis water.

5.3.2 Fabrication of gratings alongside the ridge

The fabrication of gratings alongside the ridge, using the electron beam lithography technology, requires background knowledge in the two following areas: **(1)** Design of the device structure, leading to writing of the corresponding patterns and production of files necessary for controlling the Beam Writer; **(2)** preparation of the samples, involving choice of suitable electron beam resists and the necessary exposure doses.

(1) Preparation of files

A brief outline of the procedure for preparation of the files is the following:

1. Design of device structure and creation of the required pattern on computer.

2. Preparation of data in Cats for the Beam Writer.

3. Preparation of the job files using the BWL programme.

4. Transfer of the files to the computer that controls the Beam Writer.

Regarding item **1,** a simple example on how to write a pattern for the Beam Writer is now explained.

Instructions:

Filename: VMgrating_db.ctxt

```
TEXTLIB 9.0.0
UNIT NM
RESOLVE 1
BEGLIB
!
!Definition of Grating 500 micros long.
!
STRUCT Grating
LAYER 1
AREF Element (0,0) 1 (0,0) 1316 (0,380)
ENDSTRUCT
!
!Definition of Element.
!
STRUCT Element
LAYER 1
B 0,0 3000,0 3000,180 0,180 0,0 ENDB
ENDSTRUCT
!
ENDLIB
```

Design

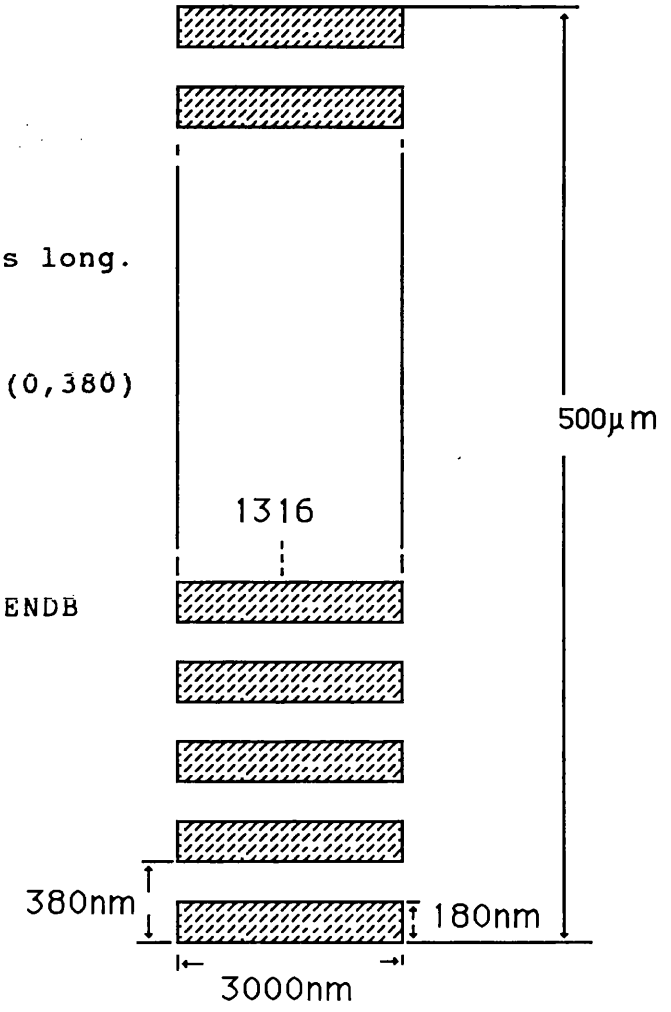

Fig.5.2: Example of pattern written in simple editor (Edit Vax) which consists of a grating characterized by a length of 500 µm, a width of 3 µm, and a period of 0.38 µm.

This grating is characterized by a length of 500 μm, a width of 3 μm, and a spatial period of 380 nm. First, the simplest structure in the pattern is defined , which is the grating Element in this example. The structure Element is a rectangle with vertices at point (0,0), point (3000,0), point (3000,180), then (0,180) and, finally, the starting point (0,0) again. The structure Element can be used to design more complex structures. The next step is to repeat this Element 1316 times in the Y direction. So, a structure Grating is defined by starting at (0,0), repeating the structure Element just one time in the X direction, and 1316 times in the Y direction, with a separation of 380nm, which is the period of the grating.

After the .txt file is created in Edit, as shown in the example above, its format is changed in order to be read by Cats (a program that translates or transcribes this data into machine readable format). This is carried out by using the program Textlib. The instructions for this operation are given below:

2. *Textlib* VMgrating_db.ctxt->VMgrating_db.clib

The file *.clib is read by Cats. In Cats, it is possible to select different layers and also the resolution. Within Cats it is also possible to look at the graphics screen to make sure that the files appear to be correct. If the files pass this inspection, the *Do* command is typed in Cats and a new file is created:

VMgrating_db.clib-> VMgrating_01.cflt

Finally, the format of *.cflt files is changed for use by the Beam Writer. The program Writefile is used for such purpose:

Writefile VMgrating_01.cflt-> VMgrating_01.iwfl

Another file must be created in which parameters, such as the position of the pattern in the sample, exposure dose, spot-size and energy (Kvolt) are specified. The program that creates the job file is called BWL. A simple example of a job file follows: VMgrating.com. It is assumed that the size of the sample is $8\times8mm^2$, so that the pattern is positioned in the middle of the sample, which has Position 4,4.

3. VMgrating.com

Substrate: Small
Kvolts: 50
Outfile: VMgrating.com
Pattern: VMgrating_01

Dose: 475 μCcm^{-2}
Resolution: 0.02 μm
Spot_size: 80 nm
Position: 4,4
Step_size: 1,1
Repeat: 1,1

4. To transfer the files to the computer that controls the Beam Writer, two commands are typed:

transfer VMgrating_01 patterns
transfer VMgrating.com Jobs

5.4 Basics of electron beam lithography[5.1]

Electron sensitive resists- In electron beam lithography, the starting point is a substrate, which may be Si or GaAs or any other material, on which patterns need to be defined. The first stage in the process is to coat the substrate with a thin layer of polymer, known as a **resist,** which is sensitive to electron beam irradiation. There are two basic sorts of resist, **positive** and **negative** resists. After exposing the resist to the electron beam, the substrate is put into a chemical known as a **developer** which selectively removes areas of resist.

With *positive resist,* the exposed area is removed by the developer; while with *negative resist,* the unexposed area is removed by the developer.
A simple picture of the process starts from the consideration that the resist is made up of long polymer chains. In a positive resist, these chains are broken down by e-beam exposure and hence become more soluble in the developer; in a negative resist, the exposed regions become cross-linked, i.e. the chains get longer, and the resist is then less soluble.

Exposure dose- This is an important parameter. In order for the developer to remove the unwanted resist correctly, the solubility of the resist has to be changed by a sufficient amount by the electron beam exposure. This requires a certain number of electrons, known as the **dose,** which is usually measured in μCcm^{-2}. Typical doses vary from 1 to 300 μCcm^{-2}.

Proximity effects- These arise because the electrons do not simply pass through the resist, exposing it and then disappearing. They have the unfortunate habit of coming back out of the substrate again as **backscattered** electrons.These electrons have approximately the same energy as those of the primary beam but are spread out across a much larger area. At 50 keV, electrons penetrate typically about 5 μm into the substrate, and this penetration gives rise to

a backscattered beam which is approximately gaussian, but with a radius on the order of 2-5 μm and a total integrated dose around half of that of the primary incoming beam. The back-scattered electrons act like a background fog to the desired exposure.

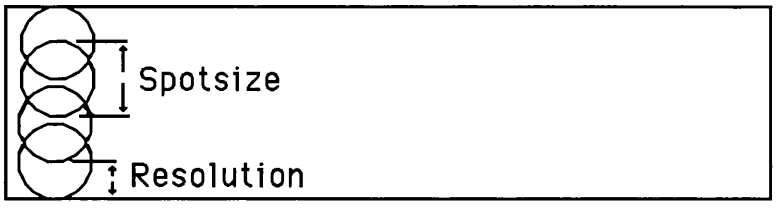

Fig.5.3: Illustration of the concepts of resolution and spot-size.

Resolution-This is essentially the beam step size pixel to pixel. It can be varied between 5 nm and 300nm. The resolution is represented in Fig.5.3 and corresponds to the distance from near the edge to the middle of the spot. The important point to notice is that any feature size in the pattern must be an integer multiple of the resolution.

Beam Energy- This is the kinetic energy of the electrons in the beam. This parameter is important because it imposes the resolution achievable with the exposure system. In optical lithography, the resolution is limited by diffraction of light. In the e-beam lithography, however, the resolution is limited by electron scattering, which is related to the energy of the beam (proximity effects).

Spotsize- This is size of the spot created by the electron beam when it impinges on the sample. The choice of spotsize available from the Beam Writer ranges from 12 nm to 400 nm.

(2) Preparation of the samples

Exposure dose:

Because the optimum exposure dose depends both on the e-beam resist used and the feature size, the process commonly used to determine the optimum exposure dose is the performance of an exposure test. An exposure test consists of exposing the same pattern with different doses and then checking in the SEM which one is the optimum. Fig. 5.4 illustrates this aspect.

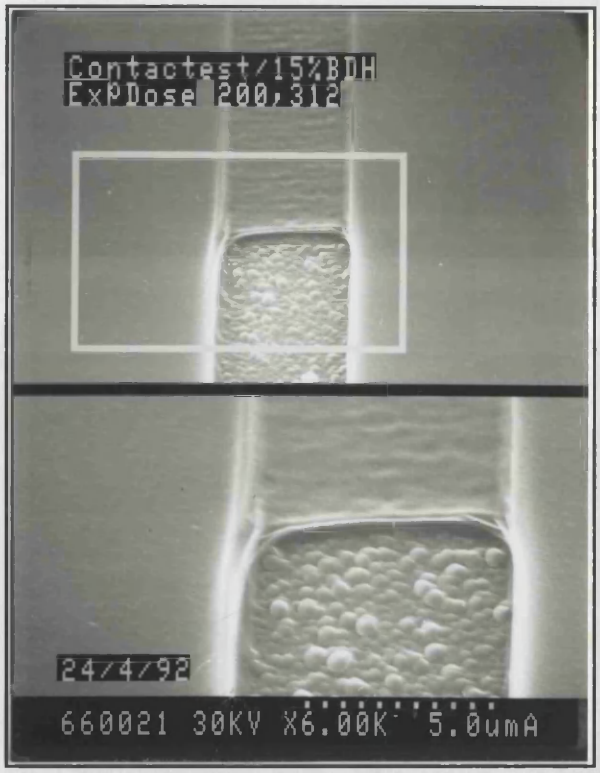

Fig.5.4: Exposure test for a 3 μm stripe. The e-beam resist used was 15%BDH, exposure doses are 200 μCcm^{-2} in the upper region and 390 μCcm^{-2} in the lower region.

The pattern of Fig.5.4 consists of a 3 μm stripe which was exposed with different exposure doses. The exposure dose for the upper part was 200 μCcm^{-2}, and it can be seen that most of the e-beam resist remains in the sample. On the other hand, the lower part of the sample was exposed with 390 μCcm^{-2} and the resist was completely removed by the developer.

Before starting the grating fabrication, alignment marks have to be defined so that the various patterns required by the fabrication process can be mutually aligned. The fabrication process requires at least two e-beam lithographic steps: one for grating fabrication; and another one to define the contact window.

5.5 Alignment marks fabrication.

The alignment marks consist of squares that are opened in each corner of the sample. The purpose of the alignment marks is their use as a reference by the Beam Writer to align the various patterns required for the fabrication process. An outline of the fabrication process is as follows:

1. Deposition of 2000A SiO_2 layer.
2. Photolithography of sample with alignment marks mask.

3. Dry etching of SiO_2 layer with C_2F_6 gas. The photoresist layer is used as a dry etching mask.

4. Removal of resist and dry etching of GaAs material with $SiCl_4$ gas. The SiO_2 layer is used as a dry etching mask.

5. Removal of SiO_2 film with buffered HF.

Alignment marks as deep as 2.5μm are shown in the following figure (Fig.5.5).

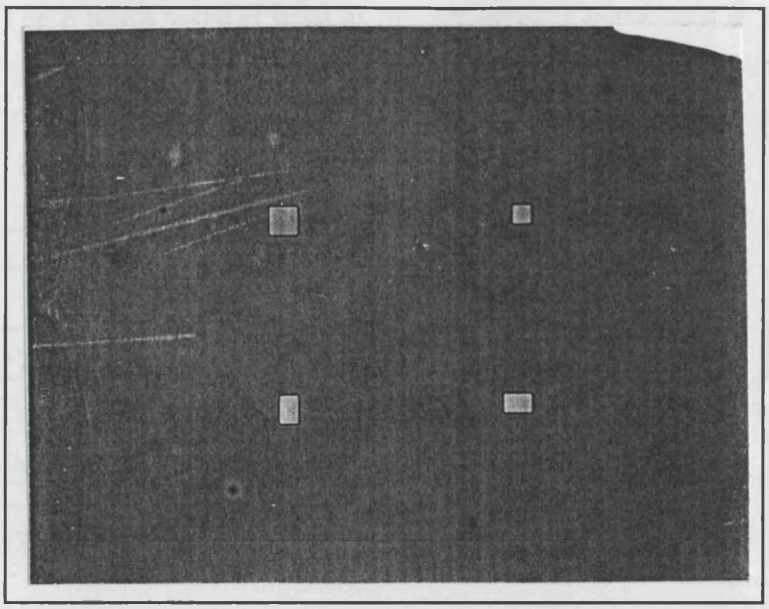

Fig.5.5: Alignment marks used to align several e-beam lithographic steps.

5.6 Fabrication of third and second-order gratings in GaAs

An outline of the grating fabrication process is now given. The characteristic parameters of the structure are: 500 μm length, 8 μm width; 0.6 μm etch depth and pitch of 380 nm for the third-order gratings and 0.58 μm etch depth and a period of 260 nm for the second-order gratings.

1. Deposition of a SiO_2 layer(1500A).

2. Spin coating of the sample with two layers of e-beam resist: 8%BDH; 4%ELV.

3. Exposure in the beam writer.

4. Development: Developer 2.5:1 (IPA:MiBK) for 30 s at a temperature of 23 °C.

5. Dry etching of SiO_2 with C_2F_6, using e-beam resist as a dry etching mask, for 4 minutes.

6. Removal of e-beam resist with acetone and dry etching of the sample with $SiCl_4$. The SiO_2 layer is used as a dry etching mask.

The process is started by depositing a new layer of SiO_2, 1500 A thick. Then, two layers of e-beam resist are spun on the samples. The first layer of e-beam resist is more sensitive than

the second one. In practical terms, the purpose of using two layers of e-beam resist is that of increasing the contrast of the resist, which means that sharper images can be transfered, and also to increase the etch resistance of the resist. The 8%BDH layer is spun at 5000 rpm and baked for 2 hours at 180 °C; the second layer, 4%ELV, is also spun at 5000 rpm and baked overnight at 180 °C. After exposure in the Beam Writer, the samples are developed in 2.5:1 (IPA:MiBK) for 30 s at a temperature of 23 °C. The SiO_2 layer is dry-etched in C_2F_6 gas for 4 minutes. The e-beam resist is used as the dry-etching mask, and it does not survive more than 4 minutes in the C_2F_6 etching, hence a SiO_2 layer of just 1500A is used. The remaining e-beam resist is removed with acetone and the samples are then dry-etched in $SiCl_4$[5.2]-[5.4] for 5 minutes.

Material	Gas	Gas Flow (sccm)	Pressure (mTorr)	RF Power (W)	Feature Size (μm)	Etching Rate(nm/mins)
SiO_2	C_2F_6	20	14	100	0.38	50
GaAs	$SiCl_4$	6	8	100	20	216
GaAs	$SiCl_4$	6	8	100	0.38	154
GaAs	$SiCl_4$	6	8	100	0.26	120

Table 5.1: Conditions of reactive ion etching(RIE) of SiO_2 and GaAs layers

The RIE of GaAs/AlGaAs layers is anisotropic. $SiCl_4$ forms volatile reaction products with both GaAs and AlGaAs:

$$SiCl_4 + GaAs + AlGaAs \rightarrow GaCl_w \uparrow + AsCl_x \uparrow + AlCl_y \uparrow + SiCl_z \uparrow$$

The etch rate depends on three parameters: pressure, gas flow, and RF power. Pressure and gas flow are interrelated, because the pump rate of the vacuum system is constant. The grating profile is changed by the gas flow. In this fabrication process, 6 sccm of $SiCl_4$ gas flow was adopted.

To dry-etch to the required etch depth accurately, test samples were used. A test sample consists of a grating 4mm long by 0.2mm wide. After $SiCl_4$ dry-etching, the test sample is selectively wet etched so as to enhance the contrast between the grown layers. This procedure improves the layer contrast for the SEM picture (see Fig. 5.8). The selective wet etching is performed using the solution $HCl:H_2O_2:H_2O$ (1:1:10) for 1 minute.

In Figs.5.6 and 5.7, dry-etched gratings in GaAs are shown: with 380 nm period for third-order gratings, and 260 nm period for second-order gratings. In Fig.5.8 a test sample is shown after selective wet etching; note that the active region is clearly seen in the figure and the gratings touch, but do not go through, the active layer.

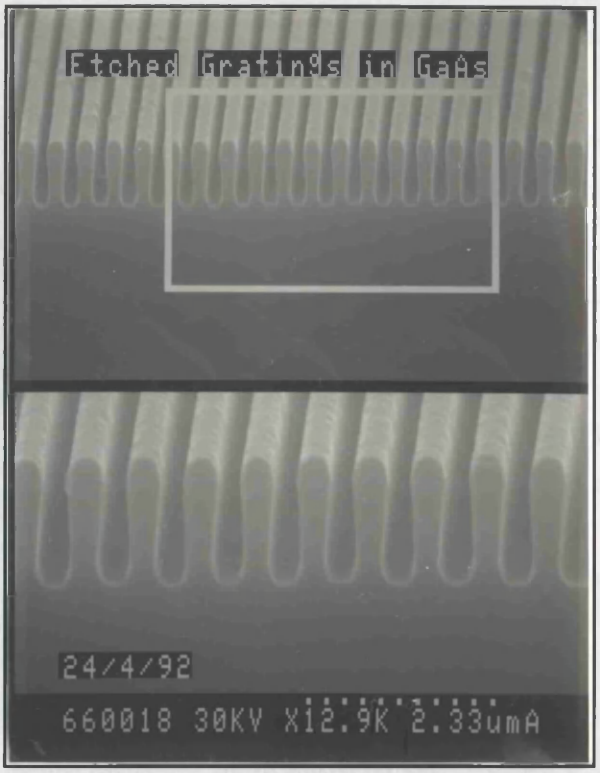

Fig.5.6: Dry-etched 3rd-order grating in GaAs

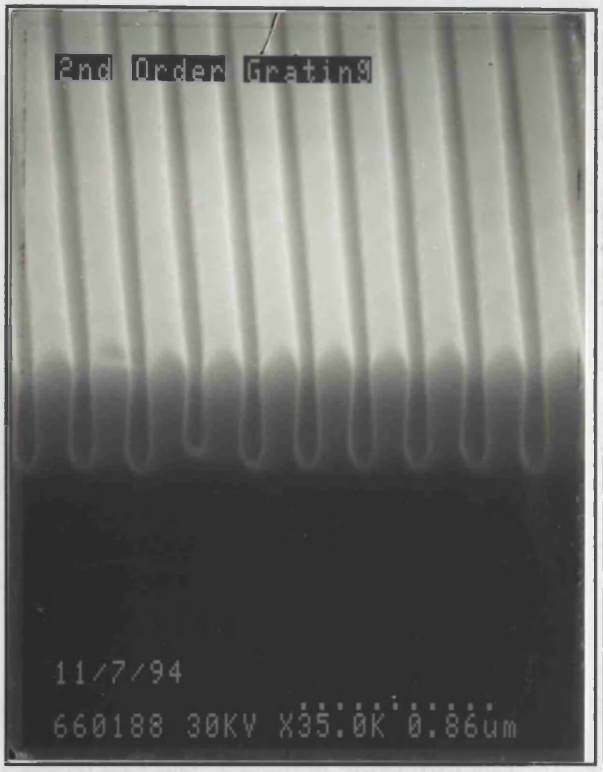

Fig.5.7:Dry-etched 2nd-order grating in GaAs

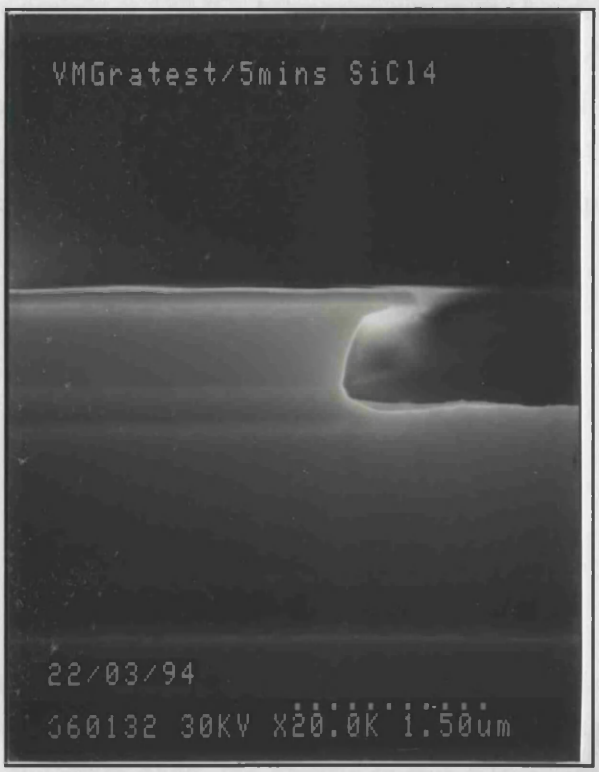

Fig.5.8: Test sample after selective wet etching

5.7 Fabrication of first-order gratings in GaAs

The following text is an outline of the grating fabrication process. The characteristic parameters of the structure are: 500 μm length, 10 μm width, 0.6 μm etch depth, and the pitch is 130 nm for the first-order grating.

1. Deposition of a SiO_2 layer (800A).

2. Spin coating of sample with two layers of e.b. resist: 4%BDH; 2.5%ELV

3. Exposure in the Beam Writer.

4. Development: Developer 3:1 (IPA:MiBK) for 30 s at 23 °C.

5. Dry etching of SiO_2 with C_2F_6, using e-beam resist as a dry-etching mask, for 2minutes.

6. Removal of remaining e.b. resist with acetone and dry etching of sample with $SiCl_4/SiF_4$.

The fabrication is started by depositing a layer of SiO_2, 800A thick. Then, two layers of e-beam resist are spun: 4%BDH and 2.5%ELV. The 4%BDH layer is spun at 5000 rpm and baked for 2hours at a temperature of 180 °C; the second layer of 2.5%ELV is also spun at 5000 rpm and baked overnight at 180 °C. After exposure in the beam writer, the samples are developed in 3:1 (IPA:MiBK) for 30 s at 23 °C. The SiO_2 layer is dry-etched in C_2F_6 gas for 2 minutes. The e-beam resist is used as a dry-etching mask, and it does not survive more than 2 minutes in C_2F_6 etching; that is why a SiO_2 layer of just 800 A thickness is used. The remaining e-beam resist is removed with acetone and the samples are dry-etched in $SiCl_4/SiF_4$.

Etching conditions:
Gas=$SiCl_4/SiF_4$
Gas flow=8/1 sccm/min.
Power=30 W
Temp. =40 °C
DC=-110 V
Time=8 min

In Fig.5.9 and 5.10, first-order gratings in GaAs are shown, the period being 130nm. Note that the sample exposed with 500 μCcm^{-2} is damaged: the top GaAs p^{++} layer collapsed, as seen in Fig. 5.10. On the other hand, the grating in Fig. 5.9, exposed with 484 μCcm^{-2}, presents a mark-space ratio of 1:1 and the problem of GaAs p^{++} collapse was avoided. These figures show clearly the importance of the exposure dose for such finely pitched grating structures.

Fig.5.9: First-order grating in GaAs material

Fig.5.10: Collapse of GaAs p^{++}

Deep surface grating DFB laser

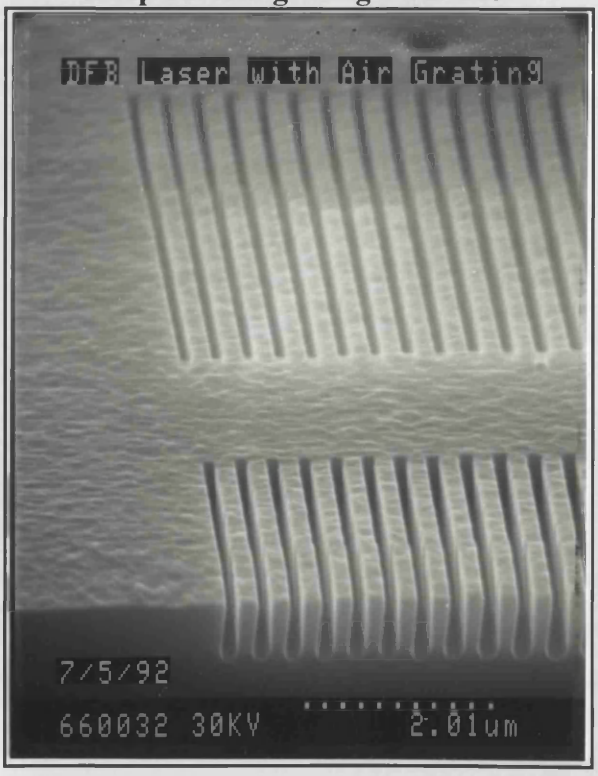

Fig.5.11: Profile and top view of deep surface 3rd-order grating DFB laser.

Fig.5.11 shows a deep surface 3rd-order grating DFB laser in its final processing stage. The DFB laser at this stage is used for assessment of the waveguide quality and also for measuring the grating coupling coefficient. However, electrically pumped DFB lasers require further processing, such as deposition of isolation layers and evaporation of metal contacts. The dimensions are 0.6 μm etch depth, 8 μm grating width and 3.5 μm stripe between gratings. Further processing is applied to these devices, as will be discussed in the following sections.

5.8 Fabrication of λ/4 phase shift and dual pitch gratings

In chapter 2, the techniques for achieving single longitudinal mode operation in DFB lasers were discussed. It was then pointed out that either a λ/4 shift or a distributed phase-shift can be used to overcome multilongitudinal mode operation. In the following exposure tests, it is shown that these techniques are possible using the e-beam lithography technology.

λ/4 Phase shift

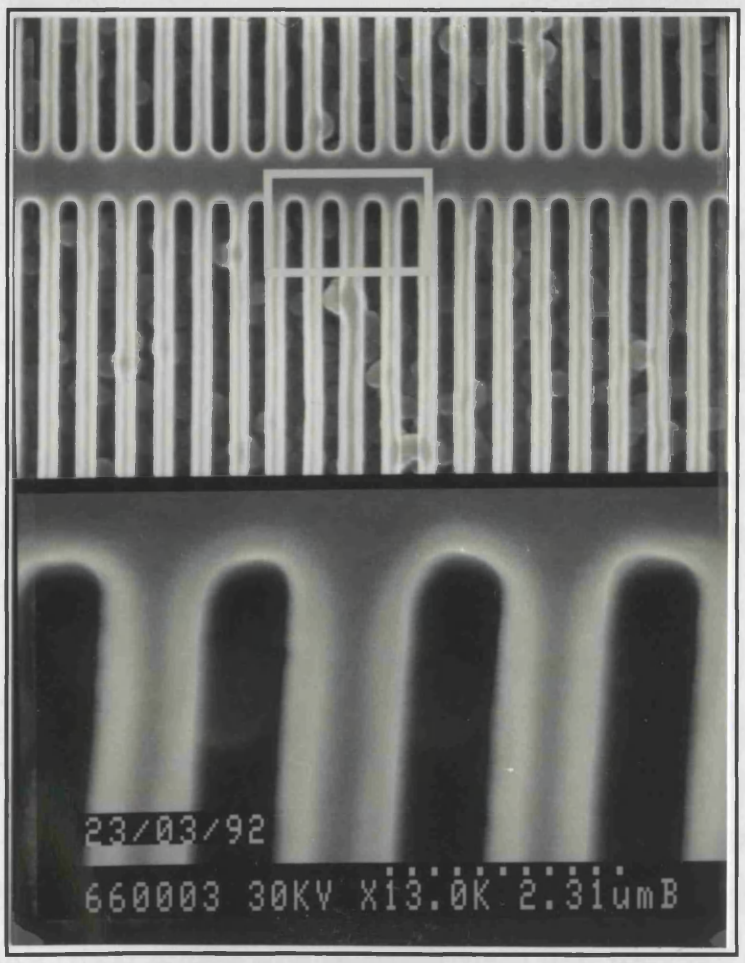

Fig.5.12: Exposure test for quarter-wavelength shift:60nm.

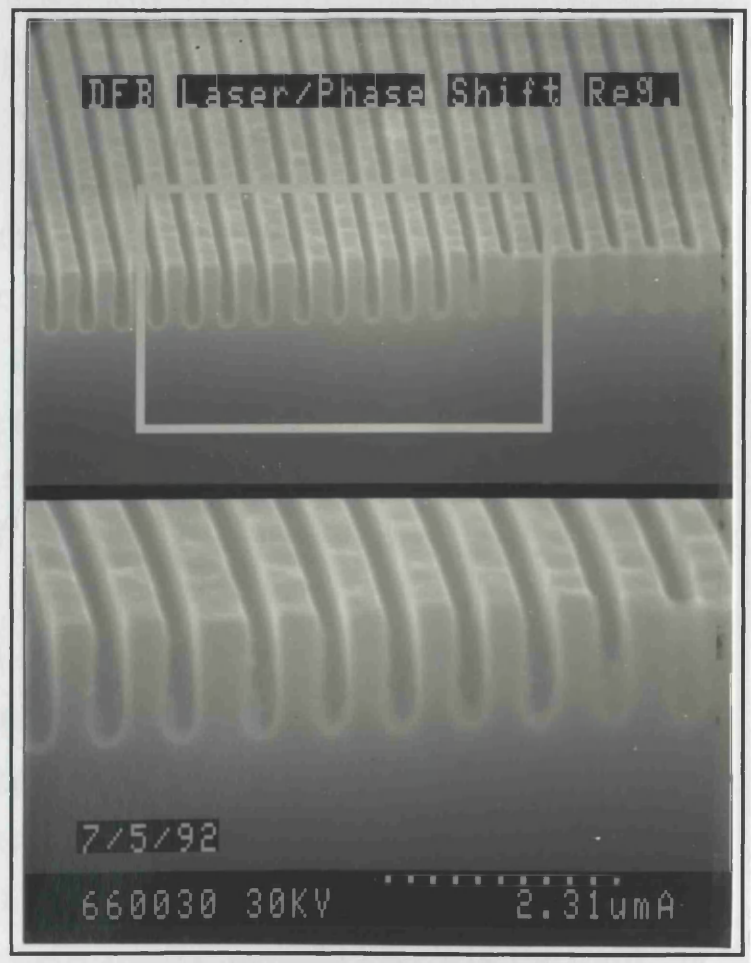

Fig.5.13: Dry-etched grating with λ/4 shift

Dual pitch Gratings

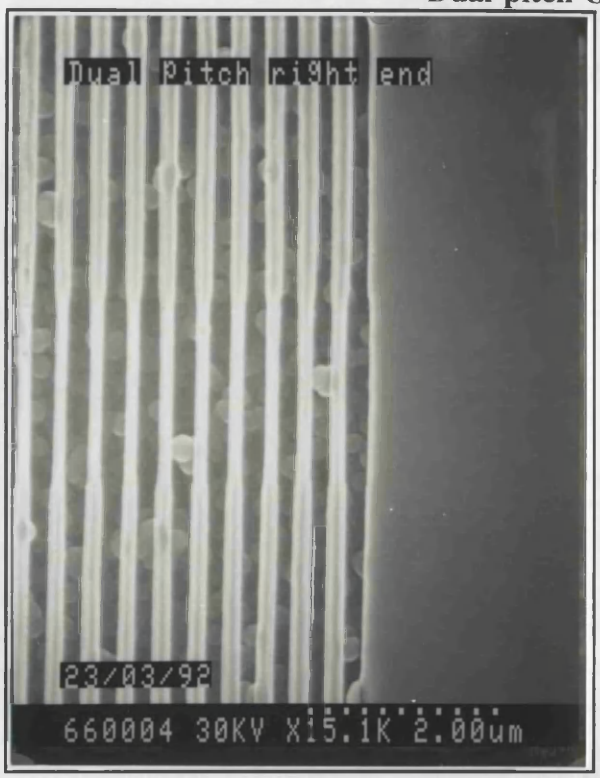

Fig. 5.14: Exposure test of dual-pitch grating; details of overlapping region located on the right end.

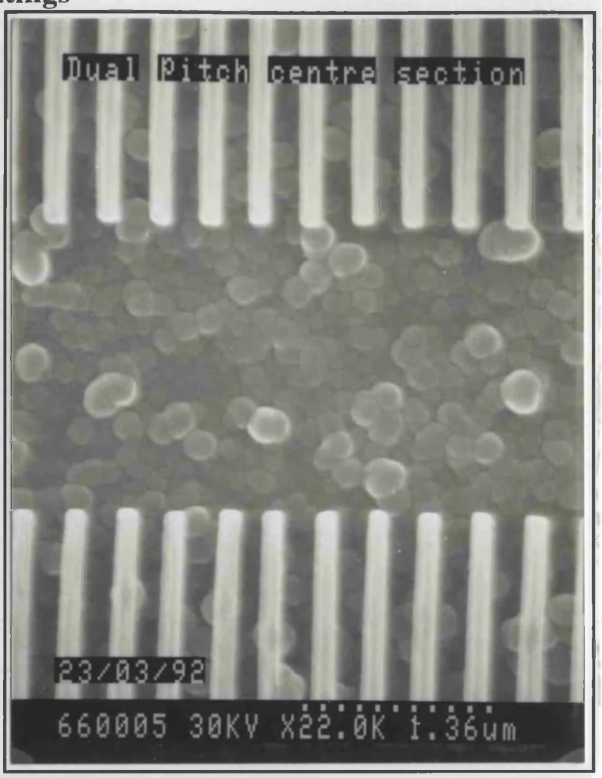

Fig. 5.15: Exposure test of dual-pitch grating; overlapping region in the middle

The λ/4 shift consists of a slight increase in the width of one tooth of the grating. For GaAs and operation at 860nm, the λ/4 shift corresponds to an increase in the tooth width of 60 nm. Fig. 5.12 shows the exposure test of two gratings: a normal grating and a grating with λ/4 shift, side by side. It can be seen that the gratings are in phase in the left-hand side of the photo and partially out of phase on the right hand side, that is, after the λ/4 shift. Fig. 5.13 shows the cross section of a dry-etched grating with a λ/4 phase shift. Note that one tooth in Fig. 5.13 is thicker by 60 nm than the others.

The structure shown in Figs. 5.14 and 5.15 consists of two gratings with different pitches. The pitch difference was chosen such that the gratings are in-phase at both ends, but they are completely out of phase in the middle. The exposure of this structure requires the use of two files, each one of them with a different resolution. Figs. 5.14 and 5.15 show the gratings described above in a position such that they are partially overlapping. In Fig. 5.14 the right end of the grating is shown, which is overexposed in the central region because the exposure dose at the overlapping region is twice as much as the exposure dose of a single grating. Another point is that the gratings are in phase, which means that drift does not occur between the writing of the two files. Fig. 5.15 shows the central region of the structure. Note that all the e-beam resist was removed in the overlapping region because the gratings are completely out of phase and, therefore, all this region was exposed.

5.9 Fabrication of a flared amplifier integrated with DFB lasers

An outline of the fabrication of flared amplifiers integrated with surface grating DFB lasers is now given. The characteristic parameters of the structure are given in Fig.5.16

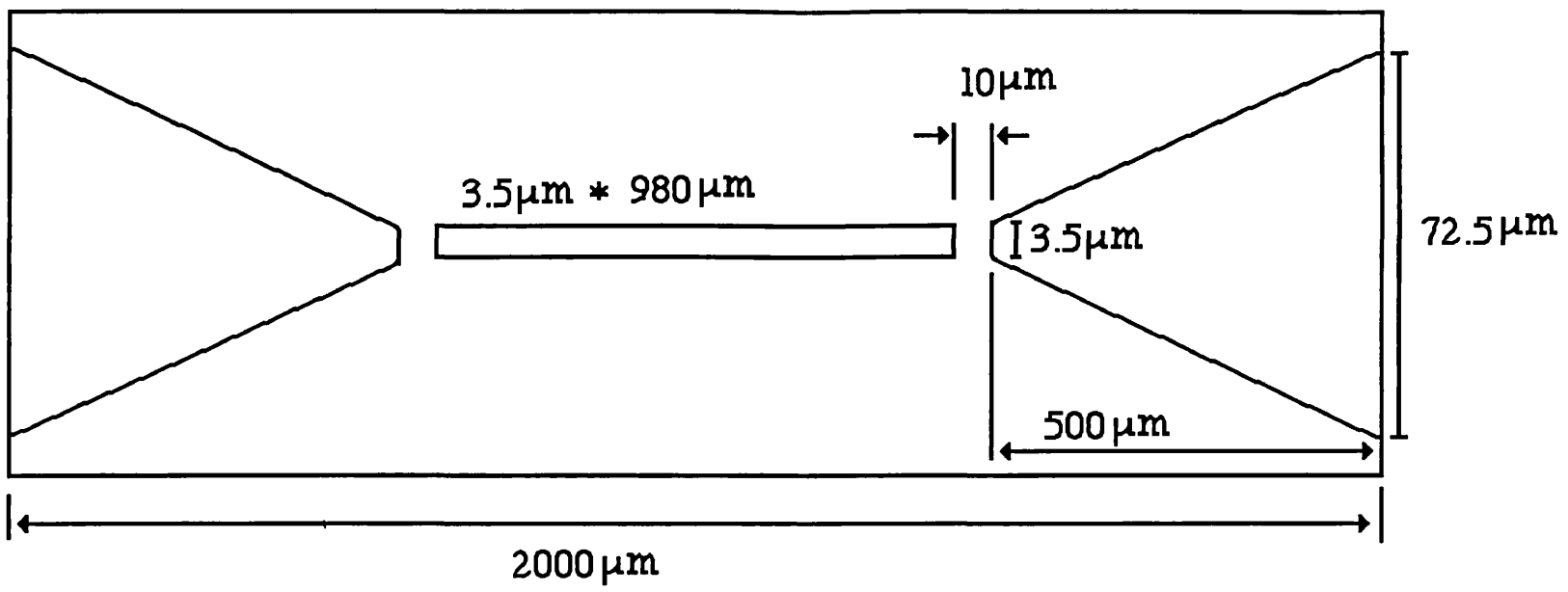

Fig.5.16: Schematic diagram of integrated flared amplifier with DFB laser

A. Fabrication of the surface grating DFB laser

1. Deposition of a SiO_2 layer (1500A)

2. Spin coating of the sample with two layers of e-beam resist: 8%BDH; 4%ELV.

3. Exposure in the Beam Writer

4. Development: Developer 2.5:1 (IPA:MiBK) for 30 s at a temperature of 23 °C.

5. Dry etching of SiO_2 with C_2F_6, using e-beam resist as a dry etching mask, for 4 minutes.

6. Removal of e-beam resist with acetone and dry etching of sample with $SiCl_4$. The SiO_2 layer is used as a dry etching mask.

B. Reverse lithography of sample so as to remove the GaAs p^{++} contact layer everywhere except on the contact stripe of the DFB lasers and amplifier regions.

1. Spin coating of the sample with photoresist AZ5214E at 4000 rpm for 20 s.

2. Pre-baking of the coated sample at 90°C for 5 minutes.

3. Exposure in mask aligner for 6 s.

4. Reverse bake at 115 °C for 15 minutes.

5. Flood exposure for 20 s (exposure of sample without mask in mask aligner).

6. Development: developer MF312: H_2O (1:1) solution for 60 s.

7. Wet etching of GaAs p^{++} contact layer. The sample was wet etched in NH_4OH:H_2O_2 (1:20) solution for 6 s.

Fig. 5.17:Sample after wet etching of GaAs p^{++} contact layer.

Fig. 5.18:Details of the same sample.

C. Open contact window

1. Deposition of a SiO_2 layer (2000A).

2. Clean sample in ultrasonic bath

3. Spin coating of the sample with photoresist S1400-31

4. Baking of sample for 30 minutes at 90 °C.

5. Exposure in mask aligner for 11 s.

6. Development: S1400-31 developer +H_2O (1:1) solution for 75 s.

7. Post-baking of sample for 10 minutes at 120 °C.

8. Wet etching of contact window with HF for 30 s.

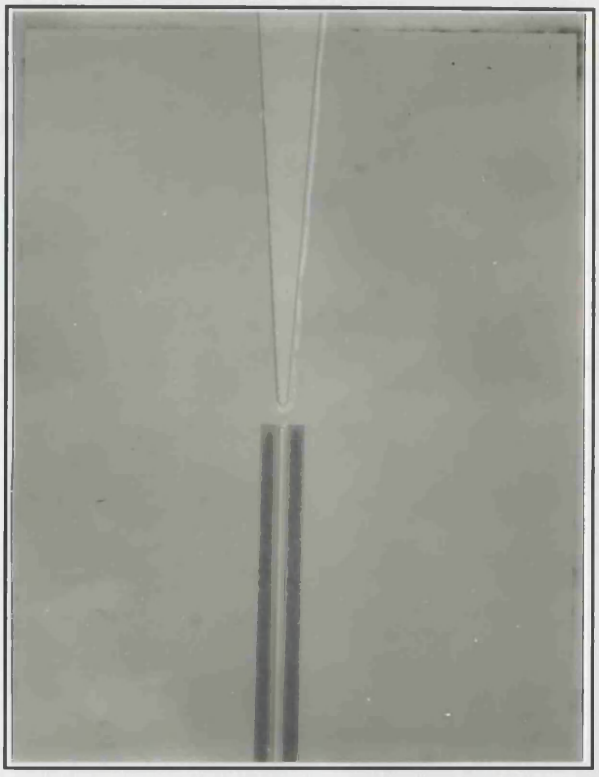

Fig. 5.19: Sample after wet etching of contact window

D. Lithography of sample before p-type contact deposition for isolation of amplifier and DFB laser sections

1. Spin coating of the sample with S1400-31 photoresist for 30 s at 4000 rpm.

2. Baking of sample for 30 minutes at 90 °C.

3. Exposure in mask aligner for 11 s.

4. Development: S1400-31 developer + H_2O (1:1) solution for 75 s.

5. Glueing of sample on glass slide with photoresist.

6. Just before loading sample in evaporator, wet etching of sample on HCl:H_2O solution for 30 s.

7. p-type evaporation:

a) Degas metals before evaporation.

b) Evaporation according recipe

Metal/	Thickness
Ni	70 nm
Au	200 nm

8. Lift-off sample in acetone

9. Thinning of GaAs substrate with Al_2O_3

10. Clean sample in reflux

a) Trichloroethylene for 30 minutes

b) Methanol for 5 minutes

c) Acetone for 5 minutes

11. Wet etching GaAs substrate with H_2SO_4:H_2O_2:H_2O (1:8:1) solution for 60s.

12. Clean sample according step 10.

13. n-type deposition:

a) Just before loading of the sample in to the evaporator, wet etching sample in NH_4OH: H_2O (1:2) solution for 60 s. This procedure is used to remove the oxide layer formed during baking (sample was glued on glass slide with photoresist and baked for 30min.).

b) Degas metals before evaporation.

c) Evaporation according to recipe

Metal /	Thickness
Au	13 nm
Ge	13 nm
Au	13 nm
Ni	11 nm
Au	240 nm

14. Cleaving devices at suitable sizes

5.10 Stitching Errors

5.10.1 Origin and Characteristics of Stitching Errors

Electron beam lithography systems have a limited area of exposure (writing-field), so field stitching has to be used in order to pattern larger areas. Writing-fields are then exposed side by side, and the stage with the wafer mounted on it is moved between each field exposure. This procedure can give rise to small overlaps or gaps between consecutive writing-fields, called stitching errors. There are two kinds of stitching errors [5.5]: systematic stitching errors that are equal for every writing field; and stochastic stitching errors that vary from border to border. The systematic errors are caused by imperfect calibration of the writing-field size and/or rotation, as shown in Figs. 5.16 (a) and (b), respectively. For example, too large beam deflection amplitude in the deflection coils yields too large a writing-field and, hence, overlap of the exposed fields. The position of the stage with the wafer holder is continuously measured by a laser beam interferometer, and the deviation from the desired position is fed back to the deflection coils, which shift the writing-field to the correct position. Due to the limited resolution of the interferometer and the quantized beam deflection, the exposed fields will be slightly shifted relative to each other, as shown in Fig. 5.16(c). This is one contribution to the stochastic stitching error. Another contribution,

shown in Fig. 5.16(d), is caused by yaw or rotation of the stage as it is moved between field exposures.

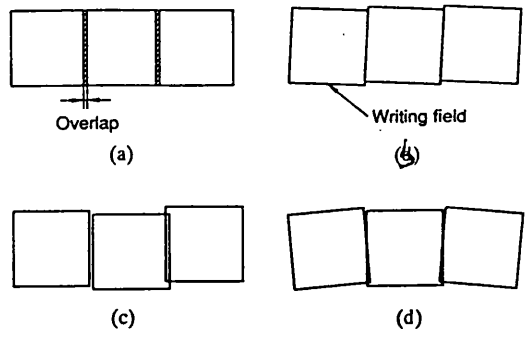

Fig.5.20: Different types of stitching errors caused by: (a) incorrect deflection amplitude (systematic), (b) incorrect writing-field rotation (systematic), (c) limited laser beam interferometer resolution (stochastic), (d) stage rotation (stochastic) [5.5].

5.10.2 Stitching Errors Measurement

Stitching errors were measured in two different electron beam writing condition: (i) Resolution=20nm, Spotsize=80nm and; Resolution=5nm, Spotsize=12nm. Stitching errors were measured by exposing a resist-coated wafer with a vernier pattern, as shown in Fig. 5.21. The Beam Writer settings were resolution of 20 nm, which gives writing fields of 640×640 μm^2, and spotsize of 80 nm.

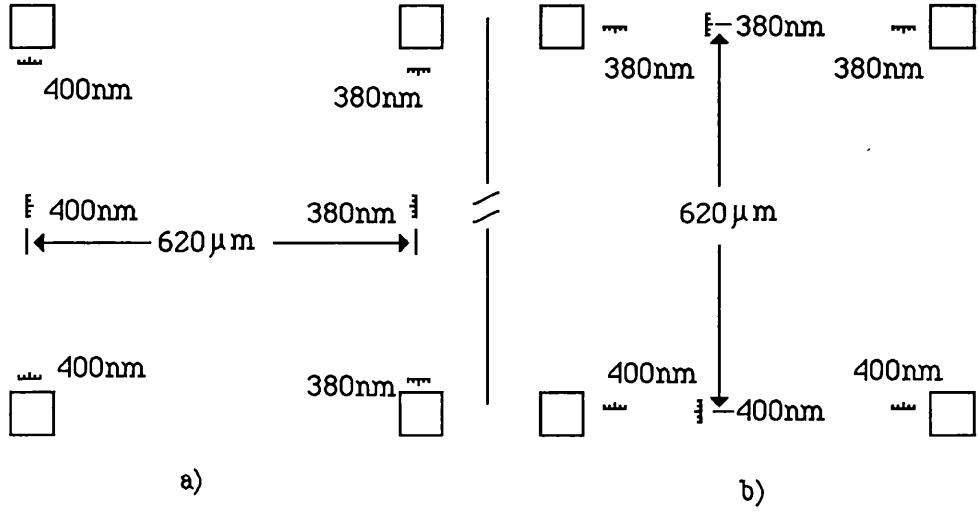

Fig.5.21: Exposed vernier patterns for stitching error measurement on a 640 µm writing-field. (a) Verniers to measure stitching errors in the X-direction; (b) Verniers to measure stitching errors in the Y-direction.

In Fig. 5.21 (a) the left gratings in the pattern have a periodicity of 400 nm and the right ones 380 nm. The distance between the center lines of the gratings is, in this case, 620 µm, as this pattern is used to measure stitching errors for 640 µm writing-fields. The stage is moved 620 µm between pattern exposures, and hence, sucessive patterns overlap by 20 µm at each border. A large number of such patterns are sequentially exposed.

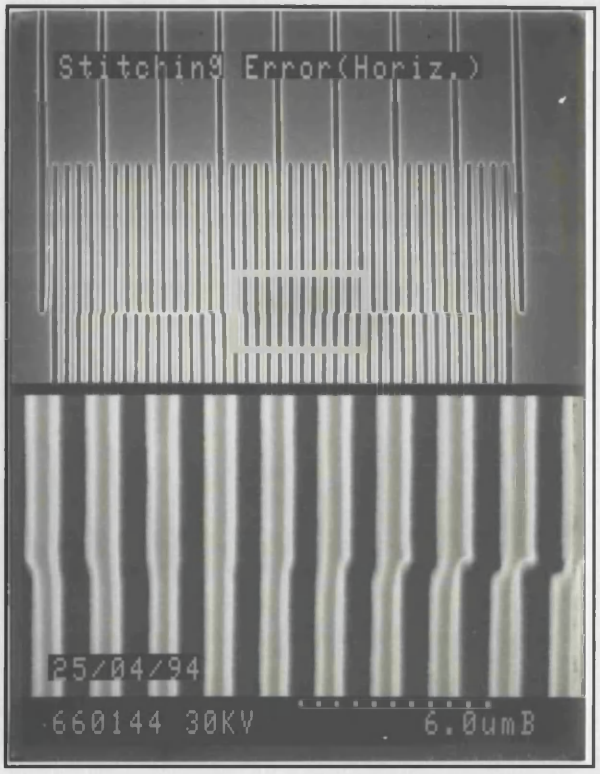

Fig.5.22 Fig.5.23

SEM micrographs of resulting vernier pattern after development. Each line corresponds to a 20 nm stitching error. Fig.5.22 shows a negligible stitching error; however, Fig.5.23 presents a stitching error of about 40 nm.

In Fig. 5.22 the vernier scales in the horizontal direction (the X-direction) are shown . The stitching error in the X direction seems to be negligible (<< 20 nm); so ΔX_1=0 nm and ΔX_2=0 nm. Fig. 5.23 shows the vernier scales in the vertical direction (the Y-direction) and the stitching error is about 40 nm. The values of ΔY_1=40 nm and ΔY_2=-40 nm (the positive signal is indicated in Fig. 5.24 below).

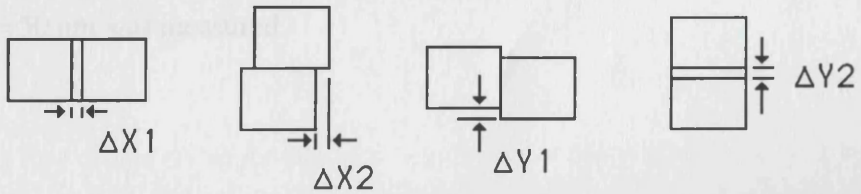

Fig.5.24: Illustration of different stitching errors measured with vernier patterns shown in Fig.5.21.

The stitching errors for different Beam Writer settings were also measured. The Beam Writer settings were: resolution of 5 nm and spotsize of 12 nm. This Beam Writer mode was used to expose very small structures, such as first-order gratings in GaAs, which imply a period of 130 nm.

Fig.5.25

Fig.5.26

SEM micrographs of resulting vernier pattern for Beam Writer settings: resolution of 5 nm and spotsize of 12 nm. Each line corresponds to a stitching error of 5 nm. Fig.5.25 shows a stitching error of about 15 nm and Fig.5.26 implies a stitching error of 50 nm.

To measure the stitching errors for new Beam Writer settings, a vernier pattern similar to Fig.5.21 was used, but in this case the writing field was 160×160 μm^2 and the gratings had periods of 395 nm and 400 nm. Therefore, a minimum stitching error of 5 nm was measurable. Fig. 5.25 shows a vernier pattern in the X-direction; the stitching error is about ΔX_1=-15nm (gaps in X the direction). Fig.5.26 shows verniers in the Y direction; a stitching error of ΔY_1=50 nm was measured.

Fig.5.27

Fig.5.28

Vernier patterns to measure stitching errors ΔX_2 and ΔY_2, respectively Fig.5.27 and Fig.5.28.

In Fig.5.27 the maximum stitching error of ΔX_2=-100 nm is shown. Fig. 5.28 shows a stitching error of ΔY_2=100 nm (overlap of writing fields). These results can be explained by the fact that the sample has drifted 33 nm in the X-direction and 140 nm in the Y-direction during exposure. In practice, the samples were left clamped in the beam writer holder for at least 2 hours before exposure. This proceeding has reduced the stitching errors to values of the order of Δx=15nm, in the writing direction, which is the only direction of interest since all the lasers are aligned along x.

5.11 Fabrication of electrical contacts

Three factors are important in the metallization of the wafer. Firstly, the metal should adhere adequately, secondly it should provide a low resistance electrical contact, and thirdly it should not introduce excessive strain into the laser chip. Strain has a deleterious effect on laser life[5.6].

During the processing steps, an oxide layer, which acts as an insulator, grows on top of the semiconductor. To remove this layer and prepare the semiconductor surface for contact metallization, various processes can be employed. For instance, bombardment with low energy Ar^+ ions has been carried out prior to the metal deposition [5.7]. In this fabrication

process, wet etching was employed in a 1:2 solution of NH_4OH and RO water for 60 seconds.

The resistivity depends approximately exponentially on the height of the potential barrier between the metal and the appropriate band of the semiconductor, and also depends on the doping concentration, decreasing fairly rapidly as the doping concentration is increased [5.8]. When the barrier height is low, good contact can be obtained relatively easily by locally increasing the doping concentration and using a simple evaporated metallic layer. This applies to p-type contacts in GaAs where a p-doping concentration of greater than 3×10^{18} cm^{-3} may be used in conjunction with a well adhering metal [5.9]. The standard p-type contacts are as follows:

(1) Ti/Au (Schottky contact)

(2) Au/Zn/Au with annealing (Ohmic contact)[5.10]

(3) Ti/Pt/Au with annealing (Ohmic contact)[5.7],[5.11]

(4) Ni or Cr/Au (Ohmic contact)[5.12]

In the present work, the p-type contact adopted was Ni(70 nm)/Au(200 nm). When the barrier is large, as in n-type GaAs, some form of alloying is necessary and Au/Ge/Ni/Au contacts with annealing have been used [5.12]. In the present work, an ohmic contact consisting of Au(13 nm)/Ge(13 nm)/Au(13 nm/Ni(11 nm)/Au(240 nm) was used, with annealing at 400 °C for 1 minute.

5.12 Deposition of anti-reflection (AR) Coatings

To prevent the Fabry-Perot mode oscillation, AR coatings consisting of a layer of Al_2O_3 were deposited on both facets (silicon nitride could be used as well[5.13]). The film thickness d satisfying the minimum reflectivity is given by:

$$d = \frac{(2m-1)\lambda}{4n}$$

where m is a positive integer, λ is the lasing wavelength and n is the refractive index of the film. In this fabrication process, a single monolayer of sputtered Al_2O_3 was used. The refractive index of sputtered Al_2O_3 was about 1.85 and the target value of the thickness was about 116 nm. The expected reflection coefficient of an Ar coated facet is probably few per cent.

5.13 Mounting and wire-bonding

Mounting of the laser chip is a process that needs special care in order to avoid stress between the laser and the heat-sink. In general, indium solder can be relied upon to yield, before excessive stresses arise. So indium solder was used for mounting of the laser chips on gold-plated steel heat-sinks. Normally, the laser chips were mounted p-side down. Wire-bonding to the n-type contacts was performed using 25 μm diameter gold wire and an ultrasonic wire bonder. A photograph of the wire-bonded laser chip is shown in Fig.5.29.

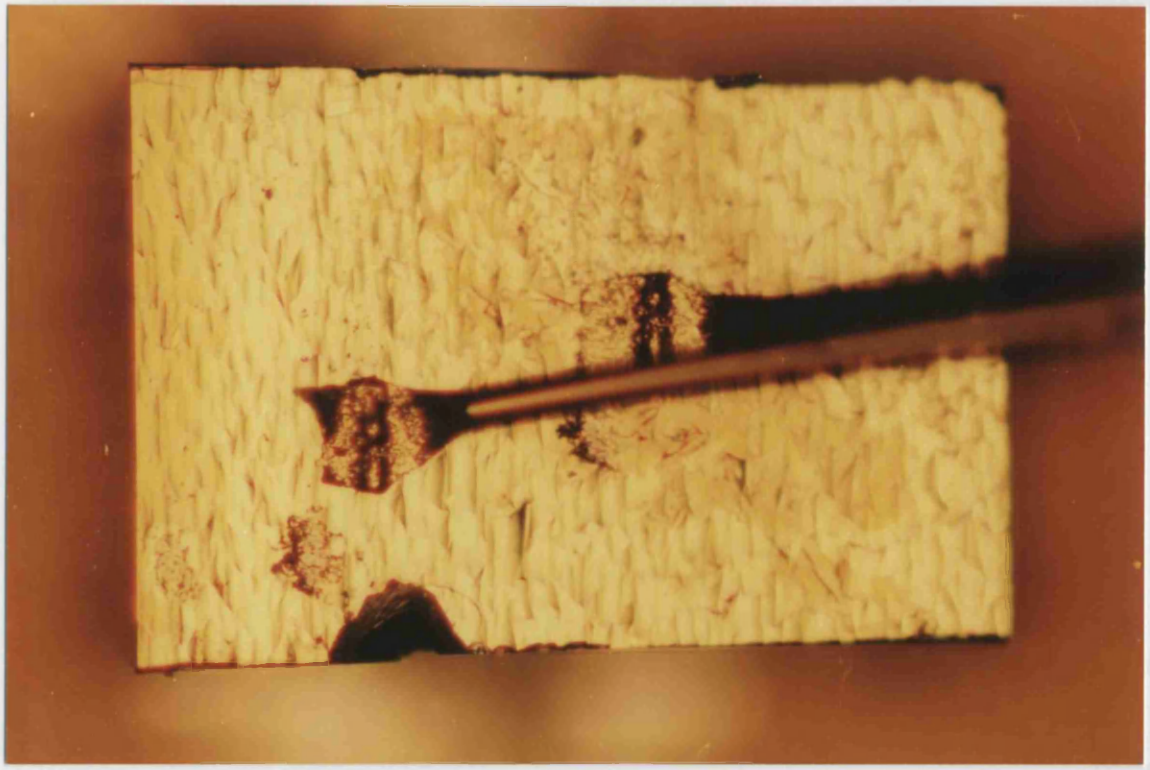

Fig.5.29: Photograph of wire-bonded laser chip

References

[5.1] S. Thoms, "Notes on electron beam lithography", Internal Report

[5.2] G.F.Doughty, "Dry etching of polymers, silica, glass and lithium niobate", Integrated Optical Technologies, pp.49-52 (1988)

[5.3] S. Semura, Japanese Journal of Applied Physics, Vol.24, pp.463 (1985)

[5.4] S. Thoms, "Ultra small device fabrication using dry-etching of GaAs", Microelectronics Engineering, Vol.5, pp.249-256 (1986)

[5.5] Torgil Kjellberg and Richard Schartz, "The effect of stitching errors on the spectral characteristics of DFB lasers fabricated using electron beam lithography", Journal of Lightwave Technology, Vol.10,pp.1256-1266 (1992)

[5.6] G.H.B.Thompson, *Physics of semiconductor laser devices*, John Wiley and Sons.,pp.25-29 (1980).

[5.7] G.Stareev, "Formation of extremely low resistance Ti/Pt/Au ohmic contacts to p-GaAs", Applied Physics Letters, pp.2801-2803 (1993).

[5.8] C.Y.Chang, "Specific contact resistance of metal-semiconductor barriers", Solid State Electronics, Vol.14, pp.541 (1971).

[5.9] G.H.B.Thompson, *Physics of semiconductor laser devices*, John Wiley and Sons.,pp.23-24 (1980).

[5.10] K.L.Klohn, Journal of Electrochem. Soc., Vol.116, pp. 507 (1969).

[5.11] N.Braslan, Journal of Vacuum Science Technology, Vol.19, pp.803 (1981).

[5.12] T.Krauss, P.J.R.Laybourn and J.Roberts, "CW Operation of semiconductor ring lasers", Electronics Letters, Vol.26, pp.2094-2096 (1990).

[5.13] M. Serenyi and H.U. Habermeier, "Directely controlled deposition of antireflection coatings for semiconductor lasers", Applied Optics, pp.845-849 (1987).

Chapter 6: Experimental Results and Discussion.

6.1 Introduction

In this chapter, the measurement methods employed, the experimental results obtained and their interpretation are discussed. The measurement of the coupling coefficient in surface grating DFB waveguides is performed using a transmission technique, described in detail in section 6.2. It consists of coupling light from a Ti-sapphire laser into the devices and measuring the light transmitted as a function of the wavelength. From these measurements, the transmission spectrum is obtained in which a dip reflection pattern is observed at the characteristic Bragg wavelength. The coupling coefficient can then be calculated using the diffraction efficiency estimated from the transmission spectrum. In section 6.3, the methods for measurement of the laser characteristics are discussed, namely the injection current-voltage (I-V) curve, the light output power-injection current (L-I) curve, the laser spectrum as a function of both operation temperature and injection current, and the far-field pattern. Comparative studies of the light output power-injection current as well as the laser spectral behaviour for surface 3^{rd}-order, 2^{nd}-order and 1^{st}-order grating DFB lasers, in pulsed and CW operation are discussed, respectively in sections 6.5 and 6.6. In section 6.7, an ageing experiment is carried out using a 900 μm long surface 3^{rd}-order grating DFB laser, aiming at assessing the electrical contacts and bonding. Finally, in section 6.8, the L-I and spectral characteristics of a monolithically integrated flared amplifier surface grating DFB laser are discussed.

6.2 Measurement of the coupling coefficient in surface grating DFB waveguides

In Fig.6.1, the basic set-up used to measure the light transmitted through the devices is represented schematically. The beam from a Ti-sapphire laser is coupled in and out of the devices with microscope objectives. The light is then spatially filtered with the pinhole and detected by the Si detector. The electric signal is amplified by the lock-in amplifier and the output is plotted. The input light is measured by the power meter and, when necessary, a slight adjustment in the current of the Ar laser is made in order to keep the input power constant. The wavelength of the Ti-sapphire laser is scanned with a motor, which rotates the birefringent filter of the Ti-sapphire laser cavity. As a final result, the transmitted light power through the device versus wavelength is obtained for each device, as characterized by a given grating spatial period (Λ_g), stripe width (W), etch depth (T) and length (L).

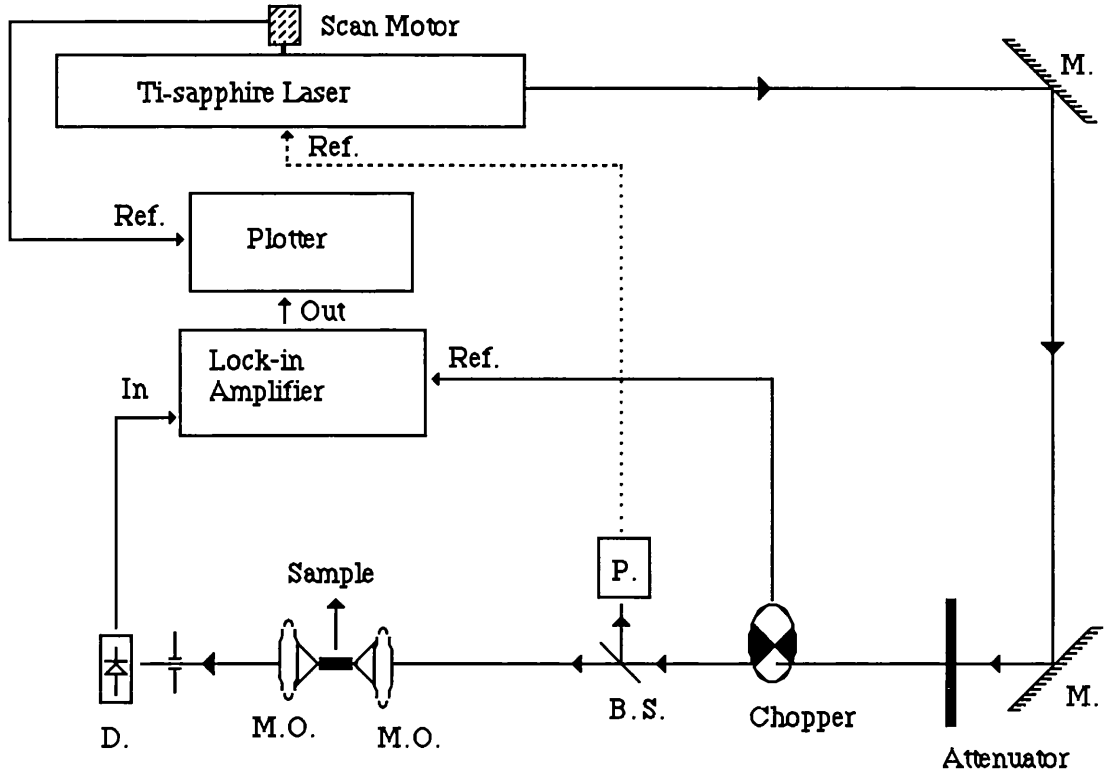

Fig.6.1: Schematic diagram of the set-up used to measure the coupling coefficient in deep surface DFB waveguides. Symbology: M.-Mirror, B.S.- Beam Spliter, P.-Power meter, M.O.-Microscope objective, and D.- Si Detector.

In order to design the deep surface lateral grating structures optimally, an accurate knowledge of the fundamental parameters is required. In particular, evaluation of the coupling coefficient κ is important, since it determines the feedback efficiency of the gratings. Conventionally, the coupling coefficient in DFB laser devices has been calculated experimentally by measuring the stopband width at or below the threshold current for lasing [6.1, 6.2]. However, in the weak coupling range ($\kappa L<2.0$, where L is the cavity length), which is the typical case for the deep surface lateral grating structures investigated in this thesis and other similar structures [6.3], this method tends to introduce large errors into the calculated value of κ because κL is extremely sensitive to small variations in the stopband width, $\Delta\lambda_S$. For example, when the stopband width is enhanced by only 10%, the corresponding increase in κL is from 1.0 to 1.5 (50% in κ for L=500μm). To overcome this problem we have attempted to measure κ more accurately using a transmission technique, instead of using measurements of the stopband width in laser operation. A systematic study of the dependence of the coupling coefficient on the design parameters of the structure is reported, including the etch depth and stripe width of the deep surface grating structures.

For the measurement of the coupling coefficient in surface grating DFB waveguides, only one type of material structure was used. It was the wafer #QT270 described in detail previously in chapter 4.

Fig. 6.2 shows typical transmission spectra for surface grating DFB waveguides. Spectrum a) is from a surface grating DFB waveguide characterised by a 390 nm grating period, 3 μm stripe width and 1 μm grating etch depth, whereas spectrum b) is from a surface grating DFB waveguide with a larger grating period of 395nm, 3μm stripe width and shallower gratings with 0.64μm etch depth. In spectrum a), a double dip reflection pattern is observed, which is caused by back reflection at the Bragg wavelength for the fundamental and second transverse modes, respectively at 875.3nm and 871.6nm. This result is typical for gratings with etch depths of 1 μm and 0.75 μm (the cut-off etch depth for the second transverse mode is about 0.7μm for the material structure used). As expected, for gratings with an etch depth of 0.64 μm, only the back reflection corresponding to the fundamental transverse mode is observed (Spectrum b). Surface grating DFB waveguides with 1 μm and 0.75 μm grating depths show a stronger reflection strength for the second transverse mode because the field distribution of this mode enhances the strength of the interaction with the gratings.

Finally, it should be pointed out that the linewidth measured from the reflection dip (Fig.6.2) agrees with the value calculated from the theoretical curve illustrated in Fig.3.4.

For calculating the coupling coefficient κ from the transmission spectra, it was assumed that the transmission is unit for longer wavelength (larger than 880nm in spectrum a) and 875 nm in spectrum b)). Then, by measuring the transmission dip depth is possible to calculate the reflectance associated to the Bragg scattering at a certain transverse mode. The last step to compute the coupling coefficient is by using the following Eq.(6.2.1), which relates the reflectance to the coupling coefficient, and grating length.

$$R_{\max.} = Tanh^2(\kappa L) \qquad (6.2.1)$$

Measuring the reflectance R, from the transmission spectrum, and knowing the length of the device L, the coupling coefficient κ can then be calculated. These calculated results are plotted in Figs. 6.3, 6.4 and 6.5.

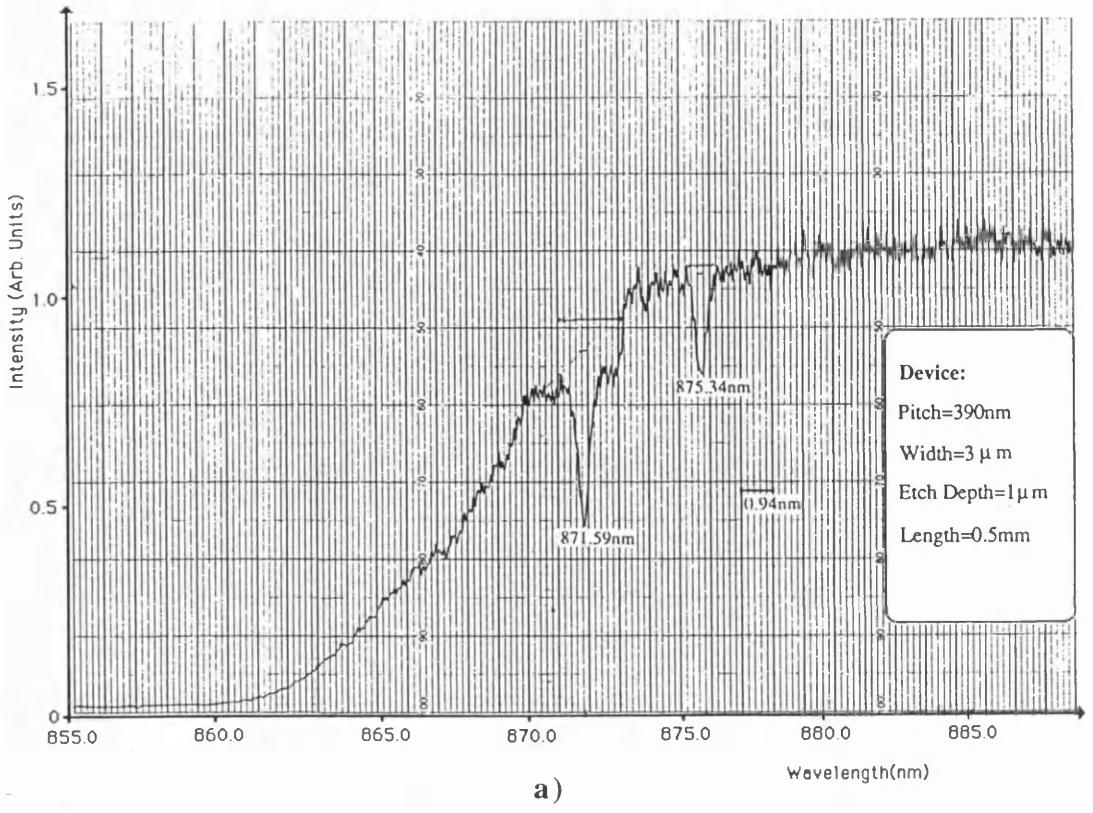

a)

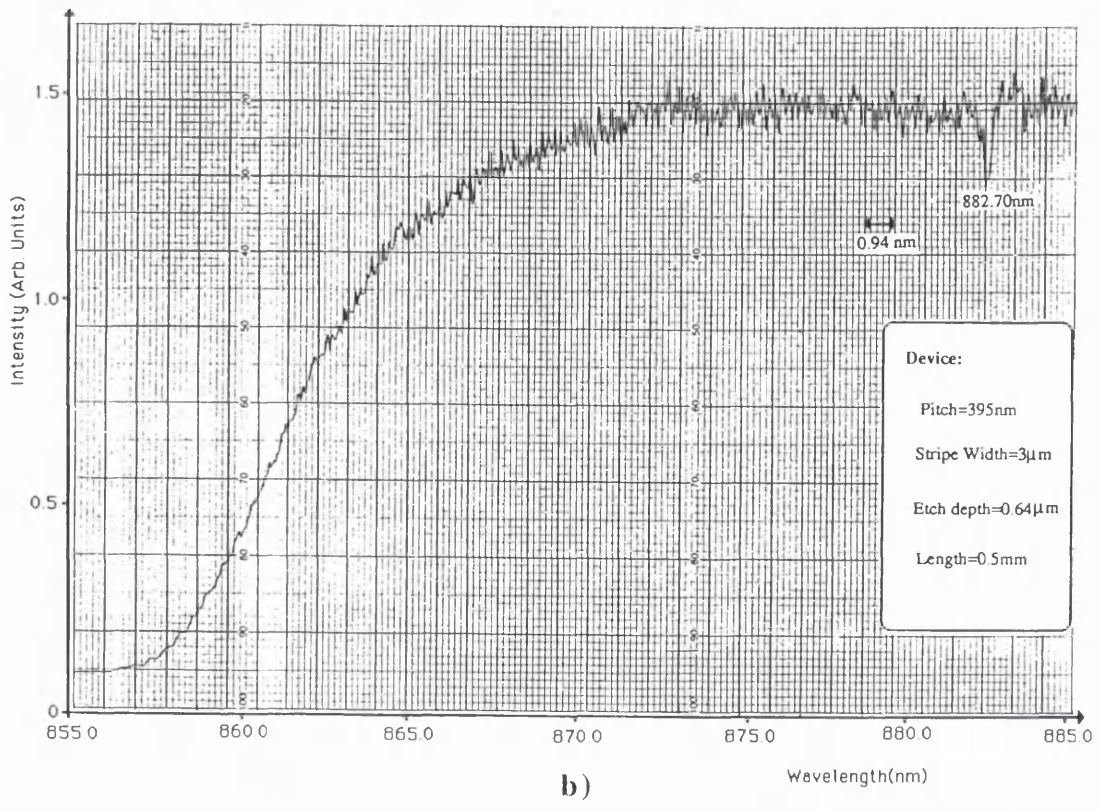

b)

Fig. 6.2: Typical transmission spectra of surface grating DFB waveguides

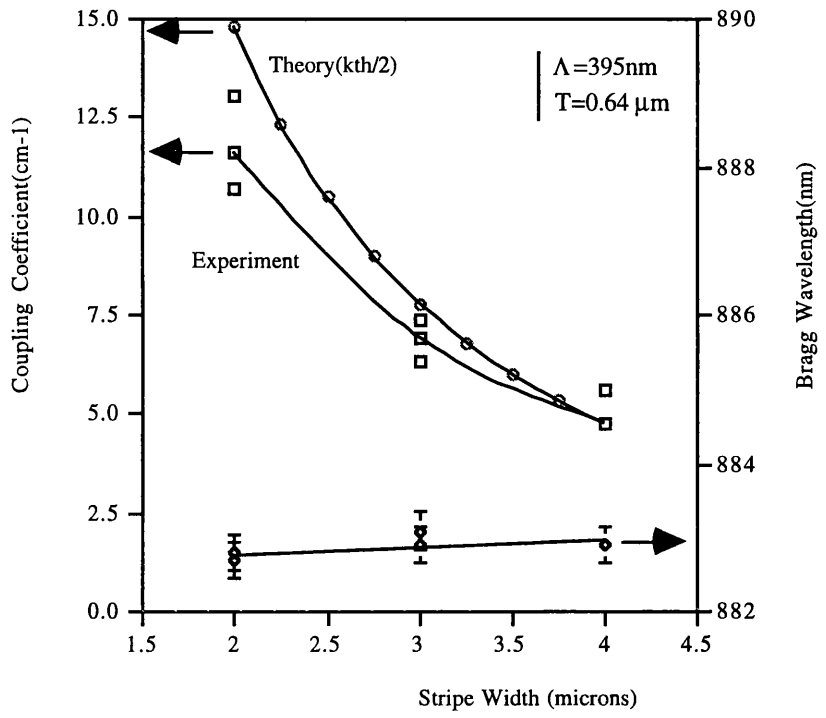

Fig. 6.3: Dependence of the coupling coefficient and Bragg wavelength on the stripe width. Results from devices with 395nm grating period and 0.64μm grating etch depth.

Fig.6.3 shows experimental and theoretical results for the coupling coefficient and the Bragg wavelength dependence on the stripe width in the range from 2μm to 4μm. The experimental results were measured on devices with a 395nm grating period and a constant etch depth of 0.64μm, i.e. the coupling coefficient and Bragg wavelength measured are for the fundamental transverse mode. The experimental coupling coefficient clearly decreases with increasing stripe width, which is in agreement with the theoretical predictions and is consistent with the weaker interaction between the light and the gratings as the stripe width increases. The approximate factor of 2 discrepancy between the theoretical and the experimental curves may possibly be due to the inherent limitations of the theoretical model. In fact, the theoretical model does not take into account the mode distribution, the losses, and also the fact that it is only the upper half of the guided mode distribution that interacts very strongly with the deep grating structure. Note also that for small stripe widths (2μm) the discrepancy between theory ($\kappa_{th}/2$) and experiment increases. This discrepancy is possibly related to the effect of the mode field distribution on the interaction between the guided mode and the gratings, as the stripe width decreases. In fact, as seen in the inset of Fig.3.21, decreasing the stripe width below a certain value leads to an increasing amount of the guided light in the lower cladding layer, consequently reducing the interaction with the gratings. The Bragg wavelength apparently increases with the stripe width. This result is in agreement with the Bragg

condition, which states that the Bragg wavelength depends not only on the refractive index periodicity along the cavity, but also on the waveguide effective refractive index defined by the stripe width and grating etch depth. Theoretical calculations have shown that the expected increase in the Bragg wavelength would be just 0.5nm if the stripe width were increased from 2μm to 4μm, which is close to the magnitude of the measured increase plotted in Fig.6.3.

The approximated factor of 2 discrepancy observed in Fig.6.3, between theory and experiment, would be certainly reduced if radiation loss were included. In fact, the effect of radiation loss at the resonant wavelength is to decrease the relative magnitude of the reflection dip depth, reducing consequently the experimentally-measured coupling coefficient.

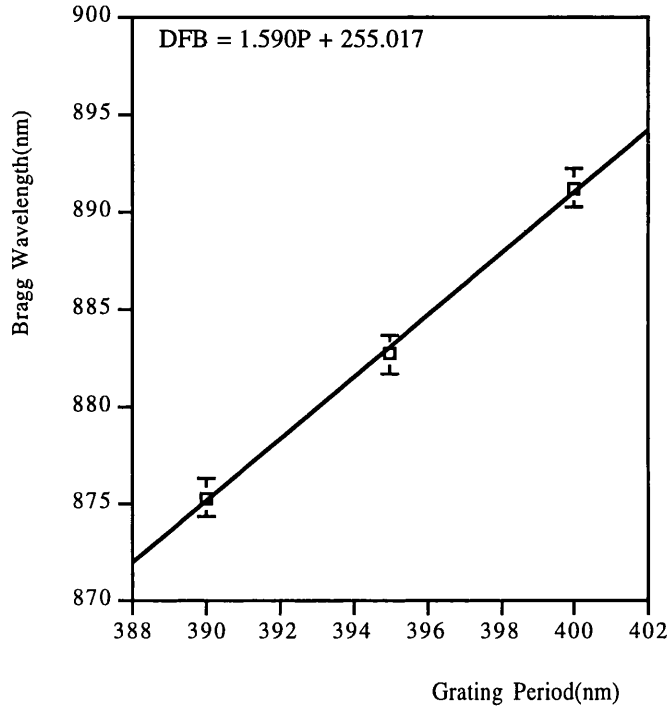

Fig. 6.4: Dependence of the Bragg wavelength on the designed grating period.

Fig.6.4 shows the experimental Bragg wavelength dependence on the grating period in the range studied, i.e. 390-400 nm. The Bragg wavelength is mainly determined by the grating period, as is shown by the very nearly linear dependence of the measured Bragg wavelength on the designed grating period. The effective index of refraction calculated by the Bragg equation is larger at Λ=390 nm (n_{eff}=3.3667) than at Λ=400 nm (n_{eff}=3.3423), which can be explained by the dispersion of the material and of the waveguide. A similar result has been measured in lasing devices [6.4].

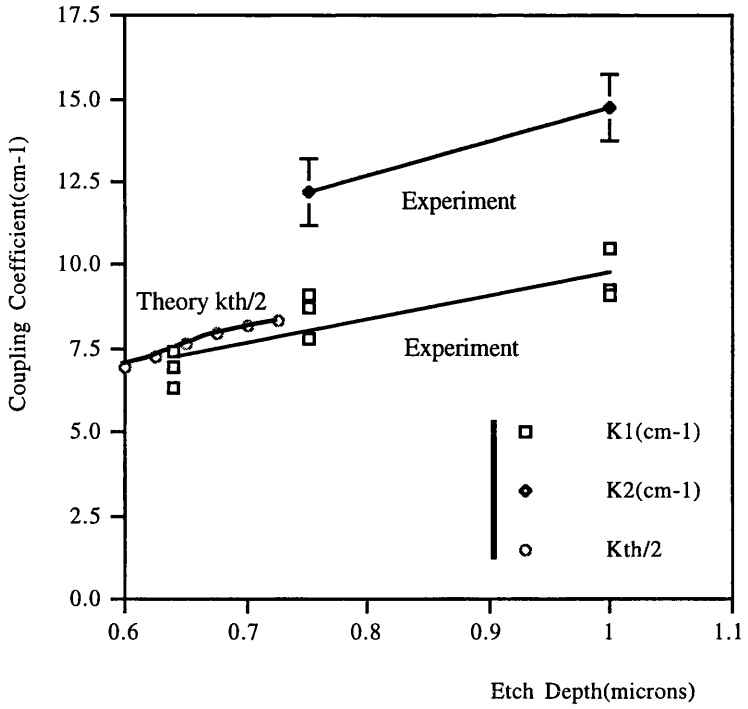

Fig.6.5: Dependence of the experimental and theoretical coupling coefficient on the grating etch depth.

Fig.6.5 shows the theoretical (only for the fundamental mode) and experimental (for both fundamental and second transverse modes) results of the coupling coefficient as a function of the grating etch depth. For etch depths less than 0.64 μm, only the fundamental mode is coupled into the waveguide and a factor of 2 agreement is obtained between theory ($\kappa_{th}/2$) and experiment. However, for devices with deeper gratings (>0.7 μm), the second transversal mode is coupled and presents a larger coupling coefficient ($\kappa_{TE1}(k_2)=1.4\kappa_{TE0}(k_1)$). In the etch depth range studied (0.64-1 μm), the value of κ of the fundamental and second transversal modes increases by 30% and 20%, respectively. For practical grating etch depths (< 0.7 μm), where only the fundamental mode is guided, the value of κ measured is $<10cm^{-1}$. This result is in reasonable agreement with previous theoretical predictions [6.5] (not the theoretical model described above) and with other experimental data [6.3].

In summary, a transmission technique was successfully used to measure the transmission spectra of DFB waveguides. From these results, the coupling coefficient was calculated as a function of both stripe width and grating etch depth. It was shown that the coupling coefficient decreases significantly with the stripe width. For deep gratings, the second transverse mode may also be coupled and presents a stronger coupling effect than the fundamental mode. Maximum coupling coefficient values of 10 cm^{-1} and 15 cm^{-1} were measured in 1μm deep surface gratings waveguides, respectively for fundamental and second transverse mode.

6.3 Method for measurement of the laser characteristics

The most important laser characteristics measured were the following:

(1) Injection current-Voltage (I-V), and Light output power- Injection current (L-I) curves

(2) Laser spectra

(3) Far field pattern

These functions were measured for both pulsed and CW operation. Under CW operation, the junction temperature generally rises significantly due to the continuous heat production. In such conditions, the laser characteristics, namely threshold current, external quantum efficiency and laser spectra, change when compared with the pulsed characteristics. In pulsed operation, with a duty-cycle below about 1:1000, the junction temperature does not change significantly. Pulsed measurements are, therefore, a more accurate way to evaluate the laser characteristics. However, the laser characteristics in CW operation are at least as important as in pulsed operation, because practical operation may be at or near CW operation. Both types of measurement, for pulsed and CW operation, were therefore carried out.

The measurements performed are briefly summarised below:

(1) Injection Current-Voltage (I-V Curve) and Light output power-Injection current (L-I curve).

The resistance of the lasers was evaluated from the I-V curves, and the threshold current and slope efficiency were evaluated from L-I curves. These parameters are important laser characteristics. The measurement method used for the L-I curves differed between pulsed operation and CW operation. Fig. 6.6 shows the measurement system for the L-I curves, in pulsed operation. The laser chip was injected with a pulsed current (duty cycle 1:2500), to prevent excessive heating of the chip, which was mounted on a brass chip. The optical power was measured by averaging the photocurrent for gate pulses of length 100 ns in electrical circuits to avoid the influence of delay time and relaxation of laser emission[6.6]. On the other hand, in CW operation, the optical power was simply measured using an optical power meter.

(2) Laser spectra

Fig.6.7 shows the system for measurement of the laser spectra. The beam emitted by the laser chip was focused on the end of the multi-mode fibre input to the ADVANTEST Q8381 spectrum analyser with objective lenses. The resolution of this spectrum analyser is about 0.1nm.

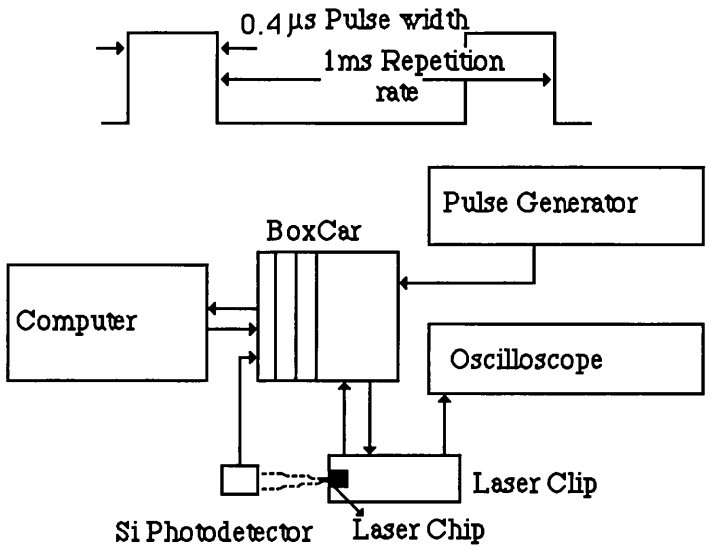

Fig. 6.6: Schematic diagram of the measurement system for the L-I curve in pulsed operation

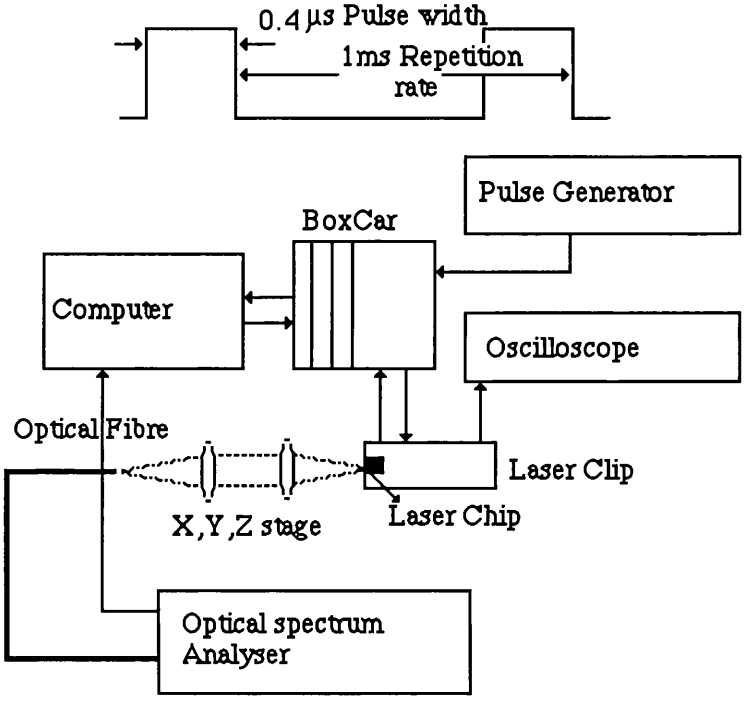

Fig. 6.7: Schematic diagram of the system for measurement of the laser spectra

6.4 Injection current-voltage characteristic (I-V curve)

All experimental results in sections 6.4 to 6.8 are from lasers fabricated from the same material structure **#QT474d**. Material structure #QT474d is schematically illustrated in Fig.4.2. The structure comprises several layers, being eight relevant for the guiding and generation of light; from top to bottom, they are : 0.1μm, 3E18 high-doped GaAs; 0.6μm, 1.2E18 40% AlGaAs; 0.1μm undoped- 40% AlGaAs; 524A undoped- 20% AlGaAs; 2Qw's 76A; 1424A undoped- 20% AlGaAs; 0.1μm, 2.2E17 80% AlGaAs and 0.4μm, 5.5E17 80% AlGaAs.

From the passive measurements of coupling coefficient κ, section 6.2, it was concluded that the stripe width of 3.5μm would be most suitable to obtain a high value of κ and also it would be an optimum practical value for fabrication purposes. It was therefore chosen **3.5μm** stripe width for all devices.

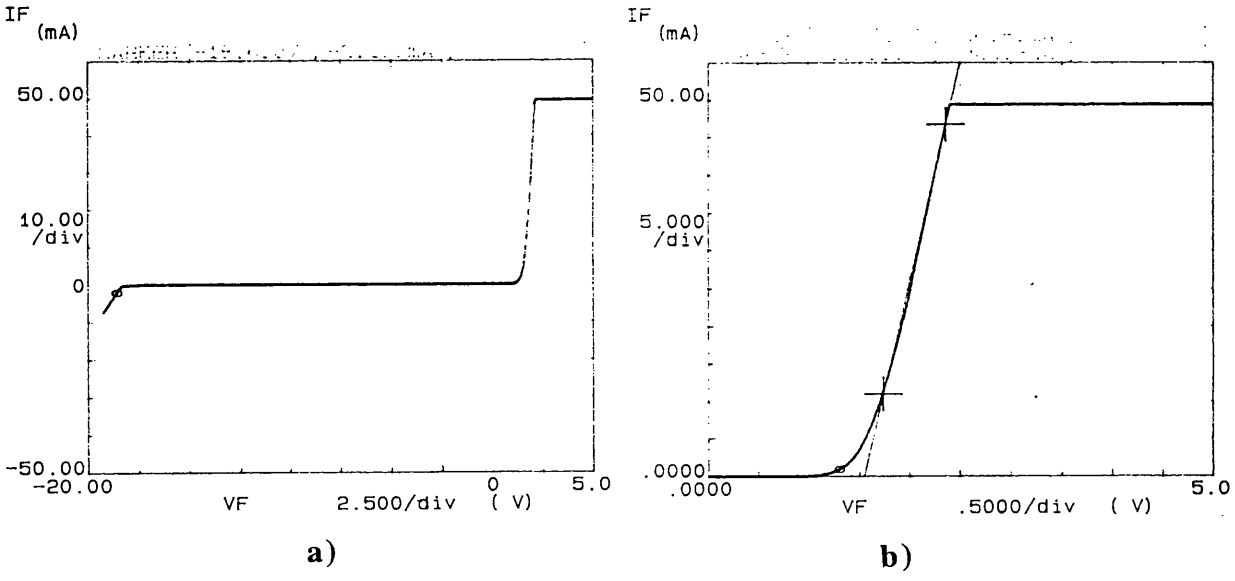

Fig. 6.8: Current versus voltage curves for surface grating DFB laser fabricated from #QT474d

Fig. 6.8 shows I-V curves for a surface grating DFB laser fabricated from epitaxial material (MOCVD) #QT474d. Fig. 6.8 a) shows the breakdown voltage, which is about -18.6V. From Fig. 6.8 b) it is possible to measure the resistance of the lasers, which is 17.2Ω.

6.5 Laser characteristics in pulsed operation

In this section, a comparative study of the light output power versus injection current characteristics (section 6.4.1), as well as laser spectra (section 6.4.2) as functions of both injection current and temperature, for surface 3rd-order, 2nd-order and 1st-order grating DFB lasers are discussed. All results shown in this section were taken in *pulsed operation*.

6.5.1 Light output power-injection current characteristic (L-I curve)

In the following discussion, the dependence of the threshold current and slope efficiency on Bragg-order as well as on the presence or absence of antireflection coatings in surface grating DFB lasers are addressed. All the devices were fabricated from wafer #QT474d, the stripe width 3.5μm is the same for all surface grating DFB lasers. Typical L-I curves of surface 3rd-order, 2nd-order and 1st-order grating DFB lasers in pulsed operation are shown and discussed.

Ref.	Laser Type	Wavelength (nm)	Threshold current (mA)	Threshold Current Density(A/cm^{-2})	slope Efficiency (mW/mA)
(1)	3rd-order Λ=380nm EtchDepth=0.6μm L=500μm	858.68 (nAR) 852.20 (AR)	20 (nAR) 25 (AR)	1143 (nAR) 1428 (AR)	0.22 (nAR) 0.28 (AR)
(2)	3rd-order Λ=384nm EtchDepth=0.6μm L=900μm	860.42 (AR)	48 (AR)	1524 (AR)	0.11 (AR)
(3)	3rd-order Λ=384nm EtchDepth=0.6μm L=1400μm	860.42 (AR)	75 (AR)	1530 (AR)	0.083 (AR)
(4)	2nd-order Λ=256nm EtchDepth=0.66μm L=500μm	860.00 (nAR) 860.75 (AR)	20 (nAR) 23 (AR)	1143 (nAR) 1314 (AR)	0.24 (nAR) 0.34 (AR)
(5)	1st-order Λ=128nm EtchDepth=0.66μm L=450μm	854.00 (AR)	20 (AR)	1270 (AR)	0.25 (AR)

Table 6.1: L-I experimental results of surface grating DFB lasers in pulsed operation at room temperature

Table 6.1 shows the L-I results of surface 3rd-order, 2nd-order and 1st-order grating DFB lasers, in pulsed operation and at room temperature. Most of the L-I results shown in Table 6.1 are for lasers with antireflection coatings (AR). However, for comparison, some L-I results of DFB lasers without antireflection coatings (nAR) are also shown. In the nAR cases, the DFB lasers are emitting a combination of DFB and FP modes, being the dominant the FP modes. The threshold current and threshold current density shown in Table 6.1 are nominal values, the current spreading was not taken into account. The slope efficiency for a single output facet is also shown in Table 6.1. These results were selected, in each case, from a laser which had the lowest threshold current among five nominally identical lasers.

The measurement errors for threshold current and slope efficiency were estimated from a six-fold repetition of measurements on the same device. The standard deviation of the threshold current was about 0.5mA and the standard deviation of the slope efficiency was about 0.01mW/mA.

The surface grating DFB lasers with 3rd-order gratings and 380nm pitch have a higher threshold current when coated with AR coatings because the Bragg wavelength differs from the peak of the laser gain curve by 7nm, as well as reflectance reduction caused by AR coatings. Consequently, lasers without AR coatings start lasing at the peak of the laser gain curve in F.P. modes at 20mA threshold current, whereas lasers with AR coatings lase in DFB mode at a higher threshold current of 25mA.

The surface grating DFB lasers with 2nd-order gratings and 256nm pitch show a behaviour similar to that of 3rd-order DFB lasers, as modified by the presence or absence of AR coatings. The reason for such behaviour, however, is not the mismatch between the peak of the laser gain curve and DFB emission, but simply the decrease of the reflectance R due to the AR coatings. The reduction of the reflectance at both ends of the cavity increases the threshold current according to Eq.(6.5.1)[6.14].

$$J_{th} = \frac{J_0}{\eta} + \frac{\alpha_i}{\eta A} + \frac{(1-\Gamma)\alpha_c}{\Gamma \eta A} + \left(\frac{1}{\eta \Gamma A}\right)\left(\frac{1}{2L}\right)\log\left(\frac{1}{R_1 R_2}\right) \qquad (6.5.1)$$

where:

J_{th}- Threshold current density (A/cm^2)

J_0- Transparency current density (A/cm^2)

η - Internal quantum efficiency

A - Differential gain taken from $g_{max}=A(J-J_0)$; ($A=amperes^{-1}cm$)

α_i- Internal loss coefficient of the active layer(cm^{-1})

α_c - Loss in the confining layers(cm^{-1})

Γ - Optical confinement factor

R_1 and R_2 - Facet reflectivities

L - Cavity length(cm)

For the AR case, the lowest threshold current density is obtained with surface 1st-order grating DFB lasers, i.e., 1270 Acm^{-2}. The surface 2nd-order grating DFB laser has a threshold current density of 1314 A/cm^2, which corresponds to an increase of 3.3% compared to 1st-order DFB lasers. Finally, the surface 3rd-order grating DFB lasers have a threshold current density of 1428 A/cm^2, corresponding to an increase of 11% compared to the value of J_{th} presented by surface 1st-order grating DFB lasers. Apparently, these results show that the coupling coefficient is strongest in 1st-order gratings since the lowest threshold current density is presented by surface 1st-order grating DFB lasers. According also to the threshold current density, the 2nd-order gratings give a stronger coupling coefficient than the 3rd-order gratings. This behaviour is generally in agreement with the theoretical calculation of κ performed in section 3.8, chapter 3. However, it is not simple to establish a relationship between threshold current density and the coupling coefficient since the grating etch depth is not the same for all devices. In fact, 2nd-order and 1st-order gratings are deeper than 3rd-order grating, which may explain the difference in threshold current density observed. In addition, the mark-space ratio in 2nd-order gratings was not optimized in order to maximise the coupling coefficient.

The maximum value of the slope efficiency is shown by surface 2nd-order grating DFB lasers, i.e., 0.34mW/mA. It is followed by 3rd-order DFB lasers with 0.28mW/mA per facet, and finally the 1st-order DFB lasers with 0.25mW/mA.

The next four figures show the light output power versus injection current for surface 3rd-order (L=500μm and no optimized grating period, and L=1400μm and optimized grating period), 2nd-order and 1st-order grating DFB lasers, as represented by **(1)**, **(3)**, **(4)** and **(5)** in Table 6.1 (left-hand side: **Ref.**).

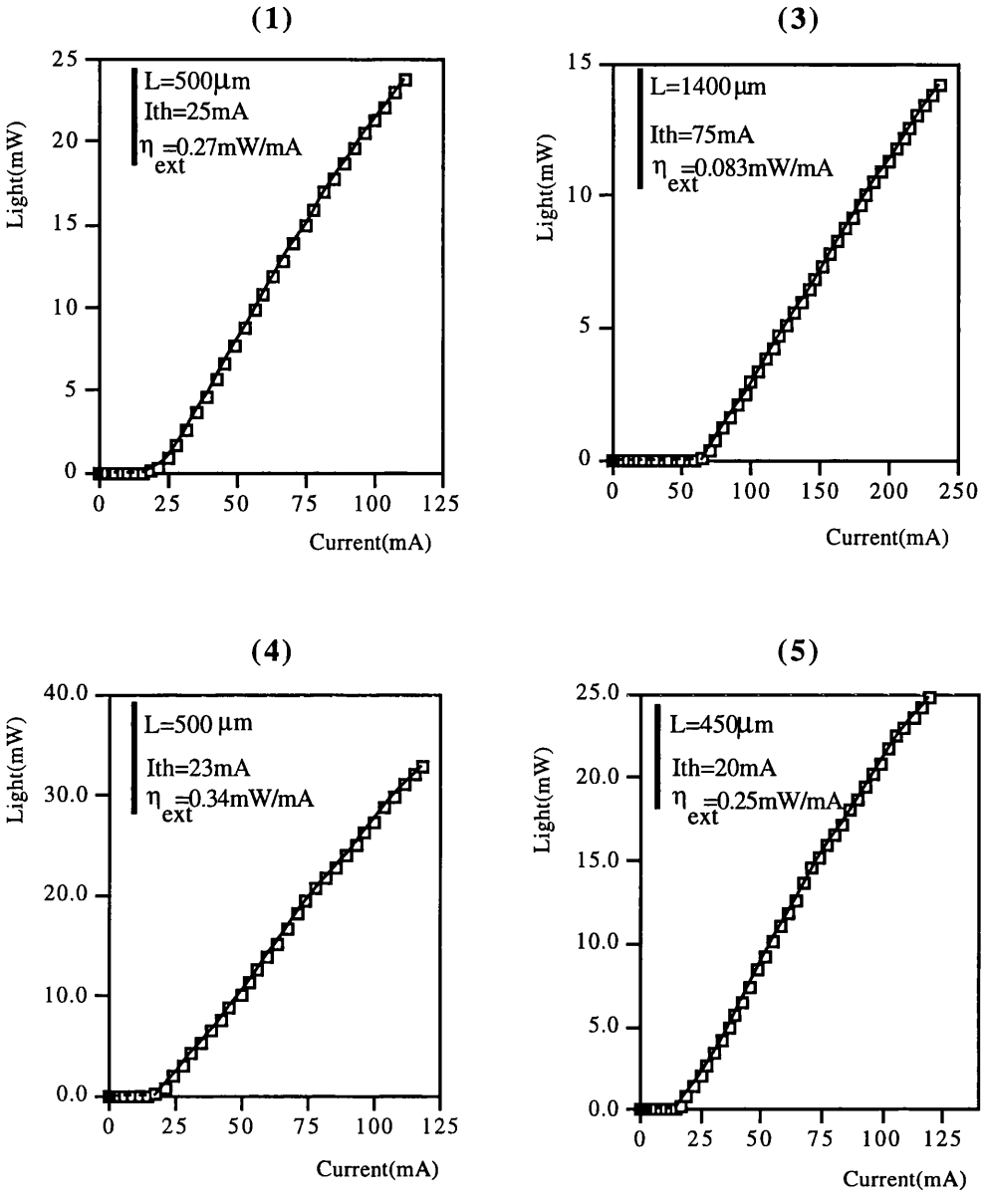

Fig.6.9: Light power versus injection current for surface 3rd-order, 2nd-order, and 1st-order grating DFB laser in pulsed operation.

Fig. 6.9 displays the light versus current characteristic (L-I curve) of surface 3rd-order, 1400 μm long 3rd-order, 2nd-order, and 1st-order grating DFB lasers. In the case of laser (**1**), the threshold current is higher for lasers with AR coatings because the Bragg wavelength differs from the peak of the laser gain curve by 7 nm, as seen in the spectrum of Fig. 6.10. For Laser (**2**), which is not shown in Fig.6.9 since is basically similar to Laser (**3**), the threshold current density was 1530Acm^{-2}. This value is higher than the threshold current density of lasers with a 500 μm cavity length; the reason for this difference may be related to the increase of light coupled out by the waveguide with optimum grating period, i.e., increase of the effective losses in the cavity.

In summary, the laser characteristics of surface 1st-order, 2nd-order and 3rd-order grating DFB lasers were measured in pulsed operation. The lowest threshold density current of 1270 Acm^{-2} was shown by surface 1st-order grating DFB laser. An increase in threshold current density of 3.3% and 11% compared to 1st-order grating DFB lasers, was obtained, respectively for surface 2nd-order and 3rd-order grating DFB lasers. No simple relationship was found between the L-I characteristics and grating Bragg-orders.

6.5.2 Laser Spectra in pulsed operation

In the following discussion, the spectral behaviour of surface grating DFB lasers with both injection current and temperature for different Bragg-orders are addressed.

6.5.2.1 Surface 3rd-order grating DFB laser

The following experimental results are from a non optimized surface 3rd-order grating DFB laser with a 380 nm grating period. These results were used to optimise the DFB design, i.e., the Bragg wavelength was designed to coincide with the peak of the laser gain curve. The stopband width near threshold was also measured in these devices and used to estimate the coupling coefficient.

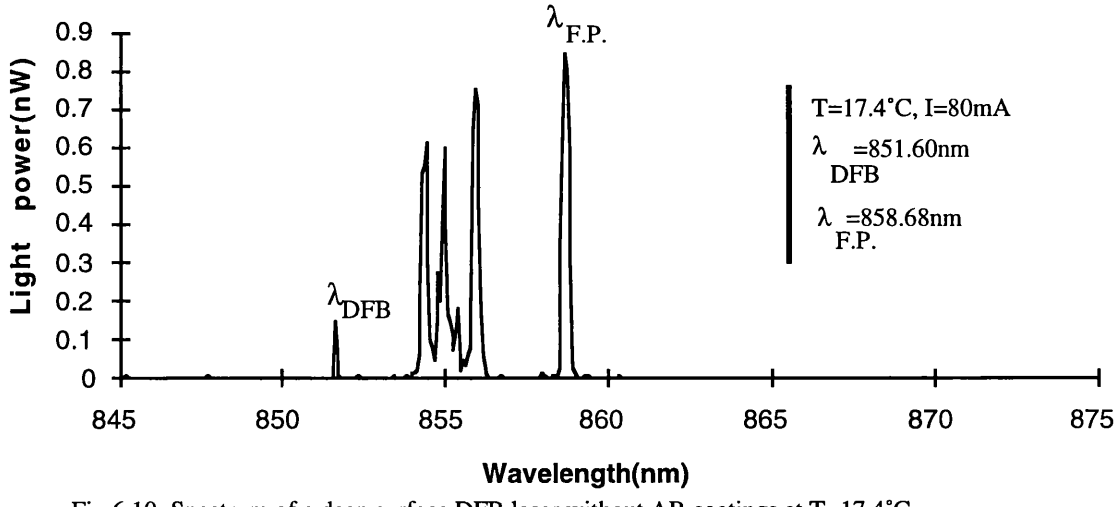

Fig.6.10: Spectrum of a deep surface DFB laser without AR coatings at T=17.4°C

Fig.6.10 shows the spectrum of a surface 3rd-order grating DFB laser at T=17.4°C, for a injection current of 80mA. This laser has no AR coatings which explains the combination of Fabry-Perot and DFB modes observed. In order to observe the DFB mode, the devices have to be pumped hard, at 3 or 4 times the threshold current. The reason for this is that, as seen above, the Bragg wavelength is very different (7nm) from the peak of the laser gain curve.

The effective refractive index of the guided mode (n_{eff}) can be determined from the relationship between the Bragg wavelength (λ_{Bragg}) and the grating spatial period (Λ_g), which is defined by

$$\Lambda_g = m\frac{\lambda_{Bragg}}{2n_{eff}} \tag{6.2}$$

where m is the order of the grating. Using the values above for the Bragg wavelength, λ_{Bragg}=851.60nm, m=3 (the grating Bragg-order is 3), the grating spatial period of 380nm, the effective mode index is calculated to be 3.36. In order to optimise the DFB laser design, the Bragg wavelength should coincide with the peak of the laser gain curve, which is 858.68nm as observed in the spectrum above ($\lambda_{F.P.}$). Using this new value for the Bragg wavelength in Eq.(6.2), and assuming that the effective mode index is almost the same as at 851.60nm (dispersion is neglected in this calculation), the new optimised grating spatial period was calculated to be 384nm.

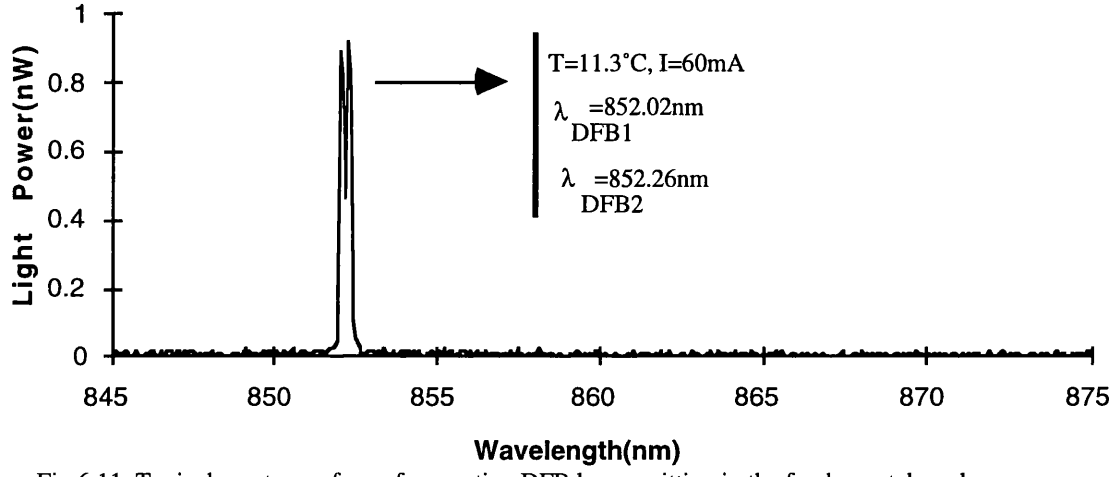

Fig.6.11: Typical spectrum of a surface grating DFB laser emitting in the fundamental mode

Fig.6.11 shows the spectrum of surface 3rd-order grating DFB laser with AR coatings, emitting in the fundamental mode. Two DFB modes are observed close to each other, which are caused by degeneracy in the conventional DFB laser. In fact, as discussed in reference [6.1], a DFB laser fabricated using a single period grating, which is the case of laser above, leads to two possible longitudinal lasing modes, one on either side of the stopband. The value of the stopband width is 0.24nm.

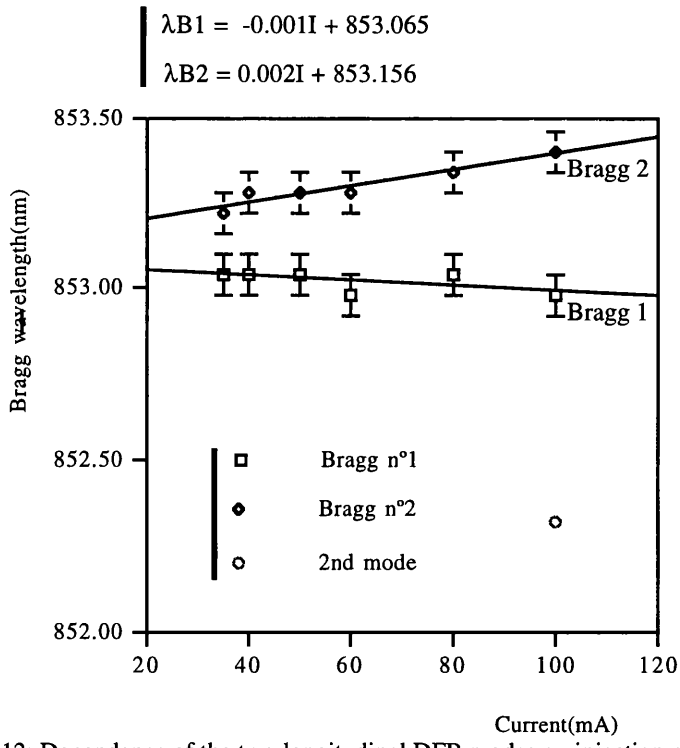

Fig.6.12: Dependence of the two longitudinal DFB modes on injection current

Fig.6.12 displays the two DFB modes that are characteristic of a spectrum emitted by a DFB laser with a single period grating, as a function of the injection current.

The separation between the two longitudinal DFB modes remains nearly constant until $I=3I_{th}$, beyond which the separation between them increases significantly. Note that $d\lambda_{B1}/dI$ is negative, which means a decrease of λ_{B1} with current, whereas $d\lambda_{B2}/dI$ is positive and twice $d\lambda_{B1}/dI$. This behaviour may be caused by changes in the transmission characteristics of the grating waveguide as the current was increased. These results are in contrast to similar measurements carried out in CW operation, where two longitudinal DFB modes were observed near threshold (next section 6.6) but, as the current was increased beyond threshold, only one mode was lasing, i.e., degeneracy was lifted for currents larger than threshold.

The coupling coefficient can be determined from the subthreshold normalized stopband width [6.7], WL, defined as the normalized mode spacing between the fundamental (lowest threshold) DFB mode and the lowest threshold adjacent DFB mode, i.e.,

$$WL = 2\pi n_{eff} L\left[\frac{1}{\lambda} - \frac{1}{\lambda_{\pm}}\right] = 2\pi n_{eff} L \frac{\Delta\lambda}{\lambda^2} \qquad (6.3)$$

In this equation λ, λ_{-1} and λ_{+1} are, respectively, the wavelength of the fundamental, shorter adjacent, and longer adjacent modes, n_{eff} is the effective index including the dispersion [6.2], and L is the laser cavity length. The relationship between WL and κL is shown in Fig.4 of reference [6.8] for the case of 0% and 2% facet reflectivity. The perfect AR case is calculated using the theory of Kogelnik and Shank [6.1]. It becomes more difficult to determine the coupling coefficient when the residual facet reflectivity is taken into account, because the phase of the grating at the front and rear facets is unknown. For the 2% case, as performed in [6.8], the phases of the grating at the front and rear facets were each varied from 0 to $15\pi/8$ in $\pi/8$ steps. Fig.4 of reference [6.8] shows that, for a given value of κL, the residual reflectivity and random grating phase of the facets introduces a large variation in the stopband width. The WL value of 3.80 was measured on subthreshold spectra of a surface 3rd-order grating DFB laser. Using the curve in Fig.4 of [6.8], the value of κL is at least 0.45, which gives a coupling coefficient of $\kappa = 9cm^{-1}$. This result is in good agreement with the passive measurement of κ presented in section 6.2.

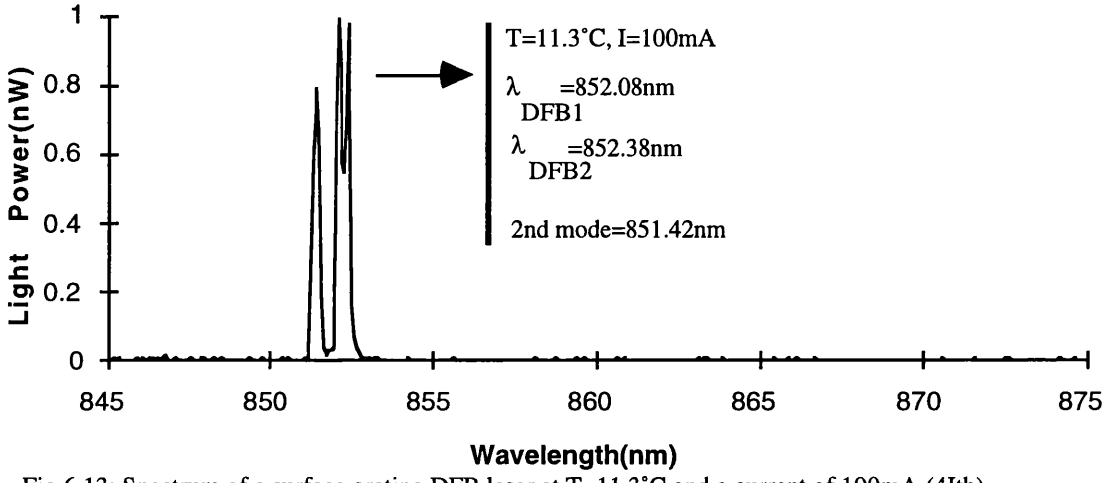

Fig.6.13: Spectrum of a surface grating DFB laser at T=11.3°C and a current of 100mA (4Ith)

Fig.6.13 displays the spectrum of a surface grating DFB laser at a temperature of 11.3°C and a current of 100mA, which is $4I_{th}$. In this spectrum, the second transversal mode is also observed at very high drive currents, being separated from the fundamental mode by 1nm.

Typically, most of the surface grating DFB lasers started lasing in the fundamental mode. Then, as the current was increased beyond $4I_{th}$, the second transverse mode was also coupled, as observed in the spectrum above. However, it was also observed that some DFB lasers started lasing in the second transverse mode. This behaviour may be caused by combined differences in the grating etch depth and variations across the wafer, which enhanced the coupling of the second transverse mode. Note also that, according to the passive measurement of κ performed in section 6.2, surface grating DFB lasers with deep

gratings (> 0.7 μm) have larger coupling coefficient for the second transverse mode than for the fundamental mode.

In summary, from the emission spectra of 380 nm grating period devices, the effective refractive index was estimated to be 3.36. A new optimized grating spatial period was calculated, to match the peak of the laser gain curve, to be 384nm. The stopband width was measured in a surface 3rd-order grating DFB laser near threshold, and using this value, the coupling coefficient was estimated to be $\kappa=9cm^{-1}$, which is in agreement with theoretical calculations and passive measurement of κ performed in section 6.2.

6.5.2.2 Long cavity surface 3rd-order grating DFB laser (#2,#3)

The following experimental results are from a pitch optimized long cavity surface 3rd-order grating DFB laser. Results for 900 μm and 1400 μm long devices are reported. In order to match the peak of the laser emission, the grating period was increased to 384 nm, corresponding a Bragg wavelength of about 860 nm. The spectral behaviour of these devices was studied with temperatures in the range between 10 °C and 50 °C. Typical spectra are shown and discussed.

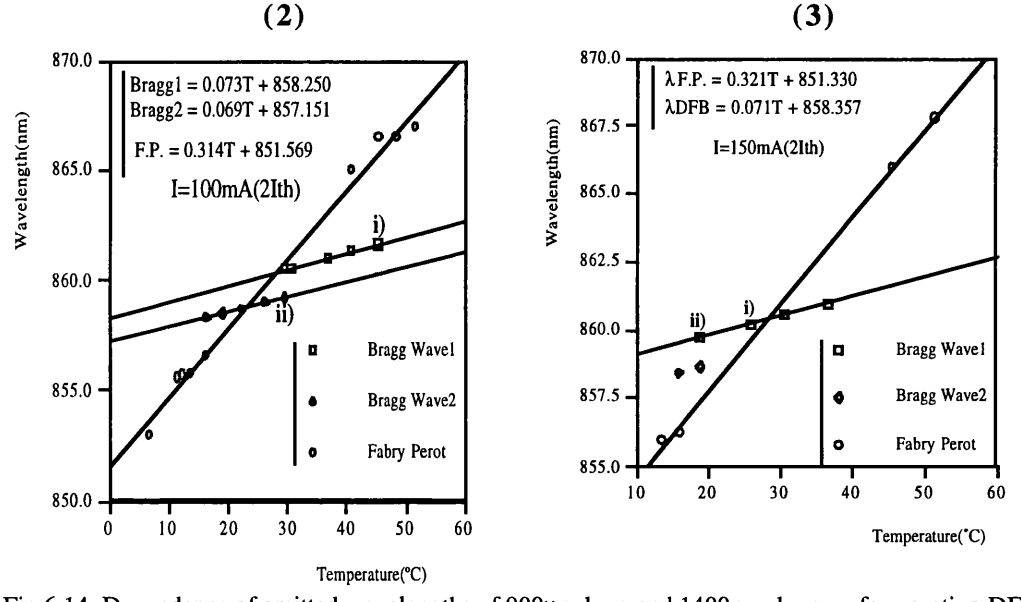

Fig.6.14: Dependence of emitted wavelengths of 900μm long and 1400mm long surface grating DFB lasers on temperature of operation. The spectra for i) and ii) are represented in the following figures.

Fig.6.14 shows the dependence of the emitted wavelength of a 900μm long and 1400μm long surface 3rd-order grating DFB laser on temperature. For values of the temperature higher than 50°C or lower than 15°C, only F.P. modes lased. In the case of laser 900μm long (**2**), the lasers emitted in the second transverse mode for the 15-30°C temperature range; however, in the 30-50°C temperature range, the lasers emitted in the fundamental mode. 1400μm long DFB laser (**3**) in the 15-20°C temperature range, the lasers emitted in the

second transversal mode; however, in the 20-40°C temperature range, the lasers emitted only the fundamental mode. The spectra for typical regimes, as represented by **i)** and **ii)** in Fig.6.14, are shown below in Fig.6.15 and Fig.6.16:

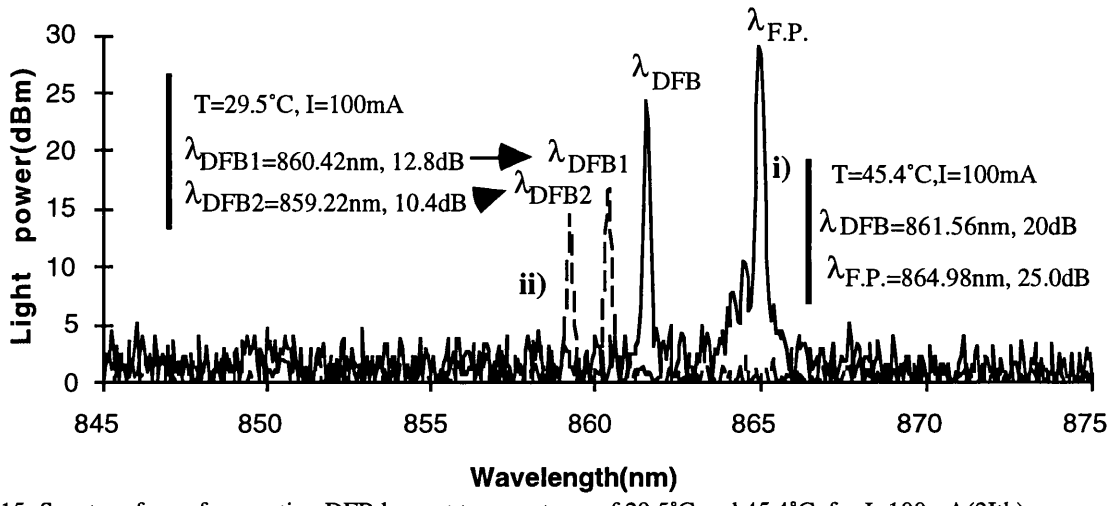

Fig.6.15: Spectra of a surface grating DFB laser at temperatures of 29.5°C and 45.4°C, for I=100mA(2Ith)

Fig.6.15 displays spectra of a surface 3rd-order grating DFB laser at temperatures of 29.5°C and 45.4°C. These spectra were taken from same laser as results shown previously. Both spectra were taken at the same injection current of 100mA (2Ith). In spectrum **i)**, the laser emitted in the fundamental mode at 861.56nm, with a side mode suppression rate of 20dB, and also in F.P. modes at a longer wavelength of 864.98nm. Spectrum **ii)** shows a laser emission which is a combination of the fundamental and of 2nd transverse modes at 860.42nm and 859.22nm respectively . The separation between modes is 1.20nm, and the side mode suppression rate is larger than 10dB.

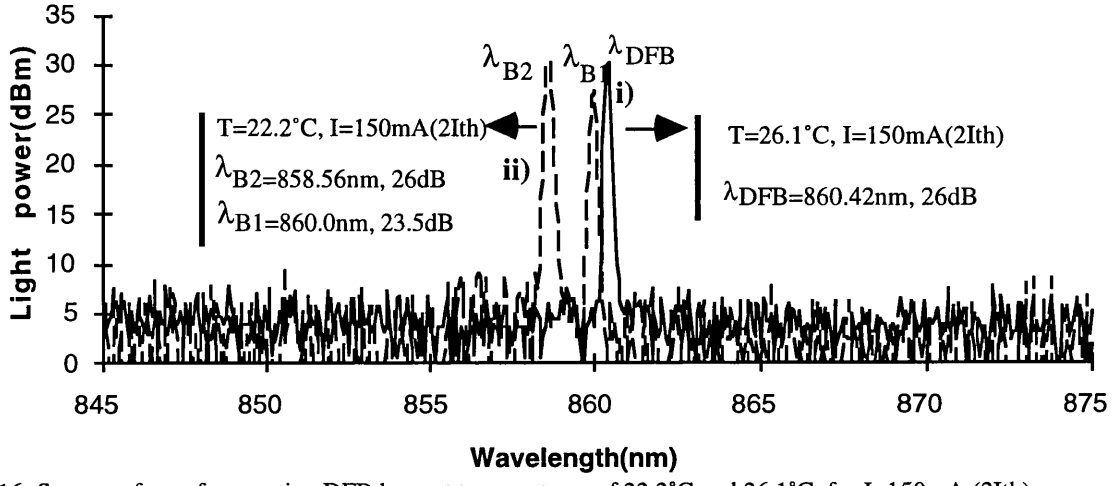

Fig.6.16: Spectra of a surface grating DFB laser at temperatures of 22.2°C and 26.1°C, for I=150mA (2Ith)

Fig.6.16 displays spectra of a 1400 μm long surface 3rd-order grating DFB laser at temperatures of 22.2 °C and 26.1 °C. The injection current is the same for both spectra, I=150 mA ($2I_{th}$). Spectrum **i)** shows typical laser emission, in the temperature range from 25 °C to 40 °C, where only the fundamental mode is present at 860.42 nm, with a side mode suppression ratio of about 26dB. In spectrum **ii)**, the surface grating DFB laser emitted a combination of the fundamental and second transverse modes, at respectively 860.0nm and 858.56nm, with a side mode suppression ratio larger than 20dB. The two transverse modes are separated by 1.44nm.

In summary, from spectra of a 500 μm long surface 3rd-order grating DFB laser, the refractive index of the waveguide and stopband width were estimated. Using this data, the grating spatial period was optimized to be 384 nm and the coupling coefficient was estimated to be 9 cm^{-1}. Laser spectra from 900μm and 1400μm long surface 3rd-order grating DFB lasers do not exhibit stopband. Temperature studies of the spectral characteristics showed different emission regimes. More specifically, emission of the second transverse mode, identified using the calculation of modal index difference, was observed in the temperature range from 15°C to 25°C; fundamental mode emission ocurred in temperature range from 25°C to 50°C, and outside this temperature range only FP modes were lasing.

6.5.2.3 Surface 2nd-order grating DFB laser (#4)

The following experimental results are from a surface 2nd-order grating DFB laser in pulsed operation. Results for antireflection (AR) coated and uncoated devices are reported. Typical spectra are discussed and compared with previous spectra of surface 3rd-order grating DFB lasers.

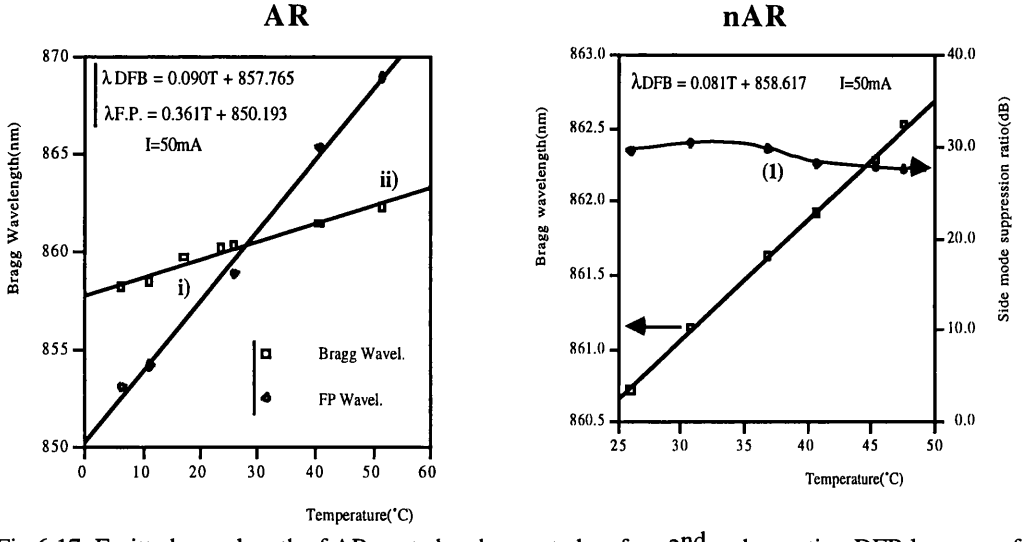

Fig.6.17: Emitted wavelength of AR coated and uncoated surface 2nd-order grating DFB laser as a function of the temperature. The spectra **i)**, **ii)**, and **(1)** are represented in the coming figures.

Fig.6.17 shows the temperature dependence of the emitted wavelength and SMSR(only left plot) of surface 2nd-order grating DFB lasers. The Bragg wavelength dependence on temperature is about 0.09nm/°C, which is higher than the typical value of 0.06-0.07nm/°C normally obtained. The F.P. wavelength dependence on temperature is 0.36nm/°C, which is the typical value usually measured. In the temperature range, 25-50°C, the side mode suppression ratio is kept constant at about 30dB.

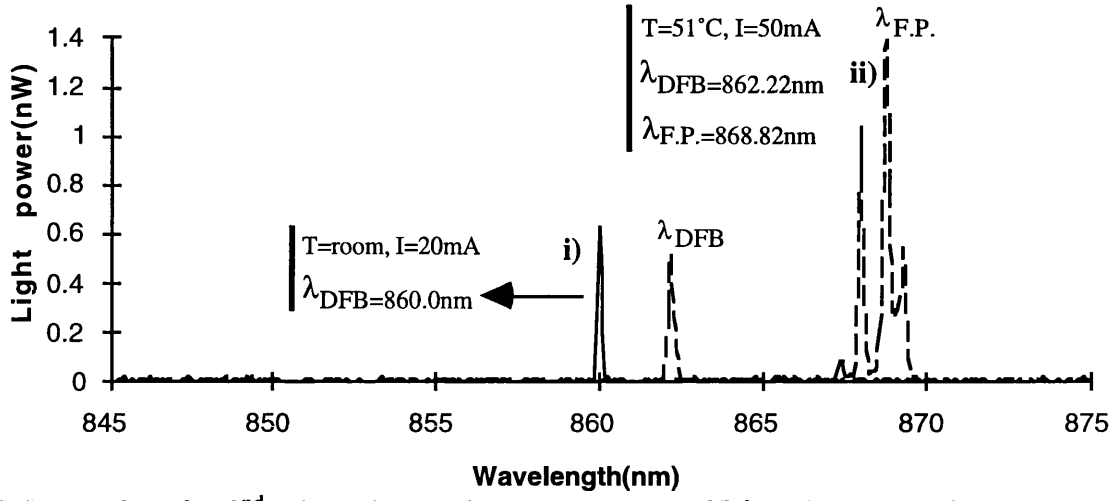

Fig.6.18: Spectra of a surface 2nd-order grating DFB laser at a temperature of 51°C and I=50mA, and at room temperature and I=20mA

Fig.6.18 displays spectra of a surface 2nd-order grating DFB laser at room temperature and at 51°C. Spectra **i)** and **ii)** were taken, respectively, at about threshold and twice threshold. In spectrum **ii)**, the DFB laser is emitting a DFB line at 862.22nm and also F.P. modes at a longer wavelength of 868.82nm. At such a high temperature (51°C), the peak of the laser gain curve is well-separated (by 6nm) from the DFB line. Spectrum **i)** shows DFB laser emission in the fundamental mode at 860.0nm.

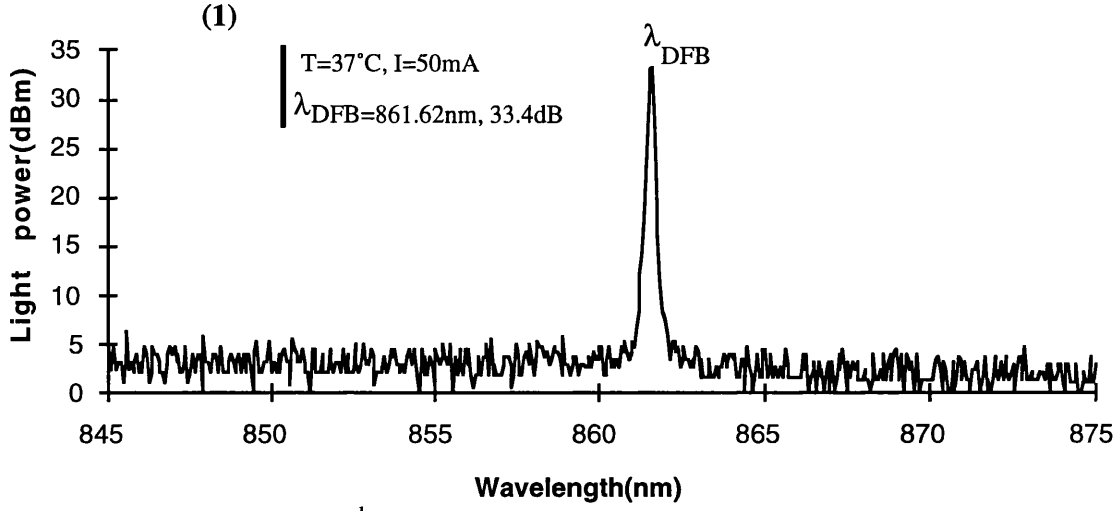

Fig.6.19: Spectrum of a surface 2nd -order grating DFB laser at a temperature of 37°C and I=50mA

Fig.6.19 displays the spectrum of a surface 2nd-order grating DFB laser at a temperature of 37°C and a current of 50mA. The DFB laser is emitting in the fundamental mode at 861.62nm with a SMSR of about 30dB.

In summary, laser spectra from surface 2nd-order grating DFB lasers AR coated and uncoated as a function of the temperature were measured. The main difference between these results and similar spectral data from a surface 3rd-order grating DFB laser, was that in 2nd-order grating devices only the fundamental mode was guided. This result may be explained by the fact that gratings in 2nd-order devices were deeper (6%), providing as a consequence better guiding properties.

6.5.2.4 Surface 1st-order grating DFB laser (#5)

The following experimental results are from surface 1st-order grating DFB lasers in pulsed operation. Only results for uncoated devices are reported. Typical spectra are shown and compared with previous results from surface 3rd-order and 2nd-order grating DFB lasers.

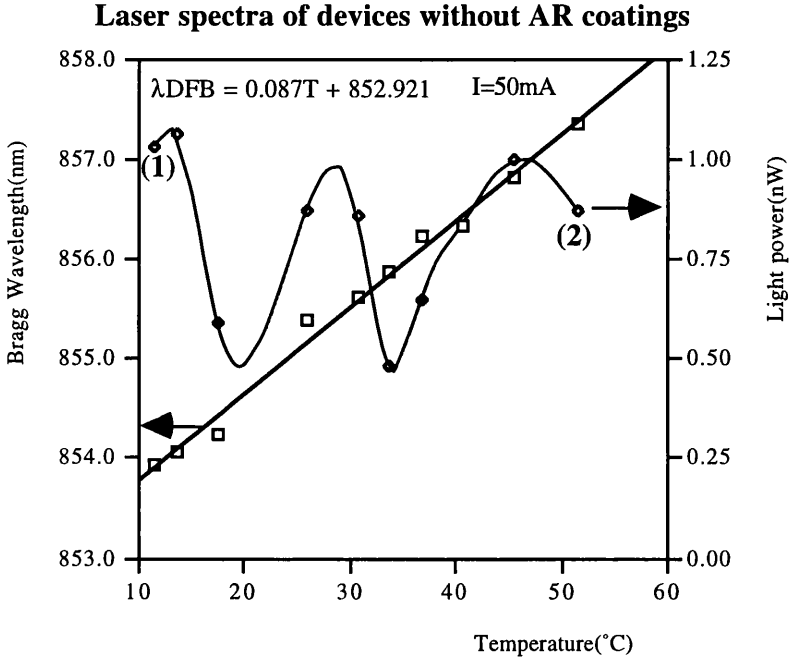

Fig.6.20: Temperature dependence of Bragg wavelength and emitted light power. The spectra at points **(1)** and **(2)** are shown in following figure.

Fig.6.20 shows the dependence of the Bragg wavelength and light power on temperature, in the range from 10°C to 50°C. The Bragg wavelength dependence on temperature is 0.087nm/°C, which is a typical value measured previously. The periodic variation of the light power with device temperature is probably caused by light interference, as the cavity expands due to the increase in temperature. Note that the devices are uncoated.

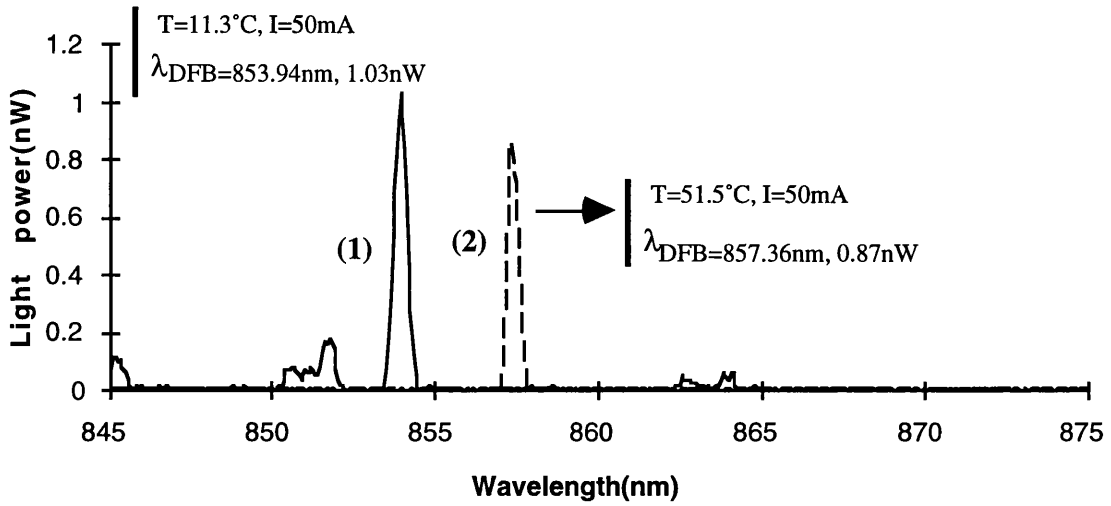

Fig.6.21: Spectra of a surface 1st-order grating DFB laser at temperatures of 11.3°C and 51.5°C, for I=50mA

Fig. 6.21 displays spectra of a surface 1st-order grating DFB laser at temperatures of 11.3 °C and 51.5 °C. Both spectra were taken at the same injection current of 50 mA($2.5I_{th}$). In spectrum (**1**), the DFB laser emitted in the fundamental mode at 853.94 nm, whereas spectrum (**2**) shows the laser emission in the fundamental mode at 857.36 nm.

In conclusion, from spectral data of 500 μm long surface grating DFB lasers, the grating spatial period was optimized (384 nm) and the coupling coefficient estimated (9 cm^{-1}). The stopband width was not observed, neither in long surface 3rd-order grating DFB laser nor in surface 2nd-order/1st-order grating DFB lasers. The grating etch depth was shown to be critical in defining the guide characteristics. In fact, the second transverse mode was observed in surface 3rd-order grating DFB lasers (grating etch depth=0.6μm), whereas in surface 2nd-order/1st-order grating DFB lasers (grating etch depth=0.66μm) only the fundamental mode was guided.

6.6 Laser characteristics in CW operation

In the previous section 6.5, L-I results and laser spectra for surface 3rd-order, 2nd-order and 1st-order grating DFB lasers in pulsed operation were considered. Now, in this section, light output power versus injection current characteristics as functions of both the κL product and Bragg-order are discussed. The dependence of the laser spectral behaviour on both temperature of operation and injection current are also discussed for all the Bragg-order surface grating DFB lasers considered. All results shown in this section were taken in *CW operation.*

6.6.1 Light output power- injection current characteristic (L-I curve)

In the following discussion, the dependence of the threshold current and slope efficiency on the κL product and Bragg-orders is analysed. All surface grating DFB lasers were fabricated from same material structure, wafer #QT474d, with a stripe width of 3.5μm. Typical L-I curves from surface 3rd-order, 2nd-order, and 1st-order grating DFB lasers in CW operation are shown and discussed. All devices considered in this section were AR coated.

Devices	**3rd-order Λ=380nm**	**3rd-order Λ=384nm**	**3rd-order (2) Λ=384nm**
Length(μm)	500	900	1400
κL	0.5	0.9	1.4
Wavelength(nm)	852.00	860.50	860.50
I_{th}(mA)	26	42	70
J_{th}(A/cm-2)	1486	1333	1428
η_{eff}(mW/mA)	0.17	0.22	0.25

Table 6.2: Dependence of the L-I results on the κL product. These experimental results were taken in CW operation.

Lasers Type	**Wavelength (nm)**	**Threshold current(mA)**	**Threshold current Density(Acm^{-2})**	**Slope efficiency (mW/mA)**
3rd-order Λ=380nm (1) L=500μm	852.00	26	1486	0.17
2nd-order Λ=256nm (3) L=500μm	860.00	25	1428	0.24
1st-order Λ=128nm (4) L=450μm	853.00	45	2857	0.05

Table 6.3: Dependence of the L-I results on the Bragg-order. These experimental results were taken in CW operation

Tables 6.2 and 6.3 show the L-I results of surface 3rd-order, 2nd-order and 1st-order grating DFB lasers with AR coatings in CW operation. The threshold current and slope efficiency shown in the tables above are from a single output facet and were selected, in each case, from a laser which exhibited the lowest threshold current among five identical lasers.

In Table 6.2, the dependence of the L-I results on the κL product (measured using passive transmission technique) is reported. The lowest threshold current density is shown by 900 μm long 3rd-order DFB lasers, being 1333 A/cm^2. This is followed by the 1400 μm long 3rd-order DFB laser, with 1428 A/cm^2, which corresponds to an increase of 6.6% compared to the lowest threshold current density described above. The 500 μm long 3rd-order DFB laser exhibits a threshold current density of 1486 A/cm^2, corresponding to an increase of 10.3% compared to J_{th} of the 900 μm long 3rd-order DFB laser. The dependence of the threshold current density on the κL product, apparently exhibited a minimum around κL=0.9, increasing then for larger and smaller values of κL. The maximum slope efficiency is exhibited by the 1400μm long 3rd-order DFB laser, being 0.25mW/mA. The 900 μm and 500 μm long devices exhibit a lower slope efficiency of 0.22 mW/mA, and 0.17 mW/mA, respectively. As expected, the slope efficiency increases with the κL product, which is in agreement with the theoretical calculations by Whiteaway et al[6.9].

Table 6.3 shows the L-I results for surface DFB lasers with different Bragg-orders, namely 3rd-order, 2nd-order and 1st-order gratings. The lowest threshold current density is exhibited by the 2nd-order surface grating DFB laser, with 1428A/cm^2. This value corresponds to an increase of 6.6% compared to lowest J_{th} reported above in table 6.2. The 1st-order devices exhibit a threshold current density of 2857Acm^{-2}, which corresponds to an increase of 53% compared to J_{th} of 900μm long 3rd-order devices. The maximum slope efficiency is exhibited by 2nd-order DFB lasers, with 0.24mW/mA per facet. The slope efficiency of 3rd-order surface grating laser follows with 0.17mW/mA. Devices fabricated with 1st-order gratings exhibit a slope efficiency of just 0.05mW/mA, which will be explained later as due to device deterioration during mounting. From these results, it is difficult to draw a conclusion about the dependence of the L-I results on the grating Bragg-order.

The next four figures show the light output power versus injection current characteristic for surface 3rd-order, 2nd-order and 1st-order grating DFB lasers in CW operation, as represented by **(1)**, **(2)**, **(3)** and **(4)** in Table 6.2, and 6.3.

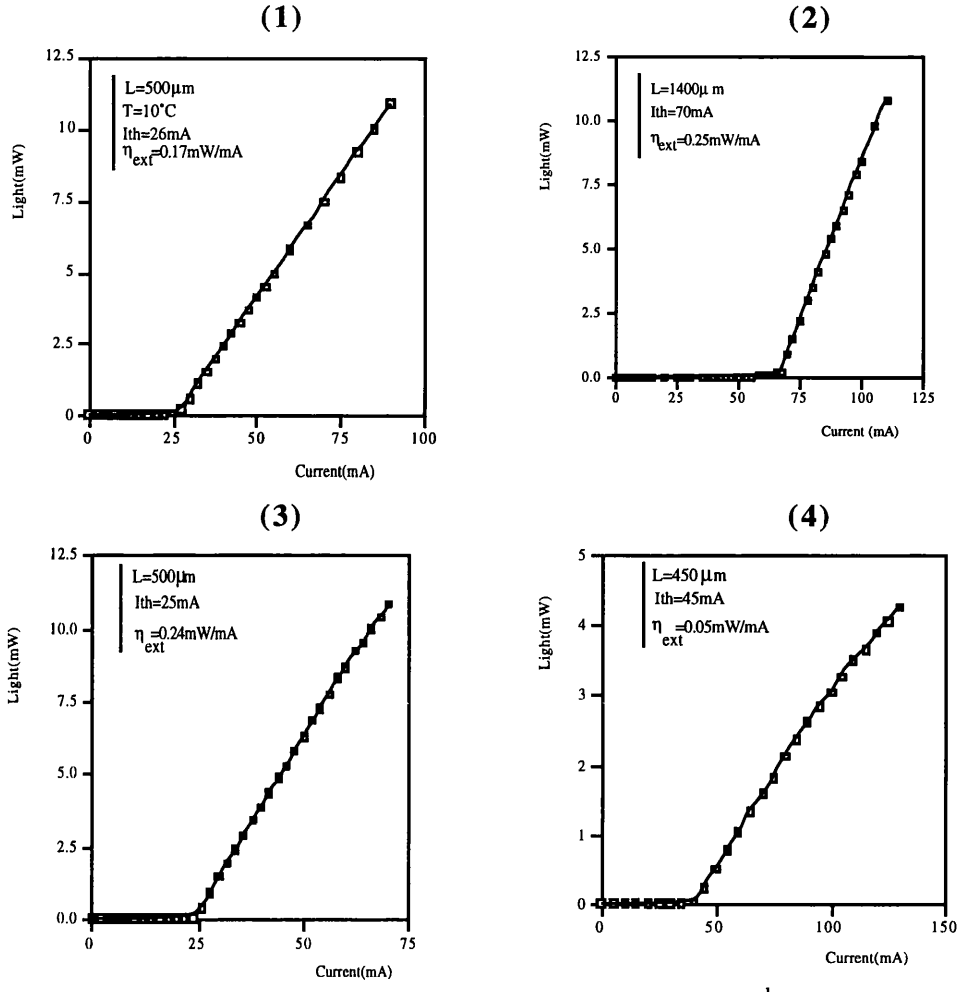

Fig.6.22: Light power versus injection current of a surface 500μm long 3rd-order, 1400μm long 3rd-order, 2nd-order, and 1st-order grating DFB laser in CW operation

In Fig. 6.22, the light-current curves of surface 500 μm long 3rd-order, 1400μm long 3rd-order, 2nd-order gratings with λ/4 phase-shift (*Note:* devices with and without λ/4 phase-shift have the same L-I characteristics), and 1st-order grating DFB lasers, in CW operation, are shown. In laser **(1),** the value of the slope efficiency decreases compared with the value measured in the pulsed regime. This is caused by thermal effects, which shift the laser gain curve further apart from the DFB line, therefore decreasing the gain and the efficiency associated. Device **(2)**, this surface grating DFB laser presents a threshold current of 70mA and a slope efficiency of 0.25mW/mA. Whereas, device **(3)** gives the threshold current of 25 mA and slope efficiency of 0.24 mW/mA. Device **(4)** is 450 μm long with a threshold current of 45 mA and slope efficiency of 0.05 mW/mA. These values of the threshold current and slope efficiency indicate that some kind of deterioration happened when the lasers were mounted. In fact, it is important to point out that the 1st-order gratings are very sensitive to handling (as compared with 3rd-order gratings) and were probably partially destroyed during mounting.

In summary, the L-I characteristics of surface 1st-order, 2nd-order and 3rd-order grating DFB lasers were measured in CW operation as functions of the κL product and Bragg-order. The threshold current density apparently exhibits a minimum around κL=0.9, whereas the slope efficiency increases with the κL product, which is in agreement with theoretical predictions. No simple relationship was found concerning the dependence of the L-I results with grating Bragg-order. The lowest threshold current density was exhibited by 900μm long 3rd-order DFB lasers with 1330 Acm^{-2}. The 1400 μm long 3rd-order and 2nd-order DFB lasers, both with 1428 Acm^{-2}, showed an increase in threshold current density of 6.6% compared to J_{th} of the 900 μm 3rd-order DFB laser.

6.6.2 Laser spectra in CW operation

In the following discussion, the dependence of the spectral behaviour of a surface grating DFB lasers (in CW operation) on both temperature of operation and injection current, for different Bragg-orders, is addressed.

6.6.2.1 Surface 3rd-order grating DFB laser

The following experimental results are from a surface 3rd-order grating DFB laser characterized by a 380 nm grating period and 500 μm length. The spectral behaviour with temperature of operation is shown and discussed.

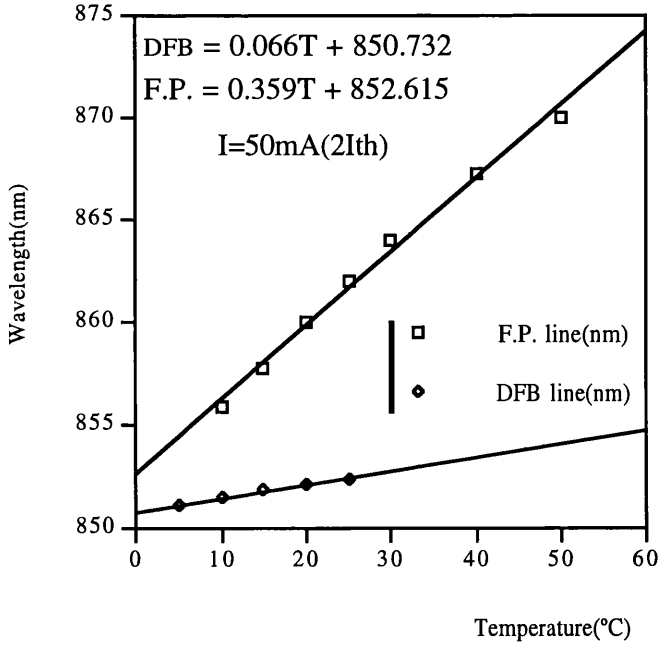

Fig.6.23: Dependence of the Bragg wavelength and Fabry-Perot lines on temperature

Fig.6.23 shows the dependence of the FP and DFB modes on the temperature of operation. This temperature dependence is 0.36nm/°C and 0.066nm/°C for the F.P. and the DFB modes, respectively.

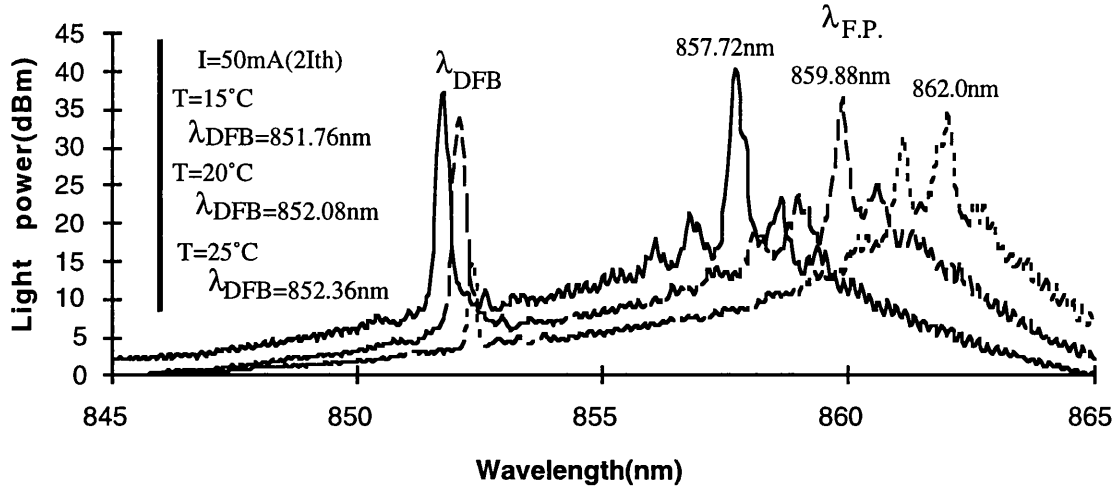

Fig.6.24: Spectra of a surface grating DFB laser at three different temperatures, 15°C, 20°C and 25°C. The current was kept constant at 50mA

In Fig. 6.24, the spectra of a 500μm long surface 3rd-order grating DFB laser in CW operation at three different temperatures, 15°C, 20°C and 25°C, is shown. In the temperature range 10°C to 20°C, the DFB laser emitted in the fundamental mode with a side mode suppression ratio (SMSR) larger than 30dB. For T=25°C, the SMSR deteriorates to 12dB, due to the fact that the peak of the laser gain curve is now about 10nm distant from the DFB emission.

6.6.2.2 Long cavity surface 3rd-order grating DFB laser

The following experimental results are from long cavity surface 3rd-order grating DFB lasers, characterized by lengths of 900 μm and 1400 μm. The spectral behaviour with temperature of operation and injection current is discussed for both 900μm and 1400μm long devices.

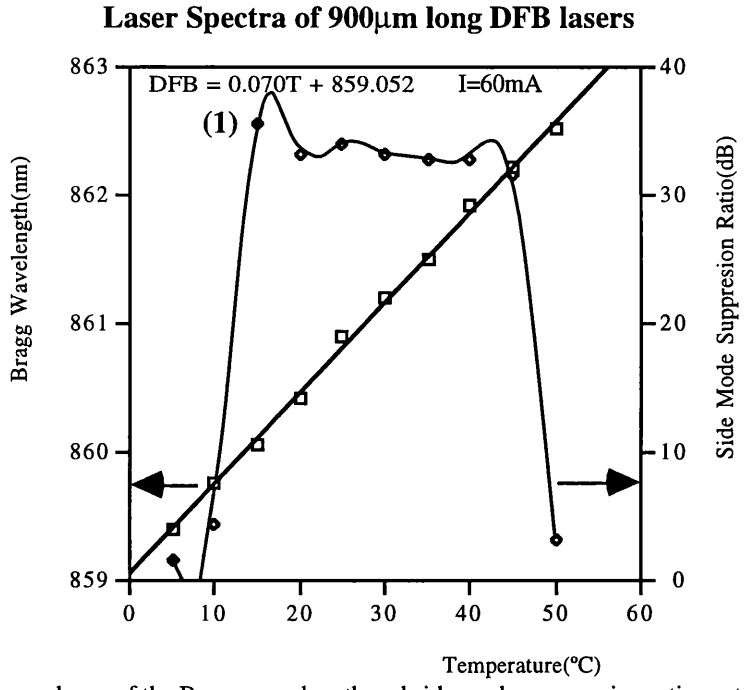

Fig.6.25: Dependence of the Bragg wavelength and side mode suppression ratio on temperature

Fig.6.25 displays the dependence of the Bragg wavelength and side mode suppression ratio on the temperature of operation. The Bragg wavelength dependence on temperature exhibits a value of 0.07nm/°C. In the temperature range from 15-45°C, the side mode suppression ratio is above 30dB. Outside this temperature range, the SMSR decreases drastically to values smaller than 10dB, as illustrated in Fig.6.25. The spectrum at point **(1)** is shown in Fig.6.26.

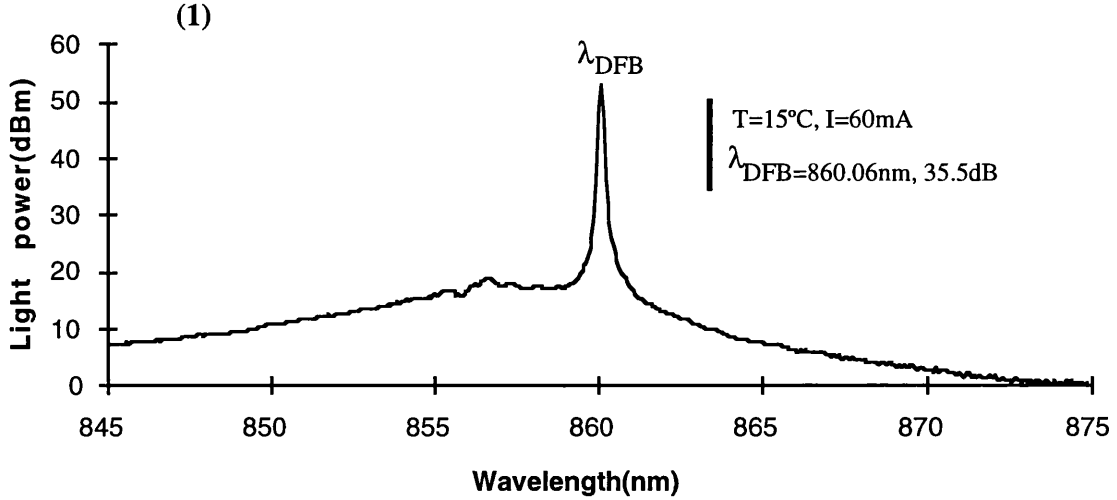

Fig.6.26: Spectrum of a surface grating DFB laser at a temperature of 15°C for I=60mA

Fig.6.26 shows the typical spectrum of a 900μm long surface 3rd-order grating DFB laser in the temperature range from 15°C to 45°C. The DFB laser emitted the fundamental mode at 860.06nm, and the SMSR is about 35.5dB.

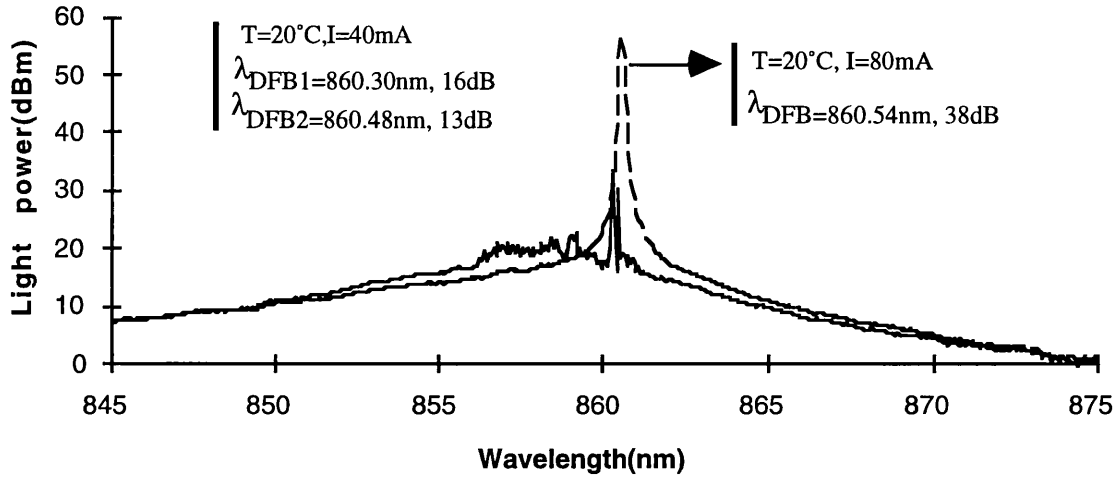

Fig.6.27: Spectra of a surface 3rd-order grating DFB laser at a temperature of 20°C, for currents of 40mA and 80mA

Fig.6.27 displays spectra of a surface 3rd-order grating DFB laser at a temperature of 20°C and a current of 40mA, at threshold, and at 80mA ($2I_{th}$). At threshold, the DFB laser emitted in two longitudinal lasing modes caused by a fundamental oscillation degeneracy (conventional DFB laser, in which two longitudinal modes have an equal probability of lasing [6.1]). As the injection current is increased, the degeneracy is lifted due to the fact that the laser medium gain and index vary with wavelength, and also due to a second factor, which is that the longitudinal modes of a DFB laser resonating in higher Bragg orders (not the first) radiate different amounts of power (i.e., there is different loss for each mode), corresponding therefore to different threshold gains [6.10].

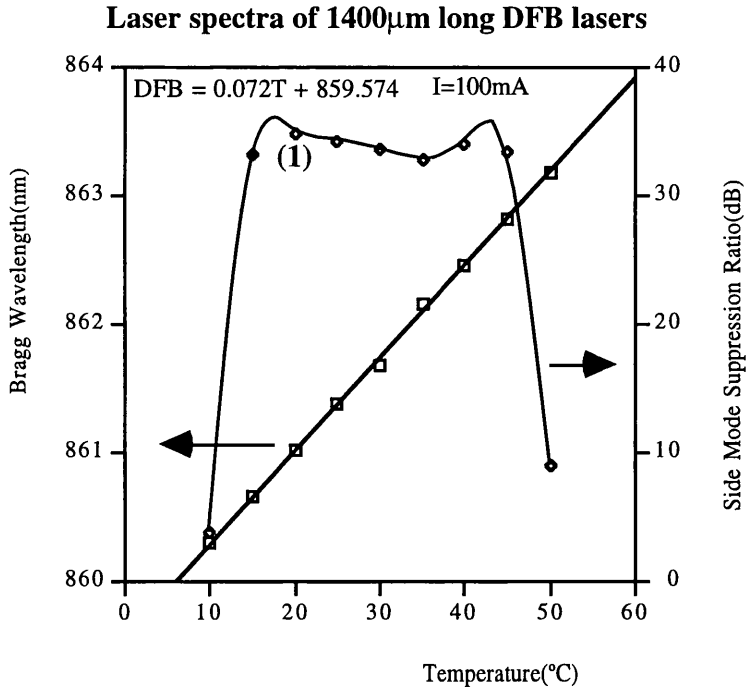

Fig.6.28: Dependence of the Bragg wavelength and SMSR on temperature

Fig.6.28 displays the dependence of the Bragg wavelength and side mode suppression ratio on temperature. The Bragg wavelength dependence on temperature exhibits a typical value of 0.72A/°C. In the temperature range from 15-45°C , the side mode suppression ratio is larger than 30dB. Outside this temperature range, the SMSR decreases drastically to values lower than 10dB, as illustrated in Fig. 6.28. The spectrum at point **(1)** is shown in Fig.6.29.

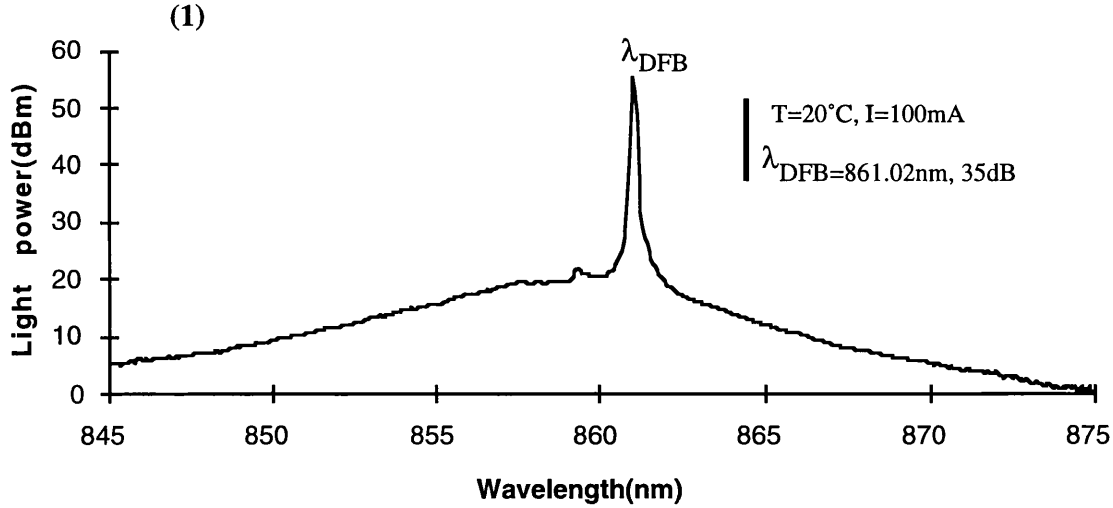

Fig.6.29: Spectrum of a surface grating DFB laser at a temperature of 20°C, for I=100mA

Fig.6.29 shows a typical spectrum of a 1400μm long surface 3rd-order grating DFB laser in the 15-45°C temperature range. The DFB laser is operating in the fundamental mode at 861.02nm, with a SMSR of 35dB.

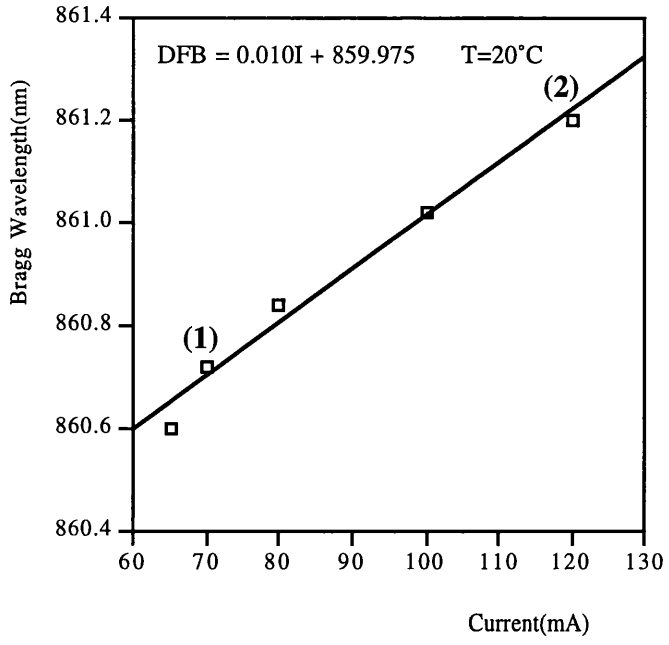

Fig.6.30: Dependence of the Bragg wavelength on current

Fig.6.30 displays the dependence of the Bragg wavelength on injection current at a temperature of 20°C. The Bragg wavelength dependence on current is 0.01nm/mA. Spectra at points **(1)** and **(2)** are shown below, in Fig.6.31.

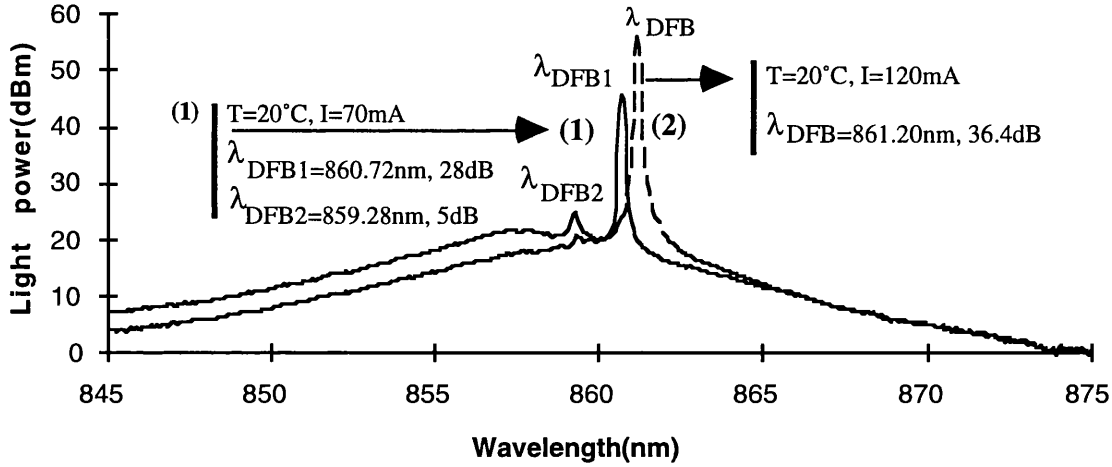

Fig.6.31:Spectra of a surface grating DFB laser at a temperature of 20°C, for I=70 and 120mA

Fig.6.31 shows typical spectra of a surface grating DFB laser at a temperature of 20°C and an injection current of 70mA, around threshold, and at 120mA ($1.7I_{th}$). The spectrum at I=70mA shows laser emission in the fundamental and also 2^{nd} transversal modes, respectively at 860.72nm and 859.28nm; the mode separation is 1.44nm and the SMSR for the fundamental and 2^{nd} transversal modes are, respectively, 28dB and 5dB. In spectrum **(2)**,

the DFB laser emitted only in the fundamental mode, at a temperature of 20°C and a current of 120mA ($1.7I_{th}$). The Bragg wavelength is 861.20nm and the side mode suppression ratio is 36.4dB.

In summary, from the spectral data of 500μm long surface 3rd-order grating DFB lasers, the dependence of the FP and DFB modes on the temperature of operation were measured to be, respectively, 0.36nm/°C and 0.066nm/°C. 900μm and 1400μm long surface 3rd-order grating DFB lasers were observed to operate in the fundamental mode, with SMSR nearly constant to 35dB, in the temperature range from 10°C to 50°C.

6.6.2.3 Surface 2nd-order grating DFB laser with λ/4 shift

The following experimental results are from a surface 2nd-order grating DFB laser with a λ/4 phase-shift, in CW operation. The spectral behaviour with both temperature of operation and injection current is discussed.

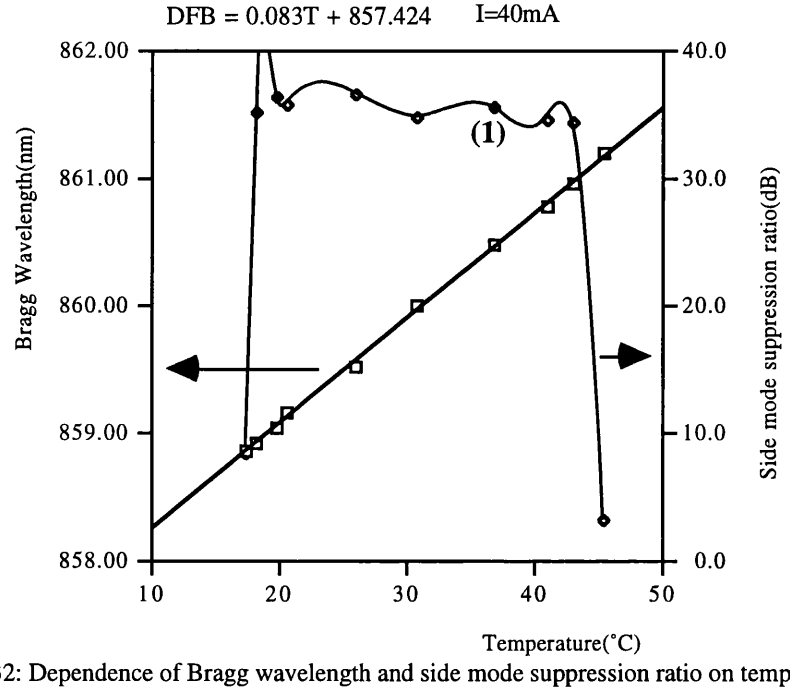

Fig.6.32: Dependence of Bragg wavelength and side mode suppression ratio on temperature

Fig.6.32 shows the dependence of the Bragg wavelength and side mode suppression ratio on temperature, for a constant current of 40mA. The Bragg wavelength dependence on temperature is 0.083nm/°C, which is of the same magnitude as the value obtained in pulsed operation. In the temperature range from 20-45°C, the SMSR is larger than 30dB. Outside this temperature range (and in agreement with previous experimental results), the SMSR decreases drastically to values lower than 10dB. The spectrum at point **(1)** is shown below, in Fig.6.33.

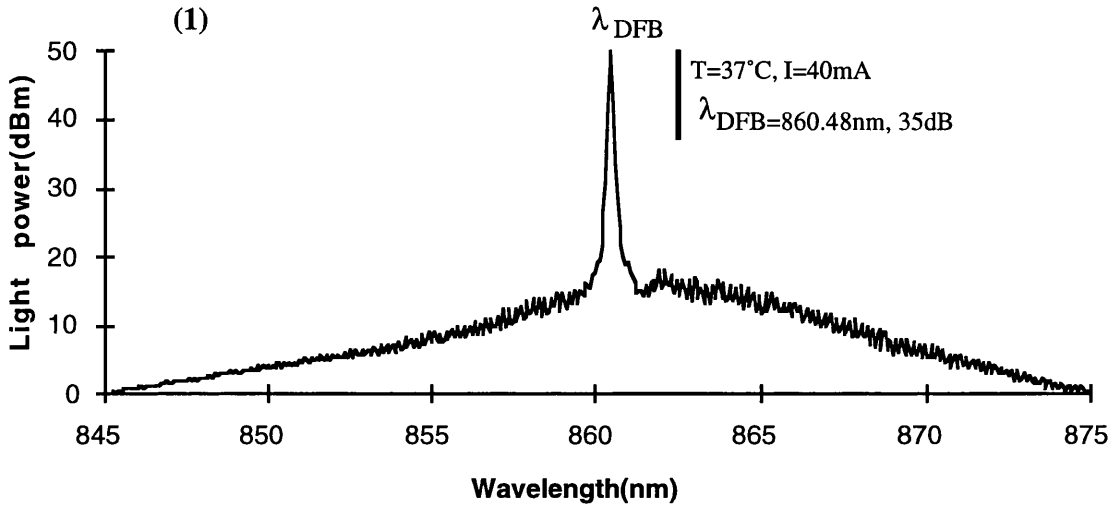

Fig.6.33: Spectrum of a surface 2nd-order grating DFB laser with λ/4 shift at a temperature of 37°C, for I=40mA

Fig.6.33 displays the typical spectrum of a surface 2nd-order grating DFB laser in the temperature range from 15°C to 45°C. The DFB laser emitted in the fundamental mode at 860.48nm, with a side mode suppression ratio of about 35dB.

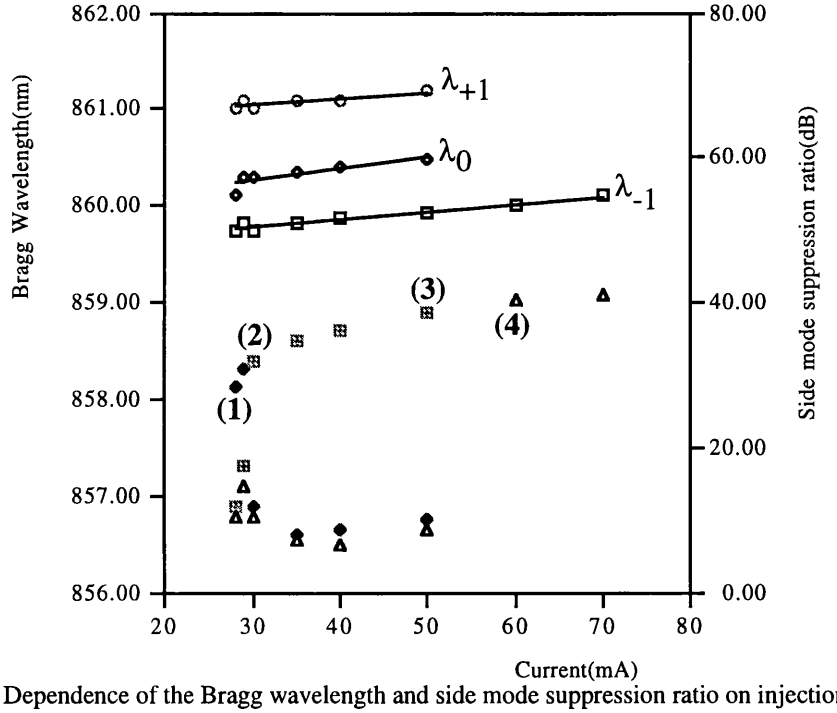

Fig.6.34: Dependence of the Bragg wavelength and side mode suppression ratio on injection current

Fig.6.34 shows the dependence of the Bragg wavelength and side mode suppression ratio on injection current. Around threshold, the dominant mode in the cavity, located at a longer wavelength, is designated by mode +1, spectrum (1). However, as the current is increased, the dominant mode becomes mode 0 for currents between 30mA and 50mA, respectively

spectra (2) and(3). Beyond 50mA, mode -1 becomes the dominant mode in the cavity, as illustrated in spectrum (4) shown below, in Fig.6.36.

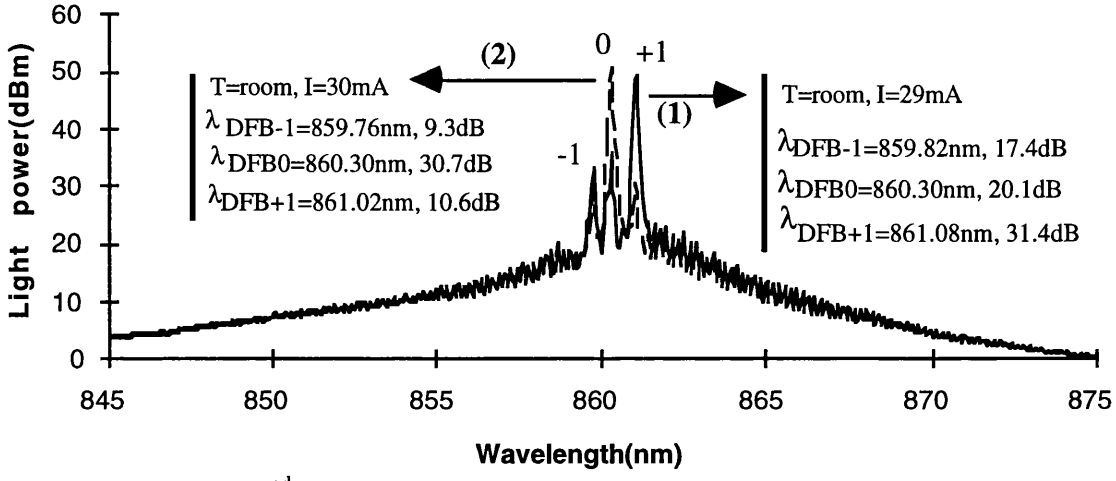

Fig.6.35: Spectra of a surface 2nd-order grating DFB laser at room temperature, for I=29mA and I=30mA

Fig.6.35 displays spectra for a surface 2nd-order grating DFB laser at room temperature and for currents of 29mA and 30mA, respectively spectrum (1) and (2). Spectrum (1) shows laser emission in which mode +1 is dominant at 861.08nm with a side mode suppression ratio of 31.4dB. Modes 0 and -1 are also present at respectively 860.30nm and 859.82nm, with a side mode suppression ratio of about 20dB. In spectrum (2), the surface 2nd-order DFB laser emitted the dominant mode 0 at 860.30nm with a side mode suppression ratio of 30.7dB. Modes +1 and -1 are also present at 861.02nm and 859.76nm, respectively, with a side mode suppression ratio of just about 10dB.

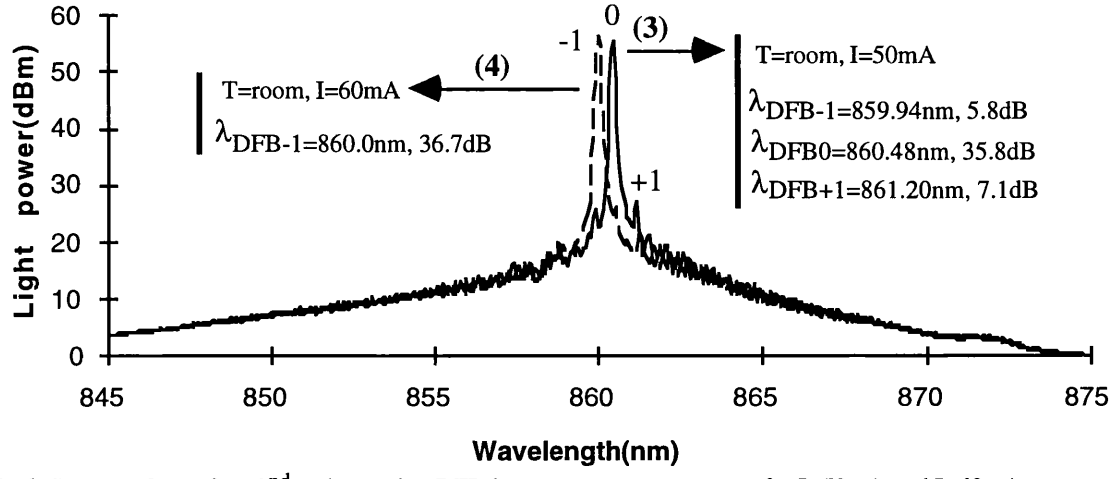

Fig.6.36: Spectra of a surface 2nd-order grating DFB laser at room temperature, for I=50mA and I=60mA

Fig.6.36 shows spectra for a surface 2nd-order DFB laser at room temperature and injection currents of 50mA and 60mA, respectively spectra (3) and (4). Spectrum (3) is typical in the current range from I=30mA to I=50mA. At I=50mA, spectrum (3) displays laser emission in

which the dominant mode is 0 at 860.48nm, with a SMSR of 35.8dB. Modes +1 and -1 are still present at 861.20nm and 859.94nm, respectively, with a side mode suppression ratio of just 6dB. In emission spectrum **(4)**, a typical laser emission for currents larger than 60mA is shown. At I=60mA, the dominant mode is -1, lasing at 860.0nm, with a side mode suppression ratio of 36.7dB.

The results observed in spectra **(1)**, **(2)**, **(3)**, and **(4)** can be explained by the spatial hole burning effect along the laser axis, and the resulting two-mode mechanism. As the injection current is increased, the light intensity in the laser cavity increases. In a $\lambda/4$ DFB laser, the distribution of the light intensity along the laser axis is not uniform. In the strongly coupled case, the light concentrates near the center. Thus, the carrier density in the active layer near the center is reduced remarkably by the stimulated recombination. Such a deformed carrier density profile causes a change in the spatial refractive index. In DFB lasers, a little change in the spatial refractive index drastically affects the lasing modes. In the strongly coupled case, the refractive index near the output facets reduces from that of the averaged value over the laser. This gives shortening of the effective Bragg wavelength near the output facets. As the side mode -1 at the shorter wavelength side matches the resultant effectively modified corrugation well, the threshold gain of the mode -1 decreases. In this way, the threshold gain difference is decreased and two-mode operation occurs.

In summary, the spectral behaviour of surface 2^{nd}-order grating DFB lasers was similar to the spectral behaviour of surface 3^{rd}-order grating DFB lasers, concerning the temperature of operation. However, the spectral dependence on the injection current is characterized, for the surface 2^{nd}-order grating DFB laser, by mode hopping due to hole burning effects. Apparently, hole burning effects are not significant in surface 3^{rd}-order grating DFB lasers.

6.6.2.4 Surface 1^{st}-order grating DFB laser

The following experimental results are from surface 1^{st}-order grating DFB lasers in CW operation. Dependence of the spectral behaviour on both temperature of operation and injection current are discussed. Typical spectra are shown.

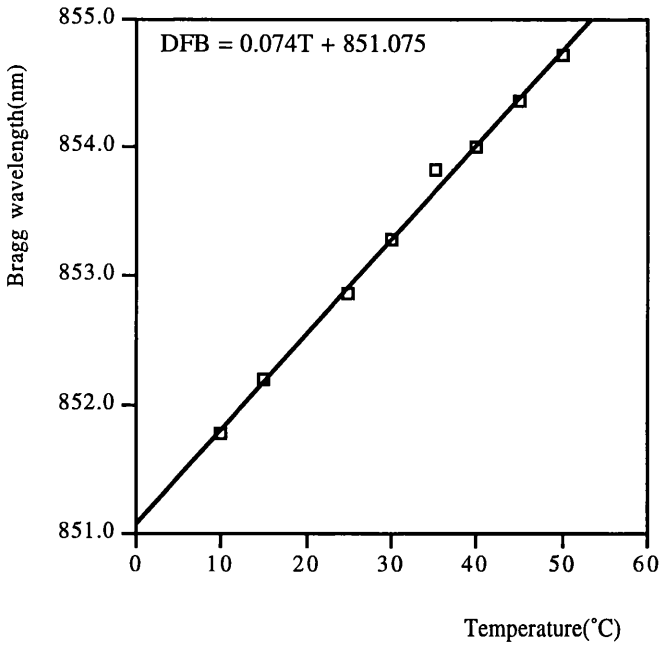

Fig.6.37: Temperature dependence of the Bragg wavelength for a surface 1st-order grating DFB laser

Fig.6.37 shows the temperature dependence of the Bragg wavelength, emitted by a surface 1st-order grating DFB laser, in the temperature range from 10°C to 55°C. The Bragg wavelength dependence on temperature shows a value of 0.074nm/°C.

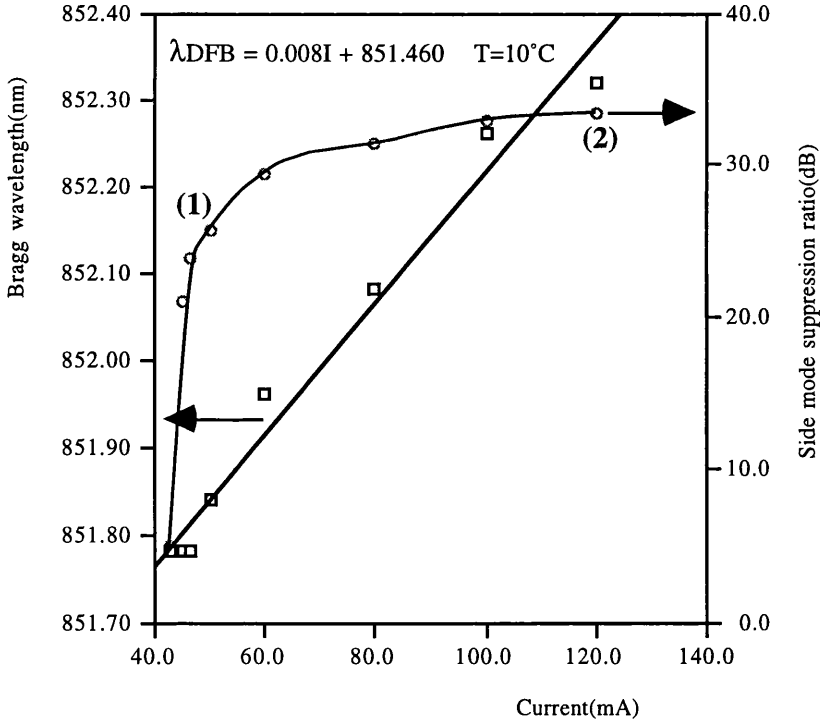

Fig.6.38: Dependence of the Bragg wavelength and side mode suppression ratio on injection current

Fig.6.38 shows the Bragg wavelength and side mode suppression ratio dependence on the injection current. The Bragg wavelength dependence on the injection current is 0.008nm/mA.

The side mode suppression ratio is larger than 30dB for currents larger than $1.3I_{th}$. Typical spectra at points **(1)** and **(2)** are shown below in Fig.6.47.

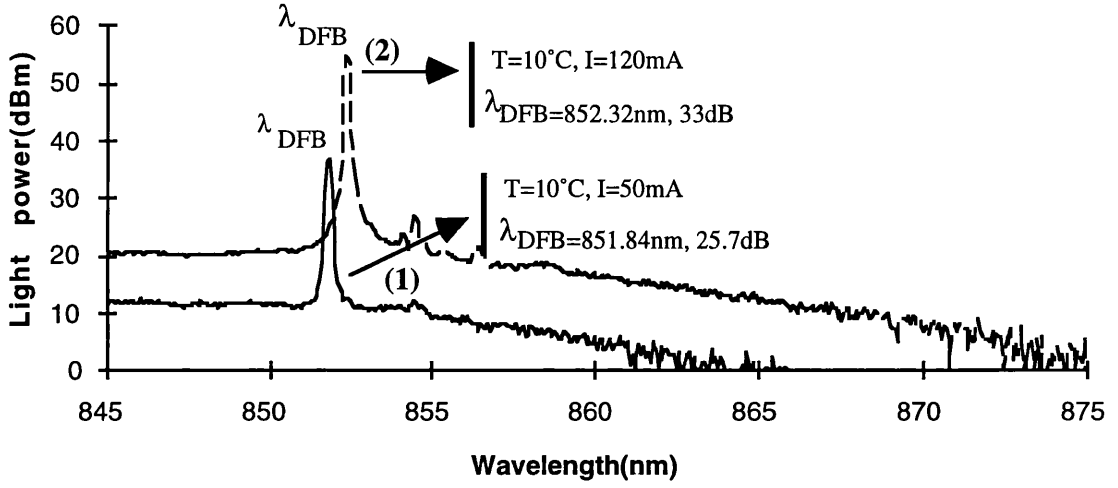

Fig.6.39: Spectra of a surface 1st-order grating DFB laser at a temperature of 10°C, for I=50mA and I=120mA

Fig.6.39 displays spectra of a surface 1st-order grating DFB laser at a temperature of 10°C and currents of 50mA and 120mA. In spectrum **(1)**, the DFB laser emitted in the fundamental mode at 851.84nm, with a side mode suppression ratio of 26dB. Spectrum **(2)** shows the laser emission of the fundamental mode at 852.32nm, with a side mode suppression ratio of 33dB.

In conclusion, the temperature dependence of both Fabry-Perot and Bragg wavelengths were measured in uncoated surface 3rd-order grating DFB laser. Values of 0.36nm/°C and 0.066nm/°C were measured, respectively Fabry-Perot and DFB wavelengths. The spectral behaviour of surface 2nd-order grating DFB lasers were seriously degraded by hole burning effects. This results are in contrast with spectral data from surface 3rd-order/1st-order grating DFB laser where hole burning effects seemed not to be significant.

6.7 Lifetime test of 900μm long surface 3rd-order grating DFB laser

In this section, a simple lifetime test, performed using a AR coated surface 3rd-order grating DFB laser, is described. The main purpose of this lifetime test was to assess the reliability of electric contacts and bonding. A 900μm long surface 3rd-order grating DFB laser was chosen to perform a lifetime test, which consisted of running the laser under constant power conditions of 6.5mW from the front facet at room temperature. The lifetime test was performed for about 250 hours (>10 days), and the output light power versus running time is shown in Fig.6.40. The L-I characteristics and spectral behaviour were also measured, before and after the lifetime test, as illustrated below in points **2** and **3**.

1. Lifetime test

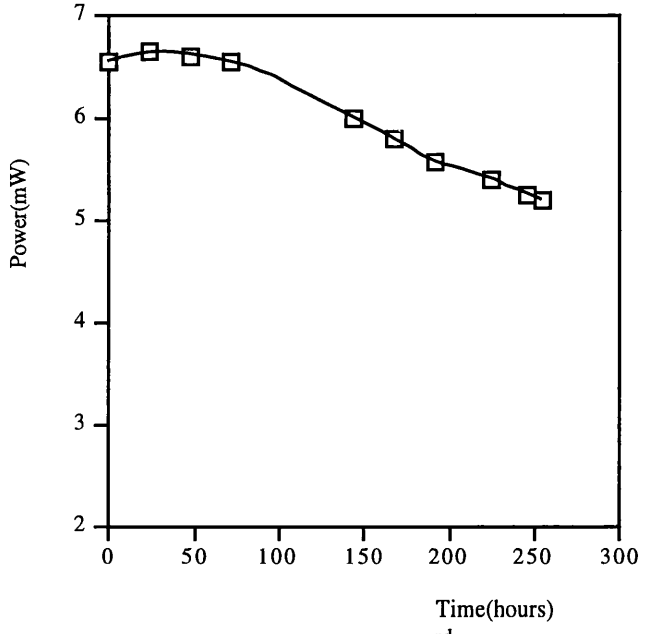

Fig.6.40: Lifetime test of a 900μm long surface 3rd-order grating DFB laser

According to Fig. 6.40, the output light power increases about 1.2% after 25 hours of running under constant power conditions of 6.5 mW. This result may be caused by further annealing of the electric contacts during the first running hours, which have improved the laser performance. However, after 50 hours of running under constant power conditions of 6.5mW, the output light power starts to decrease. The decreasing rate of the light power with time is 0.006 mW/hour, in the time range from 50 to 250 hours.

2. LI curves

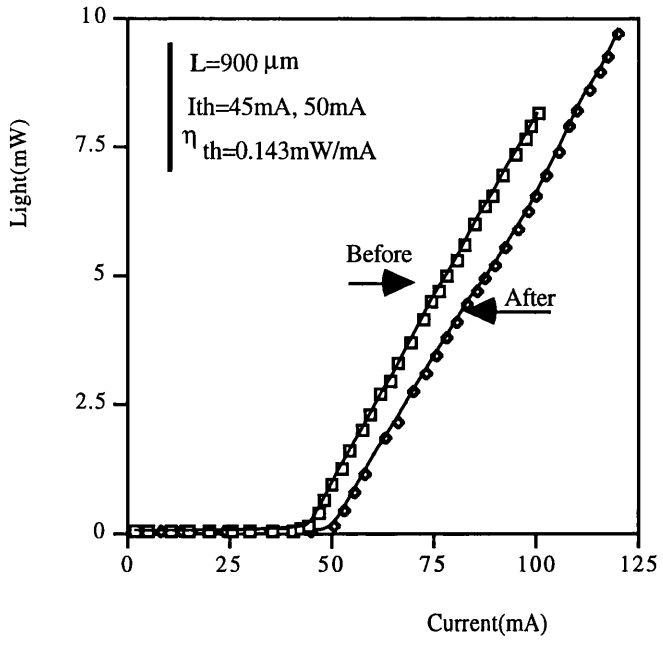

Fig.6.41: Light versus injection current before and after lifetime test

Fig.6.41 shows the light power versus injection current of 3rd-order DFB laser before and after the lifetime test. The threshold current increased by 10% after 250 hours of running under average power conditions of 6 mW. This increase in the threshold current is probably related to degradation of the facets. The external quantum efficiency has about the same value before and after the lifetime test, which is 0.143 mW/mA.

3. Spectral behaviour

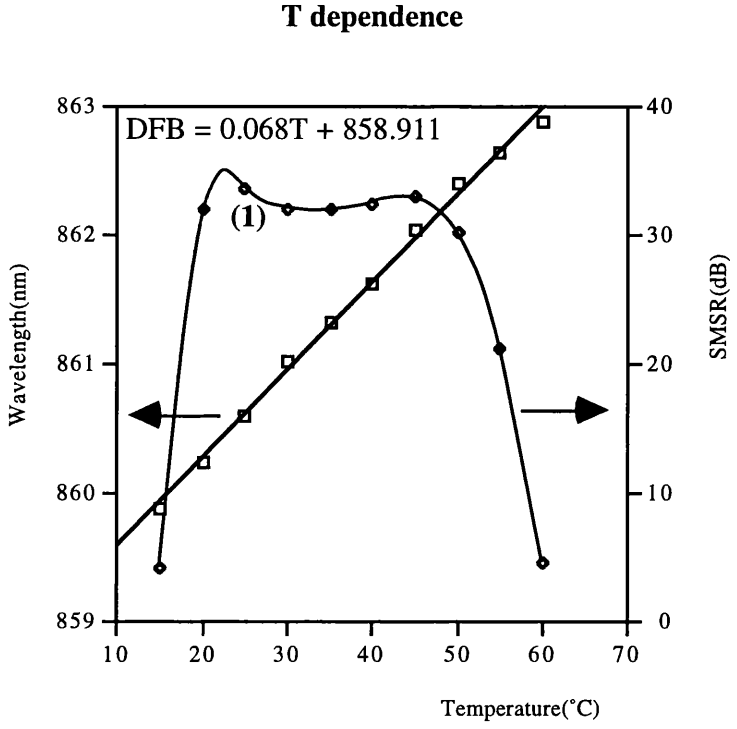

Fig.6.42: Bragg wavelength and side mode suppression ratio as function of the temperature before lifetime test

Fig.6.42 shows the dependences of the Bragg wavelength and side mode suppression ratio on temperature before the lifetime test. The fundamental mode is the only one to lase and exhibits a side mode suppression ratio larger than 30dB in the entire temperature range from 20°C to 50°C. The Bragg wavelength dependence on temperature is 0.068nm/°C, which is a value normally measured. Similar results were measured using the same laser after ageing experiment, the only difference observed was a decrease of the SMSR, since the second transverse mode was coupled. A typical spectrum in the temperature range from 20°C to 50°C, represented as **(1)** in Fig.6.42 above, is shown below in Fig.6.43.

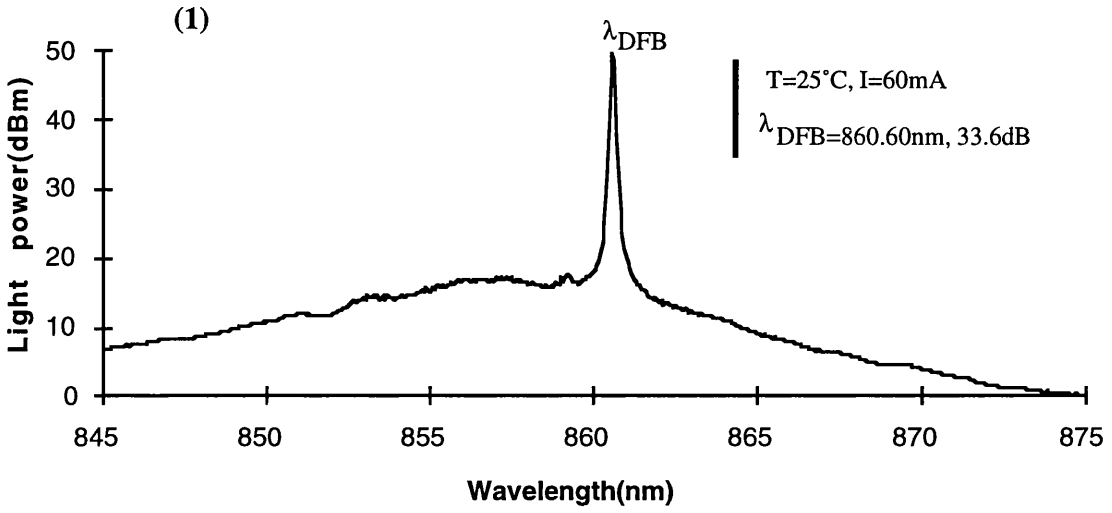

Fig.6.43: Spectrum of surface grating DFB laser before lifetime test

Fig.6.43 shows the spectrum of the 900μm long 3rd-order DFB laser at a temperature of 25°C and an injection current of 60mA; this spectrum is typical in the temperature range from 20°C to 50°C. The spectrum shows the fundamental mode at 860.60nm, with a side mode suppression ratio of 33.6dB. A similar spectrum was measured from the same laser after the ageing experiment, the only difference to be pointed out was a decrease of the SMSR of the fundamental mode to 30dB and coupling of the 2nd transverse mode, which exhibited a SMSR of 2.5dB.

In conclusion, an ageing test consisting of running a 900μm long surface 3rd-order grating DFB laser under constant power constant of 6.5mW at room temperature was performed for about 250 hours. The decreasing rate of light power with time was measured to be about 0.006nW/hour and the increase of the threshold current, after running in CW operation, was 10%. Simple mode operation was observed in the temperature range from 20°C and 50°C. A slight decrease of the SMSR was measured after the ageing experiment, due to the coupling of the second transverse mode.

6.8 Measurement of the laser characteristics of flared amplifier integrated with a surface grating DFB laser

Previous sections of this chapter have been concerned with characterization of simple devices consisting of surface grating DFB lasers. Now, in this section, a more complex device, consisting of a flared amplifier integrated with a surface grating DFB laser, is described and characterized. As mentioned previously, surface grating DFB lasers are particularly attractive for integration because of its entirely planar processing. This characteristic motivated the integration of these devices with optical power amplifiers.

Optoelectronic integrated circuits have the potential for greatly reducing the assembly costs and improving the performance of complex optoelectronic circuits. The ideal integrated light source for such circuits would be a laser with some form of internal feedback, removing the necessity of cleaved facets. Surface grating DFB lasers negate the need for any regrowth, as the fabrication is entirely planar and can be applied to a fully characterised epitaxial structure. The gratings of the DFB laser were produced by electron-beam lithography, but other features were defined by photolithography.

The amplifier expands at an angle of 3.7°, to allow for the adiabatic expansion of the DFB mode. The amplifier is formed by etching a tapered window in the insulating silicon dioxide capping layer. The light in the amplifier is only gain guided to prevent any additional lateral modes from appearing. Further design details can be found elsewhere [6.11]-[6.13].

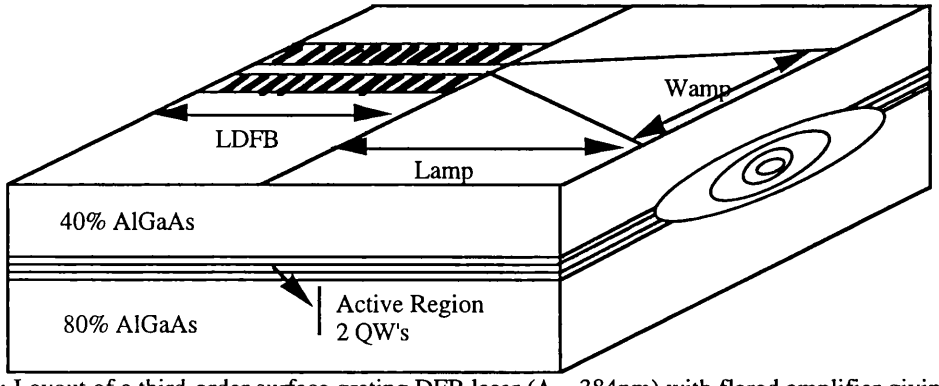

Fig.6.44: Layout of a third-order surface grating DFB laser (Λ_g=384nm) with flared amplifier giving a high power, narrow spectrum, single transverse mode output at 861nm. The laser is L_{DFB}=450μm long and 3.5μm wide. The amplifier section is L_{amp}=500μm long and expands from 3.5μm to W_{amp}=72.5μm in width.

The characterization of the device represented in Fig.6.44 above, which consisted of measuring the L-I characteristics as well as the spectral behaviour for different regimes of current in the amplifier and DFB laser sections, is now described. All characterization results discussed in this section were taken in *CW operation*.

1. L-I curves

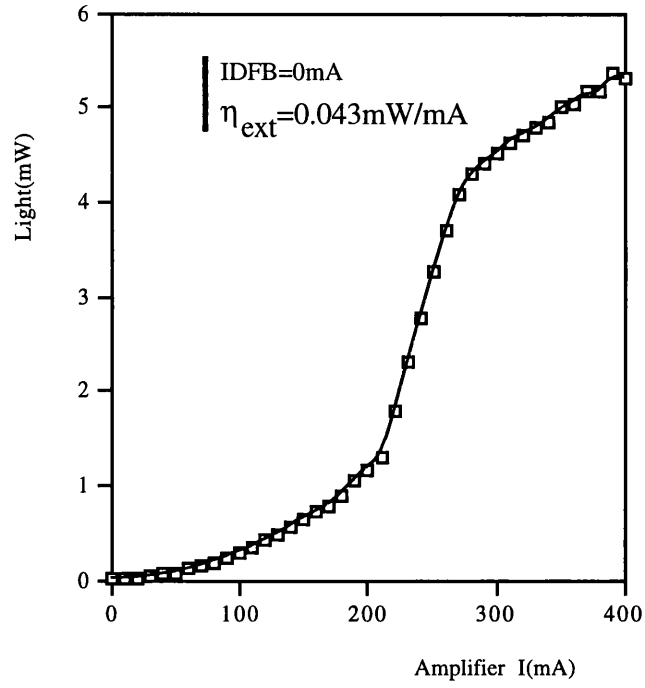

Fig.6.45: Light power versus current in the amplifier section for I_{DFB}=0mA

Fig.6.45 shows the light power versus injection current characteristic in the amplifier section, for I_{DFB}=0mA. Despite the AR coatings, the device works as a rudimentary DBR laser, since the current in the laser section is zero and there is still a significant output power when the amplifier section is pumped beyond 200mA. Further evidence of this DBR behaviour is given later, when the spectral behaviour at I_{DFB}=0mA is discussed. The cavity of such a DBR laser is formed by the DFB laser and the residual reflectivity of the amplifier facet, which is AR coated. From I_{amp}=0 to 200mA, the light emission is generated by spontaneous processes in the amplifier section. However, in the range from I_{amp}=200 to 300mA, the device is lasing as evidenced by an increase in the slope efficiency and a narrow spectral emission (Fig.6.48). Beyond I_{amp}=300mA, the device is still lasing but it has reached a saturation regime. The threshold current, as expected, is very high at about 220mA, and the external quantum efficiency is 0.043mW/mA, measured using points from I_{amp}=200 to 300mA.

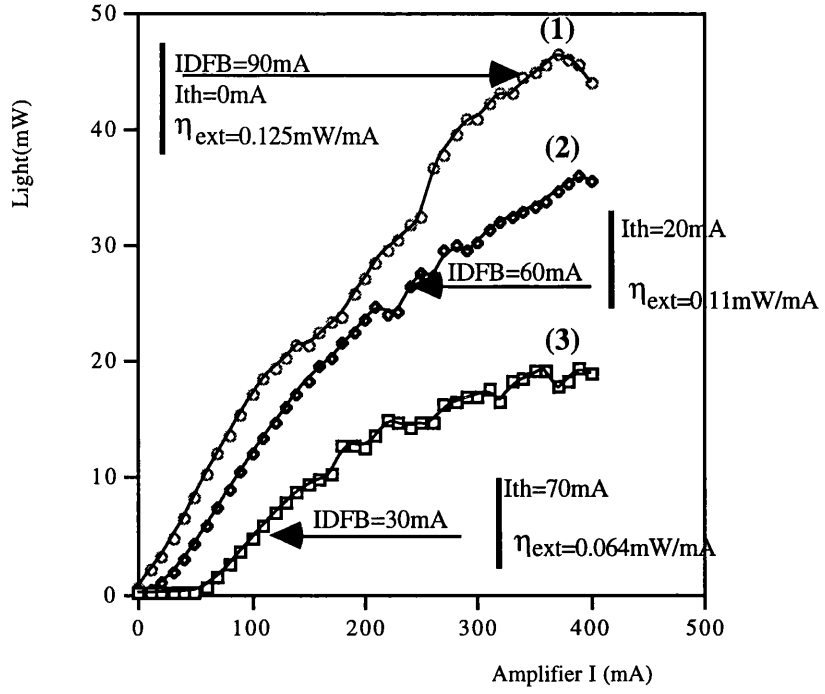

Fig.6.46: Light power versus current in the amplifier section for I_{DFB}=30,60,90mA

Fig.6.46 shows the light power versus injection current characteristics in the amplifier section, using the current in the DFB laser section as a parameter. The L-I curves **(1)**, **(2)**, **(3)**, respectively for I_{DFB}=90, 60, 30mA, give different values of the threshold current and external quantum efficiency. The **(1)** L-I curve, for I_{DFB}=90mA, gives a threshold current of I_{amp}=0mA, that is, the light emitted by the DFB laser at I_{DFB}=90mA is enough to cross the unpumped amplifier section, and the external quantum efficiency is 0.125mW/mA. In this regime, curve **(1)**, powers as high as 45mW CW were measured. For the L-I curve **(2)**, the threshold current is I_{amp}=20mA and the external quantum efficiency is 0.11mW/mA. Finally, the L-I curve **(3)** gives a threshold current of I_{amp}=70mA and an external quantum efficiency of 0.064mW/mA.

2. Spectral behaviour

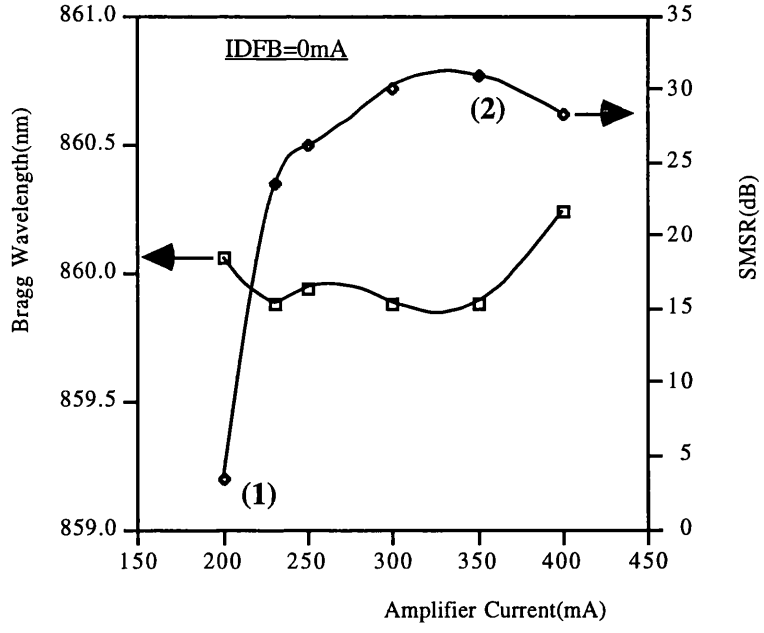

Fig.6.47: Bragg wavelength and side mode suppression ratio versus amplifier current for I_{DFB}=0mA

Fig.6.47 displays the dependence of the Bragg wavelength and side mode suppression ratio on the amplifier injection current, for I_{DFB}=0mA. The Bragg wavelength is nearly constant over the range from 230mA to 350mA. At 200mA, the laser is below threshold and thus the wavelength represented is the peak of the electroluminescence, which is located at a longer wavelength than the Bragg wavelength. At 400mA, the Bragg wavelength is red-shifted, probably by thermal effects, i.e., an increase in operation temperature.

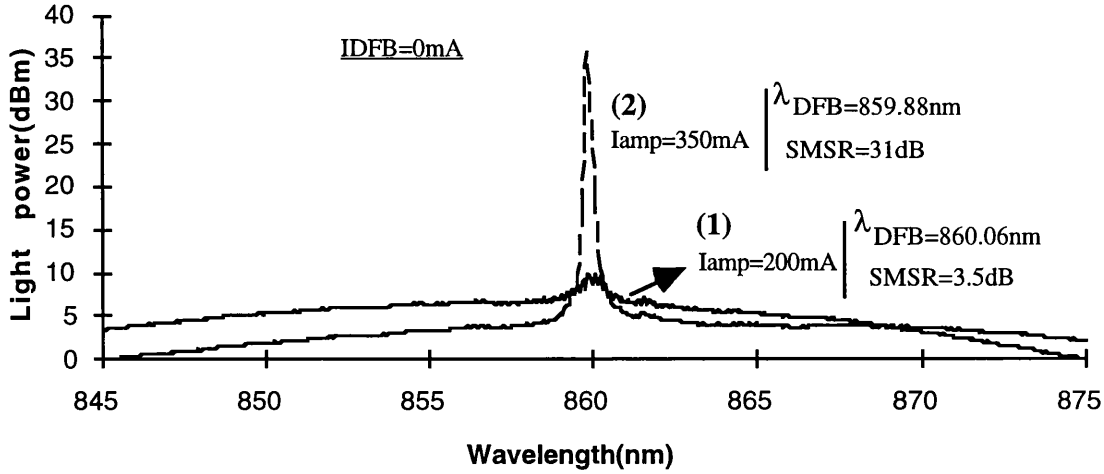

Fig.6.48: Spectra of flared amplifier integrated with DFB laser for I_{DFB}=0mA

Fig.6.48 shows spectra of a flared amplifier integrated with a surface grating DFB laser, for I_{DFB}=0mA. At I_{amp}=200mA, the laser is below threshold and the spectrum is broad, representing the electroluminescence emission, the spectrum being already strongly

influenced by the grating. The spectrum at I_{amp}=350mA represents the fundamental mode at 859.88nm, with a side mode suppression rate of 31dB.

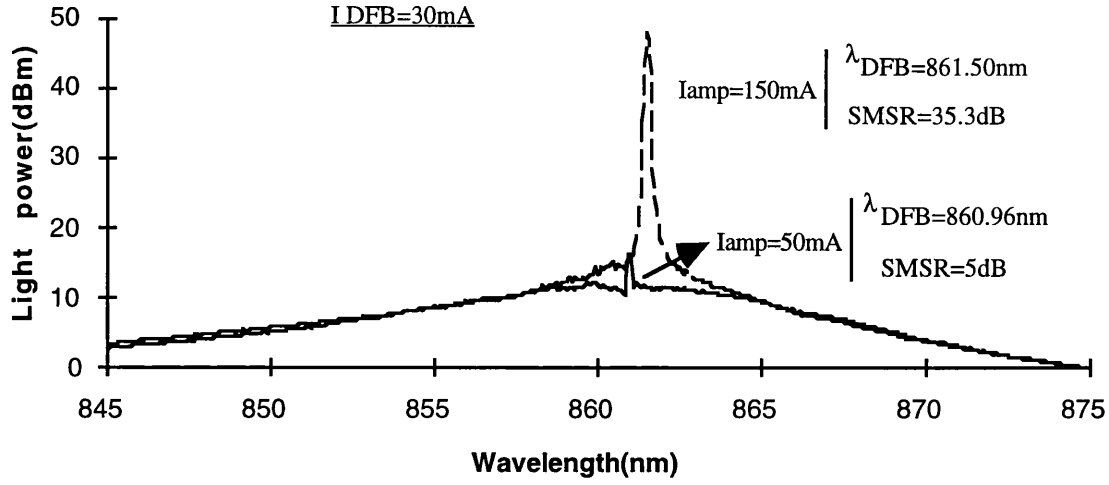

Fig.6.49: Spectra of a flared amplifier integrated with a DFB laser for I_{DFB}=30mA

Fig.6.49 displays spectra of a flared amplifier integrated with a surface grating DFB laser, for I_{DFB}=30mA. The threshold current is about 50mA, as shown in the spectrum at I_{amp}=50mA. At I_{amp}=50mA, the device emitted in the fundamental mode at 860.96nm, with a side mode suppression ratio of 5dB. The spectrum at I_{amp}=150mA shows the fundamental mode at 861.50nm, with a side mode suppression ratio of 35.3dB.

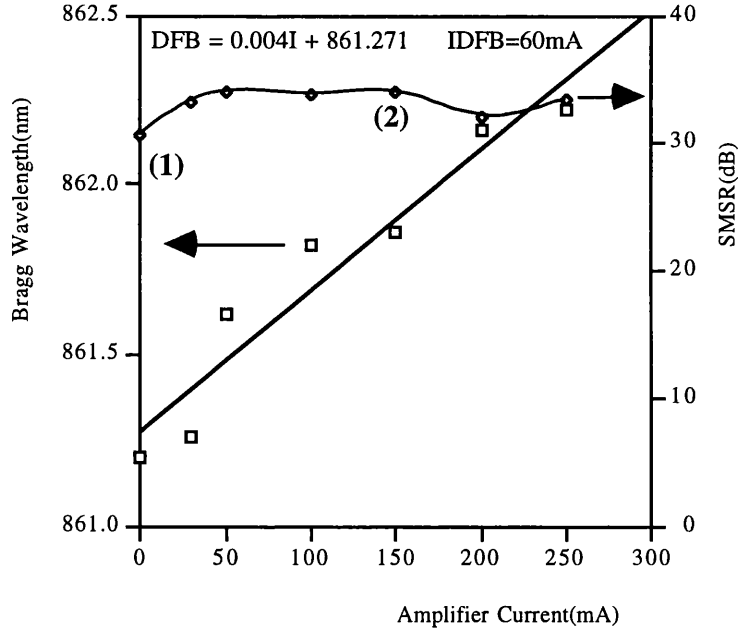

Fig.6.50: Bragg wavelength and side mode suppression ratio versus amplifier current for I_{DFB}=60mA

Fig.6.50 shows the dependence of the Bragg wavelength and the side mode suppression ratio on the amplifier injection current. The Bragg wavelength is red-shifted with the amplifier injection current at a rate of 0.004nm/mA. The side mode suppression ratio remains constant

and larger than 30dB in the amplifier current range from 0mA to 250mA. Spectra at I_{amp}=0 and 150mA, represented respectively by (1) and (2) in Fig. 6.50, are shown below in Fig.6.51.

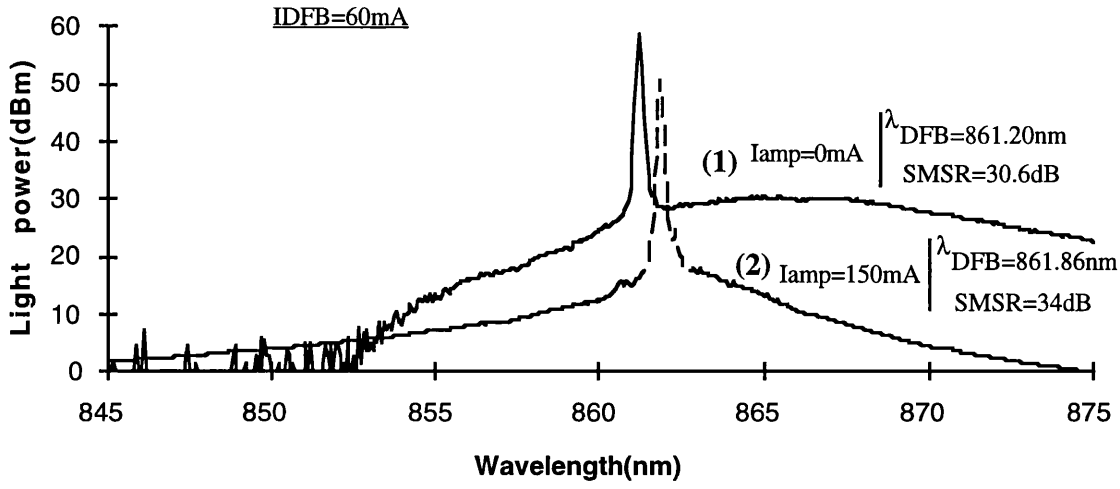

Fig.6.51: Spectra of integrated flared amplifier with DFB laser for I_{DFB}=60mA

Fig.6.51 displays spectra of flared amplifier integrated with a surface grating DFB laser for I_{DFB}=60mA. Despite the fact that the amplifier section is unpumped at I_{amp}=0mA, spectrum (1), the light emitted by the DFB laser when I_{DFB}=60mA is enough to cross the amplifier section at 861.20nm and gives a side mode suppression ratio of 30.6dB. At I_{amp}=150mA, the device emitted in the fundamental mode at 861.86nm, with a side mode suppression ratio of 34.0dB.

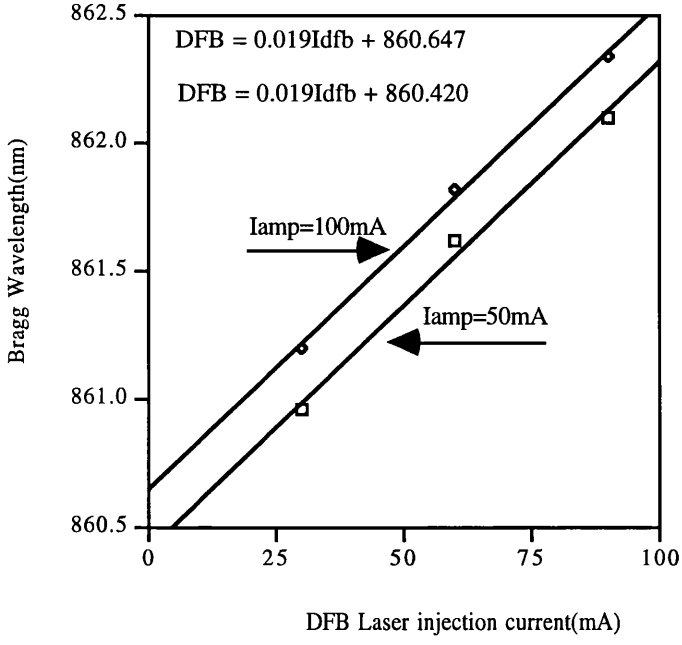

Fig.6.52: Emitted wavelength as a function of injection current in the DFB laser section

Fig.6.52 shows the emitted wavelength from the amplifier facet versus injection current in the DFB laser section, with the current in the amplifier section being used as a parameter. The dependence of the emitted wavelength on the DFB laser injection current is about 0.02nm/mA, whereas the dependence of the emitted wavelength on the amplifier current is five times lower, being 0.004nm/mA. According to these results, the injection current in the DFB laser section can be used to tune the emitted wavelength of this integrated device.

In conclusion, the integration of a flared amplifier with a surface grating DFB laser was realized using a combination of electron-beam lithography, photolithography and reactive ion etching (RIE). The L-I characteristics of the device were measured for different combinations of current in amplifier and DFB laser sections. For I_{DFB}=90mA, a maximum external quantum efficiency of 0.125 mW/mA and power as hight as 45mW CW were measured. The emitted wavelength was about 861 nm and the SMSR was larger than 30dB, for I_{DFB} in the current range from 60mA to 90mA. The dependence of the Bragg wavelength on the DFB laser injection current was measured to be 0.02 nm/mA, whereas the dependence of the Bragg wavelength on the amplifier current was five times lower, being 0.004 nm/mA.

References

[6.1] H. Kogelnik, and C.V. Shank, "Coupled Wave Theory of Distributed Feedback Lasers", J. Appl. Physics, Vol.43, pp.2327-2335 (1972)

[6.2] K. Iga, "On the use of the effective Refractive Index in DFB Laser mode Separation", Jpn J. Appl. Physics, Vol.22, pp.1630 (1983)

[6.3] L.M. Miller, K.J. Beernink, J.T. Verdeyn, J.J. Coleman, J.S. Hughes, , G.M. Smith, J. Honig, and T.M. Cockerill, "Characterization of an InGaAs-GaAs-AlGaAs Strained-Layer Distributed Feedback Ridge-Waveguide Quantum-Well Heterostructure Laser", IEEE Photonics Technol. Lett., Vol.4, pp.296-299 (1992)

[6.4] M. Korn, T. Korfer, A. Forchel, P. Roentgen, "First Order Distributed Feedback Grating (92.5-105nm period) for GaInP/AlGaInP Lasers emitting in the visible range", J. Vac. Science Technol., B8, pp.1404-1407 (1990)

[6.5] R. Schimpe, "Design Considerations of the Metal-Clad Ridge-Waveguide laser with Distributed Feedback", IEE Proceedings, Vol. 132, pp.133-135 (1985)

[6.6] M.J. Adams, A.G. Steventon, W.J. Devlin, and I.D. Henning, *Semiconductor lasers for long-wavelength optical-fibre communications systems*, Peter Peregrinus Ltd, 1987

[6.7] K. Kihara, H. Soda, H.Ishikawa, , and H. Imai, "Evaluation of the coupling coefficient of a distributed feedback laser with residual facet reflectivity", J.Appl.Phys., Vol.42, pp 1526-1527, (1987)

[6.8] R.D. Martin, S. Forouhar, S. Keo, R.J.Lang,, R.G. Hunsperger, R.C. Tiberio, P.F. Chapman, "CW performance of an InGaAs-GaAs-AlGaAs laterally-coupled distributed feedback (LC-DFB) ridge laser diode" IEEE Photonics Technol. Lett., Vol.7, pp.244-246, (1995)

[6.9] J.A. Whiteaway, G.H.B. Thompson, A.J. Collar, and C.J. Armistead, "The design and assessment of $\lambda/4$ phase-shifted DFB laser structures", IEEE J. Quantum Electron., QE-25, pp.1261-1279, (1989)

[6.10] W. Streifer, R.D. Burnham, and D.R. Scifres, "Radiation losses in Distributed Feedback Lasers and longitudinal mode selection", IEEE J. Quantum Electron., QE-12, pp.737-739, (1976)

[6.11] G. Bendelli, K. Komori, and S.Arai, "Gain Saturation and Propagation Characteristics of Index-Guided Tapered-Waveguide Traveling-Wave Semiconductor Laser Amplifiers (TTW-SLA's), Journal of Quantum Electronics, Vol.28, pp.447-458, (1992)

[6.12] R. J. Lang, A Hardy, R. Parke, D. Mehuys, S. O´Brien, J. Major, and D. Welch, "Numerical analysis of flared semiconductor laser amplifiers", IEEE Journal of Quantum Electronics, Vol.29,pp. 447-458, (1993)

[6.13] S. O'Brien, D.F. Welch, R.A.Parke, D. Mehuys, K.Dzurko, R.J.Lang, R.Waartsn and D. Scifres, "Operating Characteristics of a High-Power Monolithically Integrated Flared Amplifier Master Oscillator Power Amplifier", IEEE Journal of Quantum Electronics, Vol.29,pp. 2052-2057, (1993)

[6.14] Section 23, pp.170, *Quantum Semicondutor Structures, Fundamentals and Applications*. Claude Weisbuch and Borge Vinter, Academic Press, Inc. Harcourt Brace Jovanovich, Publishers

Chapter 7: Conclusions and Future Work

7.1 Conclusions

The original purpose of this research work was to fabricate and characterize surface grating DFB lasers and also demonstrate integration potential of these devices. The distributed feedback structure was achieved by deep, dry-etched, gratings alongside the ridge in the top cladding layer of the laser. The material structure was optimized for this type of device and consisted of two 80A GaAs quantum wells surrounded by a 0.7μm thick 40% AlGaAs top cladding layer and a 0.5μm thick 80% AlGaAs lower cladding layer. The typical emission wavelength of the lasers was about 860nm.

Chapter 2 was concerned with hole burning effects both on the L-I curve and on the spectral characteristics of λ/4-shifted DFB lasers. Several techniques proposed to reduce the hole burning effect were reported, namely: (i) optimization of the normalized coupling coefficient, κL, so that the intensity distribution in the DFB laser cavity is constant along the longitudinal axis; (ii) introduction of a λ/4 phase-shift, located in the centre of the cavity or distributed over a certain section; (iii) use of a DFB laser configuration with multiple phase-shifts regions; (iv) use of a dual-pitch DFB laser; (v) use of a DFB laser configuration with an amplitude modulation grating; (vi) use of a non-uniform injection current scheme; (vii) use of a gain coupling mechanism for DFB action. The monolithic integration of a master oscillator with a power amplifier (MOPA) was also reviewed.

In chapter 3, the theory of periodic structures and DFB lasers was reviewed. In particular, the coupled-mode equations were analysed for the passive periodic waveguide and also for distributed feedback lasers. The transmission characteristic of a passive DFB waveguide was plotted as a function of the wavelength in the weak coupling case: κL=0.5-1.5. This result is important for analysing of the measurement of κ in passive DFB waveguides using a transmission technique. The spectrum of a conventional DFB laser, consisting of a single period continuous grating, was calculated using typical values for the coupling coefficient ($\kappa=10cm^{-1}$) and cavity length (L=500μm). The benefits of λ/4 phase-shifts on gratings have also been discussed. The calculation of the coupling coefficient, κ, (in shallow gratings), as a function of the grating depth was performed using different theoretical models, namely: (i) use of the normal coupled-mode analysis; (ii) use of the improved coupled-mode analysis; and (iii) use of a simple effective refractive index analysis. The coupling coefficient, κ, was also calculated in deep surface grating guide structures using a model based on the effective refractive index method. Using typical parameters of the surface grating waveguide, such as

3rd-order grating, stripe width=3.5μm, etch depth=0.5μm, the coupling coefficients obtained by the theoretical model were lower than κ=20cm^{-1}. Finally, a theoretical model based on the perturbation solution of the Floquet-Bloch expansion was used to calculate radiation losses introduced by higher-order gratings.

Improvements in the epitaxial wafer structure for use in surface grating DFB laser fabrication were discussed in chapter 4. To improve the epitaxial wafer structures in terms of internal quantum efficiency, optical losses, gain coefficient per well g_0, transparency current J_t, as well as increasing the interaction between the guided electric field and the grating, different parameters of the wafer structure and composition were optimized. These parameters were namely the Al concentration in the cladding layers, the position of the quantum wells, the number of wells, the doping level in different layers and the layers thicknesses. The final optimized epitaxial structure was an improved asymmetric structure with two quantum wells. The p-type layer was doped with carbon instead of Zn, so as to avoid the damaging effect of Zn diffusion into the active layer. The upper cladding layer was designed with 40% AlGaAs, which provides an optimum electric and optical confinement, while the lower cladding layer was 80% AlGaAs in order to increase the interaction between the guided mode and gratings located in the upper cladding layer. The position of the quantum wells was also optimized to be in the maximum of the electric field, which did not peak in the central position due to the asymmetric cladding layers.

In chapter 5, the surface grating DFB laser structure and its fabrication procedure were discussed. Basically, the fabrication procedure consisted of several steps, namely: (i) sample preparation; (ii) fabrication of the grating alongside the ridge; (iii) fabrication of the contact window and contacts; (iv) cleaving and deposition of anti-reflection coatings; finally (v) mounting and wire-bonding. The most demanding step was the fabrication of the grating alongside the ridge, which required electron beam lithography technology and reactive ion etching (RIE). The design of the device structure, leading to writing of the corresponding patterns and production of files necessary for controlling the e-beam writer; and preparation of the samples, involving choice of suitable electron beam resists and the necessary exposure doses, were thoroughly described in section 5.2. The origin and characteristics as well as techniques to measure stitching errors were also discussed.

Measurement methods, and experimental results were described and interpreted in chapter 6. Measurement of the coupling coefficient, κ, in surface grating DFB waveguides was performed using a transmission technique, consisting of coupling light from a Ti-Sapphire laser into the devices and measuring the light transmitted as a function of the wavelength. For a 1μm deep surface grating waveguide, maximum coupling coefficient values of 10 cm^{-1} and 15 cm^{-1} were measured, respectively for the fundamental and the second transverse mode. An

approximated factor of 2 discrepancy between theory and experiment was observed. This discrepancy can be explained by the impact of loss in the experimentally-measured coupling coefficient, which led to a lower coupling coefficient estimate than actual. This result implies that the discrepancy observed is traceable to loss. In fact, theoretical calculations showed that $10cm^{-1}$ waveguide power loss is responsible for an increase in the coupling coefficient of 50%. This value for the waveguide power loss is reasonable considering theoretical model in section 3.9.

A comparative study of the L-I curves and laser spectra for surface 3rd-order, 2nd-order and 1st-order grating DFB laser in pulsed and CW operation was thoroughly discussed. Typical threshold current, threshold current density, and slope efficiency values for 500μm long devices were, respectively, 25mA, 1400A cm^{-2}, and 0.25mW/mA per facet in CW operation. A lifetime experiment was carried out for 250 hours with the purpose of assessing the reliability of electrical contacts and bonding. The ageing test consisted of running a 900μm long surface 3rd-order grating DFB laser under almost constant power conditions of 6.5 mW per facet at room temperature. After 250 hours of running at 6.5mW CW output power, the threshold current decreased by 10% and the rate at which the light power decreased with time was 0.006mW/hour.

The lasing characteristics of a flared amplifier integrated with a surface grating DFB laser were also discussed in section 6.8. In the DFB laser current range between 60mA and 90mA, the emitted wavelength was about 861nm with a single mode suppression rate (SMSR) larger than 30dB. For I_{DFB}=90mA, the external quantum efficiency was measured to be 0.125mW/mA and a power as high as 45mW CW was achieved. The dependence of the Bragg wavelength on the DFB laser injection current was about 0.02nm/mA, whereas the dependence of the Bragg wavelength on the amplifier current was five times lower, being 0.004nm/mA.

In conclusion, a reliable fabrication process for surface 3rd-order grating structures was developed using electron-beam lithography and reactive ion etching. The same fabrication process was successfully applied in fabricating surface 2nd-order grating structures, but its mark-space ratio requires further optimization. Surface 1st-order grating structures were also fabricated using a more demanding fabrication procedure, which consisted of utilizing thinner layers of electron-beam resist and SiO_2 layer in order to achieve higher resolution. It was demonstrated that DFB laser sources fabricated with surface grating structures are particularly suitable for integration due to its fabrication simplicity, entirely planar processing, and single growth requirement.

7.2 Future work

Possible extensions of the research work carried out in this thesis fall into the following areas:

> **(1)** Measurement of the coupling coefficient, κ, and waveguide loss, α, in surface 2^{nd}-order and 1^{st}-order grating DFB waveguides using the transmission technique (section 6.2) and Fabry-Perot technique.

An accurate knowledge of the fundamental parameters of surface grating DFB waveguides is required so as to optimise the device design. In particular, evaluation of the coupling coefficient, κ, is essential, since it determines the DFB longitudinal mode thresholds and resonant wavelengths. In 2^{nd}-order and 1^{st}-order grating structures, the coupling coefficient is critically dependent of the mark-space ratio. In order to maximise κ, fabrication procedures have to be established so that the mark-space ratio is about 3:1 and 1:1, respectively in 2^{nd}-order and 1^{st}-order gratings. For such purposes, the transmission technique described in detail in section 6.2 can be used for optimizing the fabrication processes of these structures.

> **(2)** Measurement of the emission linewidth of surface 3^{rd}-order, 2^{nd}-order and 1^{st}-order grating DFB lasers using a Fabry-Perot interferometric technique or self-homodyne /heterodyne method.

The narrow linewidth achieved in DFB lasers results from the fact that the grating is much more wavelength selective than a laser based on cleaved or polished end-faces. The single-mode linewidth of a conventional FP laser is typically about 10GHz, whereas in a InGaAsP/InP DFB laser it is 10MHz-98kHz [7.1]. The narrower linewidth of a DFB laser is particularly important for optical communication applications, in which the maximum bit-rate is ultimately limited by the linewidth of the laser source. The emission linewidth may be measured using a Fabry-Perot interferometric technique, which offers a resolution of typically 10 MHz, or a self-homodyne/heterodyne method with improved resolution of about 50kHz [7.2]. In general, the self-homodyne/heterodyne method requires a more complicated set-up. However, a reflection-type delayed self-homodyne method has been recently proposed, which is considerably simpler [7.3].

> **(3)** Modulation performance of these lasers.

The modulation characteristics of a DFB laser are clearly important, specially if these lasers are to be used in optical communication systems

(4) Improvement of the fabrication procedures in order to accurately control the grating etch depth.

The grating etch depth is definitely very important not only to define the waveguiding characteristics (it was shown that 0.6μm grating etch depth waveguides allowed the 2nd transverse mode to be coupled, whereas for a 0.66μm grating etch depth only the fundamental mode was coupled), but also to maximise the coupling coefficient, κ. Improvements in the fabrication process could be obtained by introducing a grown-in etch-depth stop layer formed by a totally different layer composition, such as InGaP in AlGaAs.

(5) Exploitation of alternative device geometries.

Other device structures have been proposed such as grating on the ridge [7.4], gratings along the side walls [7.5], ridge lasers with laterally-coupled distributed feedback [7.6,7.7]. These device structures present the advantage of a larger coupling coefficient, κ, compared to surface grating DFB laser structures. DBR type lasers using surface grating structures could also be considered [7.8].

(6) Transfer of fabrication technology to lasers with similar structure but operating at 1.3μm, 1.55μm, or short wavelengths.

Surface grating structures require only a single epitaxial growth process. Therefore these structures can be fabricated in any material system with any standard growth process for the laser structure. In particular, this fabrication approach can be useful for short wavelength devices with high Al content and long wavelength GaSb based devices.

(7) Improvement of the flared amplifier integrated with a surface grating DFB laser.

Further improvements can be made in the flared amplifier integrated with a surface grating DFB laser presented in section 6.8. In particular, deposition of better AR coatings, and an increase of the amplifier section length.

References

[7.1] M. Okai and T. Tsuchiya, "Tunable DFB lasers with ultra-narrow spectral linewidth" Electronics Letters, Vol.29, pp.349-351, (1993)

[7.2] T.Okoshi, K.Kikuchi and A. Nakayama, "Novel method for high resolution measurement of laser output spectrum", Electronics Letters, Vol.16, pp. 630-631, (1980)

[7.3] K. Iiyama, K. Hayashi, Y.Ida and S.Tabata, "Delayed self-homodyne method using solitary monomode fibre for laser linewidth measurements", Electronics Letters, Vol.25, pp.1589-1590, (1989)

[7.4] M. Korn, T. Korfer, A. Forchel, and P. Roentgen, "First-order distributed feedback grating (92.5-105nm period) for GaInP/AlGaInP lasers emitting in the visible range" J. Vac. Sci. Technol., B8, pp.1404-1407, (1990)

[7.5] V.V.Wong, W.Y.Choi, J.M. Carter, C.G. Foustad, H.I. Smith, Y.Chung, and N. Dagli, "Ridge -waveguide sidewall-grating distributed feedback structures fabricated by x-ray lithography" J. Vac. Sci. Technol., B11, pp.2621-2624, (1993)

[7.6] R.D. Martin, S. Forouhar, S.Keo, R.J.Lang, R.G.Hunsperger, R. Tiberio, and P.F. Chapman, "InGaAs-GaAs-AlGaAs laterally-coupled distributed feedback (LC-DFB) ridge laser diode", Electronics Letters, Vol.30, pp.1058-1060, (1994)

[7.7] R.D. Martin, S. Forouhar, S.Keo, R.J.Lang, R.G.Hunsperger, R. Tiberio, and P.F. Chapman, "Cw performance of an InGaAs-GaAs-AlGaAs laterally-coupled distributed feedabck (LC-DFB) ridge laser diode", IEEE Photon. Technol. Lett., Vol.7, pp.244-246, (1995)

[7.8] G.M. Smith, J.J. Hugles, M.L. Osowski, D.V.Forbes, and J.J. Coleman, "Ridge waveguide distributed Bragg reflector InGaAs/GaAs quantum well lasers", Electronics Letters, Vol.30, pp.651-653, (1994)